Phosphate-Based Cathode Materials for Rechargeable Batteries

A thesis presented for the award of the degree of

Doctor of Philosophy

from

University of Technology Sydney

by

Katja Ramona Kretschmer, Dipl. Ing.

May, 2018

CERTIFICATE OF ORIGINAL AUTHORSHIP

I, Katja Ramona Kretschmer, certify that the work presented in this thesis has not previously been submitted for a degree nor has been submitted as part of requirements for a degree except as fully acknowledged within the text.

I also certify that the thesis has been written by me. Any help that I have received in my research work and the preparation of the thesis itself has been acknowledged. In addition, I certify that all information sources and literature used are indicated in the thesis.

Production Note:
Signature removed prior to publication.

Katja Ramona Kretschmer

Sydney, Australia

May, 2018

DEDICATION

This thesis is dedicated to my family. Thank you for all your love and support.

ACKNOWLEDGEMENTS

Firstly, I would like to thank my supervisor and co-supervisor, Professor Guoxiu Wang and Dr. Bing Sun, for their encouraging and continuous support and invaluable advice throughout my Ph.D. studies.

I would also like to acknowledge Dr. Jane Yao for her assistance and support essential to my laboratory work and professional development.

I gratefully acknowledge the friendship and joint professional accomplishments of my past and present colleagues at the University of Technology Sydney, Dr. Xiuqiang Xie, Dr. Jinqiang Zhang, Dr Yufei Zhao, Dr. Anjon Kumar Mondal, Dr Ying Wang, Dr. Shuangqiang Chen, Dr. Hao Liu, Dr. Zhimin Ao, Dr. Devaraj Shanmukaraj, Dr. Dawei Su, Mr. Xin Guo, Mr. Jianjun Song, Mr. Kefei Li, Miss Jing Xu, and Mr. Weizhai Bao.

In addition, I appreciate the administrative and technical support I received from Dr. Ronald Shimmon, Dr. Linda Xiao, Katie McBean, Mark Berkahn, Sarah King, Emaly Black, and Elizabeth Gurung Tamang.

The financial support from UTS and AutoCRC 2020 (now Excellerate Australia) throughout my Ph.D. studies are highly appreciated.

And finally, I would like to thank my parents, my partner, and family in Germany and Australia for continuously supporting me throughout all my personal and academic adventures.

Katja Ramona Kretschmer

RESEARCH PUBLICATIONS

1. Xiuqiang Xie, **Katja Kretschmer**, Babak Anasori, Bing Sun, Guoxiu Wang, and Yury Gogotsi, Porous $Ti_3C_2T_x$ MXene for Ultrahigh-Rate Sodium-Ion Storage with Long Cycle Life, ***ACS Applied Nano Materials***, 2018, In Press, DOI: 10.1021/acsanm.8b00045.
2. Xiuqiang Xie, Shijian Wang, ***Katja Kretschmer***[1], and Guoxiu Wang, Two-dimensional layered compound based anode materials for lithium-ion batteries and sodium-ion batteries, ***Journal of Colloid and Interface Science***, 2017, 499, 17-32.
3. Tianyi Wang, ***Katja Kretschmer***, Sinho Choi, Huan Pang, Huaiguo Xue, and Guoxiu Wang, Fabrication Methods of Porous Carbon Materials and Separator Membranes for Lithium–Sulfur Batteries: Development and Future Perspectives, ***Small Methods***, 2017, 1, 1700089.
4. Anjon Kumar Mondal, ***Katja Kretschmer***, Yufei Zhao, Hao Liu, Hongbo Fan and Guoxiu Wang, Naturally nitrogen doped porous carbon derived from waste shrimp shells for high-performance lithium ion batteries and supercapacitors, ***Microporous and Mesoporous Materials***, 2017, 246, 72-80
5. Jinqiang Zhang, Bing Sun, Yufei Zhao, ***Katja Kretschmer***, and Guoxiu Wang Modified Tetrathiafulvalene as an Organic Conductor for Improving Performances of Li−O_2 Batteries, ***Angewandte Chemie International Edition***, 2017, 56, 8505-8509.
6. Jinqiang Zhang, Bing Sun, Andrew M. McDonagh, Yufei Zhao, ***Katja Kretschmer***, Xin Guo, and Guoxiu Wang, A multi-functional gel co-polymer bridging liquid electrolyte and solid cathode nanoparticles: An efficient route to Li–O_2 batteries with improved performance, ***Energy Storage Materials***, 2017, 7, 1-7.

[1] Shared first author with X. Xie and S. Wang.

7. Bing Sun, ***Katja Kretschmer***, Xiuqiang Xie, Paul Munroe, Zhangquan Peng, and Guoxiu Wang, Hierarchical Porous Carbon Spheres for High-Performance Na–O_2 Batteries, ***Advanced Materials***, 2017, 29, 1606816.
8. Katja Kretschmer, Bing Sun, Jinqiang Zhang, Xiuqiang Xie, Hao Liu, and Guoxiu Wang, 3D Interconnected Carbon Fiber Network-Enabled Ultralong Life $Na_3V_2(PO_4)_3$@Carbon Paper Cathode for Sodium-Ion Batteries**,** ***Small***, 2017, 13, 1603318.
9. Anjon Kumar Mondal, ***Katja Kretschmer***, Yufei Zhao, Hao Liu, Chengyin Wang, Bing Sun, and Guoxiu Wang, Nitrogen-Doped Porous Carbon Nanosheets from Eco-Friendly Eucalyptus Leaves as High Performance Electrode Materials for Supercapacitors and Lithium Ion Batteries, ***Chemistry – A European Journal***, 2017, 23, 3683-3690.
10. ***Katja Kretschmer****,* Bing Sun*,* Xiuqiang Xie*,* Shuangqiang Chen*,* and Guoxiu Wang, A free-standing $LiFePO_4$–carbon paper hybrid cathode for flexible lithium-ion batteries, ***Green Chemistry***, 2016, 18, 2691-2698.
11. Anjon Kumar Mondal, Hao Liu, Xiuqiang Xie, ***Katja Kretschmer***, and Guoxiu Wang, Hydrothermal Synthesis of Multiwalled Carbon Nanotube–Zinc Manganate Nanoparticles as Anode Materials for Lithium Ion Batteries, ***ChemPlusChem***, 2016, 81, 399-405.
12. Ying Wang, ***Katja Kretschmer***, Jinqiang Zhang, Anjon Kumar Mondal, Xin Guoa, and Guoxiu Wang, Organic sodium terephthalate@graphene hybrid anode materials for sodium-ion batteries, ***RSC Advances***, 2016, 6, 57098-57102.
13. Dawei Su, ***Katja Kretschmer***, and Guoxiu Wang, Improved Electrochemical Performance of Na-Ion Batteries in Ether-Based Electrolytes: A Case Study of ZnS Nanospheres, ***Advanced Energy Materials***, 2016, 6, 1501785.
14. Jinqiang Zhang, Bing Sun, Xiuqiang Xie, ***Katja Kretschmer***, and Guoxiu Wang, Enhancement of stability for lithium oxygen batteries by employing electrolytes gelled by poly(vinylidene fluoride-co-hexafluoropropylene) and tetraethylene glycol dimethyl ether, ***Electrochimica Acta***, 2015, 183, 56-62.

15. Anjon Kumar Mondal, Shuangqiang Chen, Dawei Su, ***Katja Kretschmer***. Hao Liu, and Guoxiu Wang, Microwave synthesis of α-Fe_2O_3 nanoparticles and their lithium storage properties: A comparative study, ***Journal of Alloy and Compounds***, 2015, 648, 732-739.
16. ***Katja Kretschmer***, Bing Sun, Dawei Su, Yufei Zhao, and Guoxiu Wang, Scalable Preparation of $LiFePO_4$/C Nanocomposites with sp^2-Coordinated Carbon Coating as High-Performance Cathode Materials for Lithium-Ion Batteries, ***ChemElectroChem***, 2015, 2, 2096-2103.
17. Xiuqiang Xie, ***Katja Kretschmer***, Jinqiang Zhang, Bing Sun, Dawei Su, and Guoxiu Wang, Sn@CNT nanopillars grown perpendicularly on carbon paper: A novel free-standing anode for sodium ion batteries, ***Nano Energy***, 2015, 13, 208-217.
18. Xiuqiang Xie, ***Katja Kretschmer***, and Guoxiu Wang, Advances in graphene-based semiconductor photocatalysts for solar energy conversion: fundamentals and materials engineering, ***Nanoscale***, 2015, 7, 13278-13292.
19. Anjon Kumar Mondal, Dawei Su, Shuangqiang Chen, ***Katja Kretschmer***, Xiuqiang Xie, Hyo-Jun Ahn, and Guoxiu Wang, A Microwave Synthesis of Mesoporous $NiCo_2O_4$Nanosheets as Electrode Materials for Lithium-Ion Batteries and Supercapacitors, ***ChemPhysChem***, 2015, 16, 169-175.
20. Jinqiang Zhang, Shuangqiang Chen, Xiuqiang Xie, ***Katja Kretschmer***, Xiaodan Huang, Bing Sun, and Guoxiu Wang, Porous poly(vinylidene fluoride-co-hexafluoropropylene) polymer membrane with sandwich-like architecture for highly safe lithium ion batteries, ***Journal of Membrane Science***, 2014, 472, 133-140.

TABLE OF CONTENTS

LIST OF TABLES

LIST OF FIGURES

ABSTRACT

The design of electrode materials depends critically on understanding the underlying electrochemical processes. Material composition, morphology, structure, and preparation method affect and can alter electrochemical performance of electrochemically active materials. In this research project, a series of phosphate-based polyanionic electrode materials have been fabricated and their electrochemical properties for the use in lithium-ion and sodium-ion batteries are evaluated.

We successfully prepared carbon-coated $LiFePO_4$ cathode materials by industrial ball milling and a solid-state reaction with Li_2CO_3, $NH_4H_2PO_4$, and $FeC_2O_4 \cdot 2H_2O$ as starting materials. Soluble starch as the primary carbon source was investigated for its capability of generating a highly graphitic carbon coating, whilst sufficiently controlling the crystal growth of $LiFePO_4$. XRD analysis, Raman spectroscopy, and electrochemical testing revealed the significant impact of the amount of starch added to the pre-sintered precursor on phase purity, carbon quality, and electrochemical performance of the final $LiFePO_4$/C composite. The optimum soluble starch content to achieve a highly sp^2-coordinated carbon coating is 10 wt%, which enabled our $LiFePO_4$/C composite to achieve competitive reversible capacities as well as improved rate performance

The spray method is well-trusted in practical applications, such as food manufacturing, fertilizers, oxide ceramics, and pharmaceuticals. The ability to produce uniformly spherical particle clusters ranging from nano- to micrometre in size is one of the main advantages of this method, which is immensely important for large scale production of electrochemically active materials for the energy storage market. In this report, we systematically evaluated spray-drying conditions and equipment settings in regards to electrochemical performance of carbon coated $LiFePO_4$ cathode materials. In an optimisation trial, the most suitable process conditions for the precursor materials and spray-dryer model used to prepare pure and practical $LiFePO_4$ cathode materials were identified. The impact

of different organic additives on the resulting particle morphology of the final product was also investigated. It was found that the addition of polyvinyl alcohol (PVA) generates particle clusters that provide a high tap density product without sacrificing electrochemical performance. The $LiFePO_4$ cathode material prepared with the addition of PVA achieved remarkable rate performance results and could maintain a capacity of 113.95 mA h g^{-1} at 10C.

Lithium-ion batteries (LIBs) are widely implemented to power portable electronic devices and are increasingly in demand for large-scale applications. One of the major obstacles for this technology is still the low cost-efficiency of its electrochemical active materials and production processes. In this work, we present a novel impregnation–carbothermal reduction method to generate a $LiFePO_4$–carbon paper hybrid electrode, which does not require a metallic current collector, polymeric binder or conducting additives to function as a cathode material in a LIB system. A shell of $LiFePO_4$ crystals was grown *in situ* on carbon fibres during the carbonization of microcrystalline cellulose. The $LiFePO_4$–carbon paper electrode achieved an initial reversible areal capacity of 197 μA h cm^{-2} increasing to 222 μA h cm^{-2} after 500 cycles at a current density of 0.1 mA cm^{-2}. The hybrid electrode also demonstrated a superior cycling performance for up to 1000 cycles. The free-standing electrode could be potentially applied for flexible lithium-ion batteries.

Sodium-ion batteries (NIBs) are an emerging technology, which can meet increasing demands for large-scale energy storage. One of the most promising cathode material candidates for sodium-ion batteries is $Na_3V_2(PO_4)_3$ due to its high capacity, thermal stability, and sodium (**Na**) **s**uper**i**onic **con**ductor 3D (NASICON)-type framework. In this work, the authors have significantly improved electrochemical performance and cycling stability of $Na_3V_2(PO_4)_3$ by introducing a 3D interconnected conductive network in the form of carbon fibre derived from ordinary paper towel. The free-standing $Na_3V_2(PO_4)_3$-carbon paper ($Na_3V_2(PO_4)_3$@CP) hybrid electrodes do not require a metallic current collector, polymeric binder, or conducting additives to function as a cathode material in an

NIB system. The $Na_3V_2(PO_4)_3$@CP cathode demonstrates extraordinary long-term cycling stability for 30 000 deep charge– discharge cycles at a current density of 2.5 mA cm^{-2}. Such outstanding cycling stability can meet the stringent requirements for renewable energy storage.

INTRODUCTION

Current estimations of population growth and consequential increased energy demand predict that we will consume 2.2 tons of oil equivalents (TOE) per capita by 2030. With our current means of using fossil fuels, this will release unsustainable amounts of greenhouse gases in addition to the fact that these sources of energy will be depleted eventually. It is generally accepted that advanced renewable energy technologies are urgently needed to support current population growth and to maintain energy security for generations to come.

Current integration of renewable energy sources, such as wind or solar energy, present the problem of reliability if directly fed into the grid. The demand for energy by households or industry and the production of energy are not naturally in synch. In the course of a day, these renewable sources might not be available or are producing an oversupply when not needed causing instability within the power grid, which is the main reason why they are not widely implemented in Australia.

Large-scale energy storage systems are believed to be the solution to this critical issue as they are able to buffer peak load energy and output fluctuations by storing and releasing energy as demand and supply are changing during the day.

Lithium-ion batteries (LIBs), as one possible energy storage system, now surpass other battery systems, such as lead–acid or nickel metal hydride batteries, in terms of energy density. Their current applications range from electric vehicles (EV) and hybrid electric vehicles (HEV) to portable devices, such as mobile phones and laptops. Although substantial progress has been made to improve LIBs, significant enhancements in energy density, cost, and cyclability are still required. The performance of LIBs is critically affected by the performance of the electrode materials used in the electrochemical cell, especially on the cathode side. This research project focuses on the development of different advanced $LiFePO_4$ cathode materials prepared by different industry-ready and low-cost preparation methods.

Furthermore, sodium-ion batteries (SIBs) have attracted attention as a low-cost alternative to LIBs because sodium is the fourth most abundant element in the earth's crust with widespread distribution of sodium minerals. With a working principle similar to that of the lithium system, SIBs are in the early stage of development with one prototype battery entering the market in 2015. Due to the larger atomic radius of the Na^+, finding suitable materials that can accommodate and tolerate electrochemical reactions with sodium is challenging. In this project, one vanadium- and phosphate-based polyanionic cathode material, $Na_3V_2(PO_4)_3$, is investigated.

For both LIBs and SIBs, the electrochemical reaction occurs at the electrode surface and requires the transport of ions into the electrode material. Consequently, electrode material design is vital to achieve high performance batteries. Methodologies such as optimization of the preparation process, material composition, and morphology as well as harmonious hybridization between each component were applied in this work to fabricate advanced electrode materials for LIBs and SIBs.

Each chapter therefore is outlined as follows:

1) Chapter 1 reviews the development of LIBs and SIBs electrode materials, with special attention given to phosphate-based polyanionic material candidates. The working principle, development of selected anode and cathode materials are presented. For sodium-ion batteries, the comparison to lithium-ion batteries is given and advances in cathode materials and anodes are summarized.

2) Chapter 2 presents the experimental methods used during this research project including material preparation, physiochemical characterizations, and electrochemical investigations. The main method to prepare the electrode materials in this work are solid-state reaction and hydrothermal synthesis. Structural and morphological investigations are carried out using X-ray diffraction (XRD), field emission scanning electron microscopy (FESEM), transmission electron microscopy (TEM), nitrogen adsorption-desorption, Raman spectroscopy,

and thermogravimetric analysis. Electrode fabrication and cell assembly protocols as well as electrochemical characterisation techniques are also presented.

3) Chapter 3 presents a carbon-coated $LiFePO_4$ cathode material prepared through industrial ball milling and solid-state reaction by using Li_2CO_3, $NH_4H_2PO_4$, $FeC_2O_4 \cdot 2\ H_2O$, and soluble starch as a carbon source to generate highly graphitic carbon coatings. Special attention has been paid to the correlation between the applied amount of carbon and the sp^2-coordinated carbon generation, as low-temperature sintering usually yields more disordered carbons.

4) Chapter 4 systematically evaluates spray-drying conditions and equipment settings in regards to electrochemical performance of the obtained carbon coated $LiFePO_4$ cathode material. This includes variations in spray-drying feed rate and drying temperature while precursor materials, suspension concertation, and amount of added carbon source remained unchanged for each parameter. After optimal conditions were established, the impact of the carbon precursor choice (namely citric acid, polyethylene glycol, and polyvinyl alcohol) on micro-particle morphology was evaluated.

5) Chapter 5 presents the design of a unique preparation method to generate a free-standing, binder-free, and metallic current collector-free $LiFePO_4$ cathode. The simultaneous carbonization of microcrystalline cellulose and the *in situ* crystal growth of $LiFePO_4$ nanoparticles achieved by a novel impregnation–carbothermal reduction technique to create an innovative $LiFePO_4$–carbon paper ($LiFePO_4$@CP) hybrid electrode is demonstrated. The hybrid $LiFePO_4$@CP electrode consists of a carbon fibre network core, which allows fast electron transport and provides a porous structure for electrolyte penetration. The thin $LiFePO_4$ shell enables fast ion diffusion over a large surface area.

6) Chapter 6 reports the development of a unique free-standing, binder-free and metallic current collector-free $Na_3V_2(PO_4)_3$-carbon paper ($Na_3V_2(PO_4)_3$@CP) cathode for SIBs. This hybrid electrode consists of an interconnected 3D carbon fibre network (CFN) enabling fast electron transport and providing a porous

structure for electrolyte diffusion. The $Na_3V_2(PO_4)_3$ nanoparticles decorated on the carbon fibre network facilitate fast ion diffusion over a large surface area achieving exceptional cycle life of over 30 000 cycles.

7) Chapter 7 briefly summarizes the research outcomes of this research project and future scope of related research is also presented.

Chapter 1: Literature Review

During unexpected weather events in the Australian summer 2016/2017, the federal state of South Australia experienced several consecutive and at times long-lasting electricity blackouts. These events sparked a debate on South Australia's integration of renewable energy sources and consequential grid reliability issues due to the lack of adequate support infrastructures.[1] Although major blackouts are not limited to areas of high renewable energy integration as cases from the Northeast of the USA in 2003 and Southern California to Mexico in 2011 show, they highlight very complex issues associated with electricity production and consumption.[2] Furthermore, it is widely recognized that reliable and affordable electricity is vital for economic growth and development. Along the way to a decreased dependence on fossil fuels and reduction of associated greenhouse gas emissions to a full integration of renewable energy sources, large-sale energy storage systems have been identified to be essential to improve and maintain grid reliability.[3] As shown in Figure 1-1a, large-scale energy storage technologies can be divided into five categories, each containing their own subcategories of available and recognised systems, wherein the pumped hydro storage accounts for more than 95% of the global energy storage capacity.[2-4] However, the pumped hydro system cannot provide appropriate infrastructure for some crucial grid applications, such as uninterrupted power supply (UPS) and transmission and distribution (T&D) support, to maintain grid reliability. As Figure 1-1b shows, different technologies can be further categorized in terms of discharge time and storage capacity (power rating) and it becomes obvious that the metal-ion battery (displayed as Li-Ion Battery) provides the widest range of possible applications in this comparison.

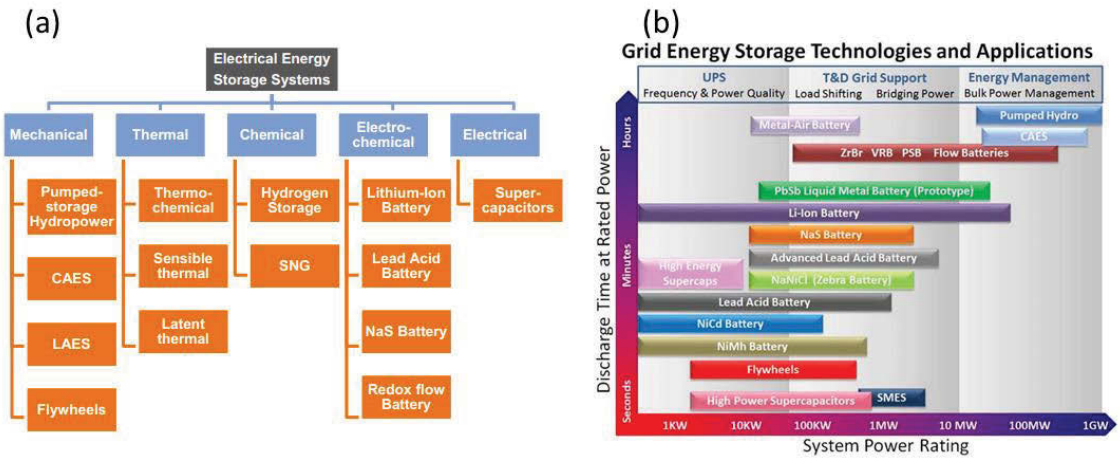

Figure 1-1. (a) Categorisation of available energy storage technologies. (CAES is Compressed Air Energy Storage, LAES is Liquid Air Energy Storage, SNG is Synthetic Natural Gas) Adapted from the World Energy Resources E-Storage Report 2016 of the World Energy Council, UK, London.[4] (b) General comparison of discharge time and power rating for various EES technologies.[2-5] (SMES is Superconducting Magnetic Energy Storage) The comparison is indicative only as several technologies may provide broader power ratings and longer discharge times. Reproduced with permission.[3] Copyright **2017**, Woodbank Communications Ltd, Chester (UK).

Therefore, it is not surprising that many countries in the developed world are heavily investing in projects boosting their electrochemical energy storage capacity. Table 1-1 gives an overview of current projects or planned installation efforts of energy storage technologies of selected countries (selected by their large number of projects and relationship to Australia). According to this list provided by the World Energy Council,[4] the majority of projects in progress focus on electrochemical energy storage technologies with the United States of America and China leading the list, followed by Japan and South Korea and members of the European Union (EU), such as Germany, the United Kingdom (pre-withdrawal from the EU), and France. Australia, Canada, and New Zealand are also investing in a diverse range of storage technologies.

Table 1-1. Nominal power (MW) of planned installations of large-scale energy storage listed by technology group and selected project location. Adapted from the World Energy Resources E-Storage Report 2016 of the World Energy Council, UK, London.[4]

Nation	*Electrochemical Storage*	*Electromechanical Storage*	*Hydrogen Storage*	*Pumped Hydro Storage*	*Thermal Storage*
Australia	19 Projects, 7 MW	2 Projects, 1 MW	0	740 MW	1 Project, 3 MW
Canada	10 Projects, 10 MW	2 Projects, 2.7 MW	0	1 Project, 174 MW	2 Projects, 2 MW
China	54 Projects, 32 MW	0	0	23060 MW	1 Project, 2 MW
France	10 Projects, 9 MW	0	1 Project, 0 MW	10 Projects, 5812 MW	1 Project, 3 MW
Germany	35 Projects, 251 MW	3 Projects, 708 MW	4 Projects, 3 MW	6806 MW	1 Project, 2 MW
Japan	47 Projects, 255 MW	0	0	27637 MW	0
South Korea	44 Projects, 206 MW	0	0	7 Projects, 4700 MW	0
New Zealand	2 Projects, 0 MW	0	0	0	0
United Kingdom	23 Projects, 24 MW	400 MW flywheel	0	4 Projects, 2828 MW	0
United States of America	227 Projects, 473 MW	21 Projects, 171 MW	0	38 Projects, 22561 MW	135 Projects, 664 MW

The main obstacle for a wider implementation of metal-ion batteries, not only for large-scale energy storage applications, remains materials and production cost,[2] which gives researchers a strong mandate to pursue novel, inexpensive, environmentally friendly, and of course high performance materials for this vital energy storage technology.

1.1 Phosphate-based Materials for Lithium-ion Batteries

The commercial and technological success of lithium-ion batteries (LIBs) can mostly be ascribed to the realization of positive electrodes based on transition metal oxides, such as Li_xMO_2 (M = Co, Ni, Mn), $Li_xMn_2O_4$, $Li_xV_2O_5$, or $Li_xV_3O_8$.[6] However, three-dimensional (3D) framework materials based on transition metals and polyanions $(XO_4)^{n-}$ have gained global attention due to the discovery and triumph of $LiFePO_4$.[6-9] Besides their obvious disadvantage in regards to gravimetric capacity due to the heavy polyanion group, these materials provide intriguing advantages, such as structural stability, high working potential, and versatility in atomic arrangement and crystal structure.[6] Therefore, this section will provide an overview of conducting polyanionic framework materials containing phosphate groups $(PO_4)^{3-}$ for LIBs as well as an introduction into the electrochemistry of this type of rechargeable battery itself.

1.1.1 Electrochemistry of Lithium-ion Batteries

The alkali metal lithium is classified as the lightest metal in the periodic table, providing the lowest electrochemical potential (-3.05 vs. SHE), and thus, the largest gravimetric energy density of all metals.[10-12] However, efforts to develop rechargeable lithium metal batteries have been plagued by problems of dendrite formation during repeated stripping/plating and electrolyte decomposition, which impose serious safety concerns and result in poor cycling efficiency.[12] Therefore, research efforts have shifted towards non-metallic lithium batteries using lithium ions provided by either the anode or the cathode material. A breakthrough for LIBs was accomplished in 1991 when the first LIB was commercialized by Sony.[13] After decades of intensive research and development, LIBs are now widely established as the power source of choice for portable electronics and are beginning to further dominate the markets of electric vehicle (EV) propulsion and residential solar battery storage.[14]

LIBs store electricity in the form of chemical energy during charging and convert this stored chemical energy into electricity during discharge. A standard LIB consists of four main components, including the negative electrode (anode), an electronically insulating separator, the positive electrode (cathode), and an ionically conducting medium as the electrolyte (Figure 1-2a). Anode and cathode are electronically connected through an external circuit to transport electrons, while the separator only allows ions to migrate through the electrolyte from one side to the other. The feasibility of an electrode depends on its electrochemical potential (μ_A for the anode and μ_C for the cathode) as well as the potential position relative to the HOMO–LUMO energy gap (E_g) of the electrolyte, as shown in Figure 1-2b.[15] Consequently, high-energy density batteries can be achieved in battery cells with maximum electrochemical potential differences between anode and cathode, high lithium storage abilities, and electrolytes with sufficiently large HOMO–LUMO energy gaps.[15, 16]

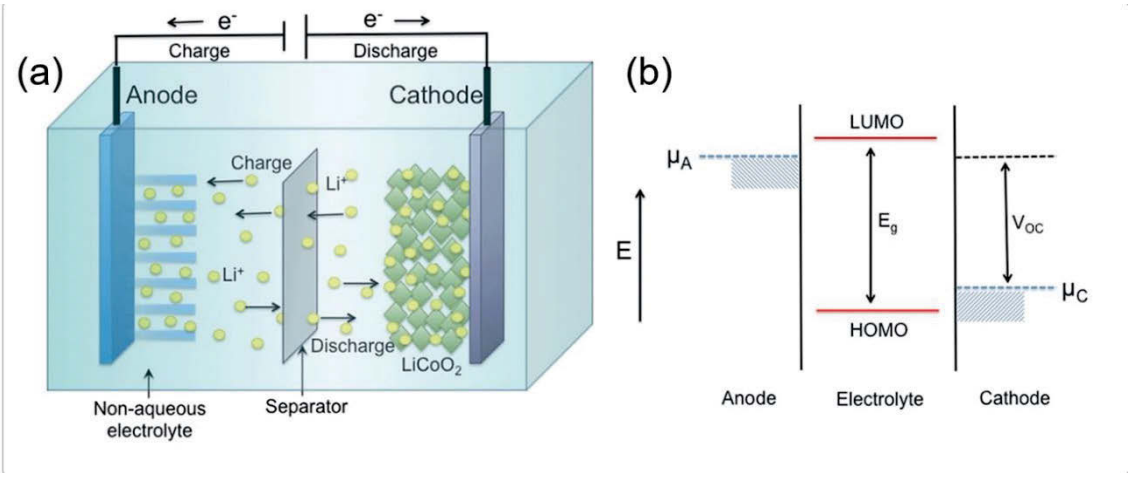

Figure 1-2. (a) Schematic diagram of the lithium intercalation–de-intercalation reaction mechanism in rechargeable LIBs containing solid electrodes and a liquid electrolyte. (b) Relative energy diagram of electrode potentials and electrolyte energy gap in LIBs. Reproduced with permission.[15] Copyright **2015**, The Royal Chemical Society.

In a commercial $LiCoO_2$//Graphite battery, electrons are transported through the external circuit from the cathode ($LiCoO_2$) to the anode (graphite) side during charging. At the same time, Li-ions are extracted from the $LiCoO_2$ cathode, migrate through the electrolyte and intercalate into the graphite electrode storing electricity within the battery in the form of chemical energy. This process is reversible and the stored energy is released during discharge as electrons flow back through the external circuit powering electrical devices, while most Li-ions also migrate back to the cathode host. Figure 1-3 summarizes some of the most common electrode materials in regards to their electrochemical potential and gravimetric capacity, which varies significantly with their chemical compositions. In the following part, recent progress in the development of electrode materials for LIBs in general will be reviewed with a detailed focus on phosphate-based polyanionic materials.

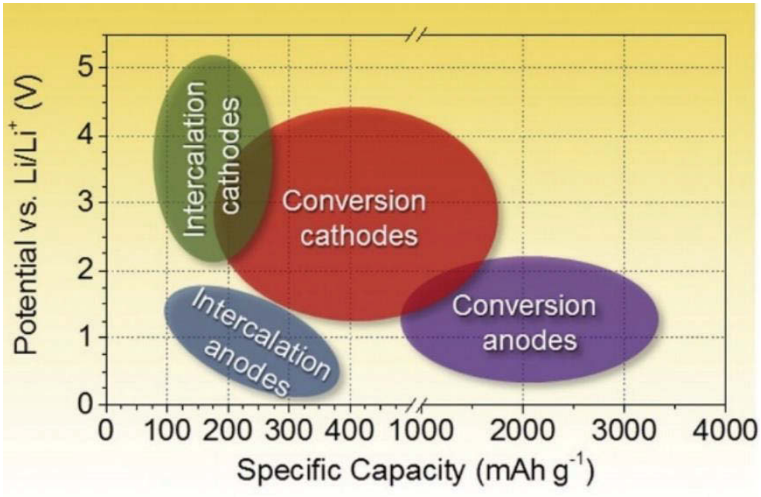

Figure 1-3. Diagram illustrating the average capacities and electrochemical potentials of important cathode and anode materials with respect to Li metal and the cell voltage of LIBs. The electrode materials are represented based on their reaction mechanism in the presence of Li^+.[17]

1.1.2 Anode Materials for Lithium-ion Batteries

Extensive research activities have been directed towards the development of advanced anode materials for LIBs in past decades. Anode materials that have been identified can be classified in three different categorise according to the underlying reaction mechanism with metal ions in an electrochemical cell. These three types of anode reactions are conversion, alloying, and intercalation, which will be discussed in a brief review of the anode material development for LIBs in the following sections. As phosphate-based polyanionic materials belong to the intercalation group, this reaction mechanism will be discussed in more detail in the last subsection.

1.1.2.1 Anode Materials based on Conversion and Alloying Reactions

Conversion

In 2000, the reversible reduction of transition metal oxide nanoparticles (TMOs NPs), such as CoO, CuO, and Fe_2O_3, in the presence of Li^+ was reported for the first time.[18] This process is known as “conversion reaction’ and its general equation can be defined as follows:

$$M_xO_y + 2yLi^+ + 2ye^- \leftrightarrow xM^0 + yLi_2O \text{ (M = transition metals)} \quad (1\text{-}1)$$

Since it was demonstrated that TMOs can deliver stable gravimetric capacities as high as three times that of carbon (372 mA h g^{-1}, see section 1.1.2.2.), they are now considered as promising anode material candidates in rechargeable batteries.[19] The family of conversion reaction-based TMOs for LIBs has grown dramatically in the last decade and includes oxides of iron,[20] manganese,[19, 21] cobalt,[22-25] copper,[26, 27] nickel,[28] molybdenum,[29, 30] zinc,[31] ruthenium,[32-34] chromium,[35, 36] tungsten,[37-39] and mixed metal oxides.[40] Figure 1-4 shows a schematic illustration of the conversion reaction of TMOs in the presence of Li^+.

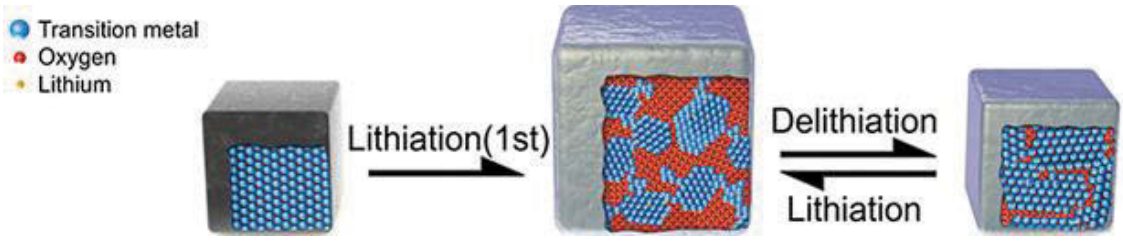

Figure 1-4. Schematic illustration of the conversion reaction of a transition metal oxide in LIBs. Reproduced with permission.[40] Copyright **2016**, WILEY-VCH Verlag GmbH & Co. KGaA, Weinheim.

From Equation (1-1), 2*y* Li^+ per formula unit of TMO can be stored through a conversion reaction, which causes structural change and amorphization of the TMO, and consequently, large volume expansions (Figure 1-4).[40] Nanoscale transition metal clusters are embedded in the lithium oxide (Li_2O) matrix after the initial lithiation is completed. During delithiation, these transition metal clusters are then oxidized to form amorphous TMOs as delithiation often results in a different, more kinetically favourable metal oxide phase.[41] Several issues that keep these compounds from commercial success still have to be resolved. Among those, the most relevant are i) the strong structural re-organization inducing large volume changes that result in electrode pulverization and poor cycling performance, ii) large voltage hysteresis between discharge and charge processes, iii) low initial Coulombic efficiency.[19, 40, 41] Nanostructured TMOs anode materials with different morphologies have been intensively investigated to minimize the strain derived from the volume change, which also improved electrode-electrolyte contact and diffusion lengths for Li^+ in the active materials, leading to high rate capabilities.[21, 42-45] Furthermore, reports of reversible conversion reactions in binary M–X compounds with X = N,[46-48] F,[49, 50] S,[51-54] P,[55-57] and H[19] have proven that the conversion reaction concept is not limited to only the TMO group.

Alloying

Like conversion reaction materials, alloying anode materials undergo a solid-state redox reaction during lithiation/delithiation. This reaction is accompanied by changes in crystalline structure that result in breaking and recombining of chemical bonds. Therefore, the alloying reaction in the presence of Li^+ can also be referred to as Type B conversion corresponding to the following equation:[17]

$$yLi + X \leftrightarrow Li_yX \quad (1\text{-}2)$$

Figure 1-5 shows an overview of elements capable of hosting Li^+ with their respective reaction mechanism towards lithium, relative abundance, and theoretical capacity (gravimetric and volumetric). As can be seen from this image, alloying (or Type B conversion) anodes exhibit theoretical gravimetric capacities up to 10 times higher as well as volumetric capacities two to five times higher than those of graphite. However, alloying materials are disreputable for their immense volume change during charge-discharge, which generally results in particle pulverization and electrical contact loss.[58] Furthermore, these volume changes can destroy the protective layer on the anode surface (solid electrolyte interface, SEI), which results in the continuous consumption of Li^+ and increasing cell impedance.[17] Therefore, alloying anodes are generally associated with short cycle life due to continuous active material loss.[59] The second issue with alloying anode materials is related to the large irreversible capacity commonly observed during the first cycle, which can be ascribed to:[60] i) Loss of active material; ii) Formation of SEI layer; iii) Trapping of Li in the alloy; iv) Surface reactions with oxide layers; and v) Aggregation of alloy particles.

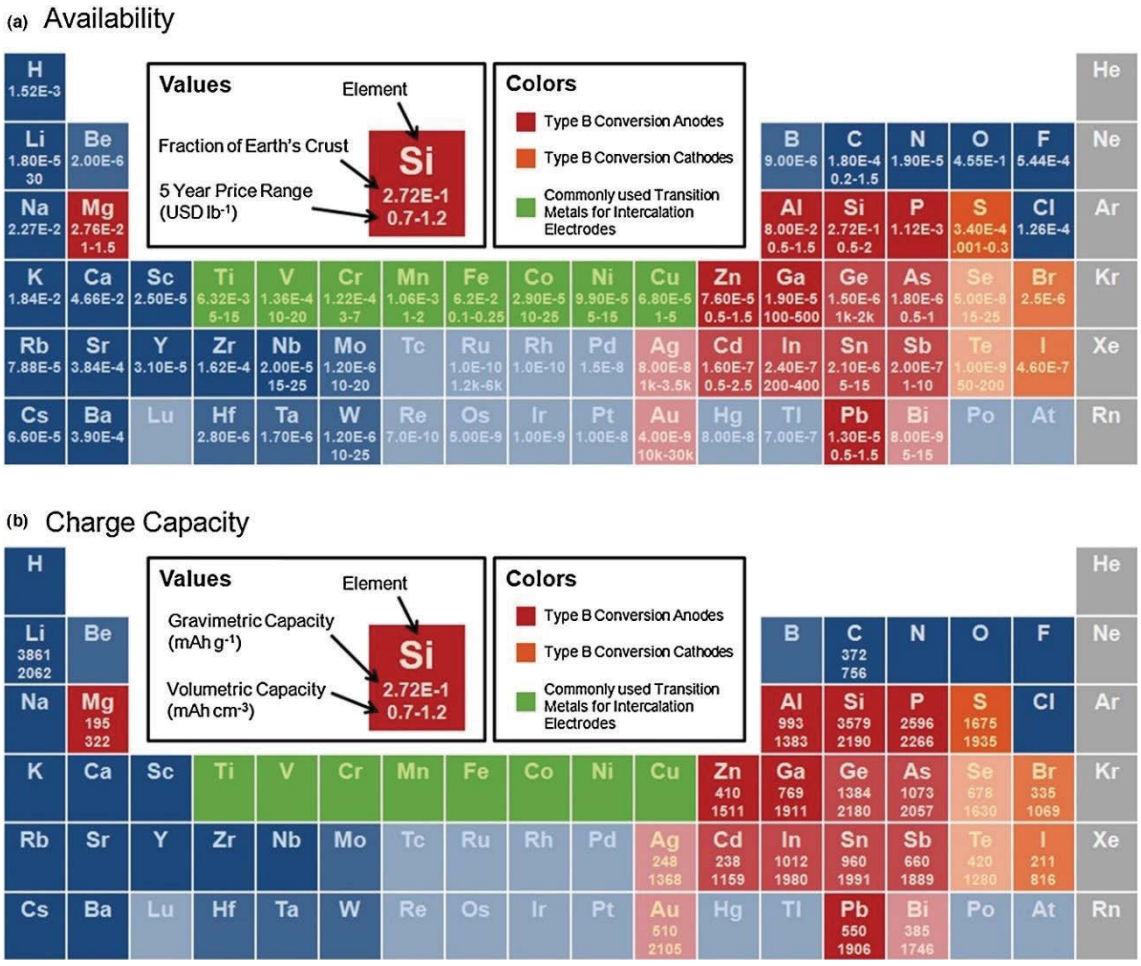

Figure 1-5. (a) Availability and (b) capacities of elements that may host Li as electrodes. Elements with abundance (as fraction of Earth's crust) below 10^{-5} are slightly faded, and elements below 10^{-7} are faded further. Gravimetric and volumetric capacities are theoretical values calculated based on delithiated mass and lithiated volume.[17]

Several strategies have been proposed to reduce irreversible capacity and improve the cycle life of alloying anodes, including: i) Dispersing alloying anode materials in carbonaceous materials[17, 61, 62] or intermetallics,[63-65] ii) Preparation of nanostructures, such as zero-dimensional (0D) nanoparticles,[66, 67] iii) Restricting either the upper or lower cut-off voltage to reduce volume changes, particle

aggregation, and structural changes,[68, 69] and iv) Optimization of applied binder materials and electrolyte composition.[70]

1.1.2.2 Anode Materials based on Intercalation

In chemistry, the term intercalation describes the reversible insertion of a guest species (Li^+ in the case of LIBs) into a laminar host structure without compromising the structural features of the host (Figure 1-6).[71] The most significant intercalation anode materials for LIBs are graphite and $Li_4Ti_5O_{12}$ (LTO). The crystal structures of their respective intercalated phases are shown in Figure 1-7.

The intercalation of Li^+ into graphite proceeds in stages through phase transition reactions[72] and can be described using the following general equation:[73]

$$C_6 + Li^+ + e^- \leftrightarrow LiC_6 \qquad (1\text{-}3)$$

A first polarization of graphite electrodes in polar aprotic Li salt electrolytes consumes irreversible charge for the reduction of solution species.

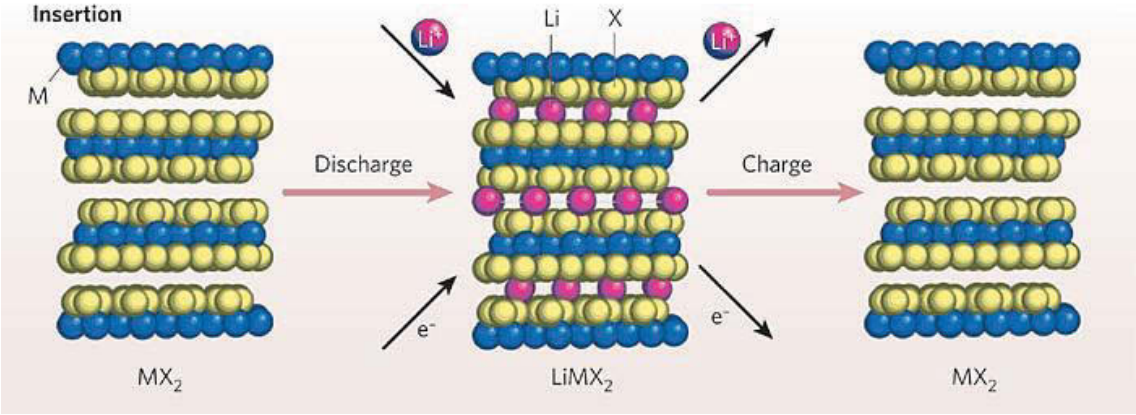

Figure 1-6. Schematic representation showing insertion/extraction of Li^+ during discharge/charge. Adapted and reproduced with permission.[74] Copyright **2008**, Nature Publishing Group.

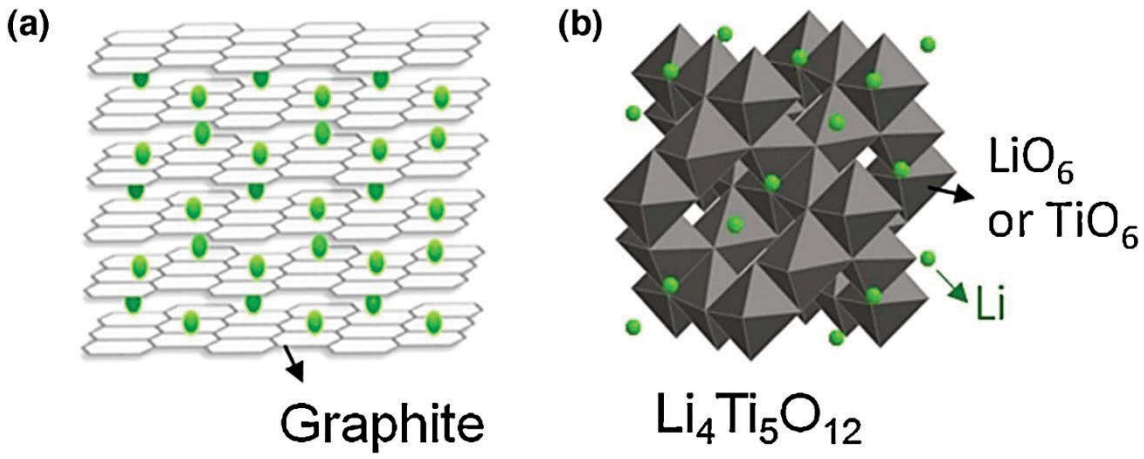

Figure 1-7. Crystal structures of (a) lithiated graphite (Reproduced with permission.[75] Copyright **2014**, American Chemical Society) and (b) lithium titanate (LTO) (Reproduced with permission.[76] Copyright **2011**, American Chemical Society).

This process results in a passivating film or SEI layer that prevents further irreversible processes.[73] Therefore, graphite containing LIBs require a Li source, the cathode material, in excess, in order to provide the Li^+ needed to form the SEI layer on the electrode surface.[45, 73] Graphite provides intriguing advantages over other anode materials, including low cost, abundance, low delithiation potential, high ionic and electronic conductivity, and low volume changes during charge-discharge. This commercially very attractive balance of low cost, availability, energy and power density, and cycle life is responsible for the commercial success of current LIBs.[17] However, although its gravimetric capacity is higher than that of most commercialized cathode materials, the small volumetric capacity of commercial graphite (330–430 mA h cm^{-3}) warrants the search for new high-performance anode materials. Apart from graphite, carbon nanostructures with improved electrochemical properties and commercialization potential have been investigated, including one-dimensional (1D) carbon nanotubes (CNTs)[77, 78] and carbon nanofibers (CNFs),[79] two-dimensional (2D) graphene,[80, 81] and porous carbonaceous materials.[82]

$Li_4Ti_5O_{12}$ (LTO) owes its commercial success to a combination of superior thermal stability, high rate capabilities, relatively high theoretical volumetric capacity (600 mA h cm^{-3}), and long cycle life.[83] However, the higher cost of Ti, high working potential (~1.55 V vs. Li/Li^+) and thus reduced cell voltage, and low theoretical gravimetric capacity (175 mA h g^{-1}) are disadvantageous to some degree.[17] Its high rate capabilities and superior cycling stability originate from a "zero strain" Li^+ intercalation mechanism combined with a lithiation potential higher than the reduction potentials of most relevant aprotic electrolyte solutions.[84] Initially conceived as disadvantage, a higher lithiation potential (>1 V vs. Li/Li^+) largely avoids the formation and growth of a passivating SEI layer to the benefit of reaction kinetics and preservation of the Li^+ reservoir.[85] However, surface reactions may not be completely avoidable. LIBs containing LTO as anode material suffer from severe gassing due to a reaction between the organic electrolyte and the LTO active material,[86] which can be suppressed by the introduction of a carbon coating sacrificing some thermal stability of the active material.[87] Furthermore, LTO greatly benefits from a carefully engineered carbon coating showing a dramatic increase in rate performance compared to carbon-free LTO electrodes.[88] Therefore, LTO is considered a practical anode material choice for lower energy but high power LIBs with a long cycle life.[17, 85]

The first report on the Li^+ storage properties of rhombohedral $LiTi_2(PO_4)_3$ (LTP) was published by Delma and co-workers in 1988.[89] The crystal structure of LTP consists of PO_4 tetrahedra and TiO_6 octahedra with large channels that provide two types of interstitial sites, which are generally referred to as M1 and M2, as shown in Figure 1-8a.[90] Li^+ in LTP selectively occupy the M1 sites whereas Li^+ intercalation occurs by filling of the M2 cavities. This involves the cooperative migration of Li^+ from the M1 to the M2 sites until the $Li_3Ti_2(PO_4)_3$ phase is established.[6, 90] With two Li^+ being inserted into the structure, a significant increase in the *c*/*a* ratio of the hexagonal unit cell occurs due to stronger

electrostatic repulsion between [$Ti_2(PO_4)_3$] lanterns along [001] when the M1 sites are being emptied, which results in the loss of the R3*c* symmetry.[91] A new pair of tetrahedral sites occupied by Li^+, which are referred to as M3' and M3", were found. With the M3' and M3" sites being included within the M2 cavity they are believed to play a vital role in the Li^+ diffusion process.[92] The expected insertion product is $Li_3Ti_2(PO_4)_3$, corresponding to a two-ion insertion at a voltage plateau of 2.48 V vs. Li/Li^+ corresponding to the redox couple of Ti^{4+}/Ti^{3+}:[6, 91]

$$LiTi_2(PO_4)_3 + 2Li^+ + 2e^- \leftrightarrow Li_3Ti_2(PO_4)_3 \quad (1\text{-}4)$$

However, several reports have shown an additional redox couple located at around 2.8 V, as seen in Figure 1-8b.[93-95] According to a study conducted by Hany El-Shinawi and Jürgen Janek,[93] this phenomenon suggests that the M1 sites of LTP are partially empty due to a disorder of lithium over the M1 and M2 sites. They explain that the reduction peak observed at around 2.75 V corresponds to the filling of the M1 sites by incoming Li^+, whereas the second reduction peak at 2.35 V correlates to the insertion of excess Li^+ into the M2 site. The specific capacity gained by this additional reduction process accounts for approximately 17% of the total gravimetric capacity or 0.38 Li per unit formula. LTP provides a satisfactory theoretical capacity of 138 mA h g^{-1} and high ionic conductivity of $\approx 10^{-6}$ S cm^{-1} but might remain only potentially viable in organic electrolyte systems for niche applications, such as monolithic integration of thin-film solar cells and LIBs.[90] However, LTP can be applied as anode material in aqueous LIB systems due its stability towards the LUMO of water. Successful aqueous full battery assemblies include the combination of LTP with cathode materials such as LiMn2O4[96] and $LiFePO_4$.[97]

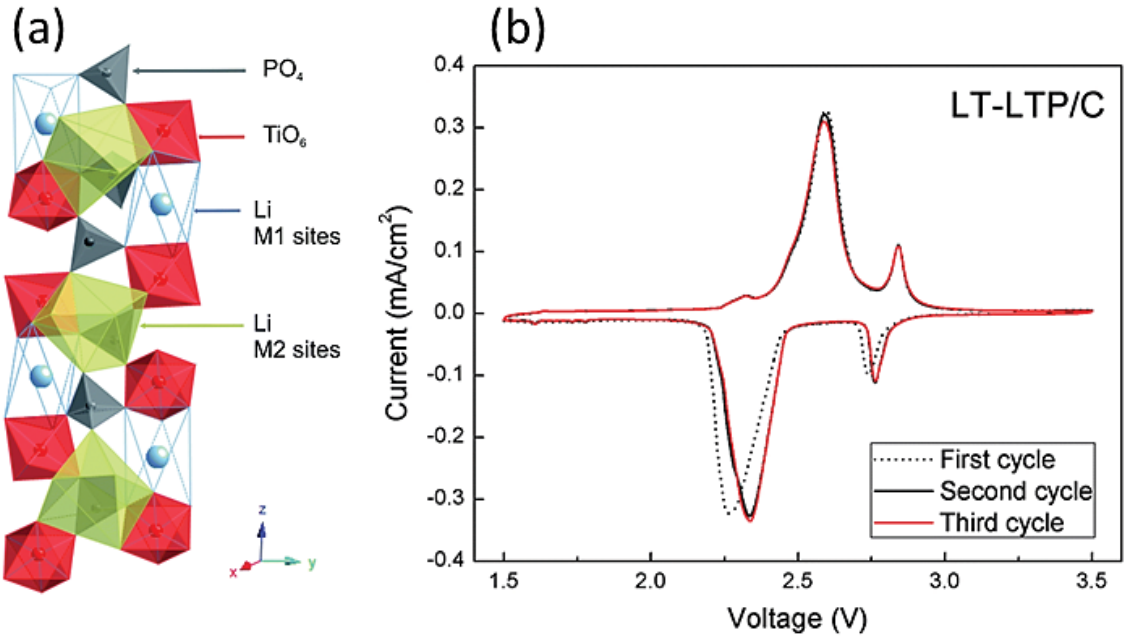

Figure 1-8. (a) Part of the NASICON-type crystal structure showing the M1 and M2 crystal sites and (b) Slow sweep cyclic voltammograms of carbon coated LTP collected at 0.1 mV s^{-1}.[93]

Vanadium-containing polyanionic phosphate materials have attracted tremendous amounts of research interest due to the possibility of multi-electron transfers, which is the result of the number of available redox couples: V^{5+}/V^{4+}, V^{4+}/V^{3+}, and V^{3+}/V^{2+}.[91] Among many high performance vanadium phosphate materials, which are generally used as cathode materials for rechargeable battery systems, $Li_3V_2(PO_4)_3$ (LVP) has also been considered as potential high power anode material for LIBs (its cathodic performance will be discussed in Section 1.1.3). LVP can be synthesized as either rhombohedral (NASICON, r-LVP) or monoclinic (anti-NASICON, m-LVP), which results in different electrochemical properties.[6, 98]

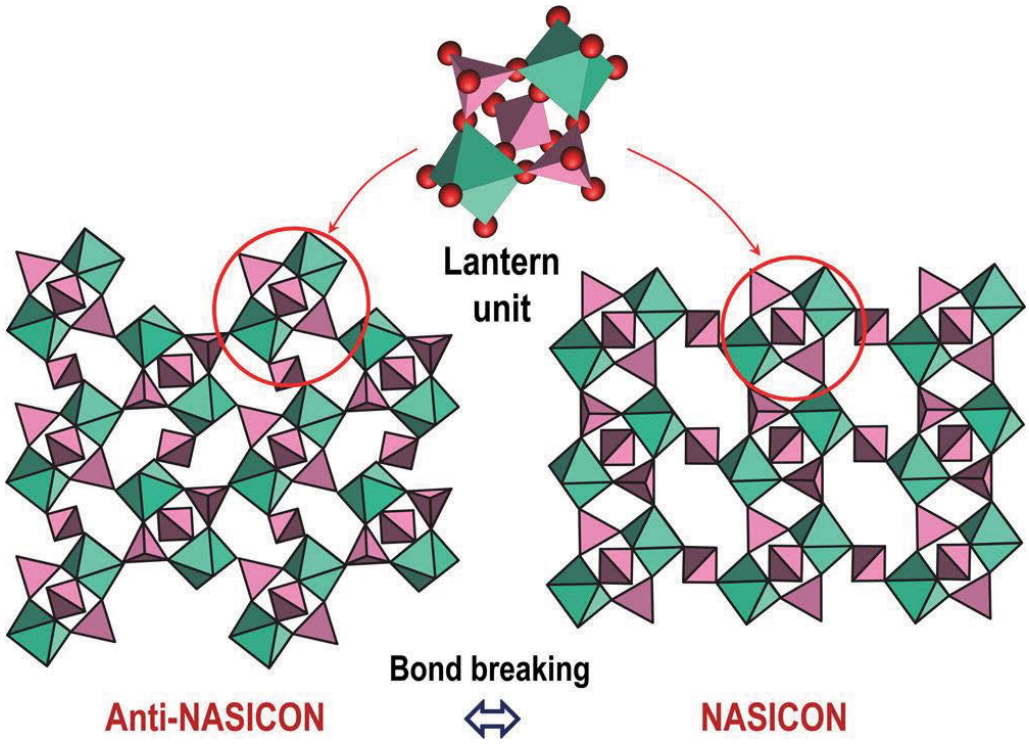

Figure 1-9. NASICON (generally rhombohedral) and anti-NASICON (generally monoclinic) frameworks of general formula $A_xMM'(XO_4)_3$. A = Li, Na, K, Mg, Ca; M or M' = Fe, V, Ti, Zr, Sc, Mn, Nb, In; X = S, P, Si, As. Reproduced with permission.[6] Copyright **2013**, American Chemical Society.

The first successful preparation of r-LVP was reported in 2000 by Nazar and co-workers,[99] which was achieved through a topotactic ion exchange procedure from its sodium analogue. To date, the only known report on the anodic performance of r-LVP was published by Jian *et al.* in 2014.[98] In this study, evidence was presented showing that two additional Li^+ can be inserted into the structure corresponding to the V^{3+}/V^{2+} redox couple at an average voltage of 1.75 V vs. Li/Li^+, similar to the anodic performance of LTO presented earlier. Further investigations at potentials below 1.0 V have not been conducted in this study; however, a successful experiment of a symmetric full cell showed potential for large-scale energy storage systems. The experimental cell provided an output of around 2 V with an energy density of 113 W h kg^{-1}.

Since r-LVP cannot directly be prepared using traditional preparation methods, more research has been focused on the thermodynamically stable monoclinic phase m-LVP. Generally, the insertion/extraction of Li^+ in m-LVP follows a complicated series of successive two-phase transitions, as seen in Figure 1-10.[6] For the anodic performance of the V^{3+}/V^{2+} redox couple, four distinct plateaus or redox peaks can be seen in this images, corresponding to the insertion/extraction of two Li^+:[6, 91, 100]

$$Li_3V_2(PO_4)_3 \leftrightarrow Li_{3.5}V_2(PO_4)_3 + 0.5Li^+ + 0.5\ e^- \quad (1\text{-}5)$$

$$Li_{3.5}V_2(PO_4)_3 \leftrightarrow Li_4V_2(PO_4)_3 + 0.5Li^+ + 0.5\ e^- \quad (1\text{-}6)$$

$$Li_4V_2(PO_4)_3 \leftrightarrow Li_{4.5}V_2(PO_4)_3 + 0.5Li^+ + 0.5\ e^- \quad (1\text{-}7)$$

$$Li_{4.5}V_2(PO_4)_3 \leftrightarrow Li_5V_2(PO_4)_3 + 0.5Li^+ + 0.5\ e^- \quad (1\text{-}8)$$

Different reports on m-LVP achieved stable reversible capacities of around 88 to 126 mA h g^{-1} when cycled between 3.0-1.0 V vs. Li/Li^+.[100-102] However, the initial study on the anodic behaviour of m-LVP conducted by Rui *et al.* also investigated the electrochemical behaviour in a potential window of 3.0-0.0 V vs. Li/Li^+.[101] Their study found that, in addition to the two-phase region at 2.0-1.6 V vs. Li/Li^+, m-LVP displays a single-phase region below 1.6 V vs. Li/Li^+ corresponding to the V^{2+}/V^+ redox couple allowing two additional Li^+ to be inserted/extracted from the lattice:

$$Li_5V_2(PO_4)_3 + 2Li^+ = 2e^- \leftrightarrow Li_7V_2(PO_4)_3 \quad (1\text{-}9)$$

This additional single-phase region increases the theoretical gravimetric capacity of m-LVP to 266 mA h g^{-1} (assuming four Li^+ are being reversibly inserted/extracted), which is much higher that the theoretical value in the cathode potential region (197 mA h g^{-1} when cycled to 4.8 V vs Li/Li^+).

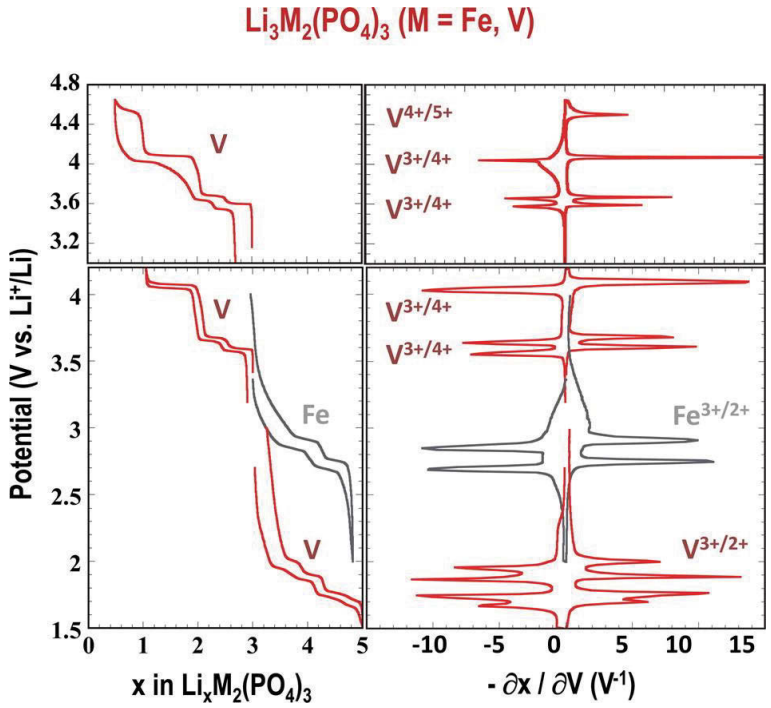

Figure 1-10. Galvanostatic Li^+ insertion/extraction and respective redox couples in anti-NASICON $Li_xM_2(PO_4)_3$ (M = Fe, V) compositions. Reproduced with permission.[6] Copyright **2013**, American Chemical Society.

A later study conducted by Zhang *et al.* confirmed this observation.[103] In their study, a nanostructured carbon-coated m-LVP material was applied as anode in a LIB achieving a reversible capacity of 236 mA h g^{-1} a 1C. Interestingly, they further found that the single-phase region below 1.6 V vs Li/Li^+ showed only minor variations and higher values in lithium diffusion coefficient compared to the behaviour observed in the two-phase region at higher potentials. This implies great potential for high power applications. As seen in Figure 1-11, this nanostructured m-LVP material provides a remarkable rate performance with a high rate capacity of 99 mA h g^{-1} at 100C (26.6 A g^{-1}). As the authors emphasize, this performance is comparable with supercapacitor applications. According to these findings, m-LVP cycled to 0.0 V vs. Li/Li^+ can be considered for both innovative high power applications as well as high energy LIBs.

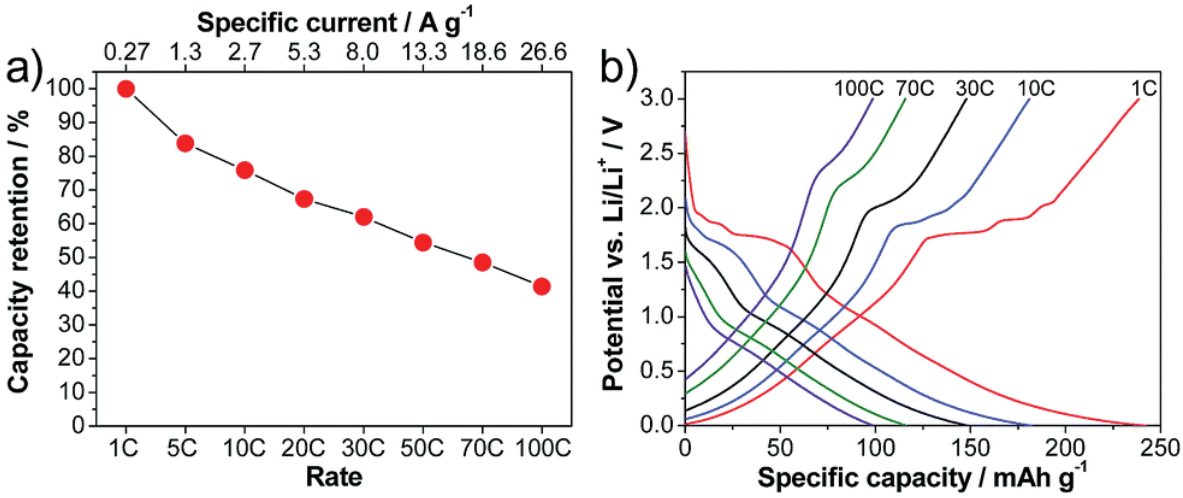

Figure 1-11. Rate performance of m-LVP cycled in the potential range of 3.0–0.0 V vs. Li/Li^+. (a) Delithiation capacity retention. (b) Corresponding potential profiles.[103]

1.1.3 Cathode Materials for Lithium-ion Batteries

The role of the positive electrode in modern LIBs has been dominantly filled by $LiCoO_2$ since it was firstly demonstrated as a possible cathode material for rechargeable lithium batteries in 1980.[104] Following this discovery, transition metal intercalation oxides have been extensively investigated;[105] however, an increasing number of new potential cathode materials have emerged since. Conventional cathode materials can be categorized by their respective structure and those materials include layered compounds $LiMO_2$ (M = Co, Ni, Mn, etc.), spinel compounds LiM_2O_4 (M = Mn, etc.), and olivine compounds $LiMPO_4$ (M = Fe, Mn, Ni, Co, etc.).[106] New intercalation materials such as silicate compounds Li_2MSiO_4 (M = Fe, Mn), borate compounds $LiMBO_3$ (M = Mn, Fe, Co), tavorite compounds $LiMPO_4F$ (M = Fe, V, Al), and NASICON compounds $Li_xM_2(PO_4)_3$ (M = Fe, V, Ti, Zr, Sc, Mn, Nb, In) are also receiving increasing attention.[6, 91, 106] The following chapter will give a brief overview of the current status of conventional LIB cathode materials and will then focus on phosphate-based polyanionic cathode materials.

1.1.3.1 Conventional Cathode Materials for Lithium-ion Batteries

Layered compounds $LiMO_2$

Within the structure of layered transition metal compounds, oxygen anions form a close-packed *fcc* lattice with cations located in the octahedral crystal sites and MO_2 slabs are stacked alternately with Li layers.[106] An illustration of the structure of layered $LiMO_2$ is shown in Figure 1-12. $LiCoO_2$ is the most popular member of the layered transition metal oxide group and has been dominating the LIBs market since its commercial launch of in 1991. The theoretical capacity of $LiCoO_2$ is 270 mA h g^{-1} assuming all Li^+ are extracted from the crystal. However, capacities of only 130-150 mA h g^{-1} can be practically achieved, which indicates that only half of the Li atoms can be utilized during cycling. These limitations originate from the intrinsic structural instability of the material when more than half of the Li^+ are extracted.[106, 107] Although $LiCoO_2$ is a successful cathode material, several disadvantages cannot be ignored by the LIB market. These drawbacks include:[108] i) Cobalt is less abundant than other transition metals, such as Mn, Ni, and Fe, and therefore more expensive; ii) $LiCoO_2$ is unstable when overcharged, due to the dissolution Co[109] or the collapse of the layered structure.[110-112]

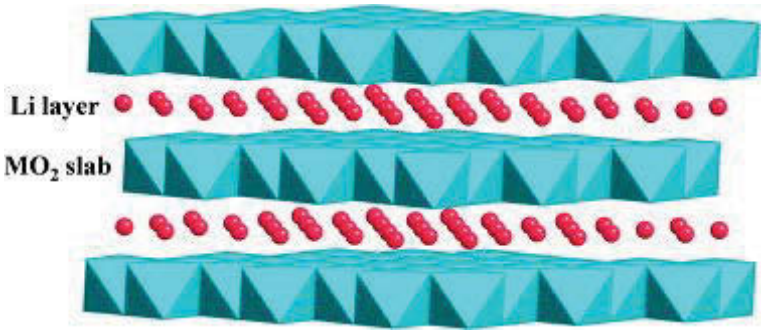

Figure 1-12. Crystal structure of layered $LiMO_2$. Reproduced with permission.[106] Copyright **2012**, Elsevier.

Therefore, research focus has shifted from $LiCoO_2$ to its derivatives in which Co ions are partially or fully substituted by more abundant and environmental friendly transition metal ions, such as Ni and Mn. Approaches to prepare better layered transition metal oxide cathodes include mixing $LiNiO_2$ and $LiMnO_2$ to generate layered $LiNi_{0.5}Mn_{0.5}O_2$, and the formation of Li–Co–Ni–Mn–O layered compounds (so-called NMC materials).[106] The electrochemical performance of $LiNi_{0.5}Mn_{0.5}O_2$ was firstly reported by Ohzuku *et al.* in 2001.[113] Different from standard layered transition metal oxides, 8–10% of Ni ions are located in the Li layer of $LiNi_{0.5}Mn_{0.5}O_2$.[114-119] With MO_2 slabs restrained by this, high and stable reversible capacities of around 200 mA h g^{-1} can be achieved at 0.2C.[106] However, the Li^+ mobility of this material was found to be impaired by un-removable Ni in the Li layers blocking Li^+ diffusion pathways, thus lowering the diffusion coefficient of $LiNi_{0.5}Mn_{0.5}O_2$ by one order of magnitude than that of $LiCoO_2$.[120] The addition of Ni and Mn to $LiCoO_2$ was found to maintain the layered structure of $LiCoO_2$ reducing the amount of defect Ni in Li layers while delivering similar reversible capacities than $LiNi_{0.5}Mn_{0.5}O_2$.[121] The most common $Li(Ni,Mn,Co)O_2$ composition contains equal amounts of the three transition metals, i.e. $Li(Ni_{1/3}Mn_{1/3}Co_{1/3})O_2$, with the valence states of Ni, Mn, and Co of +2, +4, and +3, respectively.[122, 123]. It was reported that $Li(Ni_{1/3}Mn_{1/3}Co_{1/3})O_2$ can operate at a voltage of 4.5 V achieving a capacity of around 200 mA h g^{-1}.[124, 125] The reversible capacity of $Li(Ni_{1/3}Mn_{1/3}Co_{1/3})O_2$ is generated by the oxidation of Ni^{2+} to Ni^{4+} (a two-electron transfer process) and subsequent oxidation of Co^{3+} to Co^{4+}.[126-128] The tetravalent Mn ions do not participate in the redox reaction between 2.7 and 4.8 V;[126, 127, 129] however, Mn in this compound has been associated with oxygen release at high charging voltages (>4.5 V vs. Li/Li^+).[106] The improved capacity of layered $Li(Ni_{1/3}Co_{1/3}Mn_{1/3})O_2$ could be the result of the improved chemical stability of the Ni^{2+}/Ni^{3+} and Ni^{3+}/Ni^{4+} redox couples compared to Co^{3+}/Co^{4+}. Unfortunately, $Li(Ni_{1/3}Mn_{1/3}Co_{1/3})O_2$ shows poor cycling stability at high voltage where the

maximum capacity can be achieved due to electrode polarization and electrolyte decomposition.[130]

Spinel compounds LiM_2O_4

The oxygen framework of LiM_2O_4 is identical to the structure of layered $LiMO_2$. Therein, M cations occupy the octahedral site with 1/4 of them located in the Li layer, leaving 1/4 of the sites in the transition metal layer vacant. Li^+ occupy the tetrahedral sites in the Li layer that share faces with the empty octahedral sites in the transition metal layer. The structure resembles a 3D MO_2 host with vacancies in the transition metal layer that ensure 3D Li diffusion pathways.[106] An illustration of the structure of spinel LiM_2O_4 is shown in Figure 1-13. Spinel lithium manganese oxide ($LiMn_2O_4$), first reported by Thackery *et al.* in 1983,[131] has attracted excessive technological and research interest because of its low cost, environmental friendliness, and high safety.[45, 132, 133]

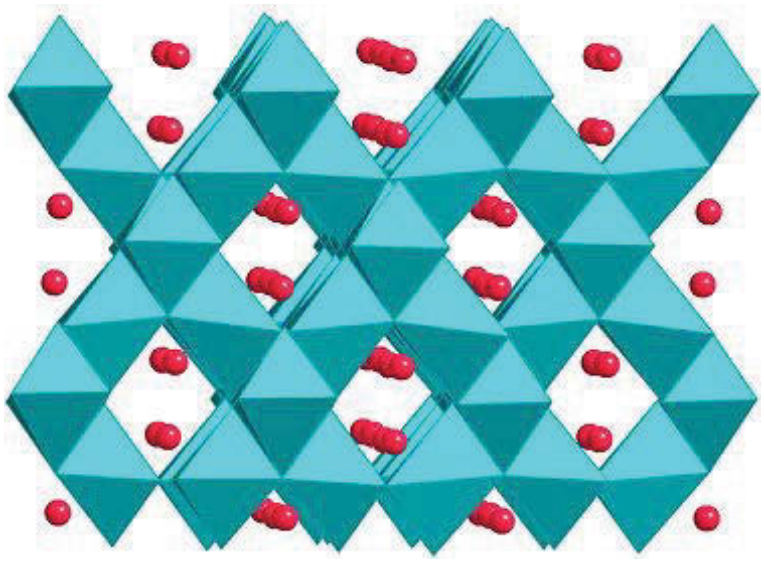

Figure 1-13. Crystal structure of spinel LiM_2O_4. Reproduced with permission.[106] Copyright **2012**, Elsevier.

The discharge of this material proceeds predominantly in two steps, one at around 4 V and the second step at around 3 V vs. Li/Li^+. During the charge process, the removal of Li from the spinel host proceeds *via* a two-step reaction at around 4 V vs. Li/Li^+.[134] Although $LiMn_2O_4$ has been demonstrated to be a promising cathode for LIBs, the material exhibits severe capacity fading problems, with main reasons for this phenomenon: i) The dissolution of Mn^{2+} into the electrolyte caused by the disproportional reaction $2Mn^{3+} \rightarrow Mn^{4+} + Mn^{2+}$;[135, 136] ii) The generation of new phases during cycling and related micro-strains.[137] The substitution of Mn with other metal ions, such as inactive Mg, Al, Zn,[138-140] transition metal ions Ti, Cr, Fe, Co, Ni, Cu,[141-145] or rare earth metal ions Nd, La,[146-148] has been used to improve cycling performance of spinel materials, with $LiNi_{0.5}Mn_{1.5}O_4$ providing the best overall electrochemical performance. The valence of Ni ions is 2^+ pushing all Mn ions to Mn^{4+}, which shifts the redox couple of $LiNi_{0.5}Mn_{1.5}O_4$ from Mn^{3+}/Mn^{4+} to Ni^{2+}/Ni^{4+} consequently increasing the working potential from 4.1 to 4.7 V vs. Li/Li^+ generating a reversible capacity of around 140 mA h g^{-1}.[106, 142] Therefore, this material not only provides enhanced energy density but is pairable with high voltage anode materials, such LTO, improving overall safety of LIBs. However, since the Li diffusion coefficient of $LiNi_{0.5}Mn_{1.5}O_4$ reportedly ranges from 10^{-10} to 10^{-16} cm^2s^{-1} morphological and composition improvements are required to allow this material to be applicable in high power applications.[106, 149-151]

Silicate compounds Li_2MSiO_4

Silicate-based cathode materials Li_2MSiO_4 (M = Fe, Mn, Co, Ni) possess a number of advantages, such as abundance, low toxicity, and thermal stability due to the strong Si–O bonding.[152-154] Additionally, Li_2MSiO_4 has the potential of the extraction of more than one lithium ion per transition metal, enabling a theoretical capacity of about 333 mA h g^{-1}.[106, 155, 156] An illustration of the crystal structure of Li_2MSiO_4 materials is shown in Figure 1-14. The crystal structure of Li_2MSiO_4

comprises of a distorted hexagonal packing of oxygen with half of the tetrahedral sites occupied by Li, M, and Si.[157] The first member of the silicate family, Li_2FeSiO_4, was identified and investigated by Anton Nytén *et al.* in 2005, which delivered an initial capacity of only 165 mA h g^{-1} indicating that only one Li^+ was effectively extracted.[158] Furthermore, an oxidation peak shift from 3.1 to 2.8 V vs. Li/Li^+ was observed using cyclic voltammetry, which suggests a phase transformation within the crystal structure. Efforts to improve the electrochemical performance of Li_2FeSiO_4, particularly its rate capabilities, have been made, which typically involves the addition of a carbon precursor.[159] However, capacities greater than 200 mA h g^{-1} are either attributed to the formation of Fe^{4+}[160] and/or electrolyte degradation.[161] Li_2MnSiO_4 was firstly reported by Dominko *et al.* in 2006.[162]

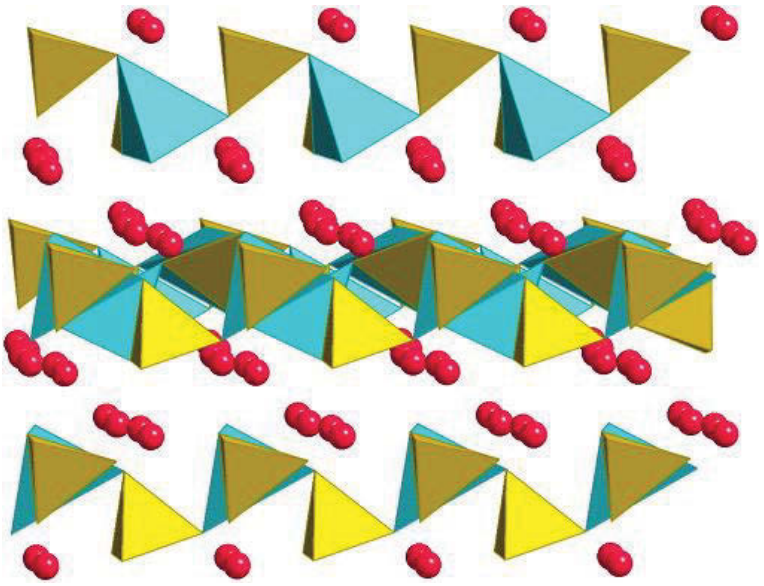

Figure 1-14. Crystal structure of lithium intercalated silicates Li_2MSiO_4 (blue: transition metal; yellow: Si; red: Li). Reproduced with permission.[106] Copyright **2012**, Elsevier.

Since then, Li_2MnSiO_4 cathode materials have been widely investigated with many failed experimental efforts to achieve good electrochemical performances, which is due to their inherent disadvantages:[163] i) Low electronic conductivity (less than 10^{-14} S cm^{-1});[164-166] ii) Jahn–Teller distortion of Mn^{3+} ions and Mn dissolution;[167, 168] iii) Li^+ and Mn^{2+} become site-exchanged during delithiation, which leads to large electrode polarization and structure destabilization;[169] and iv) inactive impurity phases, such as MnO and Li_2SiO_3.[170] More research is needed to improve physical and electrochemical properties of silicate-based materials by optimizing their structure, synthesis procedures, and morphology. Interestingly, recent reports on the performance of silicate-based materials as negative electrode in LIBs have emerged.[171, 172] Both studies report reversible discharge capacities of 450-550 mA h g^{-1} for Fe- and Mn-containing silicates. The authors proposed that the silicates undergo a highly reversible conversion reaction at low potentials, similar to that of transition metal oxide anode materials, which also requires further investigation.

Borate compounds $LiMBO_3$

As polyanionic materials generally come with a weight penalty in form of reduced energy density due to the heavy polyanion group, $LiMBO^3$ compounds have attracted interest because of the light borate (BO_3^{3-}) group.[173] The crystal structure of monoclinic $LiMBO_3$ is illustrated in Figure 1-15. In 2001, Legagneur *et al.* first reported the electrochemical properties of $LiMBO_3$ (M = Mn, Fe, Co) showing very poor electrochemical activity (only 0.04Li per formula, or 9 mA h g^{-1}), whereas the theoretical capacity was calculated to be as high as 220 mA h g^{-1}.[174] The redox couple Fe^{3+}/Fe^{2+} in the voltage window of 2.9–3.1 V vs Li/Li^+ was proposed, which implies superior energy density of around 660 W h kg^{-1}. Until 2010, all attempts to improve the electrochemical performance of borate-based cathode materials remained unsatisfactory and their poor conductivity and kinetic limitations were blamed for their poor performance.[106, 175-177]

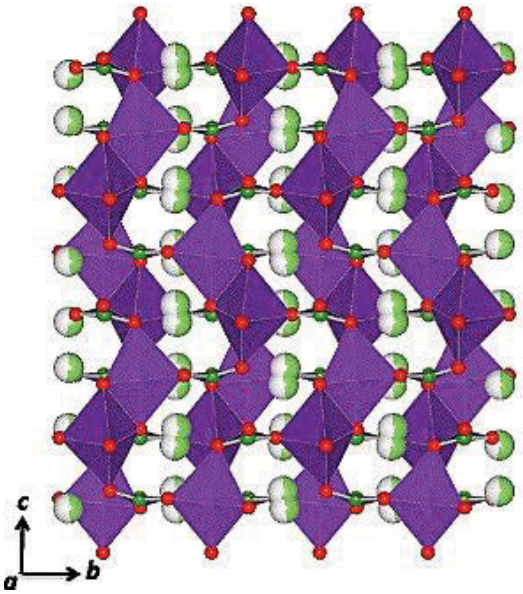

Figure 1-15. Illustration of the monoclinic $LiMBO_3$ (M = 3d metals) family crystal structure showing corrugated MO_5 chains along *c*-axis connected by planar BO_3 units. Reproduced with permission.[173] Copyright **2015**, Springer Berlin Heidelberg.

In 2010, Yamada *et al.* reported their work on carefully optimized $LiFeBO_3$, which delivered near theoretical capacity approaching 200 mA h g^{-1} supported by both experimental and computational results.[178] According to their findings, surface poisoning due to atmospheric moisture was the main reason for previous failed attempts to optimize the electrochemical performance of borate-based cathode materials. This sparked renewed interest with studies conducted on synthesis, crystal structure, stability, and electrochemical performance.[179, 180] Electrochemical studies on Mn-based borates have also emerged.[181] In contrast to $LiFeBO_3$ and $LiCoBO_3$, $LiMnBO_3$ exists in two polymorphs, hexagonal (h-$LiMnBO_3$)[174, 182] and monoclinic (m-$LiMnBO_3$).[179, 180] The hexagonal phase provides an initial discharge capacity of 75.5 mA h g^{-1} at high voltage showing a conversion-type reaction at low potentials.[182] This low voltage conversion and its poor cathode performance make h-$LiMnBO_3$ an attractive anode material with a reversible capacity of 287 mA h g^{-1}.[183] Only recently, Nesper and co-workers have

succeeded in enabling the h-$LiMnBO_3$ polymorphs capabilities by nanoparticle engineering delivering a discharge capacity of around 140 mA h g^{-1} with good cycling stability.[184, 185] For the monoclinic phase, electrochemical performances were first shown in 2011.[179, 180] Although a capacity of around 100 mA h g^{-1} was achieved, large polarization and improved performance at elevated temperatures indicate intrinsic kinetic limitations. Chemical analysis of partially oxidized $Li_{1-x}MnBO_3$ suggests that progressive delithiation induces structural disintegration and phase decomposition.[173] Furthermore, irreversible Mn dissolution originating from the chemical instability of Mn^{3+} in $Li_{1-x}Mn^{II/III}BO_3$ may occur.[179, 186] In recent years, some groups have reported the usage of mixtures of both polymorphs (m + h-$LiMnBO_3$) as cathode candidate produced by several different preparation methods.[187-190] This approach generated m + h-$LiMnBO_3$ compounds achieving a reversible capacity of over 170 mA h g^{-1}, close to the theoretical capacity for $LiMnBO_3$ of 222 mA h g^{-1}. The last member of the $LiMBO_3$ family is $LiCoBO_3$. With a theoretical capacity of 215 mA h g^{-1} and working potential of 4 V vs Li/Li^+ utilizing the Co^{3+}/Co^{2+} redox couple, this material can provide a theoretical energy density of 860 Wh kg^{-1}.[191] However, efforts to enhance electronic conductivity, Li diffusivity, and mechanical stability have been widely unsuccessful and $LiCoBO_3$ remains the least explored and most challenging member of the LiMBO3 family.[173]

1.1.3.2 Phosphate-based Cathode Materials for Lithium-ion Batteries

Olivine compounds $LiMPO_4$

Olivine $LiMPO_4$ materials have received tremendous research attention because of the stability of the polyanion group, which minimizes oxygen loss observed in traditional layered and spinel oxides.[106] The crystal structure of olivine LiMPO4 is displayed in Figure 1-16a. Since it was first reported by Goodenough and co-workers, olivine $LiFePO_4$ has received the most research attention due to its

excellent electrochemical properties, low cost, non-toxicity, excellent thermal stability, and environment friendliness.[7, 8] In $LiFePO_4$, P occupies the tetrahedral sites, Fe occupies the octahedral sites, and Li forms 1D chains along the [010] direction. $LiFePO_4$ undergoes a reversible transition to $FePO_4$ during discharge/discharge utilising the Fe^{2+}/Fe^{3+} redox couple at 3.4 V vs. Li/Li^+, as schematically shown in Figure 1-16b, providing a theoretical capacity of 170 mA h g^{-1}.[43] Unfortunately, $LiFePO_4$ is known for its low electronic conductivity (around 10^{-9} S cm^{-1})[192] and sluggish Li^+ diffusion (around 10^{-14} cm^2 s^{-1}).[193] Li^+ in the lattice of $LiFePO_4$ can only migrate along the [010] direction because there are no continuous LiO_6 octahedra in the direction of the a- and c-axis.[194-196] Furthermore, the Li^+ diffusion in $LiFePO_4$ is not only insufficient but also easily affected by crystal defects.[197, 198] To improve the electrochemical performance of $LiFePO_4$, strategies such as surface decoration[199-201], nanocrystallization,[202-205] and lattice substitution (doping)[206-209] have been employed to promote electronic conductivity and Li^+ diffusion. Olivine compounds can also be prepared with other transition metal ions, such as Mn, Co, and Ni, each providing different active redox couples and corresponding working voltages: 4.1 V vs. Li/Li^+ for $LiMnPO_4$,[210] 4.8 V vs. Li/Li^+ for $LiCoPO_4$,[211] and 5.1 V vs. Li/Li^+ for $LiNiPO_4$.[212]

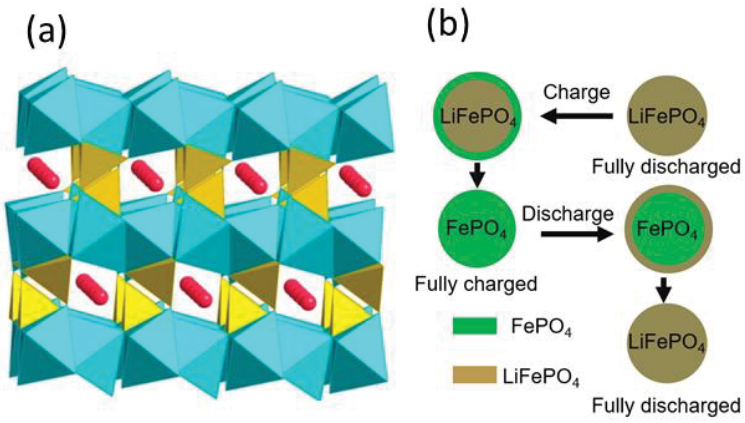

Figure 1-16. (a) Crystal structure of olivine $LiMPO_4$ (blue: transition metal ions; yellow: P ions; red: Li ions) Reproduced with permission.[106] Copyright **2012**, Elsevier. (b) Schematic representation of the processes during charge/discharge of $LiFePO_4$. Reproduced with permission.[43] Copyright **2008**, WILEY-VCH Verlag GmbH & Co. KGaA, Weinheim.

Due to the stability limitation at high potentials of current organic electrolytes, most research has been focused on $LiMnPO_4$ and divalent doping of $LiFePO_4$ to optimize working potential electrochemical performance.[106, 213, 214] Besides electrochemical optimization efforts, fundamental studies on olivine materials are also intensively conducted. For bulk $LiFePO_4$, the working voltage profile plateau is located at around 3.45 V vs. Li/Li^+, which is indicative of a two-phase lithiation/delithiation process.[7] The two-phase mechanism proposed suggested the so-called shrinking core model, wherein the phase boundary moves from the outside to the inside of the particles for both charge and discharge processes, becoming diffusion limited after reaching a critical surface area (see Figure 1-17).[7, 106, 215] Once Li^+ diffusion through the interface cannot sustain the given current density, the reaction comes to a halt without consuming the residual active material inside the two-phase interface, which greatly affects the utilization of active material (residual $LiFePO_4$ in state C of Figure 1-17).[214]

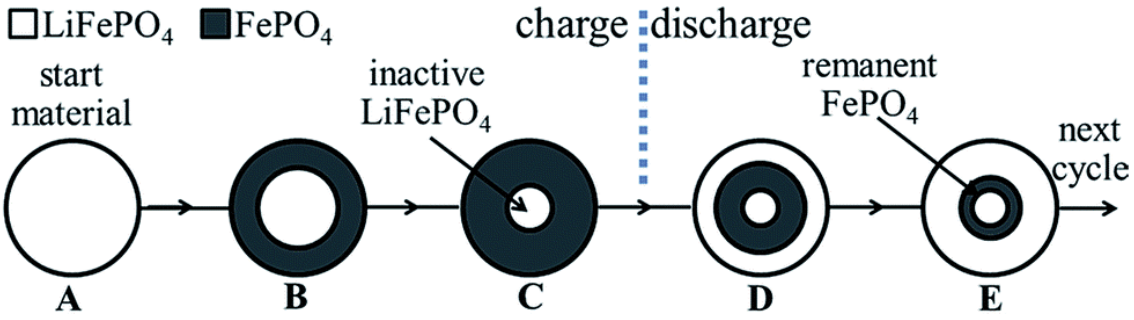

Figure 1-17. Two phase mechanism of $LiFePO_4$. Reproduced with permission.[214] Copyright **2016**, The Royal Society of Chemistry.

In 2006, Chen *et al.* conducted TEM studies and observed the occurrence of disordered transition zones in the *bc*-plane, as the phase boundary progresses in the direction of the *a*-axis, with the Li^+ moving in a direction parallel to the phase boundary, implying that the well adopted shrinking core model does not apply to individual crystallites.[216] Laffont *et al.* conducted a high-resolution electron energy loss spectroscopy study and confirmed that the classical shrinking core model cannot sufficiently describe the lithiation/delithiation mechanism in $LiFePO_4$.[217] Later in 2008, the domino-cascade model to describe the delithiation mechanism was introduced by Delmas *et al*. (Figure 1-18).[218] The intercalation and deintercalation processes are described to proceed in waves moving through the crystal along *a*-axis without any energy barrier that allows lithium intercalation/deintercalation to advance at very high rates, explaining the fast kinetics of $LiFePO_4$ crystals in the nano scale. This was further confirmed using precession electron diffraction in 2011 where phase maps at the nanometre scale of a large number of particles between 50–300 nm in size in a partially charged cell showed that the particles are either fully lithiated or fully delithiated.[219] However, the authors state that the classic shrinking core model may still be valid in the mesoscale (scale of agglomerates of particles). The debate on the validity of either of these models still continuous.[214, 220, 221]

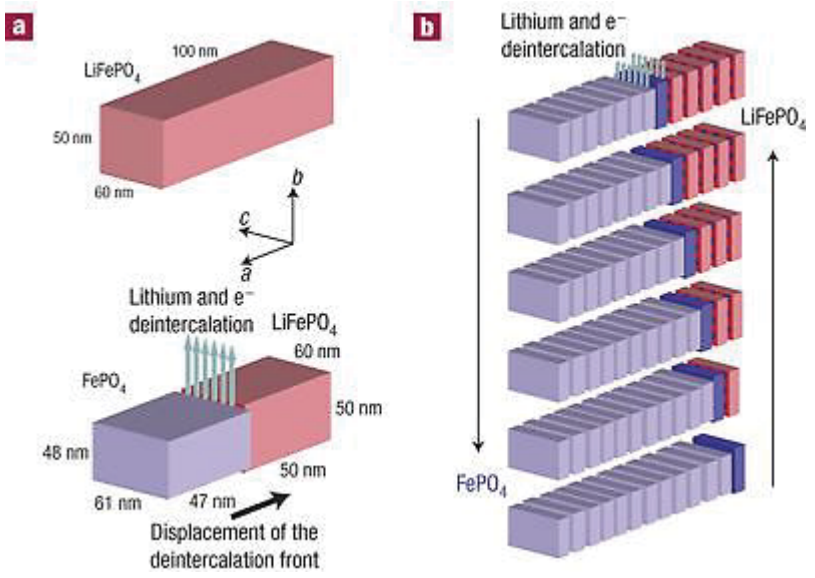

Figure 1-18. (a) Scheme showing a view of the strains occurring during lithium deintercalation. (b) Layered view of the lithium deintercalation/intercalation mechanism in a $LiFePO_4$ crystallite. Reproduced with permission. [218] Copyright **2008**, Nature Publishing Group.

Tavorite compounds $LiMPO_4F$

Tavorite with the general formula $AM(TO_4)X$ (A = alkali or alkaline-earth element, M = metal, T = p-block element, and X = O, OH, or F) consists of vertex-linked 1D chains of MO_4X_2 octahedra connected by TO_4 tetrahedra wherein X anions are located at the vertices shared by neighbouring MO_4X_2 octahedra, and A cations located at a number of sites throughout the framework (Figure 1-19).[222] $LiVPO_4F$ represents the typical tavorite material and its Li^+ insertion properties were firstly reported by Barker *et al.* in 2003.[223] The lithium extraction/insertion behaviour for $LiVPO_4F$ relies on the reversibility of the V^{3+}/V^{4+} redox couple operating at around 4.2 V vs. Li/Li^+ and can be described as follows:

$$LiV^{3+}PO_4F \leftrightarrow V^{4+}PO_4F + Li^+ + e^- \qquad (1\text{-}10)$$

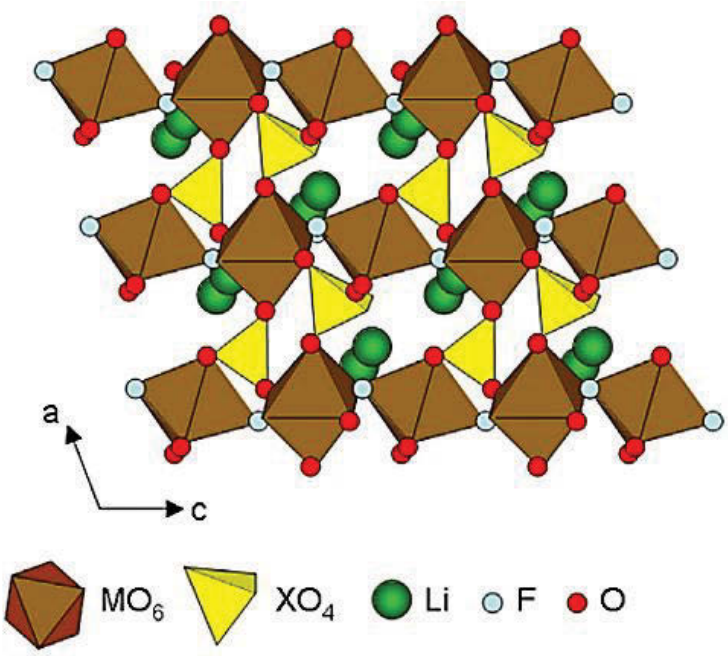

Figure 1-19. Schematic illustration of the tavorite structure along the *b*-crystallographic direction. Reproduced with permission.[222] Copyright **2013**, American Chemical Society.

Later studies improved phase purity and electrochemical performance, which achieved discharge capacities around 140 mA h g^{-1} (approaching the theoretical capacity of 156 mA h g^{-1}) combined with reasonable cycling stability (90% capacity retention after 400 cycles at 0.5C) suggesting excellent structural stability.[224, 225] Furthermore, two distinct lithium insertion/extraction potentials at 1.8 and 4.2 V vs. Li/Li^+ allows this material to be used in symmetric cells containing $LiVPO_4F$ as both positive and negative electrodes with an average voltage output of 2.4 V,[226] comparable to the performance of $LiFePO_4/Li_4Ti_5O_{12}$ high-power full cells.[227] Multidimensional Li^+ diffusion pathways that allow for high rate capabilities in the micron/submicron size realm combined with excellent structural and thermal stability make this material of interest for future LIBs.[228] $LiFePO_4F$ is another member of the tavorite class receiving some attention, providing a theoretical capacity of 152 mA h g^{-1} at a working potential of 2.9 V vs. Li/Li^+.[229]

Interestingly, $LiFePO_4F$ is in its charged state and is subsequently discharged to form Li_2FePO_4F, which is different to the behaviour of other intercalation materials.[230] It was first synthesized in 2007 by Barker *et al.*[231] and Ramesh *et al*. reported its fully lithiated structure in 2010 with a reversible capacity of around 145 $mA \cdot h \cdot g^{-1}$.[229] However, additional investigations encountered challenges for the preparation a high-purity $LiFePO_4F$ and substantial optimization is needed to advance this material further.[181]

NASICON compounds $Li_xM_2(PO_4)_3$

Phosphate-based NASICON compounds as possible LIB cathode materials have not been studied widely although many different compositions may exist theoretically.[232, 233] The two most studied examples of phosphate-based NASICON cathode materials are iron-based $Li_3Fe_2(PO_4)_3$ and vanadium-based $Li_3V_2(PO_4)_3$. $Li_3Fe_2(PO_4)_3$ has been reported to exist in two polymorph structures, monoclinic and rhombohedral, exhibiting very distinct electrochemical properties. The monoclinic phase of $Li_3Fe_2(PO_4)_3$ consists of corner-sharing PO_4 tetrahedra and FeO_6 octahedra, where Li^+ occupy two distinct 5-coordinate sites and a single 4-coordinate site.[234] The theoretical capacity of m-$Li_3Fe_2(PO_4)_3$ is 128 mA h g^{-1} at a working voltage of 2.8 V vs. Li/Li^+ using the Fe^{2+}/Fe^{3+} redox couple corresponding to the insertion of two additional Li^+. The monoclinic phase displays two distinct intercalation plateaus at voltages between 2.9 and 2.6 V vs. Li/Li^+ suggesting the existence of an intermediate composition $Li_4Fe_2(PO_4)_3$.[9] Its initially poor Li^+ diffusion properties have been addressed using traditional particle size control and coating techniques.[235, 236] The rhombohedral phase of $Li_3Fe_2(PO_4)_3$ can be prepared from the monoclinic sodium compound $Na_3Fe_2(PO_4)_3$ by ion exchange in a $LiNO_3$ melt or in a concentrated aqueous solution.[9] Its structure consists of PO_4 tetrahedra and FeO_6 octahedra connected through their vertices, forming $[Fe_2(PO_4)_3]$ lantern units stacked along the [001] direction.[237, 238] Two

extra Li^+ can be inserted to form $Li_{3+x}Fe_2(PO_4)_3$; however, different to the monoclinic phase, the insertion occurs in one continuous step or one sloping plateau at around 2.8 V vs. Li/Li^+.[9] Apart from early fundamental studies, both polymorphs have not received much research interest, possibly due to their low operating voltage and theoretical capacity. In contrast, $Li_3V_2(PO_4)_3$ has been studied intensively both as anode (see Section 1.1.2.2) and cathode material due the series of vanadium redox couples at different voltage regions. For instance, $Li_3V_2(PO_4)_3$ as a cathode exhibits a capacity of 197 mA h g^{-1} with the two redox couples, V^{5+}/V^{4+} and V^{4+}/V^{3+}, operating at high working potentials.[91, 239] As mentioned earlier, LVP exists in two polymorph structures, rhombohedral and monoclinic, which exhibit very different voltage–composition curves as a result of their structural differences. The rhombohedral structure displays only one voltage plateau at around 3.7 V vs. Li/Li^+ corresponding to the V^{3+}/V^{4+} redox couple and a two-phase transition between $Li_3V_2(PO_4)_3$ and $Li_1V_2(PO_4)_3$.[239] The monoclinic phase, where all three Li are mobile, exhibits better electrochemical properties than the rhombohedral phase. The thermodynamically stable monoclinic form of $Li_3V_2(PO_4)_3$ provides three Li^+ occupying different lattice sites, where Li1 is located at the tetrahedral site, and Li2 and Li3 occupy different pseudotetrahedral sites. All three Li^+ are mobile resulting in a theoretical capacity of 197 mA h g^{-1} and multi-plateau potential profiles, depending on the cut-off voltage window applied.[91, 239] As seen in Figure 1-20a, there are four plateaus in the charge profile located at around 3.6, 3.7, 4.1, and 4.6 V vs. Li/Li^+, corresponding to a sequence of phase transition processes between the single phases of $Li_xV_2(PO_4)_3$ (x = 3.0, 2.5, 2.0, 1.0, and 0).[240-242]

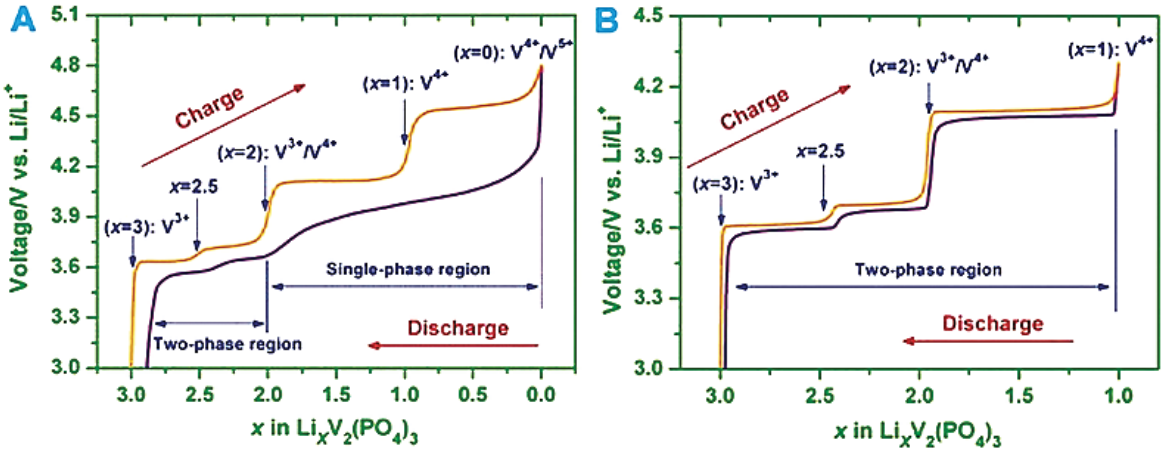

Figure 1-20. The electrochemical voltage–composition curves of m-$Li_3V_2(PO_4)_3$ in the voltage ranges of 3.0–4.8 V (A) and 3.0–4.3 V (B) vs Li/Li^+. Reproduced with permission.[239] Copyright **2014**, Elsevier.

In the discharge process, one long slope and two short plateaus can be seen corresponding to the insertion of two Li^+, 0.5 Li^+, and 0.5 Li^+.[243] Interestingly, when the upper cut-off voltage is set to 4.3 V vs. Li/Li^+, no solid solution region is observed (Figure 1-20b) and the charge/discharge proceeds via the two-phase transition processes as follows:[244]

$$Li_3V_2(PO_4)_3 \leftrightarrow Li_{2.5}V_2(PO_4)_3 \quad (1\text{-}11)$$

$$Li_{2.5}V_2(PO_4)_3 \leftrightarrow Li_2V_2(PO_4)_3 \quad (1\text{-}12)$$

$$Li_2V_2(PO_4)_3 \leftrightarrow LiV_2(PO_4)_3 \quad (1\text{-}13)$$

Although this voltage restriction strategy results in reduced reversible capacity, a more stable capacity retention upon cycling can be obtained.

1.2 Phosphate-based Materials for Sodium-ion Batteries

After decades of efforts, LIBs have pervaded our daily lives. As their applications progress from solely portable consumer electronics to grid-scale electric energy

storage and electric vehicles, cost has been one of the most severe obstacles for batteries used in these applications.[74] As a consequence, the development of LIBs heavily depends on the market price of lithium resources. Replacing lithium with cheaper alternatives might relief the stress of future batteries originating from price fluctuations when the market inevitably expands. In view of the various rechargeable batteries systems being currently under development, sodium-ion batteries (SIBs) are particularly interesting alternatives to LIBs due to their chemical similarity combined with higher abundance compared to lithium.[245, 246] The similarities and differences between Li and Na are summarized in Table 1-2. SIBs and LIBs share identical working principles that involve the reversible migration of cations/anions across a separator towards the electrodes upon charge-discharge. Besides the low cost and abundance of sodium, Al also does not form a binary alloy with sodium at a low voltage, unlike in LIBs, which enables the use of aluminium as a current collector for anodes of SIBs, leading to further reduced cost. However, the larger ionic radius of Na^+ (1.02 Å) compared to that of Li^+ (0.76 Å) makes it difficult to identify suitable electrode materials for SIBs. Successful reversible intercalation hosts must possess channels and interstitial sites large enough to accept the larger Na^+ cations. The following sections will introduce a selection of electrode materials for SIBs with a special focus on phosphate-based polyanionic materials.

Table 1-2. Characteristic properties of sodium and lithium.[245, 247, 248]

Category	***Sodium***	***Lithium***
Cation radius	1.02 Å	0.76 Å
Atomic weight	23 g mol^{-1}	6.9 g mol^{-1}
E (vs. SHE)	-2.7 V	-3.04 V

Melting point	97.7 °C	180.5 °C
Cost, carbonates	$150 per ton	$5000 per ton
Cost, current collector anode	Al $2000–2500 per ton	Cu $7000–8500 per ton
Capacity, metal	1165 mA h g^{-1}	3829 mA h g^{-1}
A–O coordination preference	Octahedral and prismatic	Octahedral and tetrahedral

1.2.1 Anode Materials for Sodium-ion Batteries

In contrast to a large number of reported cathode materials, progress in anode material research for SIBs proceeds much slower. Anode materials that have been reported can be categorized into carbon materials, intercalation-based materials, conversion and alloy compounds. Figure 1-21 summarizes operating voltage over specific capacities of various successful anode materials. This section will give a brief overview over the development of anode materials for SIBs.

1.2.1.1 Anode Materials based on Conversion and Alloying Reactions

Compared to LIBs, few conversion metal oxides/sulfides have been reported as anode materials for SIBs, including iron oxides, cobalt oxides, and copper oxides. For instance, Hariharan *et al.* demonstrated the electrochemical reaction of Na^+ with Fe_3O_4 to form Fe metal and Na_2O achieving a specific capacity of around 400 mA h g^{-1} less than half of its theoretical capacity of 926 mA h g^{-1}.[249] This can be attributed to sluggish kinetics of the Na^+ transfer due to the larger ion size and the nature of the SEI layer formed in Na cells.[250-256]

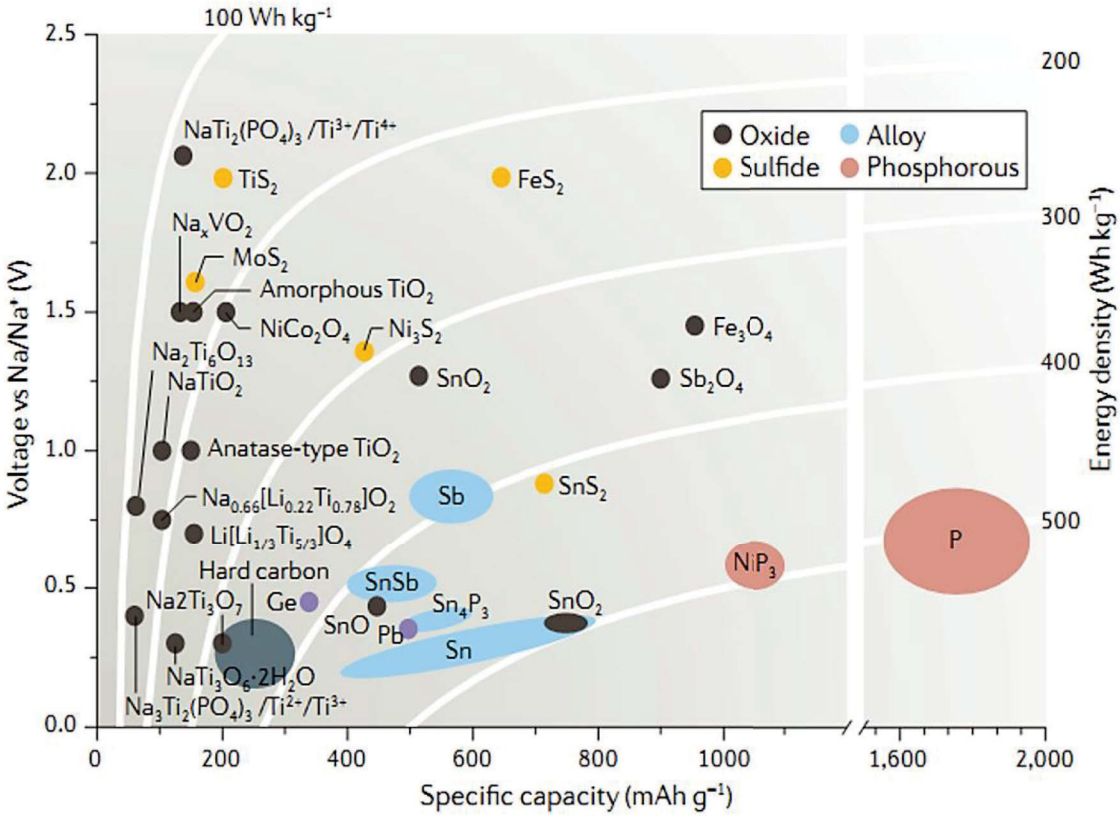

Figure 1-21. Operation voltages vs. specific capacities of various anode materials for SIBs. Reproduced with permission.[257] Copyright **2016**, Nature Publishing Group.

Jiang *et al.* further reported the reversible conversion reaction with Na^+ of a series of transition metal oxides including Fe_2O_3, Mn_3O_4, Co_3O_4, and NiO.[258] Experimental results by Klein *et al.* obtained for different copper compounds showed that the conversion of copper-based compounds, such as CuO and CuS, with sodium proceeds over intermediate phases, as evidenced by XRD and electrochemical measurements.[259] Therein, the sodiation of CuO was shown to consist of three steps. In the first step, Cu_2O and Na_2O were predominantly formed followed by the formation of an intermediate NaCuO phase in step two. The final sodiation products were found to be $Na_6Cu_2O_6$, Na_2O, and Cu.[260]

Metal sulfides have attracted attention as potential anode materials for SIBs because of their unique layered structure which is favourable for ion intercalation/de-intercalation during the initial discharge process. The subsequent conversion reaction can then generate high theoretical capacities. Molybdenum disulfide (MoS_2), for instance, consists of a lamellar structure. Within this structure, Na^+ intercalation leads to a series of two-phase structural transitions from 2H-MoS_2 to 1T-MoS_2.[261] Depending on the depth of intercalation, the structure of MoS_2 can be partially recovered (to 1T-MoS_2) during the subsequent charge process if less than 1.5 Na^+ per formula of MoS_2 were intercalated. Nevertheless, its structure cannot be restored once it was fully converted to Na_xS and metallic Mo. Incorporating MoS_2 into a carbon matrices showed promise in enhancing its electrochemical properties;[262-268] however, large irreversible capacities in the first cycle and a lack of understanding of possible interactions between MoS_2 and carbon still hinder a wider implementation of MoS_2 as anode material for SIBs. As another member of the metal sulphide family, SnS_2 has been identified as one of the highest capacity anode materials for SIBs because it undergoes a combination of both conversion and alloying reaction during cycling.[269] Meng and co-workers investigated the sodiation/desodiation process of SnS_2/reduced graphene oxide composites and discovered that Na_2S_2 was formed instead of Na_2S at the fully discharged state.[270] The as-formed Na_2S_2 functions as a matrix to relieve the strain caused by the volume expansion of the Na-Sn alloy reaction. Upon completion of a full cycle its crystal structure could not be retained and amorphous SnS_2 is formed. Furthermore, efforts have been devoted to develop freestanding SnS_2-based electrode materials with the aim to improve electrochemical performances and durability this material.[271, 272]

Alloy anodes, mainly Group IVa and Va elements, accommodate Na^+ by forming alloys with sodium at low potentials, which generates high theoretical specific capacities as summarized in Table 1-3. Among all reported alloying anode

materials, tin is inexpensive (around 20 USD kg^{-1}), relatively safe to handle in its powder form (moderately pyrophoric), nontoxic, highly abundant, and exhibits high storage capacities both by weight and by volume. In addition, Sn is able to form a variety of compounds, such as SnO, SnO_2, SnS, SnS_2, and Sn_4P_3, which offer opportunities to manipulate and improve electrochemical performances. As mentioned earlier, these Sn-based compounds provide high specific capacities as a consequence of their ability to undergo both conversion and alloying reactions.[273]

Table 1-3. Summary of properties of typical metal, metalloid, and non-metal materials for SIBs.[273]

Alloying material	***Reduction product***	***Theoretical capacity***	***Volumetric expansion (Na_xX/X)***	***Average voltage (vs. Na/Na^+)***
Sn	$Na_{3.75}Sn$	847 mA h g^{-1}	520%	0.2 V
Sb	Na_3Sb	660 mA h g^{-1}	393%	0.6 V
P	Na_3P	2596 mA h g^{-1}	408% (red)	0.4 V
			500% (black)	
Si	NaSi	954 mA h g^{-1}	243%	0.5 V
Ge	NaGe	369 mA h g^{-1}	305%	0.3 V

The main issue with Sn-based anode materials is their large volume change (up to 300%) during cycling, which leads to electrode pulverization and consequently poor cycle stability. The incorporation of carbon materials has shown potential to improve the cycling stability as they not only provide electronic conductive networks but also prevent agglomeration of Sn nanoparticles.[274, 275] For instance, the integration of Sn-based anode materials into 2D graphene/reduced graphene oxide is among the most popular strategies due to the simplicity of the preparation process and effectiveness to improve the cycling performance of Sn-based anodes.

For example, Wang *et al.* reported ultrafine SnO_2 nanoparticles (around 5 nm) on a reduced graphene oxide framework using a simply hydrothermal method, which delivered a reversibly capacity of 330 mA h g^{-1} and an outstanding capacity retention of 81.3% over 150 cycles.[276] Furthermore, highly effective wet-mechanochemical processes[251] and ice-templated preparation methods[277] have been proposed to prepare high performance Sn- and carbon-based anode materials for SIBs.

1.2.1.2 Anode Materials based on Intercalation

In contrast to the difficulties associated with graphitic carbons,[278-282] the Na^+ storage in non-graphitic carbon materials (i.e. hard carbon, soft carbon, and amorphous carbon) is thermodynamically feasible. The extent of Na intercalation depends critically on the microstructure and the particle size of the carbon used.[283] Among them, hard carbon has been widely studied as a promising anode. The storage mechanism of Na^+ in hard carbons can be described using a so-called "card-house" model: i) Na^+ intercalation between graphene sheets (corresponding to the sloping-voltage region) and (ii) Na^+ filling in the pores between nano-graphitic domains (corresponding to the plateau region).[284] Therein, the number of defect sites in hard carbon strongly affect the Na storage capacity in the slope-voltage region;[285] however, there is no consensus on the Na storage mechanism in the low-voltage plateau region with the debate focusing on whether Na metal nanoclusters are formed in this region.[286-288]

Ti-based oxides have been widely investigated as anode materials for Na intercalation because of their low cost and environmental benignity. Pioneering work by Xiong *et al.* reported amorphous TiO_2 nanotubes as anodes in the voltage range between 0.9 and 2.5 V.[289] This work ignited further investigations of Ti-based oxides with different polymorphs and nanostructures as intercalation materials for SIBs utilizing the Ti^{3+}/Ti^{4+} redox couple.[290] Na insertion into TiO_2

proceeds as follows: i) pseudo-capacitive reactions during the initial discharge process, ii) structural rearrangement, iii) a disproportionation reaction and formation of Ti^0 and O_2 during further discharge, and iv) reversible Na de/insertion in $Na_x(TiO_2)$ ($0.28 \leq x \leq 0.69$).[291] Furthermore, $Li_4Ti_5O_{12}$ has also been found to accommodate Na^+, delivering a reversible capacity of about 150 mA h g^{-1}.[292] Since the Na^+ diffusion coefficient of $Li_4Ti_5O_{12}$ is 5 orders of magnitude smaller than its Li^+ diffusion coefficient, research efforts have been focused on the development of nanosized $Li_4Ti_5O_{12}$ to improve its electrochemical performance in SIBs.[293] Sodium titanium oxides, such as $Na_2Ti_3O_7$,[294] $Na_2Ti_2O_5$,[295] layered $NaTiO_2$,[296] $Na_2Ti_6O_{13}$,[297] and $Na_2Ti_7O_{15}$,[298] have also been investigated as anode materials for SIBs.

Two-dimensional (2D) metal carbides, carbonitrides, and nitrides, denoted as MXenes, were first reported by Naguib *et al.* in 2011.[299] MXenes feature a 2D structure similar to that of graphene and are of the general formula $M_{n+1}X_nT_x$ (M = transition metal, X = carbon or nitrogen, T = surface terminations such as OH, O, and F) with n values varying from 1 to 3. MXenes are prepared from their corresponding MAX phases (A is mainly a group IIIa or IVa element), which are layered hexagonal with A slaps sandwiched between M and X layers. The known MAX phases are listed in Table 1-4. In MAX phases, the M–A bonds are weaker than the M–X bonds, which allows the selective etching of the A layers. MXenes successfully prepared from the corresponding MAX phases include Ti_2C, Nb_2C, V_2C, Mo_2C, Ti_3C_2, Ti_3CN, Mo_2TiC_2, $Mo_2Ti_2C_3$, and Ti_4N_3.[300-303] When applied as anode material for SIBs, multilayered Ti_2CT_x MXene delivered a reversible capacity of 175 mA h g^{-1} at a current density of 20 mA g^{-1} and showed good rate capabilities even at a current density of 5000 mA g^{-1}. Furthermore, multilayered $Ti_3C_2T_x$ has also been investigated as potential negative electrode for SIBs and exhibited a capacity around 100 mA h g^{-1}.[304, 305] It was also found that the Na^+ insertion potentials of MXenes can be tuned by changing the transition metal and surface

functional groups[306, 307] and V_2CT_x was successfully used as positive electrode in SIBs.[308] Paired with hard carbon, the resulting full cell delivered a maximum cell voltage of 3.5 V and a cell capacity of 50 mA h g^{-1}.

Table 1-4. A selection of reported MAX phases.[309]

211 (M_2AX)						**312 (M_3AX_2)**	**413 (M_4AX_3)**
Tl_2ALC	Ti_2CdC	Ti_2GaC	Ti_2InC	Ti_2TlC	Sc_2InC	Ti_3AlC_2	Ti_4AlN_3
V_2ALC	V_2GaC	Cr_2GaC	Ti_2AlN	Ti_2GaN	Ti_2InN	V_3AlC_2	V_4AlC_3
V_2GAN	Cr_2GaN	Ti_2GeC	Ti_2SnC	Ti_2PbC	V_2GeC	Ti_3SiC_2	Ti_4GaC_3
CR_2ALC	Cr_2GeC	V_2PC	V_2AsC	Ti_2SC	Zr_2InC	Ti_3GeC_2	Ti_4SiC_3
ZR_2TLC	Nb_2AlC	Nb_2GaC	Nb_2InC	Mo_2GaC	Zr_2InN	Ti_3SnC_2	Ti_4GeC_3
ZR_2TLN	Zr_2SnC	Zr_2PbC	Nb_2SnC	Nb_2PC	Nb_2AsC	Ta_3AlC_2	Nb_4AlC_3
ZR_2SC	Nb_2SC	Hf_2InC	Hf_2TlC	Ta_2AlC	Ta_2GaC		Ta_4AlC_3
HF_2SNC	Hf_2PbC	Hf_2SnN	Hf_2SC				

Phosphate-based polyanionic compounds with a working potential low enough to be applicable as anode in SIBs are rare and to the best of my knowledge only two types have been reported so far. These are NASICON-type $NaTi_2(PO_4)_3$ and $Na_3V_2(PO_4)_3$. The anodic performance of $NaTi_2(PO_4)_3$ has firstly been reported by Delmas *et al.* in 1987.[310] TiO_6 octahedra are connected by PO_4 tetrahedra, which create the NASICON framework with two sodium ions providing a high theoretical capacity of 133 mA h g^{-1} through a two-phase reaction between $NaTi_2(PO_4)_3$ and $Na_3Ti_2(PO_4)_3$. The working potential of this material is around 2.1 V vs. Na/Na^+ utilizing the Ti^{4+}/Ti^{3+} redox couple, which is high enough to avoid the formation of a charge consuming solid electrolyte interphase.[311] A second redox couple Ti^{3+}/Ti^{2+}

at around 0.4 V s Na/Na^+ has also been identified allowing for a high reversible capacity of 208 mA h g^{-1} when both redox couples are utilized.[312] Although a large number of publications investigate the performance of $NaTi_2(PO_4)_3$ in aqueous SIB systems due to its high operating potential,[311] its performance in organic SIBs has also been studied in recent years. The main focus in these studies, however, is to improve the inherent low electronic conductivity induced by the phosphate group. Strategies to accomplish this include carbon coatings,[313-315] transition metal oxide coatings,[316] and nanostructuring.[317] $Na_3V_2(PO_4)_3$ can be applied as anode for SIBs by utilizing the sodiation voltage plateau at 1.6 V vs. Na/Na^+, which corresponds to the insertion of one Na^+ to form $Na_4V_2(PO_4)_3$.[318, 319] However, this reaction results in a capacity half of that of its cathode reaction at a potential of around 3.4 V vs Na/Na^+. As discussed in section 1.1.2.2, rhombohedral $Li_3V_2(PO_4)_3$ can accommodate two additional Li^+ when applied as anode material for LIBs with a capacity of around 120 mA h g^{-1}. Furthermore, $Na_3V_2(PO_4)_3$ and $Li_3V_2(PO_4)_3$ share the same skeleton structure of $V_2(PO_4)_3$ consisting of corner-shared VO_6 octahedra and PO_4 tetrahedra differing in the occupancies of Na^+ and Li^+. For $Na_3V_2(PO_4)_3$, two Na^+ occupy the 18e sites and one Na^+ occupies the 6b site, while all three Li^+ occupy the 18f sites of $Li_3V_2(PO_4)_3$. During lithiation, $Li_3V_2(PO_4)_3$ accommodates two Li^+ in the 3a (0.5 Li), 3b (0.5 Li), and 6c (1 Li) sites, respectively.[98] $Na_3V_2(PO_4)_3$, on the other hand, accommodates one Na^+ in the last empty 18e site, which results in a voltage plateau at 1.6 V vs. Na/Na^+ while the 6a site was found to accommodate one additional Na^+ at a potential of around 0.3 V vs. Na/Na^+.[320] Figure 1-22 shows the calculated sodiation voltage profile (red dotted line) of $Na_3V_2(PO_4)_3$ compared to an experimentally determined voltage profile (blue solid line). This results in theoretical capacity of 117 mA h g^{-1} for the anodic performance of $Na_3V_2(PO_4)_3$ which is identical to its cathodic capacity and makes this material of high interest for the construction of symmetric SIB cells.[321, 322]

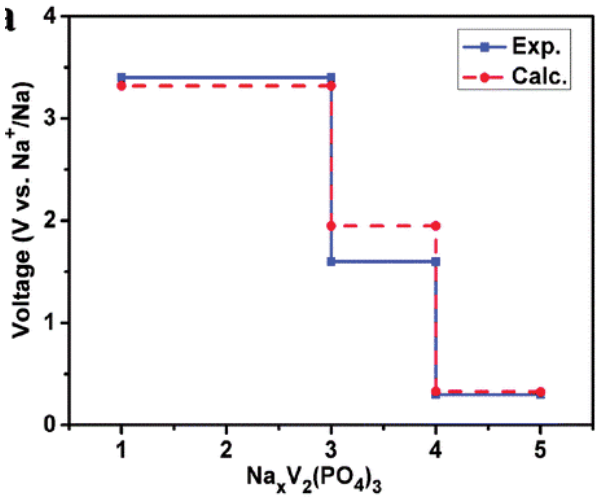

Figure 1-22. Calculated sodiation voltage profile (red dotted line) of $Na_3V_2(PO_4)_3$ in comparison to the experimentally determined voltage profile (blue solid line). Reproduced with permission.[320] Copyright **2015**, Royal Society of Chemistry.

1.2.2 Cathode Materials for Sodium-ion Batteries

A large number of potential cathode materials for SIBs has been identified as summarized in Figure 1-23. These cathode materials can be categorized into three main categories: layered transition-metal oxides, Prussian blue, and polyanionic (phosphates, fluorophosphates, pyrophosphates, fluorosulfates, and sulfates) cathodes. This section will briefly introduce a selection of conventionally used cathode materials for SIBs and will then give a more detailed overview over cathode materials based on polyanionic frameworks at the end of this chapter.

1.2.2.1 Commonly used Cathode Materials for Sodium-ion Batteries

Layered sodium transition-metal oxides

The most common layered structures are composed of a sheet of edge-sharing MeO_6 octahedra (Me = 3d transition metals), which are stacked along the *c*-axis direction hosting Na^+ in between the MeO_2 motifs.

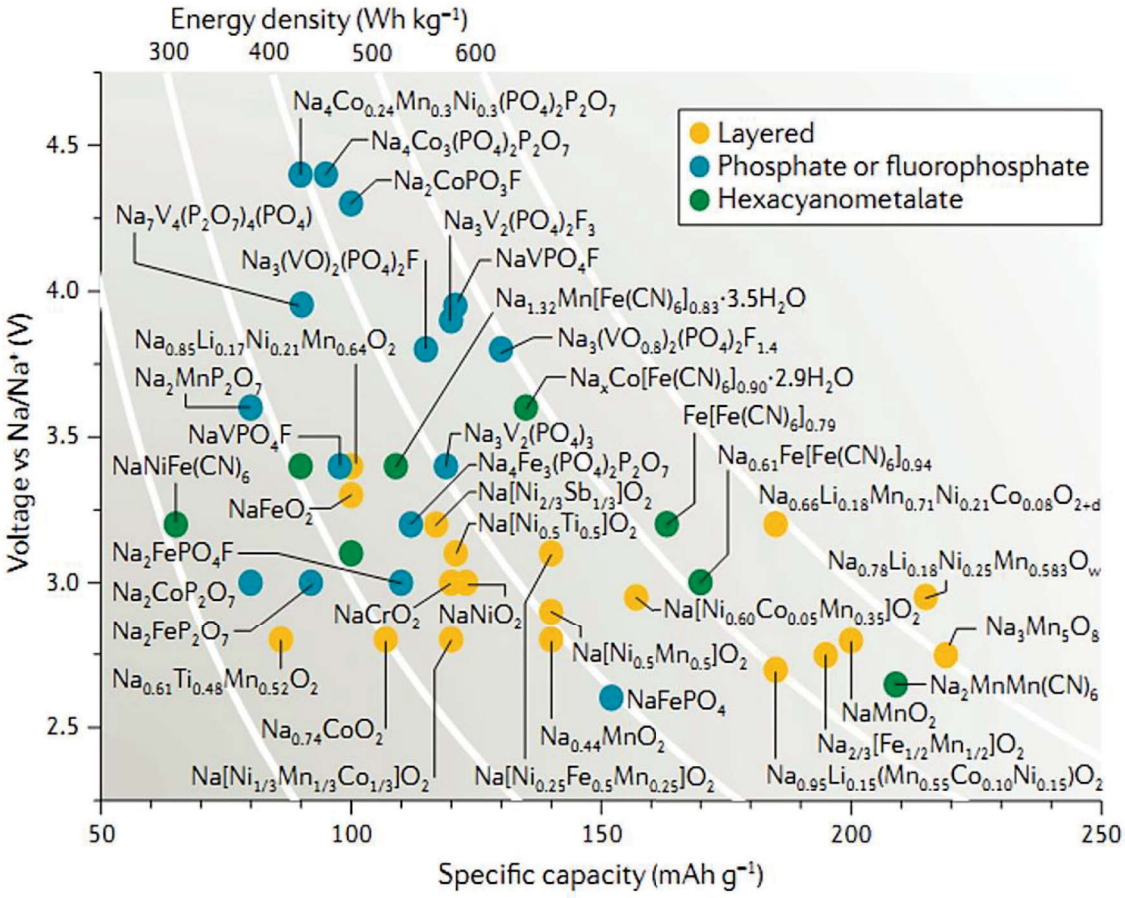

Figure 1-23. Operation voltages versus specific capacities of various cathode materials for SIBs. Reproduced with permission.[257] Copyright **2016**, Nature Publishing Group.

As shown in Figure 1-24, there are two types of sodium-based layered materials, O3-type and P2-type, where O and P represent octahedral and trigonal prismatic coordination of Na^+ and 3 or 2 stands for the number of distinguishable sodium layers. The sodium extraction from O3- and P2-type phases induces phase transitions. This occurs, for instance, when Na^+ are extracted from the O3- phase, which causes vacancies to form. As a result, Na^+ become energetically stable at prismatic sites, which are formed by gliding of MeO_2 slabs.[323, 324] Consequently, oxygen packing changes from “AB CA BC” to “AB BC CA”, becoming the P3-type phase as shown in Figure 1-24.[275]

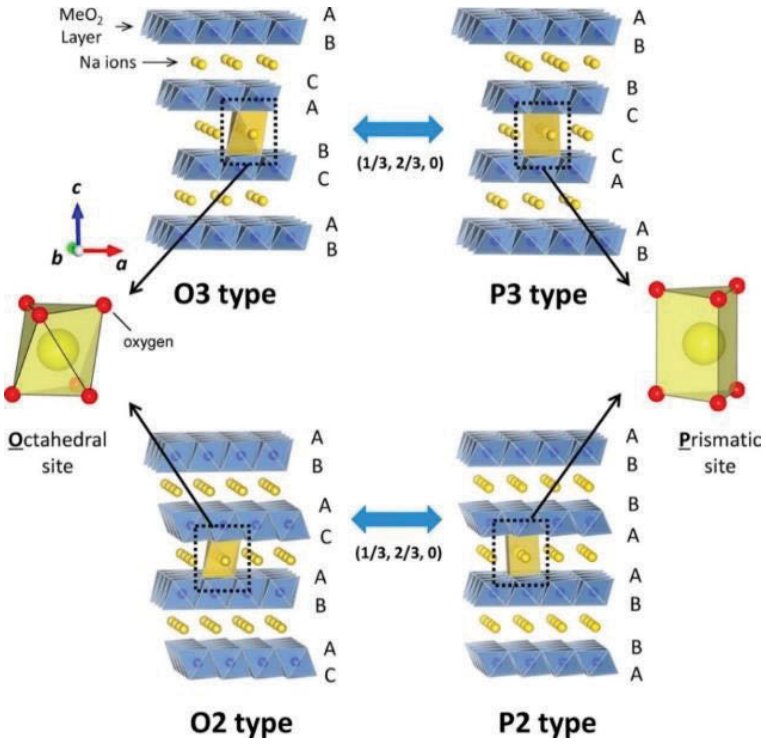

Figure 1-24. Classification of Na-Me-O layered materials with sheets of edge-sharing MeO_6 octahedra and phase transition processes induced by sodium extraction. Reproduced with permission.[275] Copyright **2014**, American Chemical Society.

When Na^+ are extracted from the P2- phase, the layered oxides transform to a O2-type phases. One of the first layered transition metal oxides investigated for SIBs was α-$NaMnO_2$ with an O3-type structure. This material exhibits a voltage profile of pronounced stepwise processes, suggesting structural transitions, and delivers a capacity of 200 mA h g^{-1}.[325]

P2-$Na_{2/3}Mn_{1/2}Fe_{1/2}O_2$ is among the most promising transition metal oxide cathode materials for SIBs in terms of both sustainability and electrochemical performance.[326] It delivers a reversible capacity of 190 mA h g^{-1} utilizing the Fe^{3+}/Fe^{4+} redox couple. However, its long-term cycling stability is not satisfactory and cation doping has been shown to improve capacity retention in materials such

as P2-$Na_{0.8}[Li_{0.12}Ni_{0.22}Mn_{0.66}]O_2$,[327] P2-$Na_{0.67}Mn_{1-y}Mg_yO_2$ (y = 0, 0.05, 0.1, 0.2),[328] and $NaFe_{1-y}Ni_yO_2$ (0.5< y <0.7).[329]

Prussian blue cathodes

The large atomic radius of the sodium ion requires cathode materials with open host frameworks containing suitable transition metal ions to host Na^+. Prussian blue analogues (PBAs) provide a cubic structure consisting of Fe^{2+} and Fe^{3+} sitting on alternate corners of corner-shared Fe octahedra bridged by cyano $(C\equiv N)^-$ ligands (Figure 1-25).[330] Their open-framework contains channels (3.2 Å) and interstitial sites (4.6 Å) that allow fast solid-state diffusion of Na^+.[331] The most intensively investigated PBA is hexacyanoferrate due to its low cost and simplistic synthesis. The pioneering work conducted by Goodenough and co-workers showed that the insertion of Na^+ into $KFe_2(CN)_6$ resulted in a reversible capacity around 100 mA h g^{-1} with no significant capacity fading after 30 cycles.[330] The $KFe_2(CN)_6$ cathode utilizes the high-spin Fe^{3+}/Fe^{2+} redox couple bonding to N at around 2.97/2.92 V vs. Na/Na^+ and the low-spin Fe^{3+}/Fe^{2+} couple bonding to C at around 3.69/3.58 V vs. Na/Na^+.

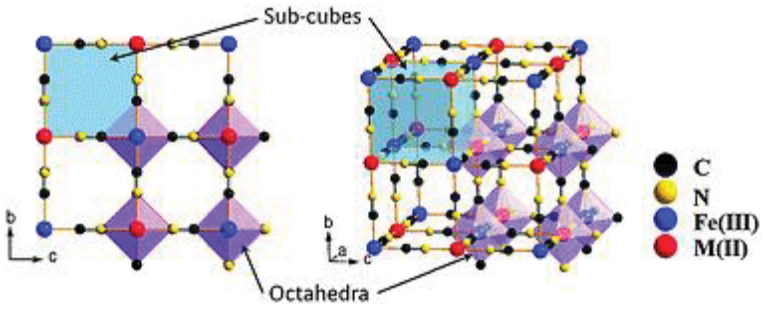

Figure 1-25. Framework of Prussian blue analogues. Reproduced with permission.[330] Copyright **2012**, Royal Society of Chemistry.

However, low coulombic efficiency in the initial cycle has been observed for $KFe_2(CN)_6$, which could be the result of residual crystal water within this PBA compound.[330]

1.2.2.2 Phosphate-based and other Polyanionic Cathode Materials for Sodium-ion Batteries

In addition to layered oxide and Prussian blue materials, a large number of polyanionic sodium compounds, such as phosphates, fluorophosphates, fluorosulfates, and sulfates, have been investigated as cathode materials for SIBs. Advantages of sodium polyanions for SIBs include:[331] i) Diverse open-framework structures; ii) Presence of low-energy Na^+ migration pathways; iii) possibilities of tuning the operating voltage by modifying the local environments; iv) structural energetics for a flat voltage response; and v) thermal and oxidative stability at high potentials due to robust covalent frameworks.

Olivine and Maricite Structures

As $LiFePO_4$ has been commercialized as a cathode material for LIBs, its sodium analogue, olivine $NaFePO_4$, has also attracted interest due to its high theoretical specific capacity (154 mA h g^{-1}) and relatively high working potential (around 2.8 V vs. Na/Na^+).[332] However, direct high-temperature synthesis cannot produce olivine-phase $NaFePO_4$ and a thermodynamically favoured maricite phase is formed instead. The maricite phase is believed to provide poor electrochemical activity because of its one-dimensional, edge-sharing FeO_6 octahedrons that form slow Na^+ pathways.[333-335] The first report on the Na^+ insertion capabilities of olivine FePO4 was reported by Le Poul *et al.* and showed that 0.65 Na can be inserted to form $Na_{0.65}FePO_4$.[335] This discovery ignited tremendous efforts to synthesize and characterize olivine $NaFePO_4$ materials for SIBs. Oh *et al.* then studied the electrochemical performance of $NaFePO_4$ obtained by an

electrochemical exchange from olivine $LiFePO_4$, and reported a stable capacity of 125 mA h g^{-1}.[336] Structural and electrochemical features of olivine $NaFePO_4$ compared to olivine $LiFePO_4$ have also been investigated. Zhu *et al.* attributed the more sluggish Na storage behaviour of $NaFePO_4$ to the lower Na^+ diffusion coefficient and higher charge transfer resistance compared to $LiFePO_4$.[337] It was also found that $NaFePO_4$ differs from $LiFePO_4$ in their surface structures and relative energies, which are important for rate performance.[338] However, density functional studies of Li^+ and Na^+ diffusion in $LiFePO_4$ and $NaFePO_4$ showed that electronic and Li or Na ionic migration in the bulk materials did not differ significantly between $LiFePO_4$ and $NaFePO_4$.[339, 340] As mentioned above, maricite $NaFePO_4$ is believed to be electrochemically inactive. However, maricite $NaFePO_4$ has been proven to exhibit excellent Na storage performance with the ability extract all Na^+ by transforming the maricite structure to amorphous $FePO_4$.[341] The maricite $NaFePO_4$ electrode delivered a capacity of 142 mA h g^{-1} displaying sloping charge/discharge curves and a stable cycle life of over 200 cycles.

NASICON Structures

More promising sodium phosphates for positive SIB electrodes are NASICON compounds, which feature large tunnels for fast Na^+ conduction. Among them, $Na_3V_2(PO_4)_3$ has been extensively studied.[342, 343] $Na_3V_2(PO_4)_3$ provides a high operating potential of around 3.37 V vs. Na/Na^+ corresponding to the V^{4+}/V^{3+} redox couple, which results in a theoretical capacity of 118 mA h g^{-1}. As for all phosphate-based materials, tremendous efforts have been devoted to improving the electrochemical performance of $Na_3V_2(PO_4)_3$, including metal ion doping, carbon coating, and nanostructuring. For instance, Kim *et al.* incorporated potassium ions with a larger ionic radius as functional pillar ions into $Na_3V_2(PO_4)_3$, and thus, enlarging Na^+ diffusion pathways and increase the lattice volume.[344] Furthermore, $Na_3V_{2-x}Mg_x(PO_4)_3/C$ composites containing various Mg^{2+} contents

were also investigated, which significantly improved ionic and electronic conductivity, resulting in enhanced rate and cycle performances.[345, 346] Iron substitution (both Fe^{2+} and Fe^{3+}) was also found to effectively activate the $V^{4+/5+}$redox couple in addition to increasing the cell volume. The Fe^{3+} substitution results in the distortion of the M1 octahedra, which allows the extraction of Na^+ residing at M1 sites.[347, 348] Similar phenomena were also found when chromium, manganese, and aluminium substitutions were investigated.[349-351] In addition to these strategies, carbon decoration has been shown to be very effective to improve the electrochemical performance $Na_3V_2(PO_4)_3$ with many different carbon matrices and coating strategies employed to prepare high-performance $Na_3V_2(PO_4)_3$.[352-356]

Sodium fluorophosphates have been explored as new cathode materials due to their high operating voltage that originates from the presence of highly electronegative fluorine atoms in the covalent polyanionic framework. Some representatives of this type of phosphate-based polyanionic material include $Na_3V_2(PO_4)_2F_3$,[357] Na_2FePO_4F,[358] and $Na_{1.5}VPO_{4.8}F_{0.7}$.[359] $Na_3V_2(PO_4)_2F_3$ was shown to provide a high average working potential of 3.9 V vs. Na/Na^+, electrochemically reacting in a single-phase transition fashion with negligible volume changes (2%).[357] Nazar and co-workers reported Na_2FePO_4F with a layer-like 2D framework of $Fe_2O_7F_2$ bioctahedra connected by PO_4 tetrahedra, which can host two Na^+ in its interlayer space. The charge/discharge profiles of this material show two two-phase plateaus centred at 2.90 V and 3.05 V vs. Na/Na^+.[358]

Sodium florosulfates, such as $NaFeSO_4F$, provide a tunnel structure with an ionic conductivity of around 7.14×10^{-7} S^3 cm^{-1} utilizing the Fe^{2+}/Fe^{3+} redox couple at a working potential of around 3.6 V vs. Na/Na^+.[311] However, only 0.07 Na^+ can be electrochemically removed from its structure resulting in poor electrochemical performance.[360] On the other hand, transition metal sulfates such as $Na_2Fe(SO4)_2{\cdot}2H_2O$ and $Na_2Fe_2(SO_4)_3$, are more electrochemically active. For

example, Barpanda *et al.* found that kröhnkite-type $Na_2Fe(SO_4)_2 \cdot 2H_2O$ operates at around 3.25 V vs. Na/Na^+ utilizing the Fe^{2+}/Fe^{3+} redox couple with good structural reversibility.[361] Interestingly, $Na_2Fe_2(SO_4)_3$ shows the highest ever reported Fe^{3+}/Fe^{2+} redox potential at 3.8 V vs. Na/Na^+ along with fast kinetics achieving a reversible capacity of around 102 mA h g^{-1}.[362]

Chapter 2: Experimental Methods

2.1 Overview

Figure 2-1 shows the methodologies and experimental techniques used in this research project, which include:

1) Design and preparation of electrode materials using solid state reaction assisted by ball milling, freeze drying, and spray drying, and solution-based hydrothermal reaction. All chemicals used throughout this research project are listed in Table 2-1.

2) Characterization of the as-prepared electrode materials using X-ray diffraction (XRD), scanning electron microscopy (SEM), transmission electron microscopy (TEM), thermogravimetric analysis (TGA), Raman spectroscopy, and Brunauer–Emmett–Teller (BET) N_2 sorption/desorption measurements.

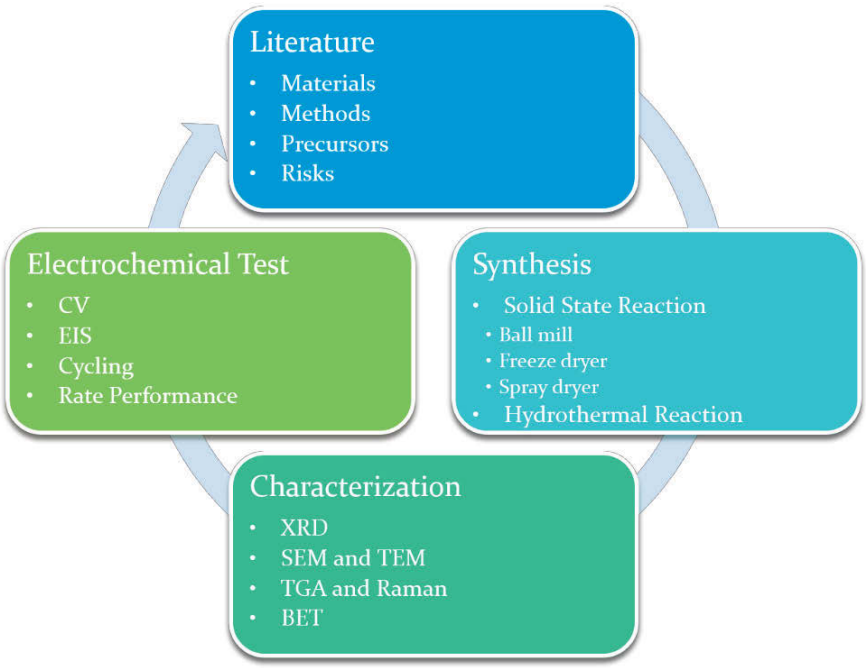

Figure 2-1. Experimental methods used in this research project

3) Electrochemical measurements of the as-prepared electrode materials for lithium/sodium-ion batteries using cyclic voltammetry (CV), electrochemical impedance spectroscopy (EIS), and galvanostatic charge/discharge profiles.

Table 2-1. List of chemicals used in this research project.

CHEMICALS	FORMULA	PURITY	SUPPLIER
AMMONIUM DIHYDROGEN PHOSPHATE	$NH_4H_2PO_4$	98%	Sigma-Aldrich
CARBON BLACK	C	100%	Sigma-Aldrich
CARBOXYMETHYL CELLULOSE SODIUM SALT (CMC)	$C_8H_{15}NaO_8$		Sigma-Aldrich
CITRIC ACID (CA)	$HOC(COOH)(CH_2COOH)_2$	99%	Sigma-Aldrich
ETHANOL	CH_3CH_2OH	95%	Chem Supply
ETHYLENE CARBONATE (EC)	$(CH_2)_2CO_3$	99%	Sigma-Aldrich
FLUOROETHYLENE CARBONATE (FEC)	$C_3H_3FO_3$	99%	Sigma-Aldrich
HYDROCHLORIC ACID	HCl	37%	Sigma-Aldrich
IRON CHLORIDE	$FeCl_3$	97%	Sigma-Aldrich
IRON OXALATE	$FeC_2O_4{\cdot}2H_2O$	99%	Sigma-Aldrich
LITHIUM FOIL	Li	99.999 %	Hohsen Corporation Japan
LITHIUM CARBONATE	Li_2CO_3	99%	Sigma-Aldrich
LITHIUM HYDROXIDE	$LiOH{\cdot}H_2O$	98%	Sigma-Aldrich
N-METHYL PYRROLIDINONE (NMP, ANHYDROUS)	C_5H_9NO	99.5%	Sigma-Aldrich
POLYETHYLENE GLYCOL (PEG)	$H(OCH_2CH_2)_nOH$		Sigma-Aldrich
POLY(VINYL ALCOHOL)	$[-CH_2CHOH-]_n$		Sigma-Aldrich

POLY(VINYLIDENE DIFLUORIDE) (PVDF)	$(CH_2CF_2)_n$		Sigma-Aldrich
POLYPROPYLENE SEPARATOR	$(C_3H_6)_n$		Celgard
PROPYLENE CARBONATE (PC, ANHYDROUS)	$C_4H_6O_3$	99.7%	Sigma-Aldrich
SODIUM	Na	99.9%	Sigma-Aldrich
SODIUM DIHYDROGEN PHOSPHATE	$NaH_2PO_4 \cdot 2H_2O$	98%	Sigma-Aldrich
VANADIUM CHLORIDE	VCl_3	97%	Sigma-Aldrich

2.2 Materials Preparation

Solid-State Reaction

The solid-state reaction is defined as the direct reaction of a mixture of solids, which generally requires temperatures 500 to 1500 °C as the starting solids would not normally react at room temperature. Generally, this method utilizes the thermal decompositions properties of the solid starting materials to create a new crystalline material. The nucleation of desired products is considered difficult because of (a) significant differences in structure between reactants and products and (b) the large amount of structural reorganization that is involved in forming the products. The growth of the product might also be hindered because of diffusion in existing product layers to the new reaction interfaces. In this context, a key step to perform a successful solid-state reaction is to mix precise amounts reactants sufficiently to maximize area of contact between reacting solids. A typical procedure is outlined as follows:

Reagents. The reactants must be dried thoroughly and weighed according to the expected nature of the product and volatility of the starting materials under the given reaction conditions. Fine grained materials should be used if possible in

order to maximize surface area and hence reaction rates. This is accomplished by incorporating the spray drying method, which generates well-dried fine particles and particle clusters.

Mixing. After acquisition of precise quantities of the solid starting materials, the reactants are mixed. For manual mixing of small quantities, usually an agate mortar and pestle are employed. For large quantities, wet ball milling is generally used to adequately combine all starting materials before solid-state reaction. Sufficient amounts of some volatile organic solvent, such as acetone or ethanol, can be added to the mixture to aid homogenization.

Heat treatment. After mixing, the reactants are put in suitable containers chemically inert to the reactants under the heating conditions and are then heated. The heating program to be used depends strongly on the form and reactivity of the reactants. According to the demands of the final products, a protection gas (argon, nitrogen, argon/hydrogen, etc.) can be applied to avoid oxidization.

In this research project, the solid-state reaction route was employed to prepare $LiFePO_4$ and $Na_3V_2(PO_4)_3$ cathode materials. The thermal decomposition behaviour of different sugars and microcrystalline cellulose was also utilized within the solid-state reaction method to generate carbon coatings or free-standing current collector substrates.

2.3 Materials Characterization

2.3.1 X-ray Diffraction (XRD)

The phase and crystallographic structure of all as-prepared materials presented in this project were characterized by X-ray diffraction. Crystalline atoms cause the diffraction of a beam of incident X-rays into many specific directions. Measuring the angles and intensities of the diffracted beams, a three-dimensional picture of the

density of electrons within the crystal can be produced, which allows the determination of the mean positions of the atoms in the crystal, as well as their chemical bonds, their disorder, and various other information. This correlation is described by Bragg's Law:

$$n\lambda = 2d \sin\theta \quad (2\text{-}1)$$

where d is the interplanar spacing, θ is the Bragg angle, n is the order of reflection, and λ is the wavelength of the X-rays. By comparing the obtained XRD pattern to the known standard diffraction datasets complied by the Joint Committee on Powder Diffraction Standards (JCPDS), the crystal phase of unknown powder or thin-film samples can be identified.

2.3.2 Scanning Electron Microscopy (SEM)

The scanning electron microscope (SEM) utilizes a focused beam of high-energy electrons to reveal information about the sample including external morphology and chemical composition. In this research project, a high-resolution field emission SEM (Zeiss Supra 55VP) was used, operated with an acceleration voltage of 10-20 kV depending on conductivity and sensitivity of the sample. The Supra 55VP is also equipped with Oxford energy dispersive spectroscopy (EDS), which enables elemental analysis. EDS mapping was conducted on a Zeiss Evo LS15 SEM equipped with a Bruker SDD XFlash 5030 detector which allows high speed elemental analysis and mapping with images generated in micron resolution.

2.3.3 Transmission Electron Microscopy (TEM)

Transmission electron microscopy is a microscopy technique in which a beam of electrons is transmitted through a specimen, creating an image from the interaction of the electron with the examined sample as the beam penetrates the specimen. Transmission electron microscopes are capable of imaging at extremely high resolutions, enabling the instrument to capture fine details as small as a single

column of atoms. In this research project, TEM was applied to generate lattice-resolved images of samples to determine their crystal orientation and interplanar spacing as well as to obtain detailed information about crystallinity and thickness of carbon coatings on the surface of different samples. Moreover, phase features of crystalline samples (to support XRD investigations) can be obtained by selected area electron diffraction (SAED). For single crystals, SAED patterns are a characteristic arrangement of dots, while for polycrystalline or amorphous materials, the pattern shows a series of rings.

2.3.4 Thermogravimetric Analysis (TGA)

Thermogravimetric analysis (TGA) is a popular method of thermal analysis in which physical and chemical changes of materials can be monitored as a function of increasing temperature. Depending on the desired information, TGA can be conducted in air or under inert atmosphere. For instance, the thermal decomposition (used to optimize solid-state reaction conditions) of solids or carbonization temperature of biomass can be determined by TGA in N_2 atmosphere. In carbon-containing composite materials, the nominal carbon content can be estimated by conducting TGA experiments in air. The resolution of the information gained by this technique can be adjusted by choosing the heating rate of the experiment accordingly. However, using TGA to determine the carbon content of a composite is only suitable for samples and reaction products with melting points above the chosen temperature limits and special considerations need to be taken into account when investing samples that are easily oxidized, such as $LiFePO_4$.

2.3.5 Raman Spectroscopy

Raman spectroscopy is a technique to observe vibrational, rotational, and other low-frequency modes in a system commonly used in chemistry to provide a structural fingerprint to identify molecules. Raman spectroscopy relies on inelastic

scattering of monochromatic light, usually from a laser in the visible, near infrared, or near ultraviolet range. The laser light interacts with molecular vibrations, photons, or other excitations in the system, which results in a shift in the energy of the laser photons. This change can be detected and assigned to specific molecules or chemical structures in organic molecules. In this research project, Raman spectroscopy is used to detect defect information of carbon in carbon-containing composites. In particular, Chapter 3 will discuss the use of Raman spectroscopy as a tool to evaluate not only the order/disorder but also the quality of the carbon coating in terms of electrochemical performance.

2.3.6 N_2 Sorption/Desorption Measurement

To measure the surface area of porous or nanostructured materials, the Brunauer-Emmett-Teller (BET) method can be applied. BET theory describes the physical adsorption of gas molecules on a solid surface for the measurement of the specific surface area. The amount of gas adsorbed depends on the exposed surface area, the temperature, gas pressure, and interaction between the gas and solid. Nitrogen is the most commonly used gas for this technique because of its availability in high purity and its strong interaction with most solids. Because the interaction between gaseous and solid phases is usually weak, the surface needs to be cooled using liquid N_2 to obtain detectable amounts of adsorption. Known amounts of nitrogen gas are then released stepwise into the sample cell under relative pressures of P/P_0 = 0.05-0.25. After the saturation pressure is reached, no more adsorption takes place regardless of any further increase in pressure, which can be precisely monitored and recorded. After the adsorption layers are formed, the sample is removed from the nitrogen atmosphere and heated to release and quantify the adsorbed nitrogen in form of BET isotherms (plots of the amount of adsorbed gas as a function of the relative pressure). N_2 sorption/desorption measurements were conducted in this research project on a Micromeritics 3Flex analyser at 77 K.

2.4 Electrode Preparation and Battery Assembly

2.4.1 Electrode Preparation

For water-sensitive powder electrode materials, electrodes were prepared by mixing the as-prepared material (80 wt%), carbon black (10 wt%) and poly (vinylidene fluoride) binder (PVdF, 10 wt%) in N-methyl-2-pyrrolidone (NMP) to form a slurry. The resultant slurry was spread onto Al foil and dried in a vacuum oven at 100 °C for 12 h, followed by pressing at 200 kg cm^{-2}. For all powder electrode materials insensitive to water, the PVdF binder was replaced by water-soluble carboxymethyl cellulose sodium salt (CMC) binder to allow the use of DI water instead the toxic solvent NMP. For the free-standing electrode materials, the as-prepared products were used directly as electrode material without further modification.

2.4.2 Cell Assembly

For LIBs, lithium foil is used as counter and reference electrode, and a Celgard 2400 as the separator. In SIBs, sodium metal pieces freshly cut for each cell where used as counter and reference electrode, and Whatmann glass fibre filters are applied separator. CR2032-type coin cells were assembled in an argon-filled glove box (UniLab, Mbraun, Germany), in which both the moisture and oxygen contents are controlled to less than 0.1 ppm. The electrolyte used for LIBs was 1 M $LiPF_6$ in a 1:1 (volume ratio) mixture of ethylene carbonate (EC) and diethyl carbonate (DEC). Non-commercial electrolyte (1 M $NaClO_4$ dissolved in a mixture of ethylene carbonate (EC) and propylene carbonate (PC) in a volume ratio of 1:1, in which 5 vol.% fluoroethylene carbonate (FEC) was added as additive) is used for SIBs.

2.5 Electrochemical Measurements

In this research project, electrochemical properties of the as-prepared materials were tested using cyclic voltammetry (CV), electrochemical impedance

spectroscopy (EIS), and galvanostatic charge-discharge profiles. The details of these electrochemical measurements are discussed as follows.

2.5.1 Cyclic Voltammetry

Cyclic voltammetry (CV) is a type of potentiodynamic electrochemical measurement conducted at a constant voltage ramping (scan rate, V s^{-1}). For this measurement, a potential between a reference electrode and a working electrode is applied and the resulting current between a working electrode and a counter electrode is recorded. Reduction or oxidation reactions on the working electrode at a certain potential are manifested in sharp increases in current visible as current peaks in the recorded profile. As a result, CV provides information about the redox potential and electrochemical reaction kinetics of electrode materials, which can be analysed to identify the reaction mechanism and to calculate metal-ion diffusion coefficients.

2.5.2 Electrochemical Impedance Spectroscopy

Electrochemical impedance spectroscopy (EIS) is a widely used method to gain deeper insights into electrochemical systems.[363] Impedance spectra of lithium/sodium-ion electrochemical cells show a characteristic type and shape of curve in a Nyquist plot, as illustrated in Figure 2-2. The sub-sections and the associated kinetic processes are explained in more detail as follows:

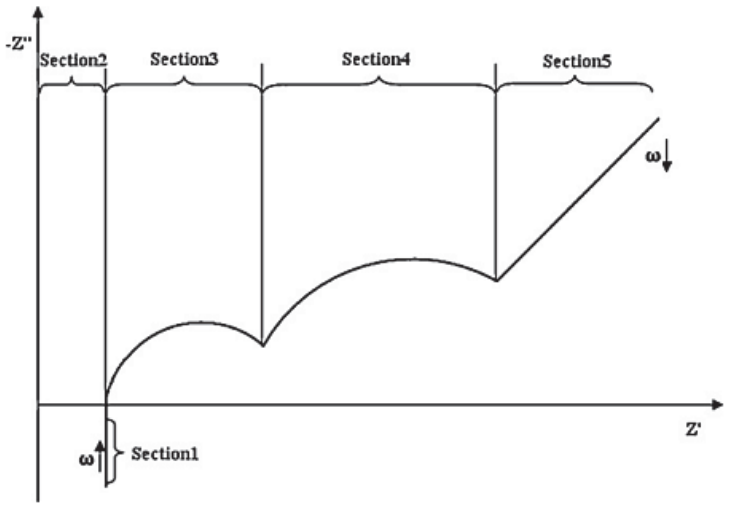

Figure 2-2. Schematic Nyquist plot of the impedance spectrum obtained for lithium/sodium-ion electrochemical cells. Reproduced with permission.[363] Copyright **2011**, Elsevier.

Section 1. At very high frequencies, the spectrum shows inductive behaviour caused by inductive reactance of metallic elements in the cell and wires.

Section 2. Ohmic resistance R_Ω of the cell at the intersection with the real axis *Z'*, which can be assumed as the sum of the resistances of current collectors, active material, electrolyte, and separator.

Section 3. First semi-circle, which is associated with the solid electrolyte interface (SEI) that is formed during the initial charge/discharge cycles on the surface of the anode.

Section 4. Second semi-circle, which represents the double layer capacity and charge transfer resistance at the electrodes.

Section 5. Diffusion processes in the electrode active material at very low frequencies.

In this research project, Nyquist plots of different electrodes were collected to investigate the kinetics of different electrode materials to evaluate their electrochemical performances.

2.5.3 Galvanostatic Charge-Discharge

Galvanostatic charge-discharge experiments are conducted at a constant charge/discharge current within a fixed voltage range. The specific charge/discharge capacities *Q* (mA h g^{-1}) of the evaluated electrode materials can then be calculated using the following equation:

$$Q = I \cdot t \qquad (2\text{-}2)$$

where *I* is the applied current density (mA g^{-1}) and *t* is the charge/discharge time. Rate performance profiles can be obtained by stepwise altering the applied current density in the galvanostatic charge-discharge measurements. Moreover, by repeating galvanostatic charge-discharge tests at a constant current density, long-term cycling performance or cycling stability of the evaluated electrode materials can be obtained.

Chapter 3: Scalable preparation of $LiFePO_4$/C nanocomposites with sp^2-coordinated carbon coating as high performance cathode materials for lithium-ion batteries

3.1 Introduction

Since the first report in 1997, olivine-type materials have attracted extensive research attention as one of the most promising cathode materials for lithium-ion batteries.[7, 8] Even though excessive research work has been performed to optimize the electrochemical performance, this type of cathode material still has to overcome several drawbacks, specifically for high-power battery applications. Primarily, its poor electronic conductivity, ion diffusivity, and stability issues have to be improved by using cheap and environmentally friendly techniques not only to satisfy performance requirements, but also to address economic and ecological aspects.

Various approaches have been investigated to overcome these ionic and electronic conductivity problems, such as size/morphology control,[364] coatings,[365-369] doping,[370, 371] or even electrode engineering methods.[372] Carbon coating techniques appear to be the most sufficient ecological solution to improve the performance of $LiFePO_4$, with the main purpose to increase the electronic conductivity on the surface of $LiFePO_4$ particles, simultaneously reducing the particle size, and alleviating aggregation.[202, 203, 373, 374] In addition, carbon can serve as reducing agent during the sintering process, which prevents the oxidation of Fe^{2+} to Fe^{3+}, and thus, simplifies the synthesis procedure.[375, 376] Chemical synthesis routes are widely adopted to achieve homogeneous carbon coatings around the surface of $LiFePO_4$ particles. For instance, chemical vapour deposition (CVD),[365] *in situ* polymerization restriction methods,[366] mechanochemical activation/sintering,[368] and hydrothermal methods[369] have shown very promising results. All these examples lead to the conclusion that carbon coating is an

effective approach to improve the electrochemical performance of $LiFePO_4$. However, more practical methods would be beneficial in a mass production scale.

Therefore, we hereby report a carbon-coated $LiFePO_4$ cathode material prepared through industrial ball milling and solid-state reaction by using Li_2CO_3, $NH_4H_2PO_4$, $FeC_2O_4 \cdot 2H_2O$, and soluble starch as a carbon source to generate highly graphitic carbon coatings. A uniform morphology could be achieved, featuring a primary particle size of less than 200 nm. Special attention has been paid to the correlation between the applied amount of carbon and the sp^2-coordinated carbon generation, as low-temperature sintering usually yields more disordered carbons.[377] The optimum carbon content is 10 wt% to achieve considerably high reversible capacities and improved rate performance compared with previous reports.[378-381]

3.2 Experimental Section

Preparation of $LiFePO_4$/C Cathode Materials: $LiFePO_4$/C was prepared by mixing stoichiometric amounts of $FeC_2O_4 \cdot 2H_2O$, $NH_4H_2PO_4$, and Li_2CO_3 (Sigma–Aldrich) through industrial-scale ball milling in ethanol (95 vol%) for 24 h. The untreated precursor mixture was filtered and vacuum dried for at least 2 h in preparation for the decomposition and degassing step. The dried untreated precursor mixture was transferred into a ceramic crucible and thermally decomposed in a tubular furnace at 350 °C for 10 h under argon protection. The pre-sintered precursor mixture was then combined with different amounts (5–20 wt%) of soluble starch (Sigma-Aldrich) as carbon source by industrial-scale ball milling in ethanol (95 vol%) for 24 h. The obtained pre-sintered precursor and starch mixture was filtered and vacuum dried for at least 2 h and sintered in a tubular furnace at 700 °C for 10 h under H_2/Ar atmosphere.

Characterization of $LiFePO_4$/C cathode materials: Crystallographic measurements were conducted with a Siemens D5000 X-ray diffractometer using CuKα radiation

between 10° and 80°. The morphology analyses of the as-prepared samples were carried out by field-emission scanning electron microscopy (FE-SEM, Zeiss Supra 55VP) and energy dispersive X-ray spectroscopy (SEM, Zeiss Evo LS15 with extended pressure and Bruker SDD EDS Quantax 400 system). The structure of the carbon network was revealed by high-resolution transmission electron microscopy (HRTEM, FEGTEM 3000 JEOL 300 KV Atomic Resolution Transmission Electron Microscope with 0.192 nm resolution) and Raman spectroscopy (Renishaw, inVia Raman Microscope). The specific surface area was calculated using the Brunauere-Emmette-Teller (BET) method on a Micromeritics 3 Flex™ surface characterization analyser at 77 K.

Electrode preparation and cell assembly: The working electrodes for electrochemical testing were prepared by mixing 80 wt% as-prepared $LiFePO_4$/C with 10 wt% carbon black and 10 wt% poly(vinyl difluoride) (PVdF, Sigma-Aldrich) in N-Methyl-2-pyrrolidone (NMP, Sigma-Aldrich). The obtained dispersion was carefully pasted onto aluminium foil, dried in vacuum at 80 °C for 12 h and pressed before cell assembly. The active material load of all tested electrodes was around 1.2 mg cm^{-2}. Lithium metal discs were used as counter and reference electrodes. The electrolyte used for each cell consisted of 1M $LiPF_6$ in dimethyl carbonate (DMC) / diethyl carbonate (DEC) / ethyl carbonate (EC) (DMC:DEC:EC = 1:1:1, Zhangjiagang Guotai-Huarong New Chemical Materials Co., Ltd.). All electrodes were stored and all standard CR2032 type coin cells were assembled in an argon-filled glovebox (UniLab, Mbraun).

Electrochemical characterization: Galvanostatic charge-discharge and cycling performance tests were performed in the voltage range of 2.00 – 4.25 V at various current densities (based on the mass of $LiFePO_4$ and 1C = 170 mA h g^{-1}) on a Neware battery tester at room temperature. The cyclic voltammograms were obtained at different scan rates of 0.1–2.0 mV s^{-1} between 2.0–4.5 V, and EIS

measurements were conducted at open circuit voltage over a frequency range from 100 kHz to 0.01 Hz by using a CHI 660C electrochemistry workstation.

3.3 Results and Discussion

3.3.1 Characterization

The particle size and morphology were investigated by using field-emission scanning electron microscopy (FESEM). Figure 3-1 shows the FESEM images of $LiFePO_4$/C prepared with 5-20 wt% soluble starch as the carbon source. It displays uniformly dispersed grape-like particles of 50–200 nm in size and highlights the influence of the added amount of carbon precursor on the morphology and agglomeration. For instance, the samples prepared with 5, 8, and 10 wt% (Figure 3-1a–c, respectively) share a similar morphology and low agglomeration features. The samples prepared with 15, 18.5, and 20 wt% soluble starch (Figure 3-1d–f, respectively) tend to show reduced uniformity and much higher agglomeration rates, as marked with white arrows. This can be confirmed by energy dispersive X-ray spectroscopy (EDS). Figure 3-2a shows the uniform distribution of the elements iron (Fe), phosphorous (P), oxygen (O), and carbon (C) throughout the mapped sample area of $LiFePO_4$/C prepared with 10 wt% starch.

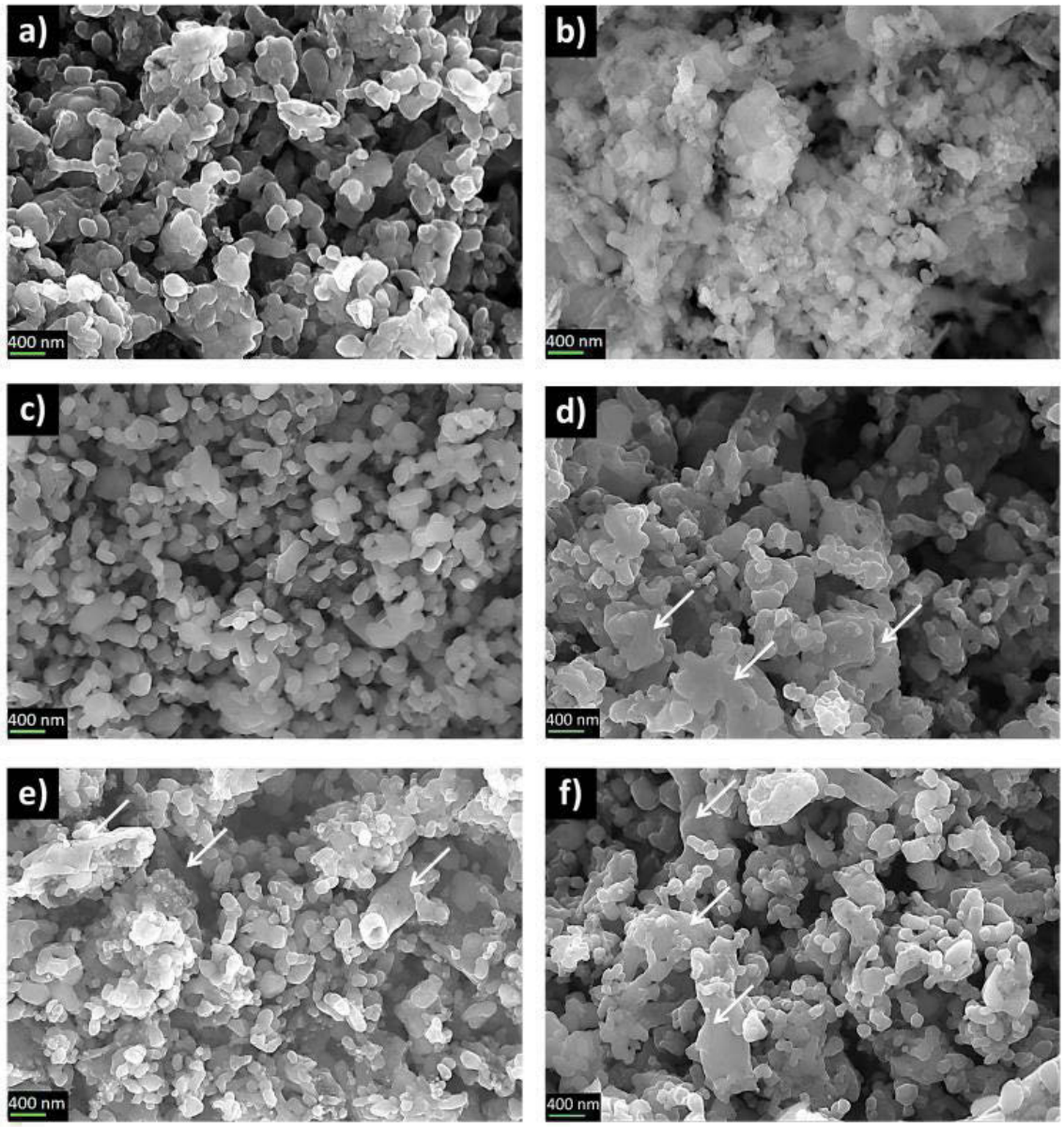

Figure 3-1. SEM images of $LiFePO_4$/C prepared with (a) 5 wt%; (b) 8 wt%; (c) 10 wt%; (d) 15 wt%; (e) 18.5 wt%; (f) 20 wt% soluble starch. Marked with white arrows are some obvious agglomerations.

In contrast, $LiFePO_4$/C prepared with 20 wt% starch (Figure 3-2b) displays very bright spots of Fe and C scattered throughout the mapped area, indicating denser areas of agglomeration in this sample.

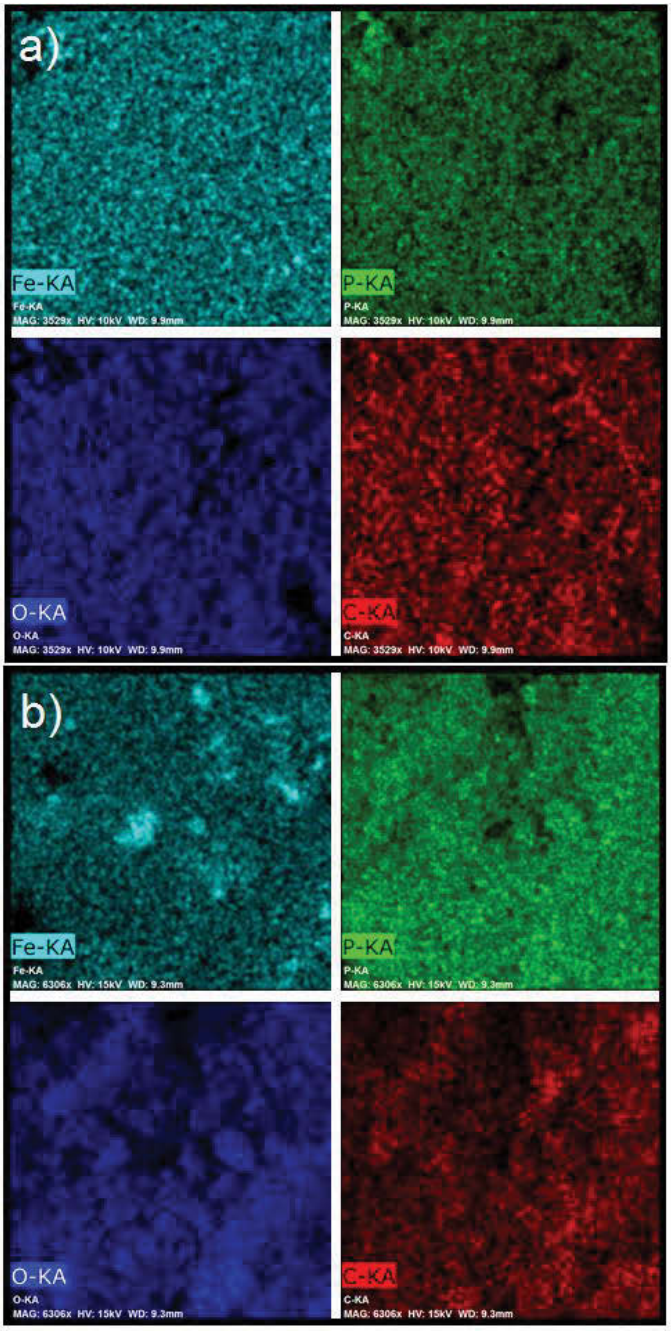

Figure 3-2. SEM energy dispersive X-ray spectroscopy (EDS) elemental mapping of $LiFePO_4$/C prepared with a) 10 wt% and b) 20 wt% soluble starch, showing the distribution of the elements iron (Fe), phosphorous (P), oxygen (O), and carbon (C).

According to this observation, it can be assumed that the addition of approximately 10 wt% soluble starch marks the optimized content regarding particle morphology and particle size, with the remark that, owing to the uncertainty of the impact of potential impurities on performance and conductivity, all six samples remain subject to further investigations, regardless of the suboptimal particle morphology.

Figure 3-3 shows the X-ray diffraction (XRD) patterns of the six $LiFePO_4$/C composites, which are consistent with the $LiFePO_4$ pattern of JCPDS card number 83-2092. This result indicates that the presence of soluble starch as the carbon source has no negative effect on the final crystal formation of $LiFePO_4$. However, the amount of starch has an effect on the formation of phase impurities. The patterns clearly indicate that, depending on the amount of added carbon precursor, conductivity enhancing impurities (*Fe_2P) can be detected, specifically for the samples prepared with 15, 18.5, and 20 wt% starch. On the other hand, for samples prepared with 10, 8, and 5 wt% starch, Fe_2P impurities become less obvious. As Fe_2P cannot contribute to the overall electrochemical capacity, it is an undesired synthesis product for high-energy applications. Yet, as aforementioned, its conductivity-enhancing properties, combined with a high-quality carbon coating, could be beneficial for the rate capability of the synthesized composites, and thus, might provide interesting features for potential high-power applications.

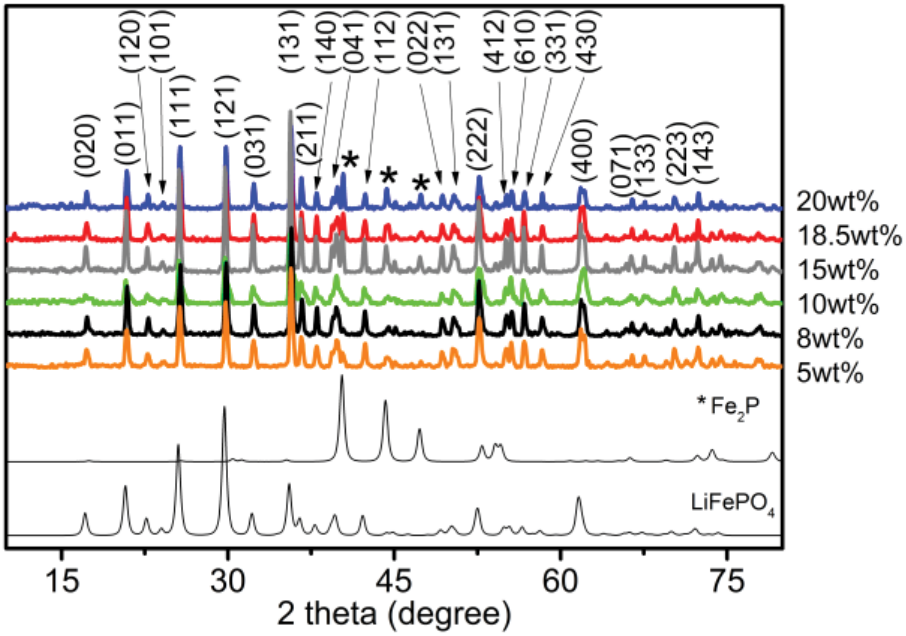

Figure 3-3. XRD patterns of $LiFePO_4$/C prepared with 5-20 wt% soluble starch compared with calculated patterns of Fe_2P and $LiFePO_4$ (JPDS card number 83-2092).

To investigate the structure and distribution of the carbon layer and to visualize the interconnection of the $LiFePO_4$ particles, a transmission electron microscopy (TEM) analysis was conducted. Figure 3-4a shows the TEM image of the $LiFePO_4$/C composite nanoparticles, and no loose carbon sheets can be seen, referring to Figure 3-4b and Figure 3-4d, which indicates that the carbon presence detected using Raman spectroscopy (Figure 3-5) can only be attributed to an existing carbon coating around the $LiFePO_4$ particles. Figure 3-4d displays the uniform, well-defined, and highly ordered carbon layer of around 3 nm thickness covering a $LiFePO_4$ crystallite, which is successfully generated through the thermal decomposition of the soluble starch precursor. The selected area electron diffraction (SAED) pattern in Figure 3-4c reveals distinct diffraction spots, which can be indexed to the $LiFePO_4$ triphylite crystal structure, confirming the previous XRD analysis.

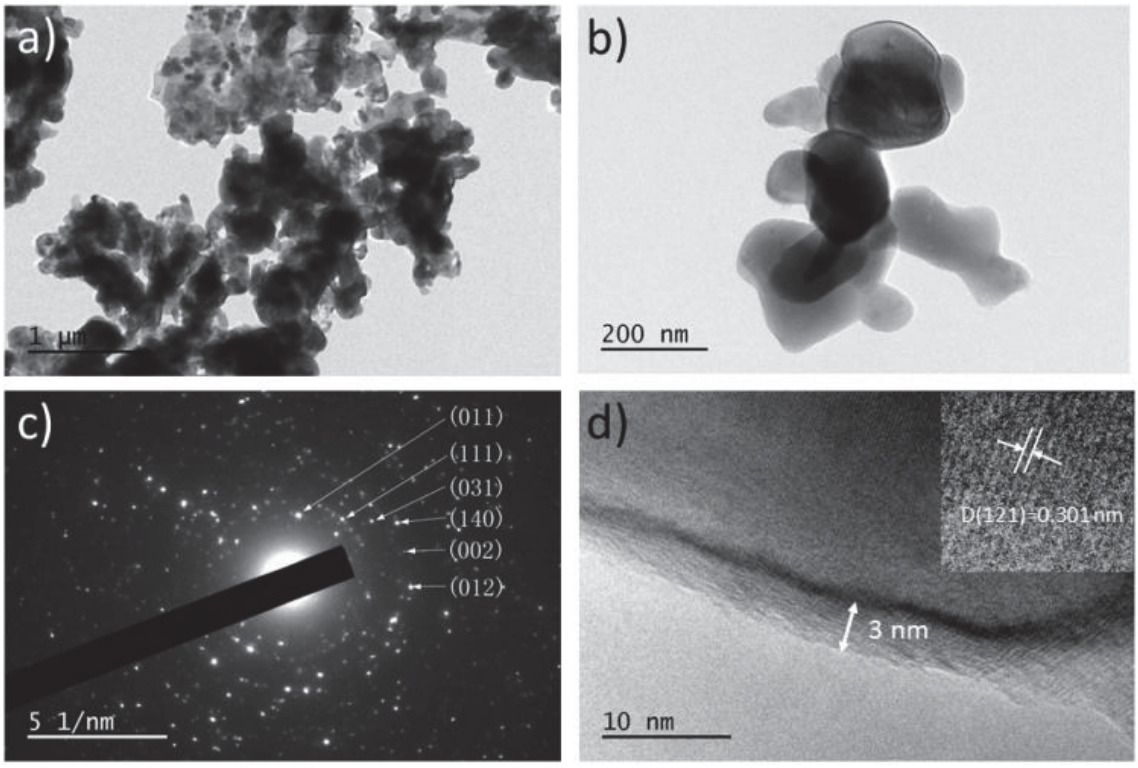

Figure 3-4. (a) and (b) TEM images; (c) the corresponding selected area electron diffraction pattern (SAED); and (d) lattice resolved HRTEM image of $LiFePO_4$/C prepared with 5 wt% soluble starch (Inset: Interplanar distance of the (121) crystal plane).

The lattice-resolved high-resolution TEM (HRTEM) image presented in Figure 3-4d shows the $LiFePO_4$ nanocrystal wrapped in a thin layer of carbon, in which the (121) crystal plane is indexed with an interplane spacing of 0.301 nm. This result demonstrates that soluble starch applied as carbon precursor during the solid-state reaction can successfully generate a very thin and uniform, conductivity enhancing carbon coating on the surface of $LiFePO_4$ particles. Moreover, Figure 3-5 shows the Raman spectra of $LiFePO_4$/C prepared with 5, 8, 10, 15, 18.5, and 20 wt% starch, which were employed to further evaluate the quality of the generated carbon coating in terms of graphitization and orbital hybridization. Basically, the intense peaks located at ~1335 cm^{-1} and ~1605 cm^{-1}

are corresponding to the D (disordered) and G (graphite) band of the carbonized soluble starch covering the $LiFePO_4$ particles, respectively. The shape and relative intensity of D/G changes with the varying amount of added carbon. However, since band fitting with two D and G lines cannot produce accurate plots of the measured curves, a four-bands Gaussian-Lorentz fit was applied to resolve the observed Raman features.[382] As shown in Figure 3-5a–f (coloured lines), the two fitted bands located at ~1335 cm^{-1} and ~1605 cm^{-1} correspond to the D band and G band of sp^2-type carbon, respectively. The other two bands at ~1150 cm^{-1} and ~1520 cm^{-1} can be assigned to sp^3-type (diamond-like) carbon. As a consequence, the integrated area ratio of the sp^3 and sp^2 bands (A_{sp^3}/A_{sp^2}) is related to the relative content of graphite carbon in a composite, which has been associated with enhanced conductivity and electrochemical performance of $LiFePO_4$/C composites.[377, 382, 383] Furthermore, the intensity ratio of D/G (I_D/I_G) can be used as estimation of the graphitization degree of this composite.[384, 385] Ultimately, to visualize the relationship of A_{sp^3}/A_{sp^2} and I_D/I_G as a function of the added carbon content, the graph displayed in Figure 3-5g was plotted and demonstrates the proposed correlation. According to the diagram, the I_D/I_G ratios are calculated as 1.03, 1.06, 1.05, 1.05, 1.05, and 0.99 for the samples prepared with 5, 8, 10, 15, 18.5, and 20 wt% soluble starch, respectively, while the corresponding A_{sp^3}/A_{sp^2} ratios are calculated as 0.598, 0.605, 0.278, 0.332, 0.328, and 0.484. Both ratios indicate the high graphitization of the carbon layer, and thus, improved electronic conductivity. In particular, the sample prepared with 10 wt% shows the lowest A_{sp^3}/A_{sp^2} and a low I_D/I_G ratio, which makes this sample the most promising for improved electrochemical performance. It is important to note that all Raman spectra feature a strong D band, which illustrates a slightly more amorphous character of the carbon coating due to the low temperature carbonization necessary for the preparation of $LiFePO_4$.[377]

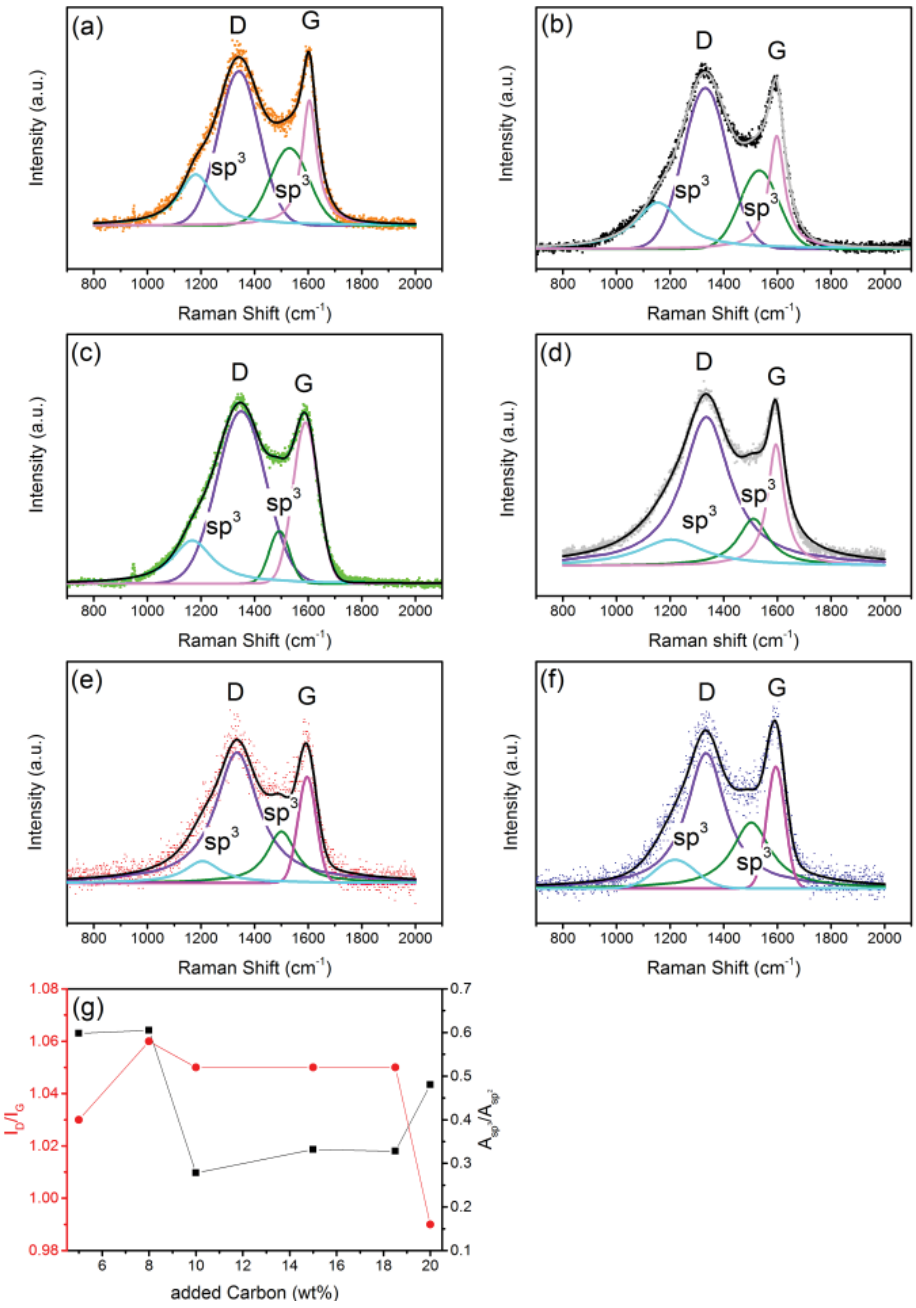

Figure 3-5. Raman spectra of $LiFePO_4$/C prepared with (a) 5 wt%, (b) 8 wt%, (c) 10 wt%, (d) 15 wt%, (e) 18.5 wt%, and (f) 20 wt% soluble starch as carbon source. The two broad bands are resolved into four coloured lines; (g) shows the A_{sp^3}/A_{sp^2} and I_D/I_G values as a function of the amount of added carbon precursor.

However, this conclusion is consistent with the HRTEM observations in Figure 3-4d. The nominal carbon contents of the as-prepared $LiFePO_4$/C composites are roughly estimated as 2.63, 3.27, 4.58, 5.86, 6.82, and 9.34 wt% for the materials prepared with 5, 8, 10, 15, 18.5, and 20 wt% starch as carbon source, respectively. The basic procedure is carried out as follows. A representative amount of composite sample is thoroughly dispersed in concentrated hydrochloric acid for 24 h. Clean filter papers are vacuum-dried overnight and the blank filter paper weight is recorded. The residual carbon of each sample is washed several times with distilled water and ethanol, vacuum dried overnight on the before-mentioned blank filter papers, and weighed to determine the nominal carbon content. The Brunauer–Emmett–Teller (BET) surface area was calculated to be around 10.6 $m^2\ g^{-1}$. In summary, the structural, morphological, and carbon quality outcomes are competitive compared with previously reported $LiFePO_4$ composites that required much more expensive and more complex preparation methods.[386-390]

3.3.2 Electrochemical Performance

The charge/discharge profiles of $LiFePO_4$/C prepared with 5–20 wt% soluble starch as the carbon source can be seen in Figure 3-6. It is demonstrated in Figure 3-6a that, due to the increasing carbon content, the initial reversible capacity of $LiFePO_4$/C prepared with 5, 8, and 10 wt% added carbon source is 153 mA h g^{-1}, whereas the sample prepared with 15 wt% added carbon source reaches 147 mA h g^{-1} and the samples prepared with 18.5 and 20 wt% only provide 135 and 137 mA h g^{-1} at 0.2C, respectively. Based on these initial galvanostatic (dis)charge profiles, the differential capacity analysis given in Figure 3-6b allows the determination of over-potential of each sample, which is a first indication for good electric conductivity. All six samples achieved very low over-potential values from 74.1 to 91.4 mV as seen in the inset of Figure 3-6b.

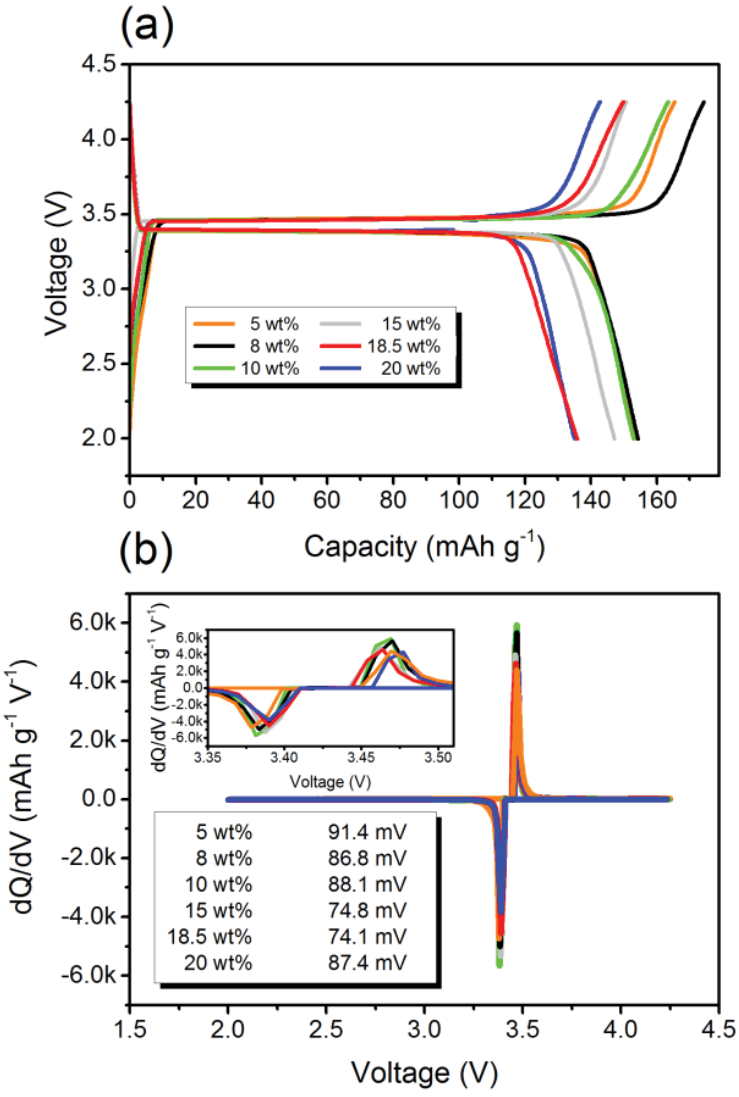

Figure 3-6. (a) Charge-discharge curves; (b) differential capacity analysis of $LiFePO_4$/C prepared with 5-20 wt% soluble starch as carbon source (insets: differential capacity analysis in the voltage range 3.35 to 3.51 V and a list of the corresponding over-potential values for all six samples).

A rate performance evaluation was conducted to compare the individual conductivity enhancing features of each sample. The rate performance test displayed in Figure 3-7a confirms the good capacity retention and appropriate rate capabilities of the $LiFePO_4$/C composites prepared with 10, 15, and 18.5 wt%

soluble starch as the carbon source. These samples provide the highest rate capability of all six tested samples, wherein the sample prepared with 10 wt% starch also achieves high reversible capacities at low current rates. This particular sample delivers reversible capacities of 154, 149, 140, 131, 114, 100, and 85 mA h g^{-1} when cycled at 0.2, 0.5, 1, 2, 5, 10, and 20C, respectively, combined with a capacity retention of 55% from 0.2 to 20C. These are highly competitive results compared with recent publications using similar methods, but which are not scalable and include much more expensive and complicated preparation methods for high performance $LiFePO_4$/C composites.[204, 365, 387, 388, 391-396] Furthermore, as an additional comparison approach, Figure 3-7b visualizes the energy and power density of the $LiFePO_4$/C composite prepared with 10 wt% starch at different current rates. It can be seen that this sample can also deliver a high specific energy of 555 Wh kg^{-1} at 0.2C and high specific power of 13.64 kW kg^{-1} at 20C Besides, the cycling stability test displayed in Figure 3-7c revealed that 80% of the initial capacity can be maintained even after 300 deep charge/discharge cycles at a high rate of 10C, which further outlines the enhanced electrochemical performance of this material. It is shown that the columbic efficiency remains steady at about 99.4% over the entire test extent. Interestingly, according to Figure 3-7a, the samples prepared with 15 and 18.5 wt% carbon precursor provide similar high rate capabilities to the discussed 10 wt% composite, but cannot deliver sufficient reversible capacities at lower current densities. On the other hand, owing to the increased carbon content, and thus stronger carbon network, the cycling stability at high rates is also increased, as seen in Figure 3-7c. The achieved capacity retentions after 300 cycles are namely 92.5 and 95.5% for the composites prepared with 15 and 18.5 wt% added carbon source, respectively, which provides them with very interesting properties for high-power applications.

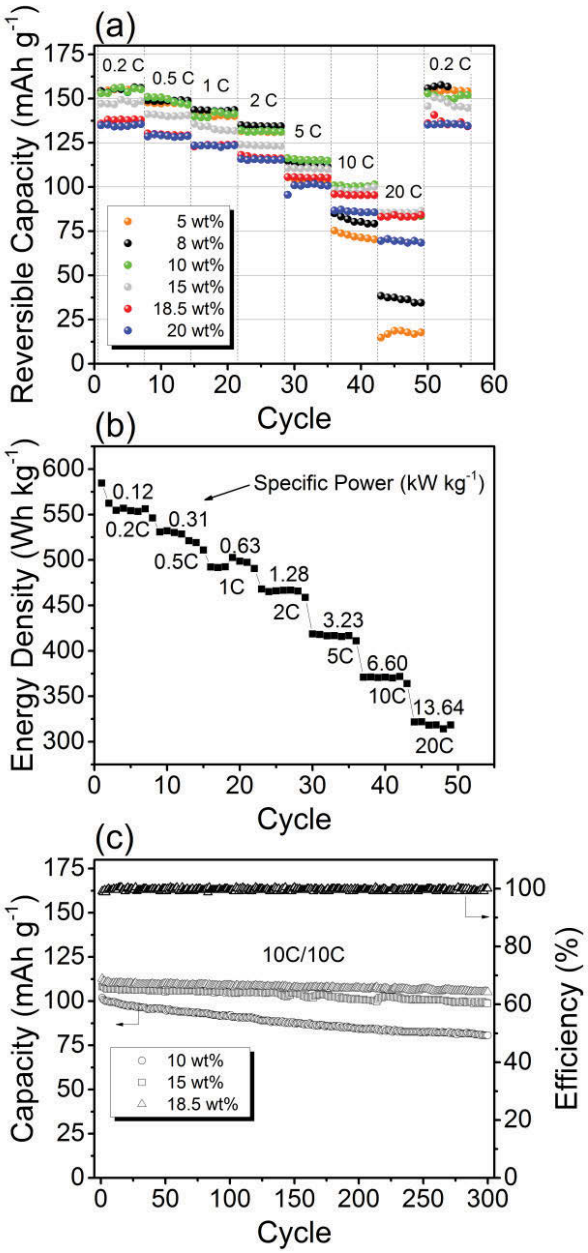

Figure 3-7. (a) Rate performance of $LiFePO_4$/C prepared with 5-20 wt% soluble starch as the carbon source; (b) Specific energy and specific power of the sample prepared with 10 wt% soluble starch at different current rates; (c) Cycling performance of the sample prepared with 10, 15, and 18.5 wt% soluble starch (dis)charged at 10C for 300 cycles.

In contrast, the samples prepared with 5 and 8 wt% starch deliver high reversible capacities at very low rates, which drastically deteriorate from 5 to 20C and only achieve a rate capacity retention of 13 and 24% from 0.2 to 20C, respectively. These drastic performance differences are visualized using charge/discharge profiles of the tested composites at different current rates, as displayed in Figure 3-8. It is evident that the (dis)charge plateaus of the $LiFePO_4$/C composites prepared with 5 and 8 wt% starch start to slope with the increase in the current rate, whereas the electrodes made with 10–20 wt% starch still generate a distinct (dis)charge voltage plateau even at 20C. Thus, the galvanostatic profiles of all six composites agree consistently with the previous evaluation of the carbon coating quality using Raman spectroscopy, as displayed in Figure 3-5, and confirm the initial assumption. The individual Raman spectra indicate that the optimal graphitization and sp^2 carbon content, for both rate performance and high specific capacity, can be achieved with 10 wt% added soluble starch to generate a conductivity enhancing carbon coating on the $LiFePO_4$ surface without compromising the specific capacity, which has certainly been validated. Furthermore, the samples prepared with 15 and 18.5 wt% carbon provide similar high rate capabilities, possibly owing to good Raman features combined with the presence of conductivity-enhancing Fe_2P, which, just like carbon, does not contribute to the overall capacity, as is evident at low charge/discharge rates, where these composites cannot reach the same values as the 10 wt% composite. Furthermore, it has been shown that a low I_D/I_G ratio or disordered carbon content of an existing carbon coating is not related to good electrochemical performance. The samples prepared with 5 and 20 wt% starch showed the two lowest I_D/I_G ratios, but, at the same time, highly sp^3-hybridized or diamond-like carbon features, which consequently caused their poor rate performance as sp^3 coordinated carbon is considered to be of insulating nature.[377, 382, 383]

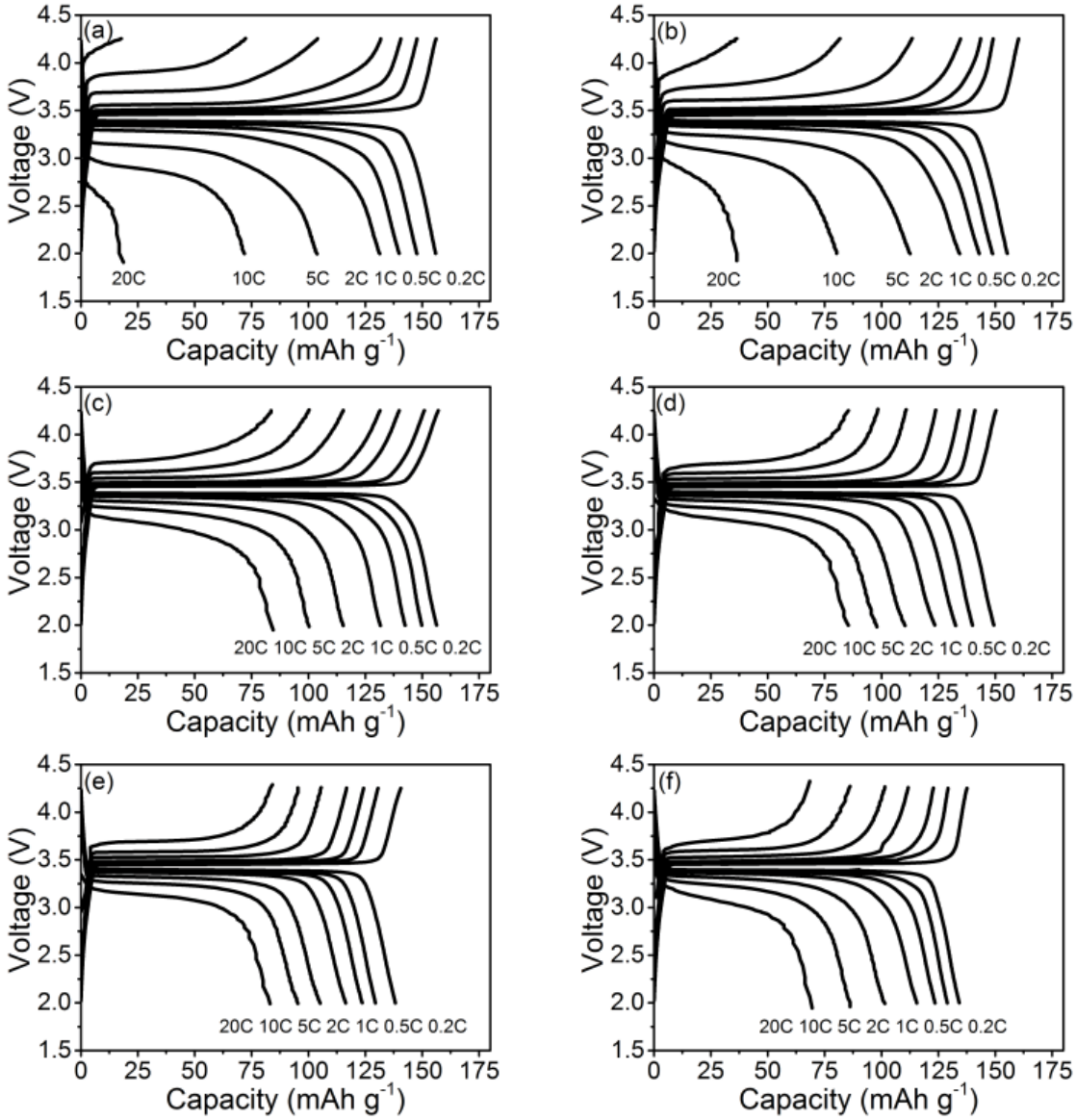

Figure 3-8. The charge-discharge voltage curves of $LiFePO_4$/C prepared with (a) 5 wt%, (b) 8 wt%, (c) 10 wt%, (d) 15 wt%, (e) 18.5 wt%, and (f) 20 wt% soluble starch as carbon source in the voltage range from 2.0 to 4.25 V at different current rates.

Finally, to conclusively assess the electrochemical behaviour of $LiFePO_4$/C, the electrochemical kinetic performance, displayed in Figure 3-9, was analysed using cyclic voltammetry (CV) and electrochemical impedance spectroscopy (EIS), respectively. Figure 3-9a unveils the CV behaviour of the $LiFePO_4$ electrode prepared with 10 wt% starch at various scanning rates in the voltage range of 2.0–4.5 V. A single pair of well-defined redox peaks is observed for all scan rates, which can be attributed to the Fe^{3+}/Fe^{2+} redox couple.

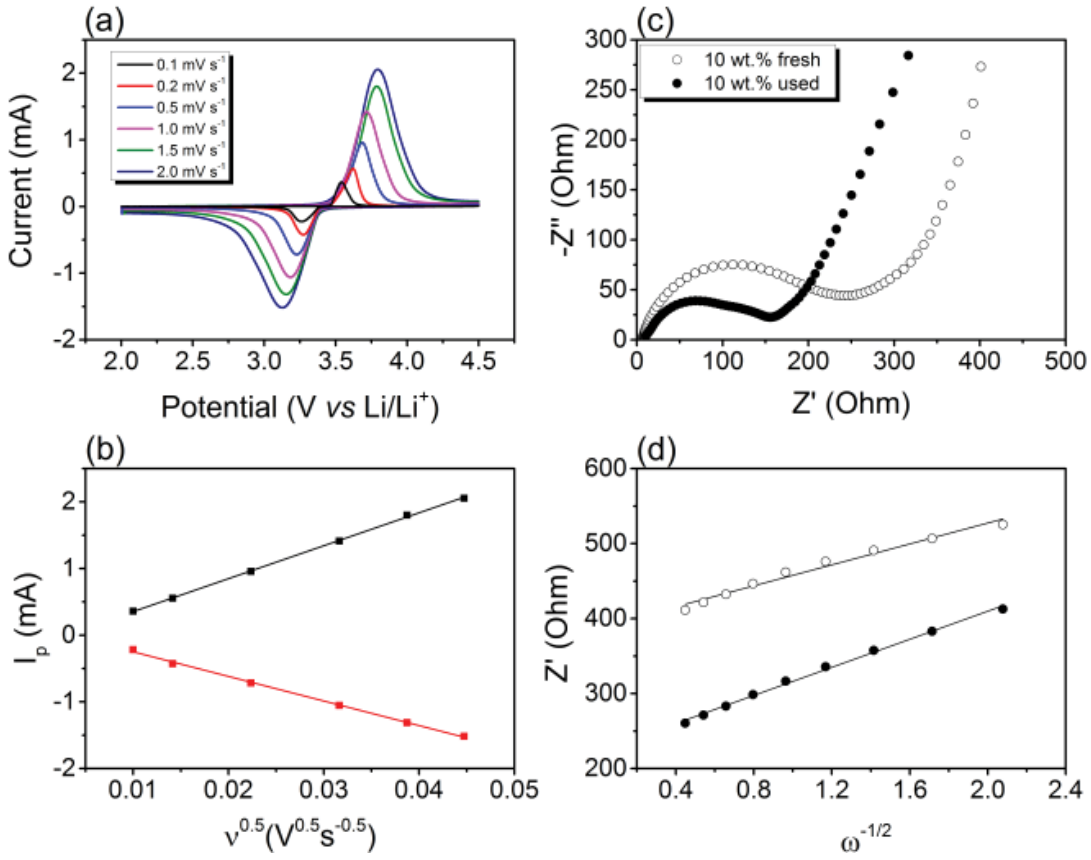

Figure 3-9. (a) CV curves at different scan rates and (b) peak current I_p versus square root of scan rate $v^{1/2}$ at 25 °C of $LiFePO_4$ prepared with 10 wt% soluble starch; (c) Impedance spectroscopy and (d) linear fitting of the Warburg impedance of fresh and cycled $LiFePO_4$/C cells prepared with 10 wt% soluble starch as carbon source.

Furthermore, the height and area of the redox peaks increase with increasing scan rates, and the anodic and cathodic peaks move to lower and higher potentials, respectively. Even at a high scan rate of 2.0 mV s^{-1}, the well-defined sharp redox reaction peaks are maintained, indicating good kinetics for lithium intercalation and deintercalation. According to these measured peak currents, a Li-ion diffusion coefficient D (cm^2 s^{-1}) can be calculated using the Randles–Sevcik equation:[387, 390, 397]

$$I_p = 2.69 \cdot 10^5 \cdot A \cdot C \cdot \sqrt{D} \cdot n^{3/2} \cdot \sqrt{v} \qquad (3\text{-}1)$$

wherein I_p is the peak current (in A), A is the surface area of the electrode, C is the concentration of Li ions in a solid (0.0228 mol cm^{-3}), n is the number of electrons involved in the half-reaction for the redox couple (n = 1 for Fe^{3+}/Fe^{2+} redox couple), and v is the potential scan rate (in V s^{-1}). As shown in Figure 3-9b, I_p is indeed proportional to $n^{1/2}$, confirming a diffusion-controlled behaviour. Moreover, from the slope of the lines, and based on Equation (3-1), the diffusion coefficient $D_{cathodic}$ (positive) is $6.49 \cdot 10^{-11}$ cm^2 s^{-1}, whereas the diffusion coefficient D_{anodic} (negative) is $3.62 \cdot 10^{-11}$ cm^2 s^{-1} for the composite prepared with 10 wt% starch. The high Li-ion diffusion coefficients achieved with this material are related to the thin and highly sp^2-coordinated carbon coating on the $LiFePO_4$ particle surface, which is reflected in its enhanced rate performance provided earlier in Figure 3-7 and Figure 3-8. Finally, the Nyquist plot (Figure 3-9c) compares the electrochemical impedance of the 10 wt% composite fresh and after the rate performance test for 57 cycles. It can be seen that the material generates a depressed semicircle in the high-frequency region and a slope in the low-frequency region. Firstly, the high-frequency intercept of the semicircle with the real axis (Z') refers to the uncompensated resistance (R_u), which combines the particle–particle contact resistance, electrolyte resistance, and the electrode–current collector resistance. Secondly, the semicircle diameter refers to the charge-transfer resistance (R_{CT}),

which is related to the electrochemical reactions at the electrode–electrolyte interface and the particle–particle contact. Lastly, the low-frequency slope corresponds to lithium-ion diffusion in the bulk of the electrode material and can be mathematically transformed to the Warburg coefficient (σ_w).[204, 389, 390, 393, 398] Consequently, the solid-state diffusion of lithium ions D_{Li} through the $LiFePO_4$/C particle collective can be estimated using Equation (3-2):

$$D_{Li}=\frac{1}{2}\left(\frac{RT}{AF^2C\sigma_w}\right)^2 \quad (3\text{-}2)$$

wherein *R* is the universal gas constant, *T* is the absolute temperature, *F* is the Faraday constant, *A* is the surface area of the $LiFePO_4$ cathode, *C* is the molar concentration of lithium ions in the cathode, and σ_W is the Warburg coefficient. It can be seen in the experimental data plot in Figure 3-9c that the R_{CT} of the fresh uncycled cell is 239 Ω, whereas the EIS analysis of the cycled half-cell reveals slight changes in R_{CT}. The value has decreased to 145 Ω, possibly owing to electrode activation processes during cycling. Additionally, the solid-state diffusion D_{Li} calculated using Equation (3-2) from the Warburg impedance (shown in Figure 3-9d) reflects the kinetic properties of the 10 wt% composite, revealing a competitive lithium-ion diffusion rate of $1.34 \cdot 10^{-14}$ cm^2 s^{-1} measured for fully lithiated $LiFePO_4$. In conclusion, it has been undoubtedly confirmed that the remarkable rate performance is achieved because of the high solid-state diffusion rates provided by the $LiFePO_4$ particles combined with the low charge-transfer resistance delivered by the highly sp^2-coordinated carbon coating. The outstanding rate performance and highly competitive reversible capacity at low charge/discharge rates marks the composite prepared with 10 wt% soluble starch as the optimal choice for high-performance and high-power $LiFePO_4$/C composites.

3.4 Conclusions

Highly graphitic carbon-coated $LiFePO_4$ cathode materials are successfully prepared through industrial ball milling and solid-state reaction using soluble starch as a carbon source and only environmentally friendly iron, lithium, and phosphate precursors. This method can generate uniform, sp^2-coordinated carbon-coated, grape-like nanoparticles, which are favourable for Li^+ transport and tap density. It has been shown that, even though Fe_2P phases in combination with a high-quality carbon network are beneficial to improve high-rate performance and stability, the capacity reduction at low rates induced by the high carbon content and the Fe_2P phase is disproportionate to justify adding more than 10 wt% carbon to the pre-sintered precursor. Furthermore, adding less than 10 wt% soluble starch as the carbon source results in high capacities at very low current rates, but fails to deliver considerable capacities at high rates, owing to a lack of a highly sp^2-coordinated carbon network to support ion diffusion through the particle collective. Ultimately, adding 10 wt% soluble starch as the carbon source combined with environmentally friendly iron, lithium, and phosphate precursor materials is a suitable and efficient approach to generate large amounts of high-performance and high-power $LiFePO_4$/C cathode materials. However, further experimental and theoretical studies are required to identify the formation mechanism of sp^2-coordinated carbon that arises from the variation in carbon precursor amount rather than variations in sintering temperature or time.

Chapter 4: Carbon coated $LiFePO_4$ clusters prepared *via* spray-drying followed by carbothermal reduction

4.1 Introduction

The spray method is well-trusted in practical uses, such as the manufacturing of dried food, fertilizers, oxide ceramics, and pharmaceuticals.[399] A large number of applications of spray methods have been reported and more than 15,000 industrial-size spray dryers are currently in operation. This number would approximately double if the use in pilot plants and laboratories was added to the calculation.[400] Several spray methods have been reported with no limitations to a particular type of process: spray-pyrolysis, spray-drying, flame-spraying, low-pressure, and electro-spraying.[401]

In general, a starting solution is prepared usually by dissolving the metal component of an intended product in a solvent. The droplets, which are atomized from the starting solution, are introduced to the solvent evaporator. Evaporation of the solvent, diffusion of solute, drying, and precipitation may occur inside the furnace to form the final product. The reaction among reactants, and sometimes with surrounding gas, is dependent on the type of the initial solution.[399, 402] The spray-drying method is similar to other types of spray methods (spray-pyrolysis, spray-freeze drying, etc.), except for the type of precursor (usually colloidal particles or sols) and the fact that there is almost no reaction during the drying process. The ability to produce uniformly spherical particles from nano to micron sizes is one of the main advantages of this method. Other merit gained from this method is that when the suspension consists of colloidal nanoparticles (primary particles), the resulting particles are comprised of nanoparticles that form a nanostructured powder. Therefore, the spray-drying method may be suitable for consolidating nanoparticles into macroscopic compacts, and submicron spherical powders that have nanometre scaled properties can be obtained.[399] This is

particularly important for industrial applications of carbon coated $LiFePO_4$ materials. Although nano-sized $LiFePO_4$ materials with highly engineered shapes have been reported previously, they rarely provide both excellent electrochemical performance and high tap density, which is critical to achieve high volumetric energy densities.[202, 203, 403] Therefore, $LiFePO_4$ nano-micro structures with uniform carbon coatings are very desirable for commercial high performance lithium-ion battery applications.[404]

In this report, we systematically evaluated spray-drying conditions and equipment settings in regards to electrochemical performance of the obtained carbon coated $LiFePO_4$ cathode material. This includes variations in spray-drying feed rate and drying temperature while precursor materials, suspension concertation, and amount of added carbon source remained unchanged for each parameter. After optimal conditions were established, the impact of the carbon precursor choice on micro-particle morphology was evaluated. For this investigation, three different carbon precursor materials were applied, namely citric acid (CA), polyethylene glycol (PEG), and polyvinyl alcohol (PVA), and their resulting particle morphology and electrochemical performance was investigated.

4.2 Experimental Section

$LiFePO_4$ named hereafter LFP-A10, LFP-A40, and LFP-A60 was prepared by mixing stoichiometric amounts of $FeC_2O_4 \cdot 2H_2O$, $NH_4H_2PO_4$, and Li_2CO_3 (Sigma-Aldrich) *via* industrial-scale ball milling in ethanol (95 vol%) for 24 h. The untreated precursor mixture was filtered and vacuum dried for at least 2 h as preparation for the decomposition and degassing step. The dried untreated precursor mixture was transferred into a ceramic crucible and thermally decomposed in a tubular furnace at 350 °C for 10 h under argon protection. The pre-sintered mixture was combined in a suspension with 10 wt% sucrose to encapsulate the precursor materials during spray-drying and to serve as carbon source in the subsequent carbothermal

reduction. The solid content of the suspension was fixed at 1 wt%. The precursor mixture was spray-dried (Mini Spray Dryer B290, BÜCHI Labortechnik AG, Switzerland) with an inlet temperature of 170 °C and a feed rate of 4 ml min^{-1} (LFP-A10), 12 ml min^{-1} (LFP-A40), and 18 ml min^{-1} (LFP-A60), respectively. The dried powder was then transferred into a ceramic crucible to be sintered at 700 °C for 10 h in H_2/Ar atmosphere.

$LiFePO_4$ named hereafter LFP-150-40-60-5, LFP-170-30-74-5, and LFP-200-40-86-5 was prepared by mixing stoichiometric amounts of $FeC_2O_4 \cdot 2H_2O$, $NH_4H_2PO_4$, and Li_2CO_3 (Sigma-Aldrich) *via* industrial-scale ball milling in deionized water for 6 h. Simultaneously, 5 wt% sucrose was added to the suspension to encapsulate the precursor materials during spray-drying and to serve as carbon source in the subsequent carbothermal reduction. The solid content of the suspension was fixed at 20 wt%. The untreated precursor mixture was spray-dried (Mini Spray Dryer B290, BÜCHI Labortechnik AG, Switzerland) with an inlet temperature of 150 °C (LFP-150-40-60-5), 170 °C (LFP-170-30-74-5), and 200 °C (LFP-200-40-86-5) and a feed rate of 15 ml min^{-1}. The dried power was then transferred into a ceramic crucible to thermally decompose in a tubular furnace at 350 °C for 5 h and sintered at 700 °C for 10 h under argon protection.

$LiFePO_4$ named hereafter LFP-C CA, LFP-C PEG, and LFP-C PVA was prepared by mixing stoichiometric amounts of $FeC_2O_4 \cdot 2H_2O$, $NH_4H_2PO_4$, and Li_2CO_3 (Sigma-Aldrich) *via* industrial-scale ball milling in ethanol (95 vol%) for 24 h. The untreated precursor mixture was filtered and vacuum dried for at least 2 h as preparation for the decomposition and degassing step. The dried untreated precursor mixture was transferred into a ceramic crucible and thermally decomposed in a tubular furnace at 350 °C for 10 h under argon protection. The pre-sintered mixture was combined in a suspension with 10 wt% sucrose to serve as carbon source in the subsequent carbothermal reduction and 0.5 g citric acid (LFP-C CA), PEG (LFP-C PEG) or

PVA (LFP-C PVA) to encapsulate the precursor materials during spray-drying. The solid content of the suspension was fixed at 20 wt%. The precursor mixture was spray-dried (Mini Spray Dryer B290, BÜCHI Labortechnik AG, Switzerland) with an inlet temperature of 200 °C and a feed rate of 15 ml min^{-1}. The dried powder was then transferred into a ceramic crucible to be sintered at 700 °C for 10 h in H_2/Ar atmosphere.

Crystallographic measurements were conducted with a Siemens D5000 X-ray diffractometer using CuKα radiation between 10° and 80°. The morphology analyses of the as-prepared materials were carried out by field-emission scanning electron microscopy (FE-SEM, Zeiss Supra 55VP). The carbon contents of the as-prepared LFP-C CA, LFP-C PEG, and LFP-C PVA were investigated using a TGA/DTA analyser (TA Instruments, SDT 2960 module, New Castle, DE, USA) at a heating rate of 5 °C min^{-1} under air flow from room temperature to 700 °C.

The working electrodes for electrochemical testing were prepared by mixing 80 wt% as-prepared $LiFePO_4$ with 10 wt% carbon black and 10 wt% poly(vinyl difluoride) (PVDF, Sigma-Aldrich) in N-Methyl-2-pyrrolidone (NMP, Sigma-Aldrich). The obtained dispersion was carefully pasted onto aluminium foil, dried in a vacuum oven at 80 °C for 12 h and pressed before cell assembly. Lithium metal discs were used as counter and reference electrodes. The electrolyte used for each cell consisted of 1M $LiPF_6$ in dimethyl carbonate (DMC) / diethyl carbonate (DEC) / ethyl carbonate (EC) (DMC:DEC:EC = 1:1:1, Zhangjiagang Guotai-Huarong New Chemical Materials Co., Ltd.). All electrodes were stored and all standard CR2032 type coin cells were assembled in an argon-filled glovebox (UniLab, Mbraun).

Cycling performance tests were performed in the voltage range of 2.00 – 4.25 V at various current densities (based on the mass of $LiFePO_4$ and 1 C = 170 mA h g^{-1}) on a Neware battery tester at room temperature.

4.3 Results and Discussion

4.3.1 Parameter Optimization

Figure 4-1 shows the XRD patterns of the six $LiFePO_4$ materials prepared for parameter optimization. The obtained patterns are consistent with the $LiFePO_4$ pattern of JCPDS card number 83-2092. The peak intensity of the LFP-150 – 200 samples (Figure 4-1b) is slightly higher than those of the LFP-A10 – A60 materials (Figure 4-1a), possibly due to the reduced amount of carbon precursor. The generated carbon coating is thinner and less X-rays are scattered by the amorphous carbon structure on the particle surface. The nominal carbon content of all six samples is 2 wt% or less as determined using thermogravimetric measurements displayed in Figure 4-2, which is very desirable for industrial applications. The carbon coating itself does not contribute to specific capacity on the cathode side of a lithium-ion battery to the extent that high carbon contents in a composite cathode material cause a significant reduction in volumetric capacity. Hence, its main purpose is to ensure good interparticle contact and surface conductivity. Therefore, a high performance $LiFePO_4$/C composite material with less than 5 wt% carbon is favourable for future large scale applications and mass production.[198, 367]

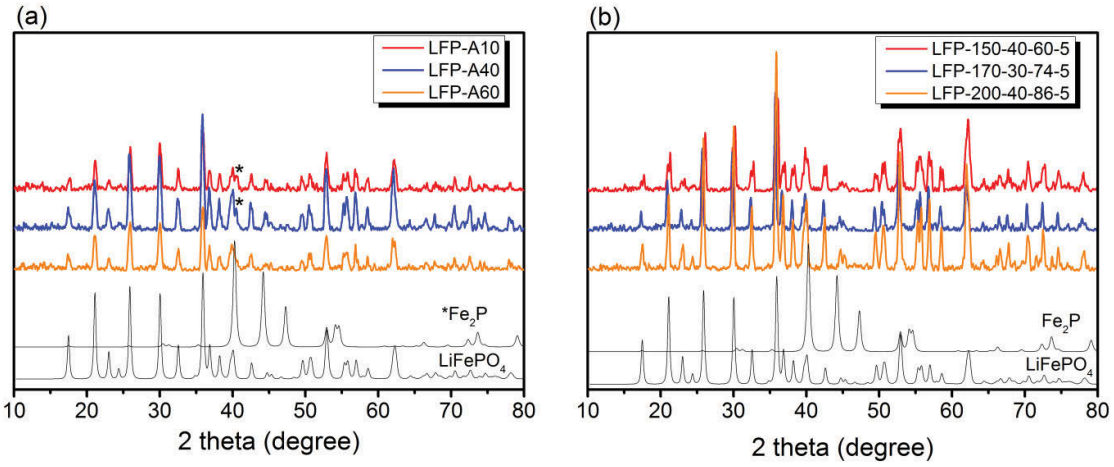

Figure 4-1. XRD patterns of (a) LFP-A10 – LFP-A60 and (b) LFP-150 – LFP-200. Both compared with the calculated pattern of JCPDS card number 83-2092 and Fe_2P.

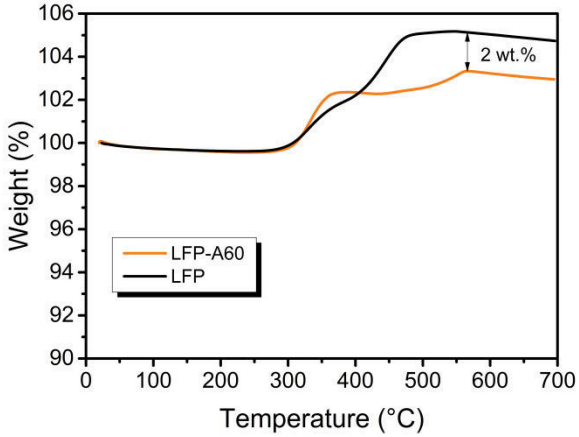

Figure 4-2. TGA curves of LFP-A60 compared to the TGA result of a carbon free $LiFePO_4$ sample.

The particle size and morphology was investigated using field emission scanning electron microscopy (FESEM) imaging. Figure 4-3 shows the FESEM images of as-prepared $LiFePO_4$/C composite materials. Figure 4-3a-c shows the as-prepared LFP-A10-A60 composites. All three images display randomly agglomerated particle clusters with a particle size of approximately 200-500 nm, which is typical for

$LiFePO_4$ products generated by a carbothermal reduction reaction. No significant difference can be observed from the SEM images regarding the pump feed rate setting during the spray-drying process. All three test settings result in similar morphology, particle size, and degree of agglomeration. A comparable observation can be made for the LFP-150 – LFP-200 samples, as displayed in Figure 4-3d-f. Large and dense particle clusters are formed for these samples. The most significant difference to the former LFP-A10 – LFP-A60 samples is an obvious highly porous appearance, as seen in Figure 4-3d-f marked there with white arrows. This porosity is possibly caused by the degassing process of the precursor material $NH_4H_2PO_4$, which releases NH_3 and H_2O upon heating.[405] The LFP-A10 – LFP-A60 samples were prepared with an already degassed precursor intermediate, and thus, do not show the same porosity. A porous structure is generally considered beneficial for electrochemical performance as it improves the electrolyte-particle interphase.[406, 407] Overall, the morphologies obtained using only sucrose as carbon source are very similar to a preparation method using ball milling to homogenize the precursor materials, as described earlier in Chapter 3.[201] The main advantage of the spray-drying process shown here is its ability to generate high yield in a very short time compared to the aforementioned ball milling approach. Additionally, spray-drying provides the opportunity to create very uniform spherical, hollow or porous structures,[399] which will be discussed in Section 4.3.2 Morphology Optimization.

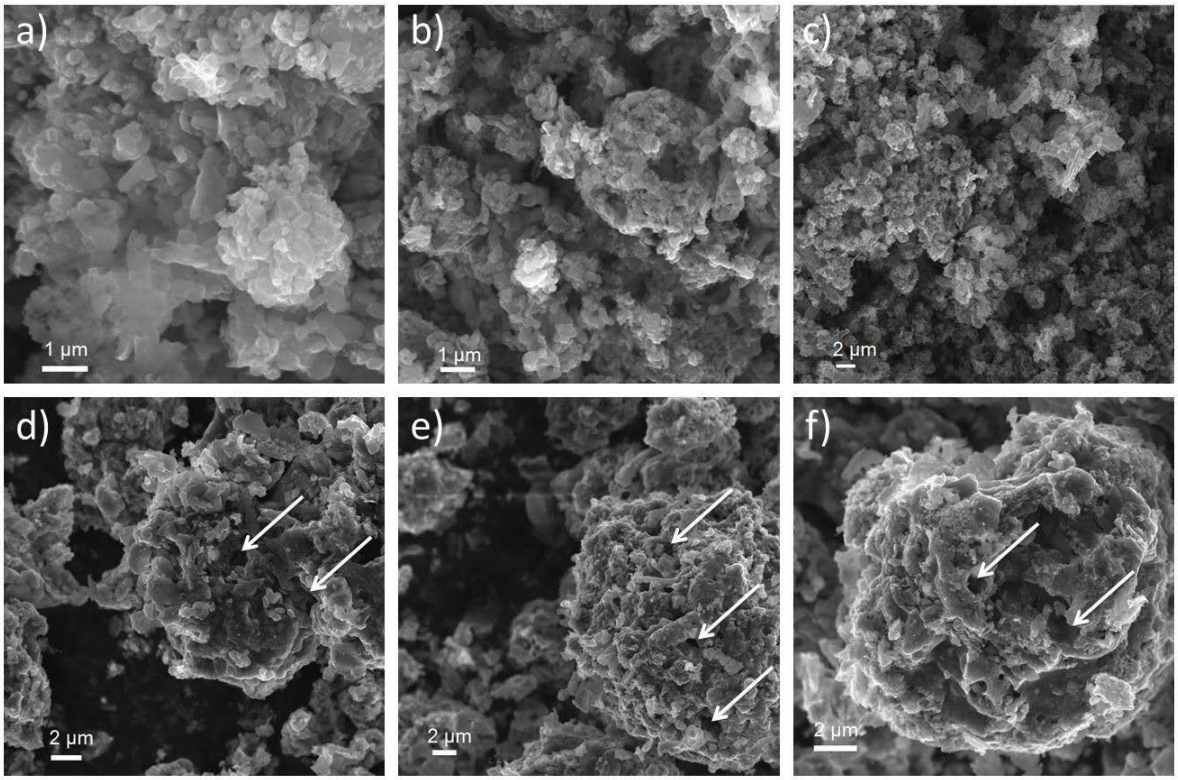

Figure 4-3. SEM images of (a) LFP-A10, (b) LFP-A40, (c) LFP-A60, (d) LFP-150-40-60-5, (e) LFP-170-30-74-5, and (f) LFP-200-40-86-5. Some obvious open pores are marked with white arrows.

Microspherical particle clusters, which contain well interconnected nanoparticles, have the advantage of higher tape density values without losing the ionic diffusion benefits of pure nanoparticle materials. First, the electrochemical performance of the LFP-A10 – LFP-A60 and LFP-150 – LFP-200 composite materials (Figure 4-4) will be discussed. The rate performances of the LFP-A10 – LFP-A60 and LFP-150 – LFP-200 are displayed in Figure 4-4a,c, respectively. It can be seen that the porous LFP-150 – LFP-200 samples show the typical electrode activation process as sometimes observed in porous materials during the initial low rate cycles.[408, 409]

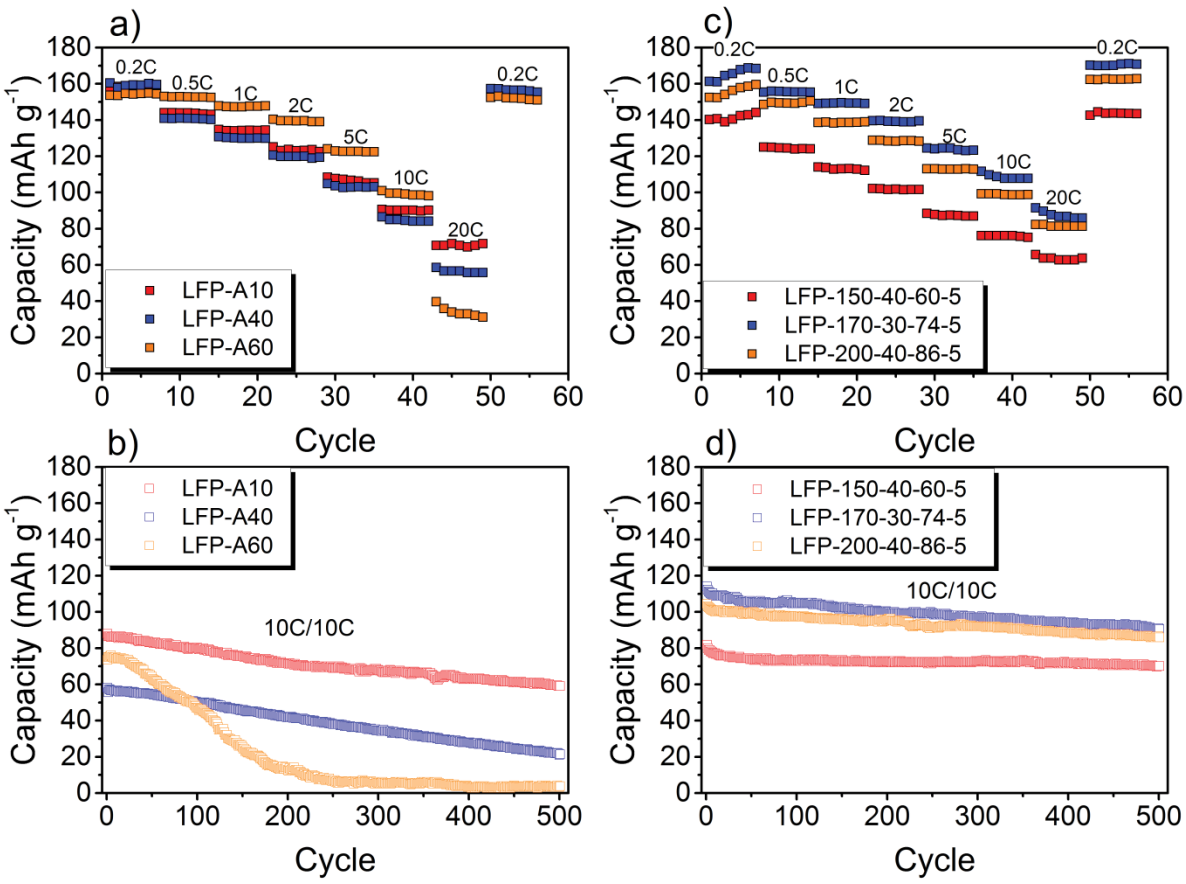

Figure 4-4. Rate performance results of (a) LFP-A10 – LFP-A60 and (c) LFP-150 – LFP-200 cycled at current densities from 0.2C to 20C in the voltage range of 2.0 – 4.25 V. Cycling stability test of (b) LFP-A10 – LFP-A60 and (d) LFP-150 – LFP-200 for 500 cycles at 10C in the voltage range of 2.0 – 4.25 V.

All three samples undergo a 4% capacity increase from the first to the seventh cycle. The nonporous LFP-A10 – LFP-A60 samples do not show the same behaviour. These samples remain steady at the initial discharge capacity for the entire seven cycles at 0.2C. Judging from the overall rate performance of the LFP-A10 – LFP-A60 samples displayed in Figure 4-4a and Table 4-1, it is obvious that a feed rate somewhere between 40 – 60% (12 - 18 ml min^{-1}) should be chosen as the optimal feed rate for high performance $LiFePO_4$/C. Even though a feed rate of 10% (4 ml min^{-1}) shows good rate performance, the much longer spray-drying

procedure caused by a low feed rate does not justify choosing this setting. Thus, a feed rate of 50% (15 ml min^{-1}) was selected for the subsequent spray-drying trial to prepare the LFP-150 – LFP-200 samples. Analysing the rate performance achievable for those samples, it is obvious that the sample prepared with an inlet temperature of 170 °C shows the best performance. Additionally, cycling the samples at a high rate of 10C, the LFP-170 sample again provides the best long-term cycling stability of all tested samples.

Table 4-1. Rate performance and cycling stability test results of $LiFePO_4$ prepared for the feed rate optimization (top 3) and the samples prepared for the inlet temperature optimization (bottom 3). Marked in green are the best results of each starting material.

Sample name	Capacity [mA h g^{-1}]							
	0.2C	0.5C	1C	2C	5C	10C	20C	0.2C
LFP-A10	158.57	143.99	134.24	123.04	106.75	90.20	70.84	155.51
LFP-A40	159.36	140.88	129.94	119.91	102.95	84.60	56.70	156.47
LFP-A60	154.33	152.84	147.27	139.49	122.70	99.14	33.05	152.19
LFP-150	140.51	124.47	113.15	101.88	87.51	76.20	62.82	143.84
LFP-170	165.69	155.57	149.56	139.26	124.51	107.84	86.80	170.21
LFP-200	156.36	149.34	138.68	128.35	112.86	98.81	81.39	162.52

4.3.2 Morphology Optimization

Figure 4-5 shows the XRD patterns of the six $LiFePO_4$ materials prepared for morphology optimization. The obtained patterns are again consistent with the $LiFePO_4$ pattern of JCPDS card number 83-2092. The nominal carbon content of these three samples is 3, 4, and 7 wt% for LFP-C PVA, LFP-C PEG, and LFP-C CA, respectively, as determined using thermogravimetric measurements displayed in Figure 4-6. The slight difference of nominal carbon content might originate from

the chemical structure, and thus, availability of carbon atoms per monomer/molecule of these different additives. PEG and PVA provide two carbon atoms per monomer unit, whereas citric acid contains six carbon atoms per molecule, which makes a more precise calculation of the amount of carbon precursor difficult. Nevertheless, a nominal carbon content of around 5 wt% can be considered feasible for large scale production of such $LiFePO_4$ materials.[198, 367] The carbon precursor not only serves as source for a carbon coating but also as reducing agent for the Fe component in $LiFePO_4$. Depending on the purity of the used protection gasses, the vacuum furnace used, and even the chemical formula of the carbon source itself, more or less carbon may be consumed during high temperature sintering to protect the Fe component from oxidation. Thus, the added amount of PEG and PVA additive can be considered acceptable whereas the citric acid or sucrose content could be reduced to generate smaller nominal carbon contents.

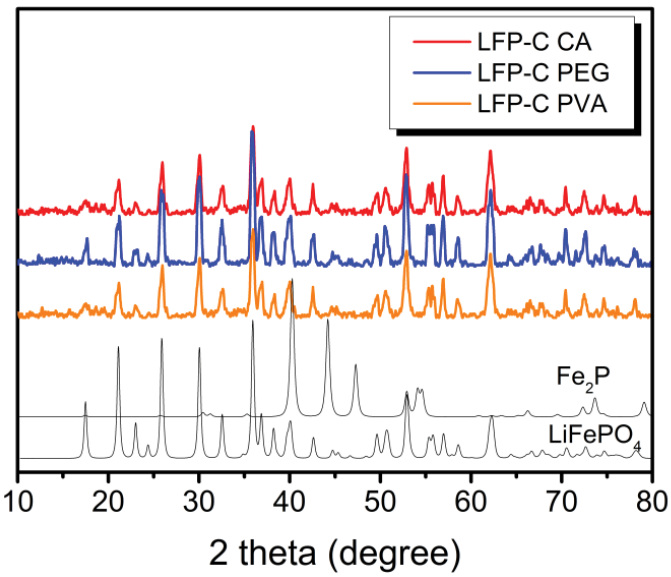

Figure 4-5. XRD patterns of LFP-C CA, LFP-C PEG, and LFP-C PVA compared with the calculated pattern of JCPDS card number 83-2092 and Fe_2P.

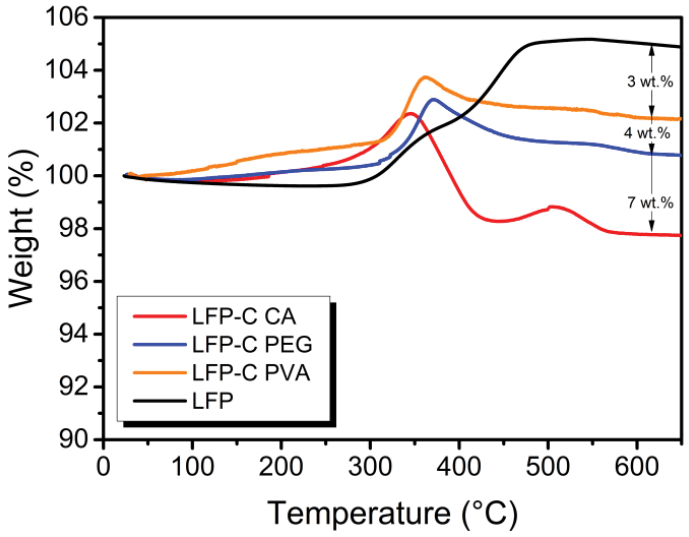

Figure 4-6. TGA curves of LFP-C CA, LFP-C PEG, and LFP-C PVA compared to the TGA result of a carbon free $LiFePO_4$ sample.

The obtained morphologies using citric acid, PEG, and PVA as additives for the spray-drying process are displayed in Figure 4-7a-c, respectively. It can be seen that the use of citric acid results in nano- to micro-sized spheres (Figure 4-7a) with rather smooth surfaces. It is difficult to identify the individual primary nanoparticles of these spheres. As mentioned before, the LFP-C CA sample showed the highest nominal carbon content, which possibly covers the $LiFePO_4$ nanoparticles in a thick carbon layer, making it difficult to distinguish them. The addition of PEG results in remotely spherical particle clusters, as seen in Figure 4-7b. And finally, using PVA as additive generates large hollow, almost donut shaped spherical particle clusters (Figure 4-7c). All three additives generate morphologies desirable for high tap density materials, and thus, it is likely that all prepared samples could be able to achieve high volumetric capacities as well as acceptable gravimetric capacities.

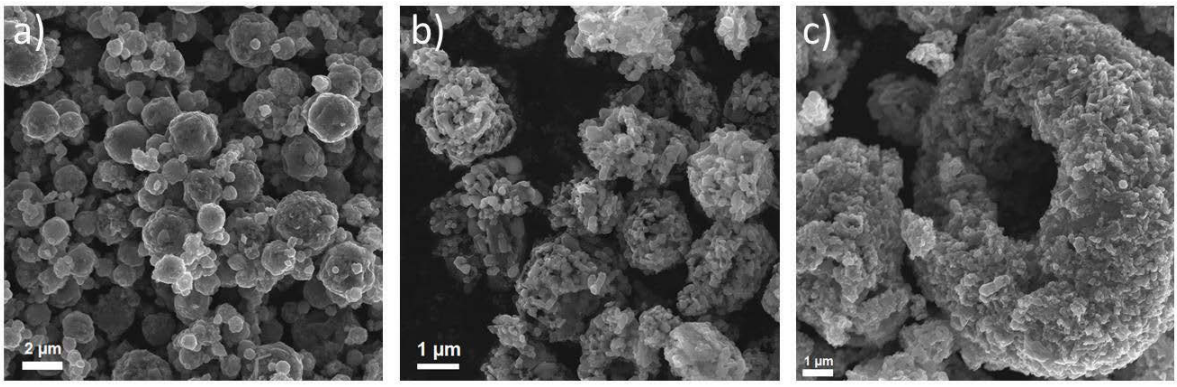

Figure 4-7. SEM images of (a) LFP-C CA, (b) LFP-C PEG, and (c) LFP-C PVA.

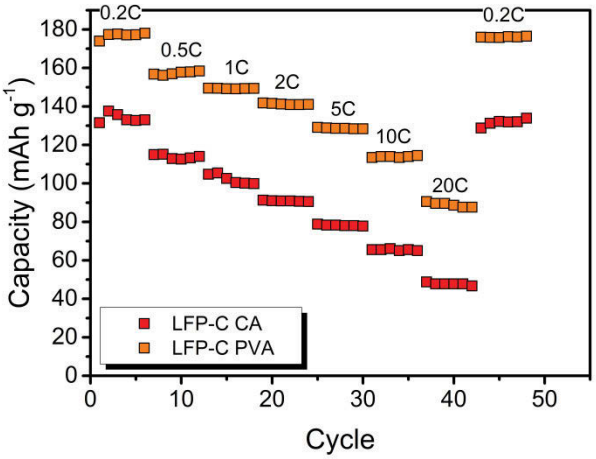

Figure 4-8. Rate performance results of LFP-C CA and LFP-C PVA cycled at current densities from 0.2 to 20C in the voltage range of 2.0 – 4.25 V.

The electrochemical performance displayed in Figure 4-8 reflects the previous assumptions that the nominal carbon content of sample LFP-C CA needs to be reduced. It can be seen that the LFP-C CA sample delivers approximately 23 to 47% less reversible capacity than the LFP-C PVA sample at the same current density (see Table 4-2). The higher carbon content causes a drastic reduction in reversible capacity for this sample. The obtained rate performance of LFP-C PVA on the other hand is very competitive compared with previous reports as well as when

compared with the test results of the additive-free sample LFP-170.[204, 365, 387, 388, 391-396]

Table 4-2. Rate performance test results of LFP-C CA and LFP-C PVA compared with the performance of additive-free sample LFP-170.

Sample name	Capacity [mA h g^{-1}]							
	0.2C	0.5C	1C	2C	5C	10C	20C	0.2C
LFP-C CA	135.74	112.87	102.55	90.96	78.30	66.04	47.74	132.20
LFP-C PVA	177.65	156.95	149.22	141.24	128.59	113.95	89.59	175.80
LFP-170	165.69	155.57	149.56	139.26	124.51	107.84	86.80	170.21

4.4 Conclusions

In summary, the spray-drying method has been successfully applied to prepare high performance carbon coated $LiFePO_4$ materials. The optimisation trial has identified the most suitable process conditions for the precursor materials and spray-dryer model used to prepare pure and practical $LiFePO_4$ cathode materials in a large scale. It was found that an inlet temperature of 170 °C, a feed rate of 15 ml min^{-1}, and a suspension concentration of 20 wt% are both practical and efficient parameter settings for the preparation of $LiFePO_4$ cathode materials. In the subsequent morphology optimisation trial, the impact of different additives on particle morphology of the final product was also investigated. In this trial, it was found that the addition of polyvinyl alcohol (PVA) generates micron-sized donut shaped particle clusters that provide a high tap density product without sacrificing electrochemical performance. The $LiFePO_4$ cathode material prepared with the addition of PVA achieved remarkable rate performance results and could maintain a capacity of 113.95 mA h g^{-1} at 10C. Further experimental work has to be

conducted in regards to further reducing the nominal carbon content of the final product, the quality of the carbon coating, and cycling stability of the composite to fully evaluate to advantages of a spray-drying process integration into the large scale production of $LiFePO_4$.

Chapter 5: Free-standing $LiFePO_4$-carbon paper hybrid cathode for flexible Lithium-ion batteries

5.1 Introduction

Lithium-ion batteries (LIBs) are the primary power source for portable electronic devices, such as mobile phones and laptops, and are now also considered for large-scale applications, such as electric vehicles and renewable energy storage. The constantly increasing demand for LIBs requires not only more cost-efficient materials and production processes but also ecological battery components in order to build a sustainable industry that eventually leads us into a renewable energy future.[410, 411]

A typical LIB consists of a graphite based anode, a $LiCoO_2$ cathode and a separator saturated with a liquid organic electrolyte. Both active materials, graphite and $LiCoO_2$, are pasted onto a metal substrate or current collector (copper and aluminium), which requires the usage of polymeric binders and appropriate organic solvents.[411, 412] One approach to reduce the drawbacks of current LIBs could be the replacement of $LiCoO_2$, an expensive and toxic layered metal oxide, which has been the most commonly used cathode material since LIBs were commercialized by Sony in 1990.[411-413] Olivine type lithium iron phosphate ($LiFePO_4$) is regarded as a suitable substitute for $LiCoO_2$ due to its low cost, non-toxicity, high theoretical capacity (170 mA h g^{-1}) and good cycling performance.[7, 198, 374, 414-416] The second improvement opportunity can be found in the replacement of the metal current collector, in case of the cathode side aluminium, with a low-cost, metal-free conductor.[417, 418] Recently, paper and textiles have been re-discovered as cheap, renewable and abundant materials for energy devices, such as supercapacitors, LIBs and Li–S (lithium–sulphur) batteries, which is mainly due to their intrinsic high surface area and porosity.[419-427] For instance, Hu *et al.*[428] developed a lithium-ion textile battery based on carbon nanotube (CNT) coated polyester, which was

soaked with a slurry containing commercial $Li_4Ti_5O_{12}$ (LTO) or $LiFePO_4$ (LFP), polyvinylidene fluoride (PVDF) binder, conducting additives and *N*-methyl-2-pyrrolidone (NMP) as the solvent. Zhang *et al.*[429] used commercially available rice paper laminated with a pre-sintered LFP precursor, PVDF and NMP slurry. The dried LFP precursor and rice paper intermediate was co-sintered to generate well-crystalized LFP and to *in situ* carbonize the rice paper substrate into a carbon fibrous film. Furthermore, the bare rice paper was used as a separator and served as an anode in a full battery design. These methods effectively substituted both metallic current collectors and stable full batteries could be assembled. Other reports also managed the polymeric binder PVDF by replacing the binder components with cellulose,[430-432] so-called bundles of carbon nanostructures[433] (highly entangled CNTs deposited onto a fibre surface *via* chemical vapour deposition) and even the use of electrostatic interactions[434] has been reported, which resulted in good cycling performance and stability.

Taking all these innovative concepts into account, we designed a unique preparation method to generate a free-standing, binder-free and metallic current collector-free LFP cathode. In this report, we demonstrate the simultaneous carbonization of microcrystalline cellulose and the *in situ* crystal growth of $LiFePO_4$ nanoparticles achieved by a novel impregnation–carbothermal reduction technique to create an innovative $LiFePO_4$–carbon paper ($LiFePO_4$@CP) hybrid electrode. No polymeric binders or conducting additives were used in this preparation process. The hybrid $LiFePO_4$@CP electrode consists of a carbon fibre network core, which allows fast electron transport and provides a porous structure for electrolyte penetration. The thin $LiFePO_4$ shell enables fast ion diffusion over a large surface area. This free-standing $LiFePO_4$@CP hybrid electrode achieved a reversible capacity of 222 μA h cm^{-2}, exceptional cycle life over 1000 cycles and high rate capabilities.

5.2 Experimental Section

Preparation of $LiFePO_4$@CP cathodes:

$LiFePO_4$@CP was prepared by a novel 2-step impregnation–carbothermal reduction technique. A commercial paper towel (PT) was used as carbon paper owing to its porous nature, structural integrity and light weight. The PT was purified by soaking in 20 ml deionized water (DI water) for 2 h. Subsequently, 4 ml concentrated hydrochloric acid was added to the solution and left for another 12 h. The purified PT was washed with DI water several times by vacuum filtration and dried overnight at 100 °C in a vacuum oven. The XRD patterns of the purified cellulose, which is in agreement with previous reports,[435, 436] is displayed in Figure 5-2c. The dried tissue was impregnated for 10 min to ensure thorough saturation with a solution containing 1.0 g $NH_4H_2PO_4$ and 0.365 g $LiOH{\cdot}H_2O$ in 5 ml DI water (solution 1). A small amount of concentrated hydrochloric acid was added to the solution to restrain Li_3PO_4 precipitation. The saturated PT was subjected to freeze-drying overnight to obtain a homogenous loading of phosphate and lithium precursors. The iron precursor was introduced in a similar procedure. The phosphate and lithium loaded PT was weighed and impregnated based on the stoichiometric amount of Fe in the compound with the exact volume of a solution containing 1 g $FeCl_3$ and 30 wt% glucose in 10 ml DI water (solution 2) and was subsequently freeze-dried overnight. The dried and pre-loaded PT was then transferred into a ceramic crucible and sintered at 312 °C for 2 h and 700 °C for 10 h under a H_2/Ar atmosphere.

Preparation of $LiFePO_4$@Al cathodes:

$LiFePO_4$ was prepared by mixing stoichiometric amounts of $FeC_2O_4{\cdot}2H_2O$, $NH_4H_2PO_4$ and Li_2CO_3 (Sigma-Aldrich) *via* industrial-scale ball milling in deionized water for 6 h. Simultaneously, 5 wt% sucrose was added to the suspension to

encapsulate the precursor materials during spray drying and to serve as a carbon source in the subsequent carbothermal reduction. The solid content of the suspension was fixed at 20 wt%. The untreated precursor mixture was spray-dried (Mini Spray Dryer B290, BÜCHI Labortechnik AG, Switzerland) with an inlet temperature of 170 °C and a feed rate of 15 ml min^{-1}. The dried powder was then transferred into a ceramic crucible to thermally decompose in a tubular furnace at 350 °C for 5 h and sintered at 700 °C for 10 h under argon protection.

Structural and physical characterization:

Crystallographic measurements were conducted using a Siemens D5000 X-ray diffractometer with Cu Kα radiation between 10° and 80°. The morphological analyses of the as-prepared material were carried out by field-emission scanning electron microscopy (FE-SEM, Zeiss Supra 55VP). The elemental mapping was conducted on a Zeiss EVO MA 15 SEM equipped with EDX. The carbon fibre/LiFePO4 particle interface and the structure of the coated carbon layer were characterized by high-resolution transmission electron microscopy (TEM, FEI Tecnai T20). The carbonization process of PT to CP and the carbon content of the as-prepared $LiFePO_4$@CP electrode were investigated using a TGA/DTA analyser (TA Instruments, SDT 2960 module, New Castle, DE, USA) at a heating rate of 5 °C min^{-1} under air or nitrogen flow from room temperature to 700 °C.

Electrode preparation and test cell assembly:

The as-prepared $LiFePO_4$@CP electrodes were used directly as working electrodes without further modification. The active material ($LiFePO_4$) mass load was 2.8 mg cm^{-2}. Lithium metal discs were used as counter and reference electrodes. The electrolyte consists of 1 M $LiPF_6$ in dimethyl carbonate (DMC)/ diethyl carbonate (DEC)/ethyl carbonate (EC) (volume ratio DMC : DEC : EC = 1 : 1 : 1).

Approximately 40 µl electrolyte was used for each coin cell. The amount of liquid electrolyte uptake is calculated using the following equation:

$$\eta = \frac{W_t - W_o}{W_o} \cdot 100\% \quad (5\text{-}1)$$

where η is the uptake of the liquid electrolyte, and W_o and W_t are the weight of the electrodes before and after absorption of the liquid electrolyte, respectively. The electrolyte uptake was calculated to be 200 wt%.

The working electrodes of $LiFePO_4$@Al for electrochemical testing were prepared by mixing 80 wt% as-prepared $LiFePO_4$ with 10 wt% carbon black and 10 wt% poly(vinyl difluoride) (PVDF, Sigma-Aldrich) in N-Methyl-2-pyrrolidone (NMP, Sigma-Aldrich). The obtained dispersion was carefully pasted onto aluminium foil, dried in a vacuum at 80 °C for 12 h and pressed before cell assembly. Lithium metal discs were used as counter and reference electrodes. The electrolyte consists of 1 M $LiPF_6$ in dimethyl carbonate (DMC)/ diethyl carbonate (DEC)/ethyl carbonate (EC) (volume ratio DMC : DEC : EC = 1 : 1 : 1). Approximately 40 µl electrolyte was used for each coin cell.

All electrodes were stored and all standard CR2032 type coin cells were assembled in an argon- filled glovebox (UniLab, MBRAUN).

Electrochemical characterization:

Galvanostatic charge–discharge and cycling performance tests were performed in the voltage range of 2.00 – 4.25 V at various current densities on a Neware battery tester at room temperature. The cyclic voltammograms (CV) were obtained at different scanning rates of 0.1 – 2.0 mV s^{-1} between 2.0 – 4.5 V and electrochemical impedance spectroscopy (EIS) measurements were conducted

over a frequency range from 100 kHz to 0.01 Hz using a CHI 660C Electrochemistry Workstation.

5.3 Results and Discussions

To prepare the free-standing $LiFePO_4$@CP electrode, all three precursor components (lithium, iron and phosphate) are pre-loaded onto the microcrystalline cellulose fibre network *via* a solution-based impregnation and freeze-drying method, shown in Figure 5-1. For the impregnation with solution 1 (Step 1 in Figure 5-1) consisting of the phosphate and lithium precursor salts, it is important to understand the precipitation mechanism of $LiOH{\cdot}H_2O$ and $NH_4H_2PO_4$ and the subsequent acid-assisted dissolution of Li_3PO_4. This allows validating the weight gain as an accurate marker to calculate the amount of solution 2, which contains the iron and carbon precursors, required to generate the correct stoichiometric ratio of $LiFePO_4$ impregnated into the PT network.

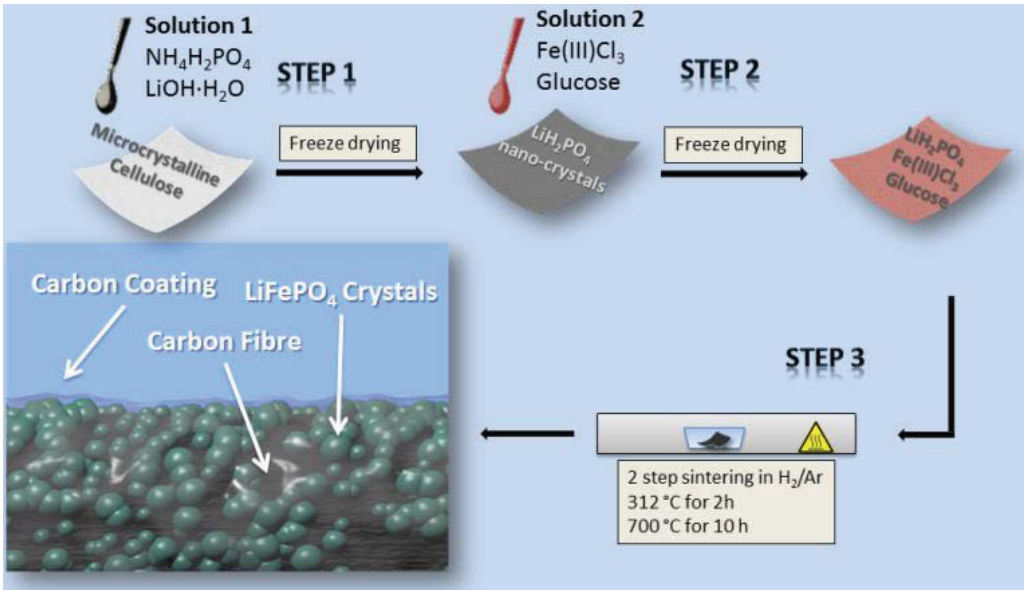

Figure 5-1. Schematic illustration of the $LiFePO_4$@CP hybrid electrode preparation process.

The first reaction between the two precursor materials is the precipitation of Li_3PO_4, wherein all Li ions are consumed (5-2). The residual $NH_4H_2PO_4$ dissolves to form aqueous phosphoric acid (H_3PO_4) and NH_3 (5-3). Hydrochloric acid (HCl) then dissolves the Li_3PO_4 precipitate to form LiCl and LiH_2PO_4 (5-4), wherein LiCl is consumed by H_3PO_4 to form crystalline LiH_2PO_4 upon solvent and HCl evaporation (5-5).[437] Consequently, the freeze-drying process leaves the PT impregnated with highly crystalline LiH_2PO_4 homogenously dispersed throughout the fibre network.

$$3LiOH{\cdot}H_2O + NH_4H_2PO_4 \rightarrow Li_3PO_4(s) + NH_3 + 6H_2O \quad (5\text{-}2)$$

$$NH_4H_2PO_4 \rightarrow H_3PO_4 + NH_3 \quad (5\text{-}3)$$

$$Li_3PO_4 + 2HCl \rightarrow 2LiCl + LiH_2PO_4 \quad (5\text{-}4)$$

$$LiCl + H_3PO_4 \rightarrow LiH_2PO_4 + HCl \quad (5\text{-}5)$$

The reaction mechanism in solution 1 as described in equation (5-2) to (5-5) was confirmed by the XRD analysis of the dried solution (Figure 5-2a). The traces of LiCl, which are possibly caused by an undersupply of phosphoric acid (H_3PO_4), are negligible due to the pure phase XRD pattern of the final product (Figure 5-2b). It can be assumed that this minor Li excess does not result in the formation of impurities, such as Li_3PO_4.[438, 439] On the contrary, a slight oversupply of lithium during solid-state reaction is considered beneficial to compensate for the loss of the lithium element caused by the evaporation of Li_2O.[440]

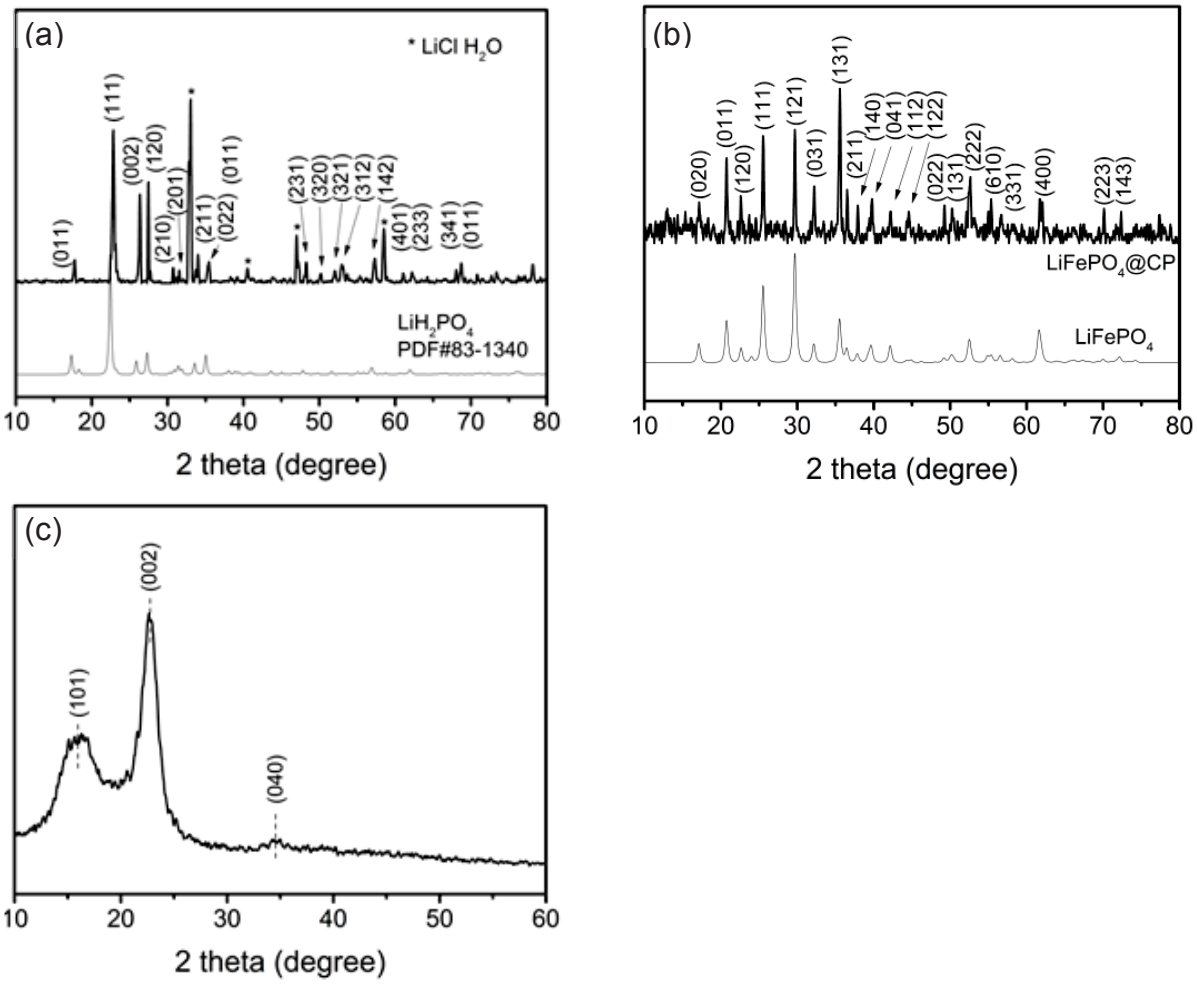

Figure 5-2. (a) XRD pattern of solution 1 after drying compared with the simulated pattern of LiH_2PO_4 calculated from JCPDS card number 83-1340 (* marks traces for $LiCl \cdot H_2O$). (b) XRD pattern of $LiFePO_4$@CP and the calculated pattern of JCPDS card number 83-2092. (c) XRD pattern of purified paper towel matching the standard XRD pattern of microcrystalline cellulose.[435, 436]

According to the theoretical assumption of the reaction mechanism during freeze-drying of solution 1, the mass of the $FeCl_3$ solution (solution 2) required to ensure an appropriate molar ratio Li:Fe:PO_4=1:1:1 can be sufficiently calculated from the mass load of PT. The impregnation of the iron precursor (Step 2 Figure 5-1) includes the dissolved carbon precursor, which is applied as reducing agent and to

generate a conductive carbon coating on the surface of the $LiFePO_4$ layer, which also serves as structural support. The next stage of the electrode preparation is the two-stage heat treatment (Step 3 in Figure 5-1). The first heat treatment stage at 312 °C was chosen to allow $FeCl_3$ to melt and consequently enable capillary forces to homogenously distribute it through the PT fibre network, whilst allowing degassing of the cellulose fibre. The decomposition of all precursor materials, the crystal formation of $LiFePO_4$, and the carbon network generation take simultaneously place in the second and final heat treatment stage from 312 °C to 700 °C. The $LiFePO_4$ shell itself consists of aggregates of $LiFePO_4$ nano-crystals, which are densely packed on the carbon fibre surface. The close contact between the carbon fibre and the crystals is supported by a thin carbon coating generated from the reducing agent used for the carbothermal reduction reaction (Figure 5-1). According to the XRD investigation (Figure 5-2b), no impurity phases have been generated during the high temperature treatment. This confirms the successful synthesis of $LiFePO_4$ covering carbonized paper by the novel impregnation–carbothermal reduction technique. The obtained pattern can be consistently indexed to JCPDS card number 83-2092 of $LiFePO_4$.

As shown in the SEM images of Figure 5-3a and b, the generated carbon paper is an interwoven network of carbon fibres, which are completely covered by $LiFePO_4$ particles. Figure 5-3c shows the as-prepared $LiFePO_4$@CP electrode wherein the individual intact carbon belts are distinguishable. The carbon fibre network is covered in a thin layer of $LiFePO_4$ showing uninterrupted contact between the two surfaces, which is evident in Figure 5-3d and the elemental mapping images in Figure 5-4. The inevitable shrinkage of the cellulose fibre during carbonization to carbon paper seemingly does not result in contact loss between the freshly generated $LiFePO_4$ crystallites and the carbonizing paper surface. Consequently, it can be seen that the $LiFePO_4$ layer was generated leaving random cavities behind (Figure 5-3d), possibly caused by de-hydrogen and de-oxygen processes during

the transition of cellulose fibre to fully-carbonized carbon paper.[441] These cavities or pores are beneficial for electrolyte penetration, and thus, ion diffusivity through the $LiFePO_4$ layer.[372]

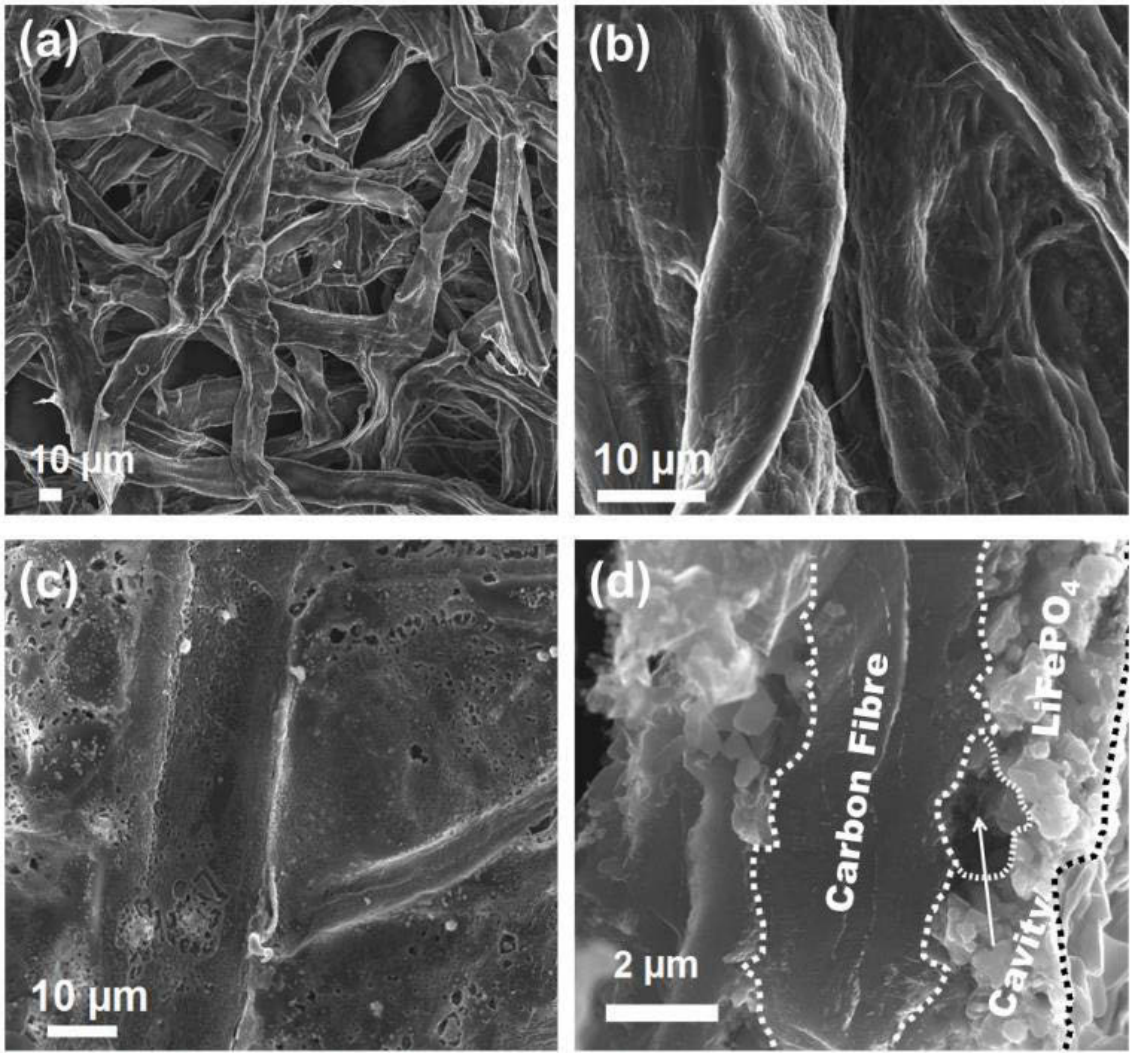

Figure 5-3. SEM images of (a) bare carbonized paper at low magnification, (b) bare carbonized paper at high magnification, (c) carbonized paper loaded with $LiFePO_4$, and (d) cross section SEM image of $LiFePO_4$@CP.

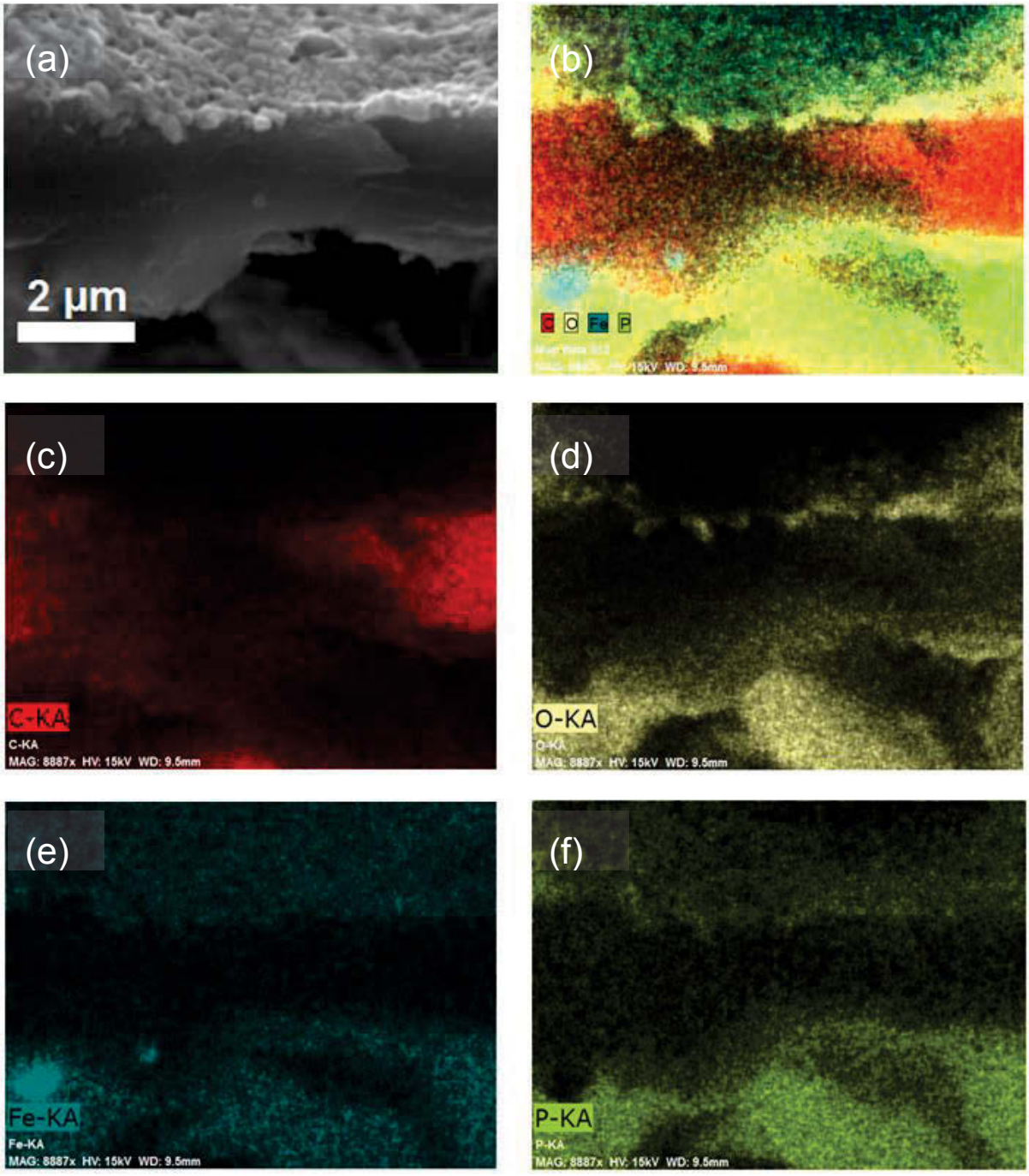

Figure 5-4. SEM energy-dispersive spectroscopy (EDS) characterization of $LiFePO_4$@CP. (a) SEM image of the selected area for EDS mapping; (b) Integrated Fe-, P-, O-, and C-elemental mapping image; elemental mapping images of (c) carbon C, (d) oxygen O, (e) iron Fe, and (f) phosphorous P.

TEM imaging was conducted to visualize the cooperative combination of carbon fibre, LiFePO4 crystallite, and carbon coating.

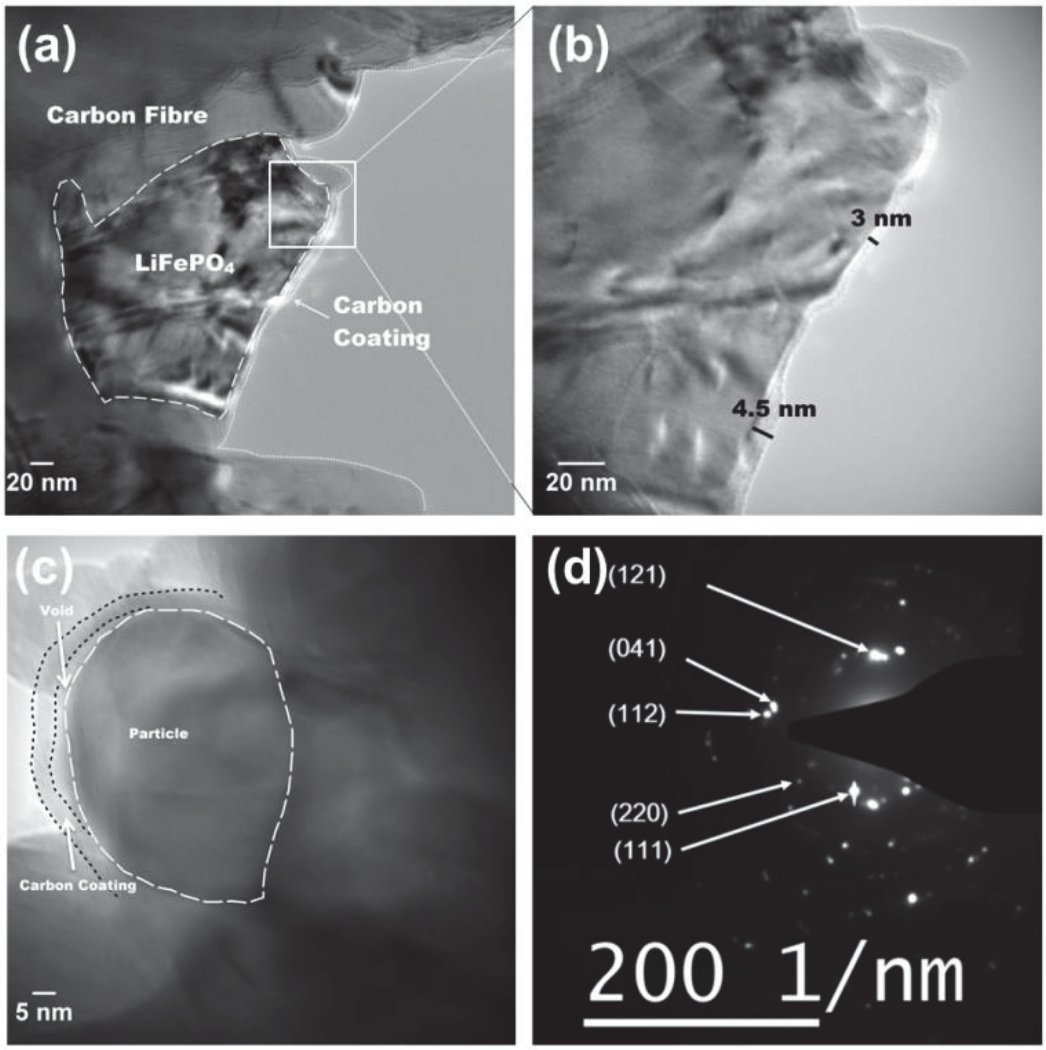

Figure 5-5. TEM images of (a) a $LiFePO_4$ single crystallite embedded into a carbon fibre and wrapped by a carbon coating and (b) the enlarged section of the $LiFePO_4$ crystal showing the approximate thickness of the carbon coating at different positions; (c) TEM image of a carbon coated $LiFePO_4$ crystal attached to a piece of carbon fibre. Small voids are formed between carbon layer and particle allowing the material to contract during battery operation. (d) Selected area electron diffraction (SAED) pattern of $LiFePO_4$@CP.

Figure 5-5a shows the TEM image of a single LiFePO4 crystal (dashed outlines) closely in contact with a piece of carbon fibre. The LiFePO4 crystals are covered by a thin layer of amorphous carbon (dotted outline) of about 3–5 nm thickness (Figure 5-5b). This carbon layer continues on the carbon fibre surface, providing a conducting network between individual $LiFePO_4$ particles and along the fibre surface. Furthermore, the carbon coating also formed a closed-packed yolk-shell structure with the $LiFePO_4$ particles leaving small voids, which allows the material to contract during (dis)charge (Figure 5-5c). The reinforcement provided by this thin carbon coating contributes to the cycling stability, which is usually determined by the added polymeric binder in a conventional electrode design due to swelling, decomposition, or poor elasticity of some commonly-used products.[156, 442] In the case of our material, the carbon coating combines the function of a strong binder and a conducting additive without the disadvantages for cycle life and rate performance.[443, 444] And lastly, the selected area electron diffraction (SAED) pattern displayed in Figure 5-5d exhibits a set of concentric rings with bright spots, which can be indexed as the olivine $LiFePO_4$ phase in consistency with the XRD investigation shown in Figure 5-2b.

Thermogravimetric measurements displayed in Figure 5-6 allow the determination of the nominal carbon content of the as-prepared $LiFePO_4$@CP material. Heating pure $LiFePO_4$ in air from room temperature to 700 °C results in a weight gain of 4.8%, slightly under the theoretical weight gain of 5.1% if Fe^{2+} is completely oxidized to Fe^{3+}.[445] The $LiFePO_4$@CP electrode shows a weight loss of 68.9% up to 475 °C, followed by a slight weight gain plateauing at 72%. This result indicates a nominal carbon content of around 33 wt%, which is very reasonable assuming that the nominal carbon content substitutes the Al current collector (CP component), carbon black additives, and polymeric binders (carbon coating component).

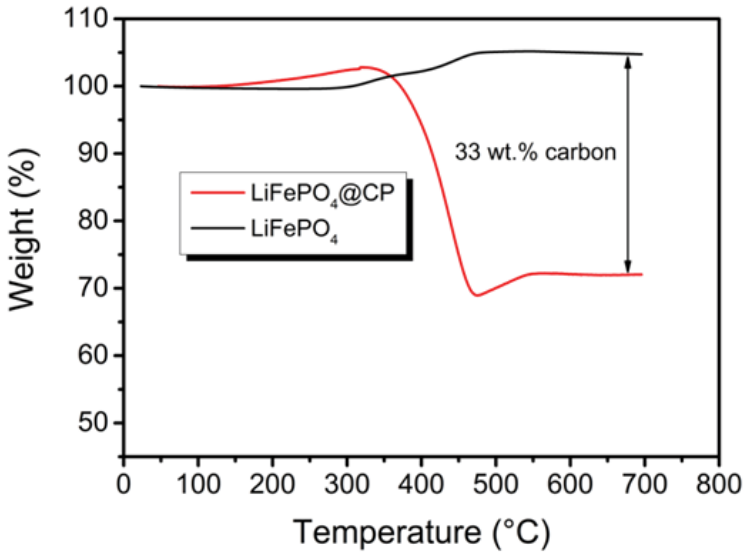

Figure 5-6. TGA curve of $LiFePO_4$@CP and carbon free $LiFePO_4$ from room temperature to 700 °C in air.

The as-prepared $LiFePO_4$@CP electrode can thus be directly used as the cathode in lithium-ion batteries without the use of an Al current collector, conducting additives, or binders.

The evaluation of cycling stability and rate performance (Figure 5-7a) was carried out using an unconventional approach, which incorporates both test conditions into one uninterrupted test sequence. This combined rate and stability performance test gives valuable insight on the durability of the as-prepared $LiFePO_4$@CP electrodes under extremely stressful conditions of long-term fast cycling and relaxation during short-term slow cycling at various rates, respectively. Individually-tested electrodes were first cycled at different current rates from 0.1 to 2.5 mA cm^{-2} and back to 0.1 mA cm^{-2} in step one. Immediately after this rate performance test in step two, the cells were cycled at 2.5 mA cm^{-2} for 500 cycles to evaluate the cycling stability at high current rates. After that, the sequence was repeated once in step three and step four to identify performance changes of the cells. As shown in Figure 5-7a, step one was completed after 42 cycles.

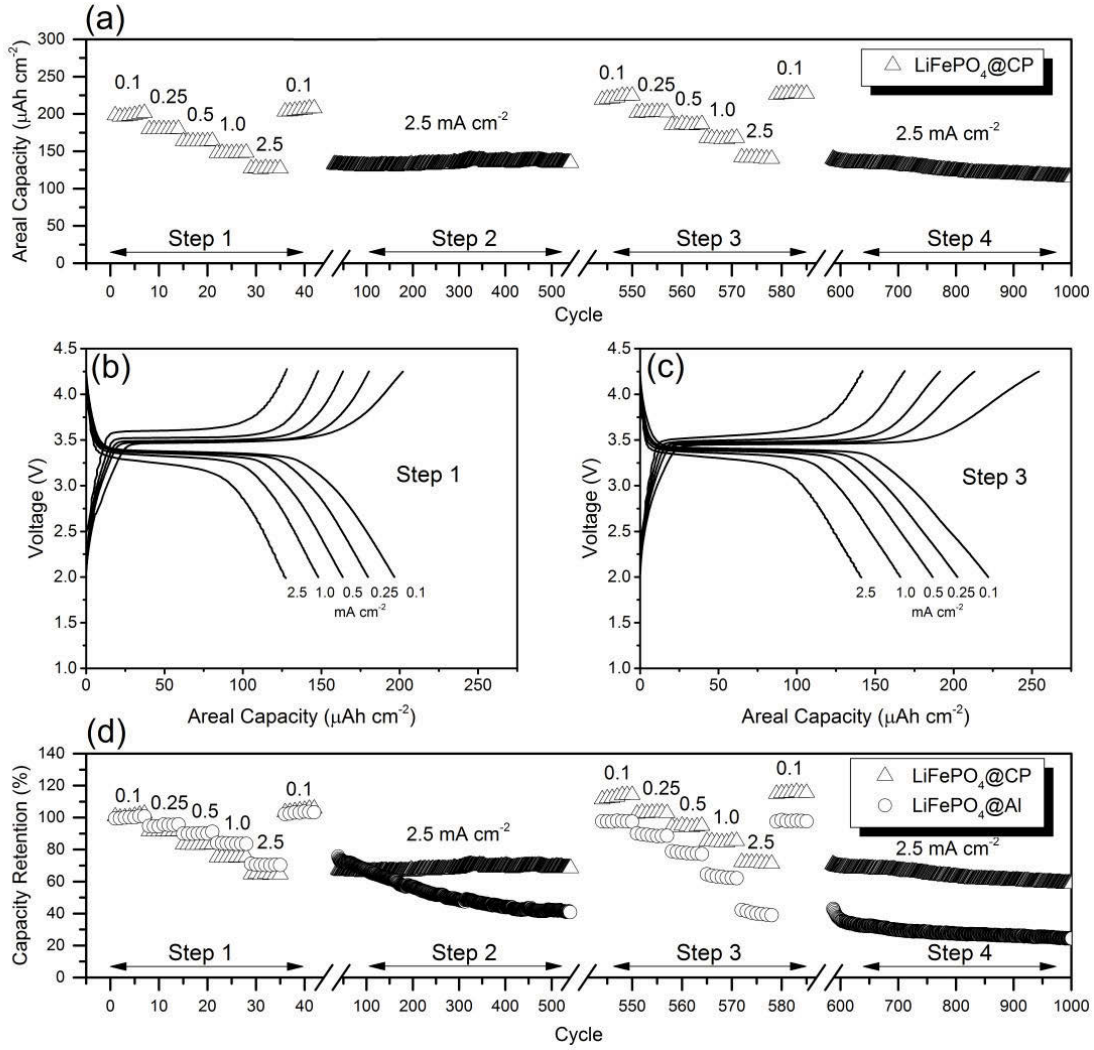

Figure 5-7. (a) Cycling stability and rate performance test of $LiFePO_4$@CP for 1000 deep (dis)charge cycles; Galvanostatic profiles of $LiFePO_4$@CP at different current densities in the voltage range of 2.0 to 4.25 V of (b) the Initial rate performance test and (c) the second rate performance test; (d) Capacity retention comparison of $LiFePO_4$@CP and $LiFePO_4$@Al at different current densities for 1000 cycles normalized to the reversible areal capacity at 0.1 mA cm^{-2}.

The $LiFePO_4$@CP electrodes achieved reversible areal capacities of 197, 180, 163, 147, and 127 μA h cm^{-2} at current densities of 0.1, 0.25, 0.5, 1.0, and 2.5 mA cm^{-2}, respectively. The capacity retention from 0.1 to 2.5 mA cm^{-2}, displayed in Figure 5-7d, is as high as 65% and the cells recovered to 205 μAh cm^{-2} after the current

density was reduced back to 0.1 mA cm^{-2}. Immediately after the rate performance test, the same cells were cycled at 2.5 mA cm^{-2} for 500 cycles in step two and a progressive capacity increase can be observed in Figure 5-7a. After this first cycling stability test, the $LiFePO_4$@CP electrodes showed no sign of capacity fading. Instead, the electrode generated a capacity increase of about 5% to 134 µAh cm^{-2} (Figure 5-7a and c). A progressive increase of reversible capacity can be observed. Similar activation phenomena have been reported previously for $LiFePO_4$ particles incorporated into fibre matrices or conducting polymers, which also showed increasing capacities even over several 100 cycles.[432, 433, 446] The reason for this might be found in the very densely packed distribution of particles forming the $LiFePO_4$ shell. In this arrangement, the electrolyte penetration might not be completed throughout the entire electrode surface of the uncycled cell. The slight volume reduction during charging[7] could open up new areas for the electrolyte, which enables the extraction of even more Li^+ in the subsequent cycles until the electrolyte was able to penetrate the entire surface of the $LiFePO_4$ shell. Furthermore, no capacity deterioration can be observed during the first rate and stability performance test sequence, which would indicate particle-particle and/or particle-CP contact loss. Both the particle collective as well as the particle-CP interface seem to remain intact even after over 500 deep (dis)charge cycles at high current densities. The second rate performance test in step three revealed reversible areal capacities of 222, 202, 186, 166, and 141 µA h cm^{-2} at current densities of 0.1, 0.25, 0.5, 1.0, and 2.5 mA cm^{-2}, respectively, which translates into an average capacity increase of 10.5% compared to the initial rate performance in step one, as illustrated in Figure 5-7d. Moreover, the capacity retention from 0.1 to 2.5 mA cm^{-2} remained steady at 64% and the cells now recovered to 227 µA h cm^{-2} after the current density was decreased back to 0.1 mA cm^{-2}. The subsequent second stability test in step four revealed a slight capacity decline starting after around 700 cycles. Consequently, the reversible capacity after 1000 cycles

reaches a remarkable 115 μA h cm^{-2}, which is 88% of the initial capacity measured during the first stability test in step two. Figure 5-7b and c show the galvanostatic (dis)charge profiles of $LiFePO_4$@CP cycled between 2.0 and 4.25 V at the current densities from 0.1 mA cm^{-2} to 2.5 mA cm^{-2} of step one and step three, respectively. It is evident that all profiles display the distinct charge-discharge behaviour of $LiFePO_4$ showing two flat plateaus, one at around 3.5 V during charging and the other one at around 3.4 V during discharge. These two plateaus are associated with the Fe^{2+}/Fe^{3+} redox couple reaction, which in detail refers to oxidizing Fe^{2+} to Fe^{3+}, and thus extracting Li^+ during the charge process and *vice versa* reducing Fe^{3+} to Fe^{2+} and inserting Li^+ during discharge.[8, 415, 447] The corresponding differential capacity analyses are displayed in Figure 5-8, respectively. From there it can be seen that the voltage gaps between charge and discharge have significantly narrowed by an average of about 35% even for very high current densities, and the length of each plateau (Figure 5-7b and c) has been increased in step three compared to step one. This result again indicates improved charge-transfer kinetics and increased Li^+ utilization due to the progressive electrode activation process.

For comparison, a similar test sequence was conducted using a traditional electrode ($LiFePO_4$@Al) with the same active material mass load as the $LiFePO_4$@CP electrodes (around 2.8 mg cm^{-2}) containing a high performance $LiFePO_4$ material, PVDF binder, and carbon black (Figure 5-7d and Figure 5-9).

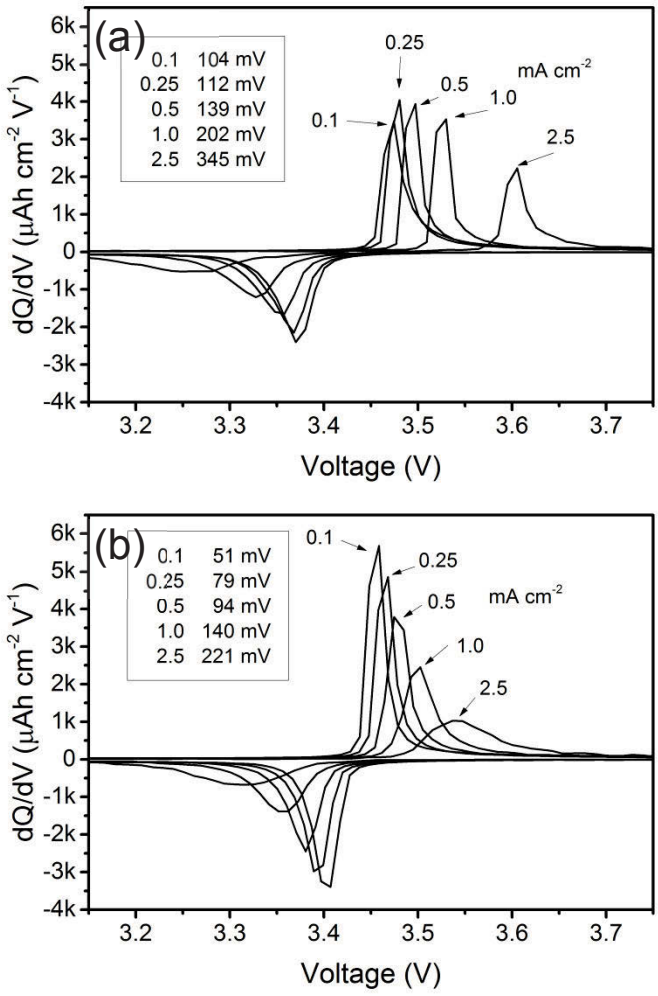

Figure 5-8. Corresponding differential capacity analysis of (a) step one and (b) step three of $LiFePO_4$@CP (Insets: Overpotentials in mV for the current densities 0.1 to 2.5 mA cm^{-2})

According to Figure 5-7d, the capacity retention from 0.1 to 2.5 mA cm^{-2} of around 70% for $LiFePO_4$@Al is very similar to $LiFePO_4$@CP in the first rate performance test of step one. As the $LiFePO_4$@Al entered the cycling stability test in step two at 2.5 mA cm^{-2} for 500 cycles, a dramatic capacity loss can be observed and only 54% of the initial capacity at the beginning of step two was maintained. At the end of step four after 1000 cycles $LiFePO_4$@Al maintained 30% of its initial capacity at 2.5 mA cm^{-2} in step two.

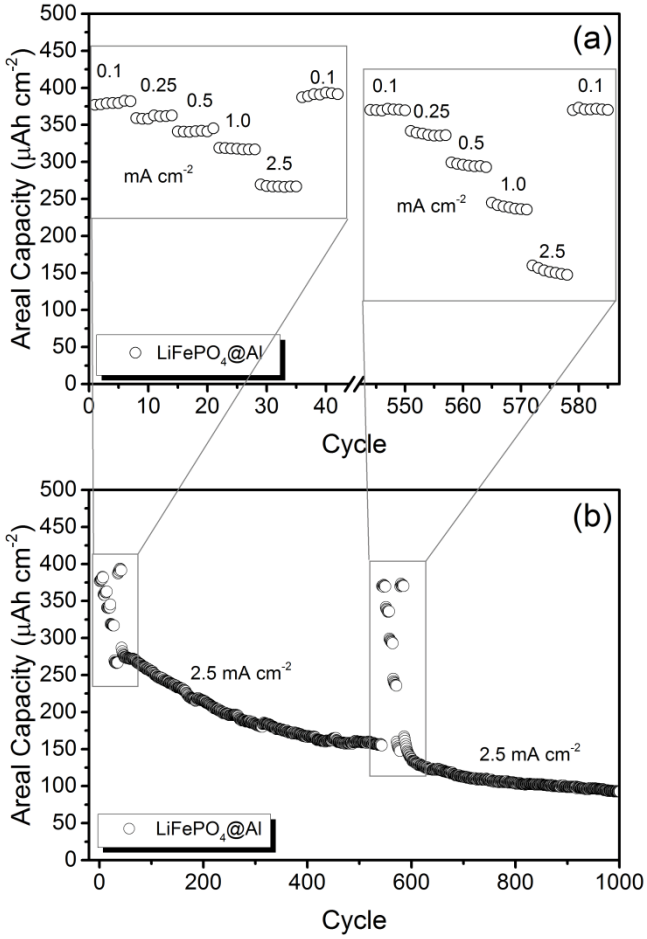

Figure 5-9. (a) Rate performance and (b) stability test sequence of a traditional LiFePO4@Al displayed in areal capacity. The active material mass load of all electrodes is around 2.8 mg cm^{-2}.

Furthermore, a second comparative test, as shown in Figure 5-10, was conducted to demonstrate capacity and stability in reference to the total weight of the electrode including Al current collector, binder and additives, which strongly supports the proposed beneficial properties of a carbon paper based electrode design.

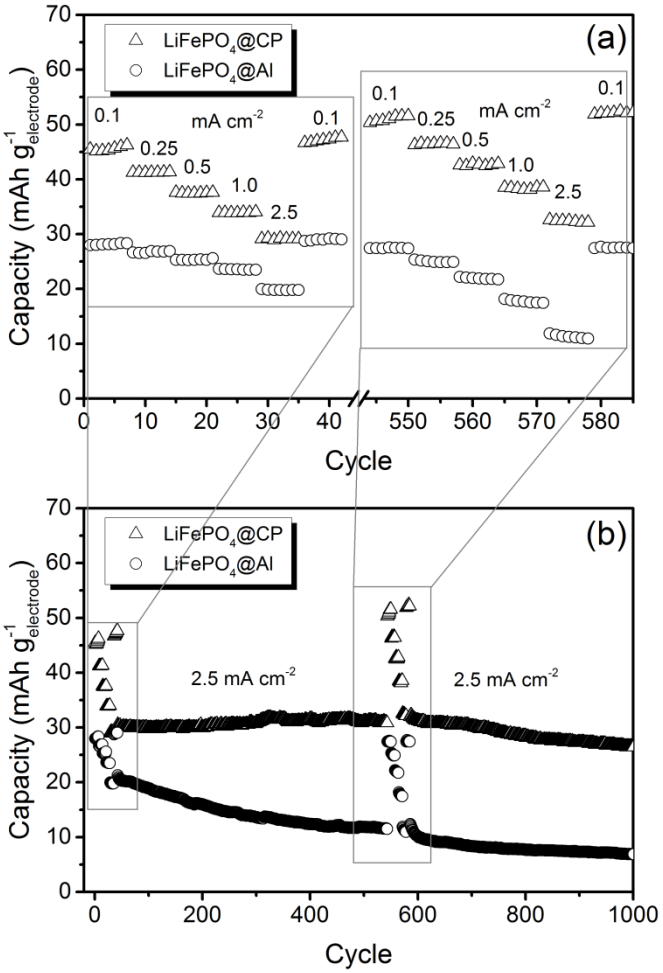

Figure 5-10. (a) Rate performance and (b) stability test sequence of $LiFePO_4$@CP and a traditional $LiFePO_4$@Al. The capacity is displayed in mA h per gram of electrode (weight including current collector, binder and additives). The active material mass load of all electrodes is around 2.8 mg cm^{-2}.

Not only is the reversible capacity at a current density of 0.1 mA cm^{-2} of the $LiFePO_4$@Al electrode (28 mA h g^{-1}) significantly reduced compared to our $LiFePO_4$@CP electrode (45 mA h g^{-1}), the cycling stability also shows much more obvious decline over the tested 1000 cycles.

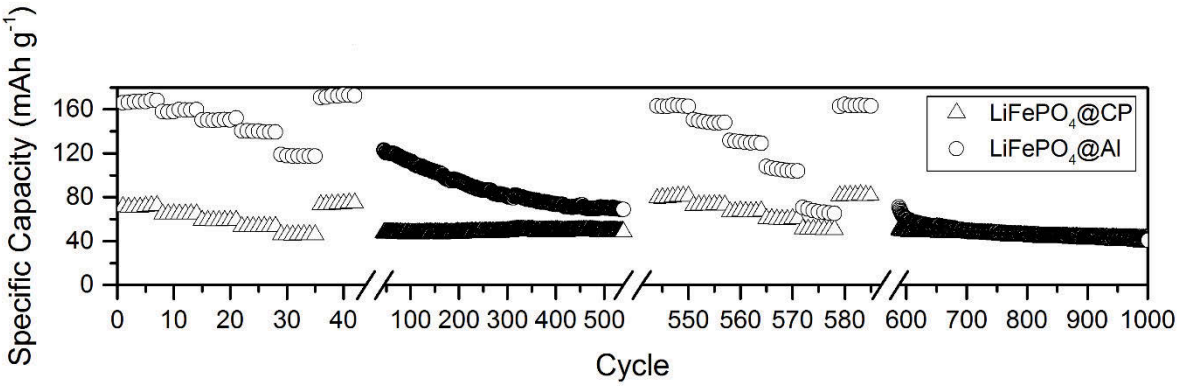

Figure 5-11. Rate performance and stability test sequence of $LiFePO_4$@CP and a traditional $LiFePO_4$@Al. The capacity is displayed in mA h per gram active material. The active material mass load of all electrodes is around 2.8 mg cm^{-2}.

This further demonstrates the superiority of the $LiFePO_4$@CP electrode over the disadvantaged traditional electrode designs containing metal current collectors, polymeric binders, and conducting additives. For the sake of completeness, however, the rate performance and cycling stability results are also converted into active material weight-specific capacity shown in Figure 5-11.

Figure 5-12a unveils the cyclic voltammetric (CV) behaviour of $LiFePO_4$@CP at various scanning rates from 0.1 to 2.0 mV s^{-1} in the voltage range between 2.0 and 4.5 V after the electrode activation process (step two) was completed. A single pair of defined redox peaks can be observed for all scan rates, which corresponds to the Fe^{3+}/Fe^{2+} redox couple as mentioned before. Furthermore, height and area of the redox peaks rise with increased scanning rates, whereas the anodic and cathodic peaks move to the lower and higher potentials, respectively. Even at a high scanning rate of 2.0 mV s^{-1}, the defined redox reaction peaks are still maintained, indicating good kinetics for lithium intercalation and de-intercalation.

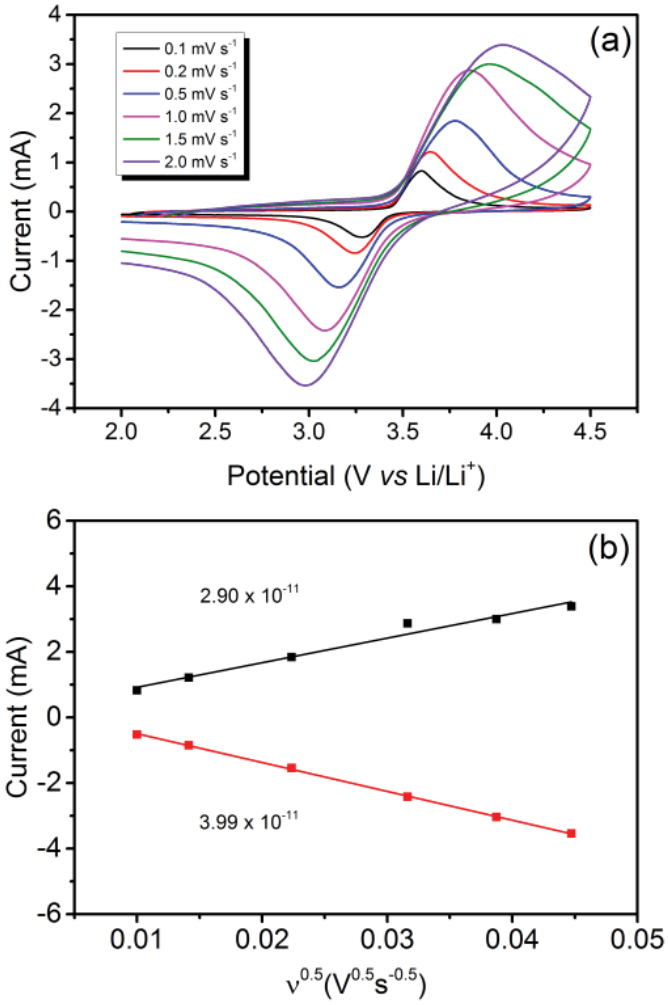

Figure 5-12. (a) CV profiles at different scan rates in the voltage range of 2.0 to 4.5 V and (b) peak current I_P versus square root of scan rate $v^{0.5}$ at room temperature of $LiFePO_4$@CP after 500 cycles.

According to the measured peak currents, a Li-ion diffusion coefficient D ($cm^2\ s^{-1}$) can be calculated using the Randles-Sevcik equation:[387, 390, 397]

$$I_p = 2.69 \cdot 10^5 \cdot A \cdot C \cdot \sqrt{D} \cdot n^{3/2} \cdot \sqrt{v} \qquad (5\text{-}6)$$

wherein I_p is the peak current (A), A is the surface area of the electrode, C is the concentration of Li-ions in a solid (0.0228 mol cm^{-3}), n is the number of electrons

involved in the half-reaction for the redox couple (n = 1 for Fe^{3+}/Fe^{2+} redox couple), and v is the potential scan rate (V s^{-1}). As shown in Figure 5-12b, I_p is proportional to $v^{1/2}$, confirming a diffusion-controlled behaviour. Moreover, from the slope of the lines, and based on equation (5-6), the diffusion coefficient $D_{cathodic}$ (positive) is $2.90 \cdot 10^{-11}$ cm^2 s^{-1}, and the diffusion coefficient D_{anodic} (negative) is $3.99 \cdot 10^{-11}$ cm^2 s^{-1}. These high Li-ion diffusion coefficients achieved by this material are related to the well maintained particle-particle contact of the $LiFePO_4$ collective, which enables rapid ion diffusion, and fast charge transfer kinetics through the carbon paper scaffold. The slight broadness of the peaks might be linked to the carbon coating generated by the glucose precursor, which has been reported to influence the shape of the redox peaks noticeably.[448]

The Nyquist plot displayed in Figure 5-13a compares the electrochemical impedance of fresh $LiFePO_4$@CP and cycled for 500 cycles. It can be seen that the material generates a depressed semicircle in the high frequency region and a slope in the low frequency region. Firstly, the high frequency intercept of the semicircle with the real axis (Z') refers to the uncompensated resistance (R_u), which combines particle-particle contact resistance, electrolyte resistance, and electrode-current collector resistance. Secondly, the semicircle diameter refers to the charge transfer resistance (R_{CT}), which is related to the electrochemical reactions at the electrode-electrolyte interface and the particle-particle contact. Lastly, the low frequency slope corresponds to the lithium-ion diffusion in the bulk of the electrode material and can be mathematically transformed to the Warburg coefficient (σ_w).

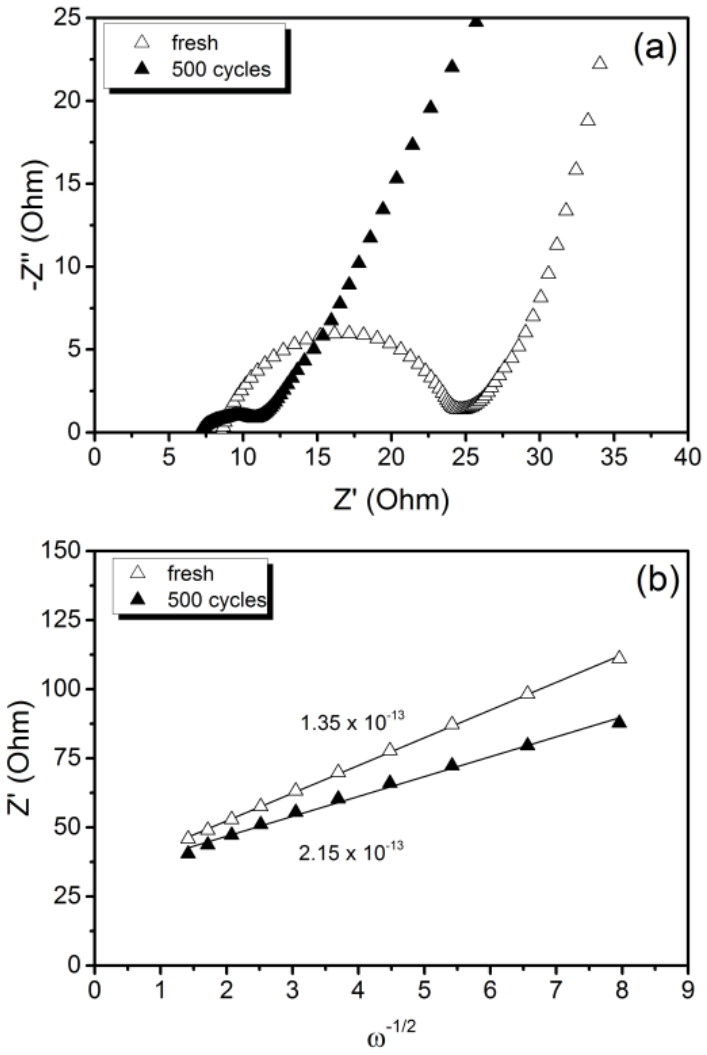

Figure 5-13. (a) Electrochemical impedance spectra and (b) linear fit of the Warburg impedance of a $LiFePO_4$@CP cell fresh and cycled for 500 cycles.

Consequently, the solid state diffusion of lithium-ions D_{Li} through the $LiFePO_4$ particle collective can be estimated using the following equation.[204, 389, 390, 393, 398]

$$D_{Li}=\frac{1}{2}\left(\frac{RT}{AF^2C\sigma_w}\right)^2 \quad (5\text{-}7)$$

wherein R is the gas constant, T the absolute temperature, F the Faraday constant, A the surface area of the $LiFePO_4$@CP cathode, C the molar concentration of

lithium-ions in the cathode, and σ_w the Warburg coefficient. It can be seen in the experimental data plot in Figure 5-13a that the charge transfer resistance (R_{CT}) of the fresh cell is 16.15 Ω, whilst the EIS analysis of the cycled half-cell reveals a reduction in charge transfer resistance. The value has decreased to 4.067 Ω, due to the aforementioned electrode activation processes during cycling. Overall, the measured charge transfer resistances are very low indicating excellent ionic and electronic transport along the electrode-electrolyte interface and strong particle-particle contact even after 500 high-rate deep (dis)charge cycles. Additionally, the solid-state diffusion D_{Li} calculated using equation (5-7) from the Warburg impedance (shown in Figure 5-13b) reflects the kinetic properties of the electrode, revealing a competitive lithium-ion diffusion rate of $1.35 \cdot 10^{-13}$ cm^2 s^{-1} for the fresh and $2.15 \cdot 10^{-13}$ cm^2 s^{-1} for the cycled cell measured from fully-lithiated $LiFePO_4$, respectively. Here again, a kinetic improvement is observed upon cycling due to the cell activation process.

5.4 Conclusions

In conclusion, a novel free-standing $LiFePO_4$@CP hybrid electrode has been developed, in which a shell of $LiFePO_4$ crystallites on interwoven carbon fibres is embedded in a conductive carbon network. In this novel architecture, the carbon fibre fabric serves as the current collector, whilst the carbon coating provides conducting pathways and structural support for the $LiFePO_4$ particle collective. This novel electrode design not only ensures close interparticle contact, but also high electronic conductivity for both mass and charge transfer. The $LiFePO_4$@CP hybrid electrode delivered high areal capacity and excellent cycling stability for 1000 cycles at a high current density. It has been shown that metallic current collectors, polymeric binders, and conducting additives can easily be substituted using commercial cellulose fibres and sugar, to generate a high performance

$LiFePO_4$@CP hybrid electrode, which could be used as the cathode in flexible lithium-ion batteries.

Chapter 6: 3D interconnected carbon fibre network-enabled ultra-long life $Na_3V_2(PO_4)_3$@carbon paper cathode for sodium-ion batteries

6.1 Introduction

Renewable energy production and energy storage have become the most essential technologies for the transition from fossil fuels to a sustainable energy supply. The key issue with most renewable energy sources is the deficiency between availability and demand due to uncontrollable natural occurrences, which generates unacceptable energy quality fluctuations within the electricity grid.[449] Large-scale energy storage systems are believed to be the solution to this problem by simply buffering this deficiency. Among various kinds of energy storage technologies, rechargeable batteries are considered a promising option for such large-scale storage requirements.[450, 451] The dominant rechargeable battery system today is the lithium-ion battery because it has been the power source of choice for portable and mobile applications for decades. However, with the increasing need for large-scale grid energy storage, low-cost sodium-ion batteries, which have a similar electrochemistry to lithium-ion batteries, are emerging as a more suitable technology due to the abundance and low cost of sodium.[451]

Among the cathode materials investigated for sodium-ion batteries, $Na_3V_2(PO_4)_3$ has attracted great interest since its first report in 2002[452] owing to the high sodium conductivity of its 3D (Na Superionic Conductor) NASICON-type framework,[9, 237] and high thermal stability and energy density.[453] Due to its poor electronic conductivity,[89, 454] providing electronically conducting networks is highly important for this type of material to be applicable in a real world application. An optimized solution for an electrode design featuring $Na_3V_2(PO_4)_3$ as the active material would be a continuous network of current collector and electrolyte, with an appropriate size of $Na_3V_2(PO_4)_3$ particles.[455, 456] The particle size needs to be

carefully designed for optimal chemical diffusion inside the particle (nanoparticle size scales are needed when a material is a poor conductor). In recently published reports, various kinds of carbon coatings are applied as a conducting network to improve electron transport[318, 319, 353, 356, 457-467] and this may be in the form of carbon nanotubes/nanofibers/nanorods[468-470] and/or graphene.[471-473] Very recently, 3D interconnected conducting network strategies, which utilize a combination of different carbons have been investigated[354, 456, 466, 474, 475] but only one publication on $Na_3V_2(PO_4)_3$ to date has explored the possibilities of a free-standing electrode design.[476]

We designed a unique free-standing, binder-free and metallic current collector-free $Na_3V_2(PO_4)_3$-carbon paper ($Na_3V_2(PO_4)_3$@CP) cathode for sodium-ion batteries. The simultaneous carbonization of microcrystalline cellulose fibre and *in situ* crystal growth of $Na_3V_2(PO_4)_3$ nanoparticles generates an innovative $Na_3V_2(PO_4)_3$-carbon paper hybrid electrode. This hybrid electrode consists of an interconnected 3D carbon fibre network (CFN), which enables fast electron transport and provides a porous structure for electrolyte diffusion. The $Na_3V_2(PO_4)_3$ nanoparticles decorated on the carbon fibre network facilitate fast ion diffusion over a large surface area. The innovative electrode design achieved high reversible capacity, exceptional cycle life over 30 000 cycles, and high rate capabilities. In a proof-of-concept experiment, we have also investigated the capabilities of this 3D carbon fibre network to function as the sole current collector of this electrode design, which extends the range of possible applications for free-standing electrodes in general.

6.2 Experimental Section

Preparation of $Na_3V_2(PO_4)_3$@CP Cathodes:

$Na_3V_2(PO_4)_3$@CP was prepared by a novel impregnation–carbonization technique. Commercial paper towel (PT) was used as a suitable carbon paper source owing

to its porous nature, structural integrity, and light weight. The PT was purified by soaking in 20 mL deionized water (DI) for 2 h. Subsequently, 4 mL concentrated hydrochloric acid was added to the solution and left for another 12 h. The purified PT was washed with DI water several times by vacuum filtration and dried overnight at 100 °C in a vacuum oven. The dried tissue was impregnated for 10 min to ensure thorough saturation with a solution containing 0.3 g VCl_3 (97%), 0.433 g $NaH_2PO_4 \cdot 2H_2O$, and 0.09 g D-glucose in 5 mL DI water. The saturated PT was subjected to freeze-drying overnight to obtain a homogenous loading of all precursors. The dried and preloaded PT was then transferred into a ceramic crucible and sintered at 350 °C for 5 h and 750 °C for 12 h under a H_2/Ar atmosphere. The carbon content was determined by acid removal of the $Na_3V_2(PO_4)_3$ component, which provides a weight difference between the dry $Na_3V_2(PO_4)_3$@CP electrode and the residual carbon paper after acid treatment. Using this method, the nominal carbon content of the as-prepared $Na_3V_2(PO_4)_3$@CP electrode was estimated to be 64 wt%.

Preparation of $Na_3V_2(PO_4)_3$@C Reference Materials:

A solution containing 0.3 g VCl_3 (97 %), 0.433 g $NaH_2PO_4 \cdot 2H_2O$ and 0.09 g D-glucose in 5 ml DI water was slowly converted into a gel using a water bath at 80 °C under constant mild stirring. The gel was dried under vacuum at 100 °C for 12 hours. The obtained dried gel was ground to fine powder, transferred into a ceramic crucible and sintered at 350 °C for 5 h and 750 °C for 12 h under H_2/Ar protection.

Structural and Physical Characterization:

Crystallographic measurements were conducted using a Bruker D8 Discovery X-ray diffractometer with CuKα radiation between 10° and 80°. Morphological analyses of the as-prepared materials were carried out by field-emission scanning

electron microscopy (Zeiss Supra 55VP). Elemental mapping was conducted on a Zeiss EVO MA 15 SEM equipped with energy-dispersive X-ray spectroscopy (EDX). The carbon fibre/$Na_3V_2(PO_4)_3$ particle interface was investigated by HRTEM (JEOL JEM-2011). SAED patterns were collected by a Gatan charge-coupled device camera in a digital format.

Electrode Preparation and Test Cell Assembly:

The as-prepared $Na_3V_2(PO_4)_3$@CP electrodes were used directly as working electrodes without further modification. The active material ($Na_3V_2(PO_4)_3$) mass load was 1.0 mg cm^{-2} with a total footprint area of 1.54 cm^2. Sodium metal was used as counter and reference electrode. The electrolyte consists of 1 M $NaClO_4$ in a mixture of ethylene carbonate (EC) and propylene carbonate (PC) (EC: PC = 1:1 volume ratio), in which 5 vol% fluoroethylene carbonate was added as the electrolyte additive. Approximately 140 µL electrolyte was used for each coin cell. The amount of liquid electrolyte uptake is calculated using the following equation:

$$\eta = \frac{W_t - W_o}{W_o} \cdot 100\% \qquad (6\text{-}1)$$

where η is the uptake of the liquid electrolyte, and W_o and W_t are the weight of the electrodes before and after absorption of the liquid electrolyte, respectively. The electrolyte uptake was calculated to be 200 wt%. As an attempt to prove the concept of carbon paper serving as the current collector, the cell assembly was modified using a small piece of aluminium foil and a purified piece of paper towel. In this proof-of-concept set-up the $Na_3V_2(PO_4)_3$@CP electrode was insulated from the stainless steel battery shell using a slightly bigger piece of purified paper towel. The battery shell was electronically connected to the $Na_3V_2(PO_4)_3$@CP electrode by folding a small piece of aluminium foil around the $Na_3V_2(PO_4)_3$@CP electrode and the insulating paper towel piece. All electrodes were stored and all standard

CR2032 type coin cells were assembled in an argon-filled glovebox (UniLab, MBRAUN).

Electrochemical Characterization:

Galvanostatic charge–discharge and cycling performance tests were performed in the voltage range of 2.5 – 3.8 V at various current densities on a Neware battery tester at room temperature. Cyclic voltammograms were obtained at different scanning rates of 0.1 – 2.0 mV s^{-1} between 2.0 and 4.0 V and EIS measurements were conducted over a frequency range from 100 kHz to 0.01 Hz using a CHI 660C Electrochemistry Workstation.

6.3 Results and Discussion

Sodium vanadium phosphate on carbon paper ($Na_3V_2(PO_4)_3$@CP) was prepared *via* a freeze-drying assisted impregnation–carbonization technique (Figure 6-1a) adapted from our previous reports.[441, 477] Purified commercial paper towel (PT) has been shown to be an excellent substrate for the growth of a variety of nanostructured electrochemically active materials in lithium-ion as well as in sodium-ion battery systems.[441, 477, 478] Its structural integrity, porosity of the fabric, and good electronic conductivity (postcarbonization) provide intriguing advantages over conventional metallic substrates, such as copper and aluminium foil. Furthermore, the freeze-drying assisted impregnation–carbonization methods can effectively restrict the particle growth on the cellulose fibre surface. First, rapid freezing of the impregnated paper towel induces immediate supersaturation by solidification of the aqueous solvent, and thus, fast recrystallization of NaH_2PO_4, which drastically limits the crystal growth of alkali metal phosphates.[479, 480]

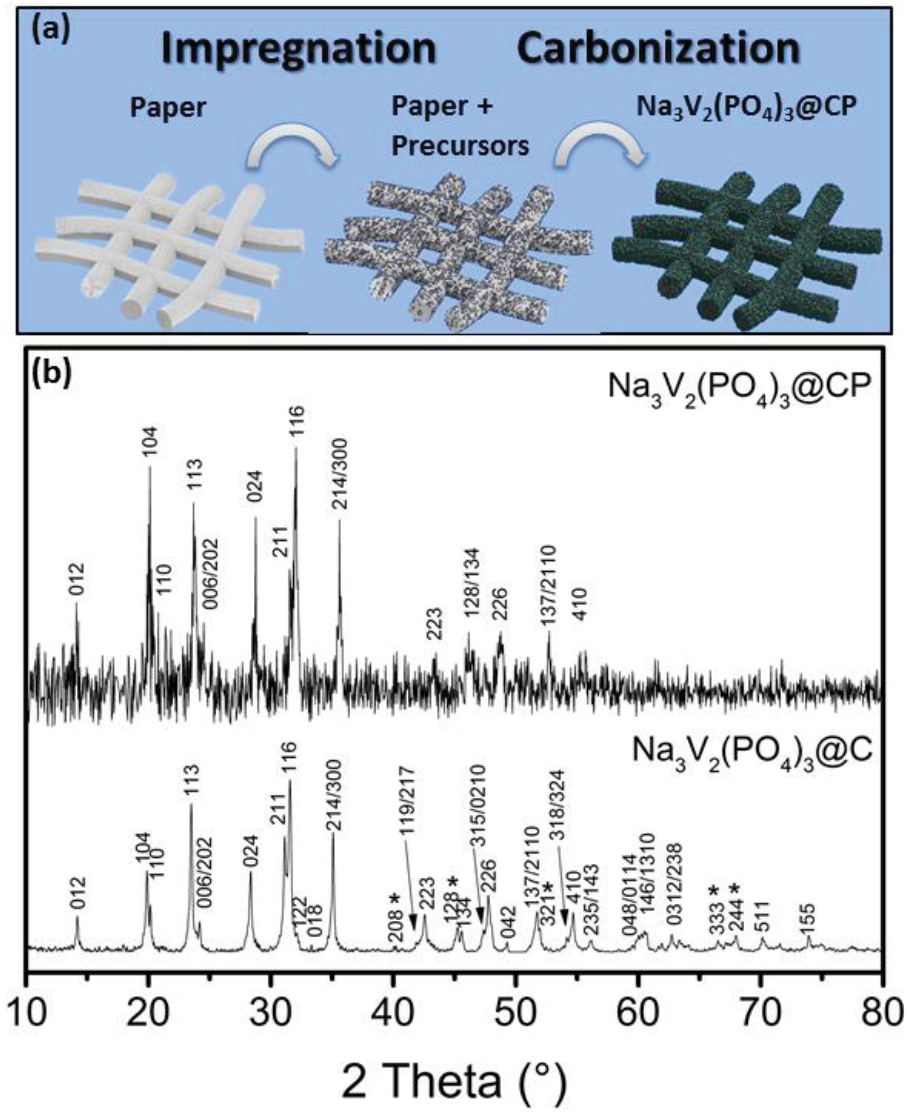

Figure 6-1. (a) Schematic illustration of the preparation procedure for $Na_3V_2(PO_4)_3$@CP. (b) XRD pattern of $Na_3V_2(PO_4)_3$@CP and carbon-coated $Na_3V_2(PO_4)_3$ ($Na_3V_2(PO_4)_3$@C) as reference sample (both resemble the standard pattern of JCPDS card number 62-0345).

Second, vanadium ions can form organometallic compounds with D-glucose, producing a homogenous glucose wrapping of the vanadium precursor salt upon solvent removal.[481, 482] After carbonization of the cellulose fibres and calcination of the $Na_3V_2(PO_4)_3$ nanoparticles on the fibre surfaces, the obtained free-standing

composite electrodes can be readily applied as cathodes in sodium-ion batteries. X-ray diffraction (XRD) patterns were collected from the as-prepared $Na_3V_2(PO_4)_3$@CP hybrid electrode and a carbon-coated $Na_3V_2(PO_4)_3$ sample, which was prepared *via* a sol-gel method using identical precursors (referred to as $Na_3V_2(PO_4)_3$@C). Both XRD patterns, as shown in Figure 6-1b, resemble the standard pattern of JCPD card number 62-0345, confirming the successful preparation of the $Na_3V_2(PO_4)_3$ nanocrystals. It is worth noting that the pattern collected from the carbon paper electrode only clearly reveals high intensity peaks of $Na_3V_2(PO_4)_3$ with very obvious background noise, and thus, most low intensity peaks are indistinguishable from the background. This is first due to the very small particle size of the $Na_3V_2(PO_4)_3$ crystals on the carbon paper surface compared to the relatively large particles generated by the sol-gel method (Figure 6-2a). Second, the amorphous carbon paper substrate has shown low signal-to-noise ratios in XRD scans before.[477] The bare carbon paper substrate exhibits an amorphous structure with no obvious peaks associated with graphitic carbon (Figure 6-2b). The slight irregularity observed below 20° can be ascribed to the low-background XRD sample holder used, and thus, be disregarded.

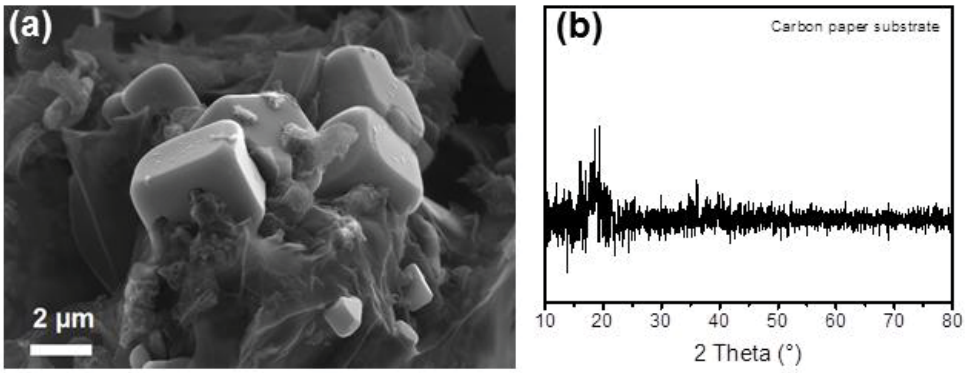

Figure 6-2. (a) SEM image of $Na_3V_2(PO_4)_3$@C prepared by a sol-gel method using identical precursor salts to $Na_3V_2(PO_4)_3$@CP; (b) XRD pattern of the carbon paper substrate.

The carbon paper substrate shows similar high noise/signal ratios as the $Na_3V_2(PO_4)_3$@CP pattern displayed in Figure 6-1b. Nevertheless, 14 clearly identifiable peaks are sufficient to confirm the successful preparation of the $Na_3V_2(PO_4)_3$ nanocrystals. Furthermore, energy-dispersive X-ray spectroscopy elemental mappings displayed in Figure 6-3 also confirm the uniform distribution of all five elements (Na, V, P, O, C) on a single fibre of the hybrid electrode. No obvious lumps or clusters of elements can be observed and no undesired precursor elements are present in these images. The morphology of the $Na_3V_2(PO_4)_3$ particles generated on the surface of carbon fibre was identified by scanning electron microscopy (SEM) and is presented in Figure 6-4a-c. As for the carbon substrate itself (Figure 6-4a), the carbonized cellulose maintains an interconnected network of micro sized fibres decorated with $Na_3V_2(PO_4)_3$ nanoparticles (Figure 6-4b). The nanoparticles resemble a spherical droplet-like morphology in the size range of around 30 nm up to 200 nm (Figure 6-4c), which is the result of the cooperative effect of D-glucose and optimized precursor solution concentration. In a trial of preparing $Na_3V_2(PO_4)_3$@CP without the addition of D-glucose it was found that the generated particle morphology was randomized and a uniform decoration of the carbon fibre surface could not be achieved (Figure 6-5a). It was also found that a 30% increase of precursor solution concentration caused aggregation, which results in the loss of individual spherical nanoparticles and the $Na_3V_2(PO_4)_3$ decoration effect shifts towards an incomplete thin film distribution (Figure 6-5b). Thus, an active material load increase requires further optimization to maintain the desired morphology. Transmission electron microscopy (TEM) images show the $Na_3V_2(PO_4)_3$ particles embedded in the carbon fibre in Figure 6-4d and the lattice orientation of one individual particle in Figure 6-4e. The lattice resolved TEM image from the square section marked in Figure 6-4e is shown in Figure 6-4h. From this image, the (012) crystal plane can be clearly seen.

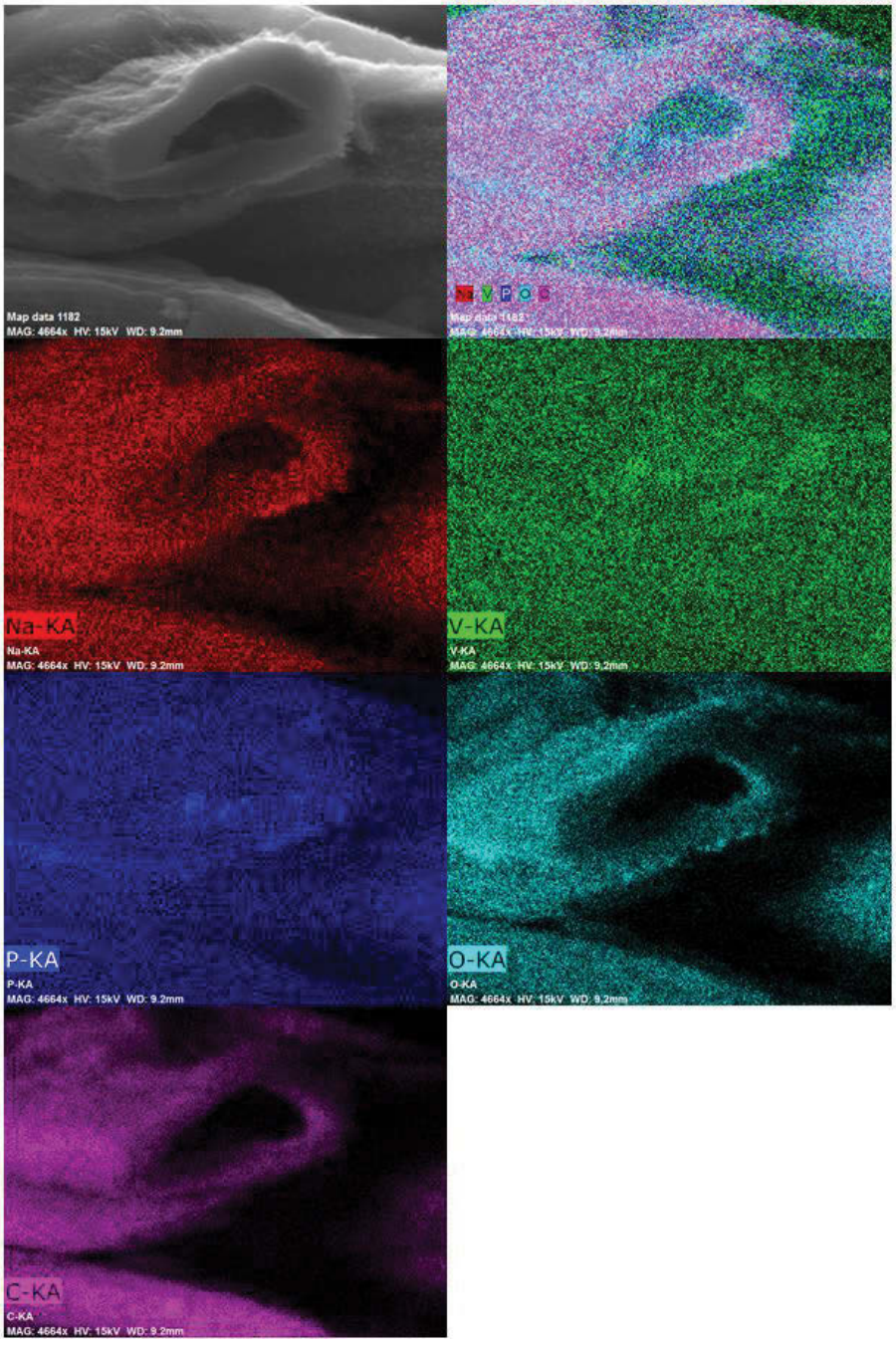

Figure 6-3. Energy-dispersive X-ray spectroscopy (EDS) elemental mapping showing the distribution on the elements sodium (Na), vanadium (V), phosphorus (P), oxygen (O) and carbon (C) of a selected area of a $Na_3V_2(PO_4)_3$@CP fibre.

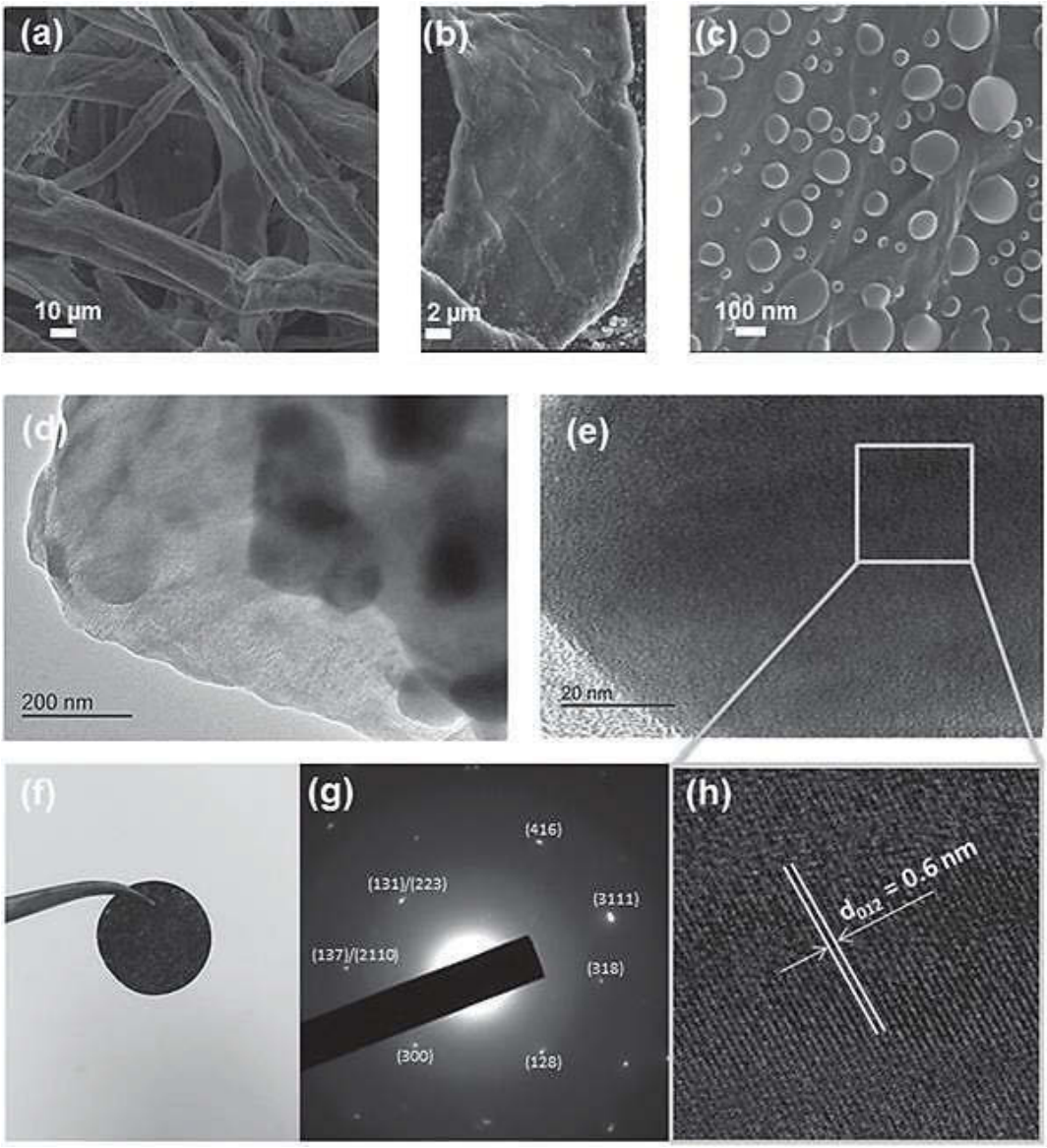

Figure 6-4. (a) Low magnification SEM view of the CFN. (b) Low magnification SEM image of a single carbon fibre decorated with $Na_3V_2(PO_4)_3$ nanoparticles. (c) High magnification SEM image of $Na_3V_2(PO_4)_3$ nanoparticles on the carbon fibre surface. (d) Low resolution TEM image of $Na_3V_2(PO_4)_3$@CP. (e) High resolution TEM image of $Na_3V_2(PO_4)_3$@CP. (f) Digital photograph of a $Na_3V_2(PO_4)_3$@CP electrode. (g) SAED pattern of $Na_3V_2(PO_4)_3$@CP. h) Lattice resolved TEM image including d-spacing along the (012) crystal plane enlarged from the section marked in image (e).

Clear lattice fringes with a d-spacing of 0.6 nm demonstrate high crystalline characteristics of the $Na_3V_2(PO_4)_3$ NASICON structure. Figure 6-4g displays the selected area electron diffraction (SAED) pattern obtained from the particle shown in Figure 6-4e and h. This SAED pattern exhibits a set of concentric rings with bright spots, which can be indexed as $Na_3V_2(PO_4)_3$ in consistency with the XRD result shown in Figure 6-1b. The as-prepared $Na_3V_2(PO_4)_3$@CP was directly used as a free-standing electrode in sodium-ion batteries (NIBs) without the usage of an additional current collector, binder, and conducting additives. The handling and flexibility of the electrode is demonstrated in Figure 6-4f. From Figure 6-4f it is evident that the as-prepared electrode can be easily processed using ordinary tweezers, which predicts good handling in a potential mass production scenario. The electrode can also sustain a reasonable degree of bend when gently held between two fingers (Figure 6-6). When the bending force on the disk was released, no collapse or cracking has taken place and the electrode can be readily used in an NIB.

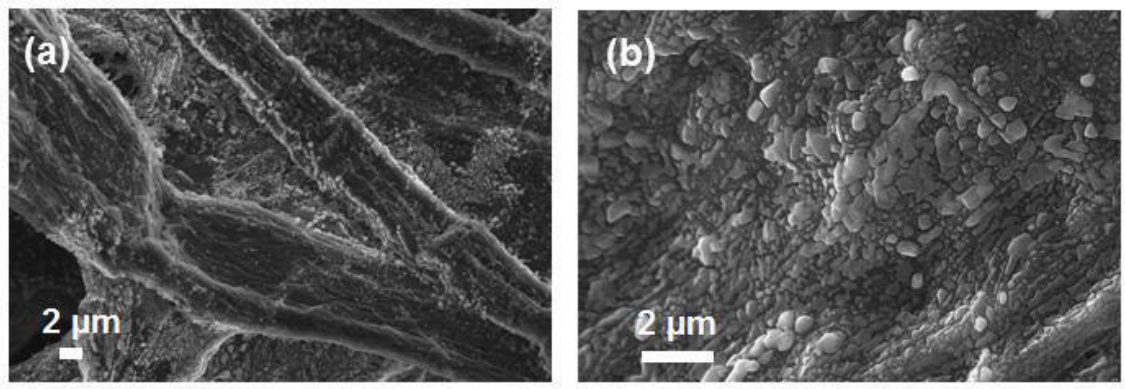

Figure 6-5. SEM images of $Na_3V_2(PO_4)_3$@CP materials prepared (a) without the addition of 30 wt% D-glucose to the precursor solution; and (b) with a 30 % higher concentration precursor solution.

Figure 6-6. Digital photograph of the $Na_3V_2(PO_4)_3$@CP hybrid electrode slightly bent to demonstrate its structural integrity under stress.

The electrochemical performances were evaluated in a series of different kinetic and stability tests. First, the galvanostatic charge–discharge profile of $Na_3V_2(PO_4)_3$@CP at a current density of 0.1 mA cm^{-2} is shown in Figure 6-7a. The cell exhibits the standard galvanostatic charge–discharge profile of $Na_3V_2(PO_4)_3$ in the voltage range of 2.5 – 3.8 V.[354, 456, 474] As can be seen, the obvious charging and discharging plateaus are observed at 3.40 and 3.30 V, respectively. Furthermore, the flat plateaus demonstrate that a reversible phase transformation between $Na_3V_2(PO_4)_3/NaV_2(PO_4)_3$ took place. The cycling performance of the as-prepared $Na_3V_2(PO_4)_3$@CP hybrid electrodes was evaluated in a combined rate performance and cycling stability test (shown in Figure 6-7b). The test sequence begins with a 30 cycle rate performance evaluation at altering current densities spanning from 0.1 to 2.5 mA cm^{-2}. The current density is then decreased back to 0.1 mA cm^{-2} to observe the capacity retention capabilities of the hybrid electrode. Directly after, a long-term cycling stability test at a current density of 2.5 mA cm^{-2} was conducted, which resulted in an overall cycle count of 30 530 cycles being attained as displayed in Figure 6-7b.

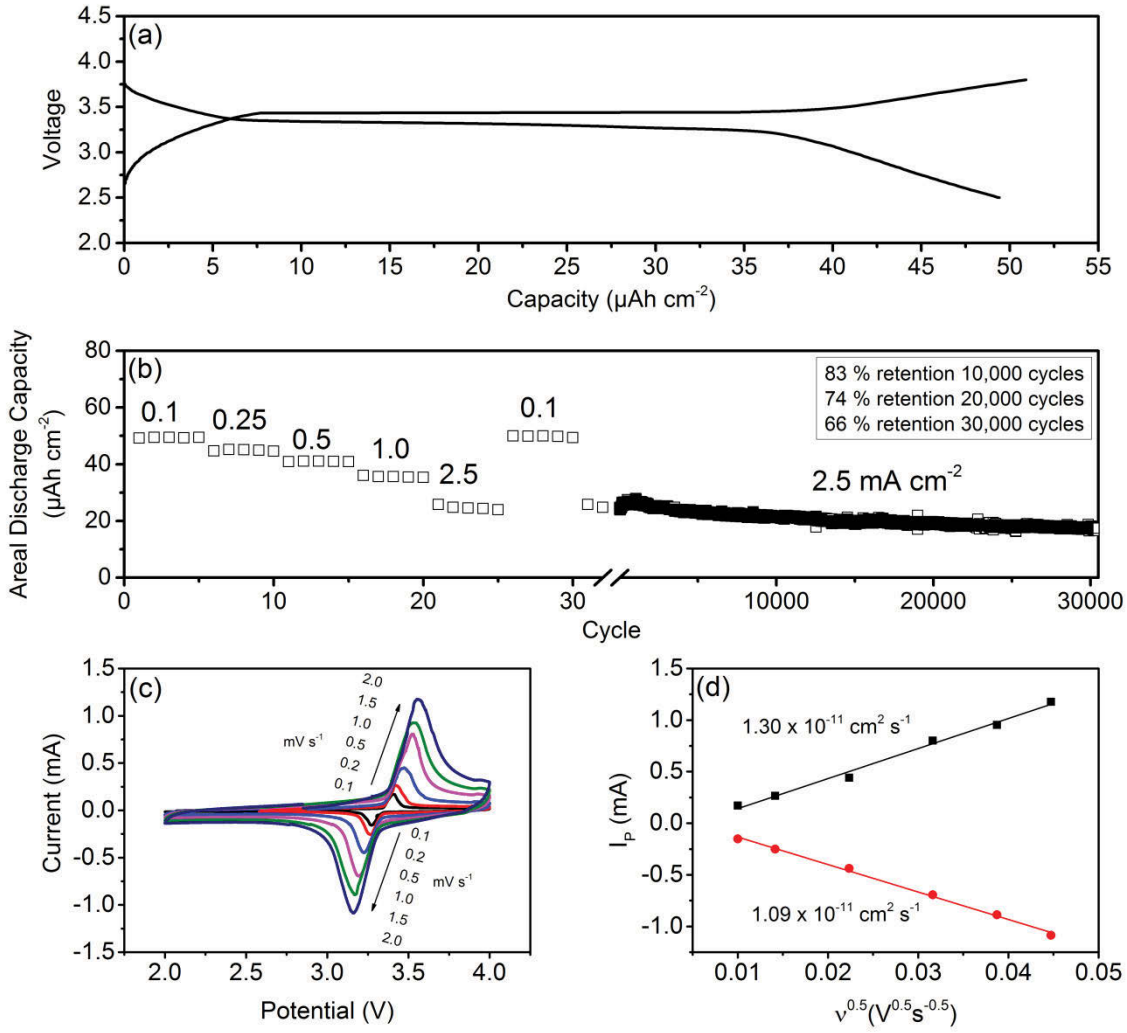

Figure 6-7. (a) Galvanostatic charge–discharge profile of $Na_3V_2(PO_4)_3$@CP at a current density of 0.1 mA cm^{-2} in the voltage range between 2.5 and 3.8 V. (b) Rate performance and cycling stability evaluation of $Na_3V_2(PO_4)_3$@CP at various current densities. (c) Cyclic voltammetry (CV) performance of $Na_3V_2(PO_4)_3$@CP at different scan rates in the voltage range between 2.0 and 4.0 V versus Na^+/Na. (d) Peak current I_P versus square root of scan rate $v^{0.5}$ at room temperature after 500 cycles with calculated ion diffusion coefficients D.

The novel $Na_3V_2(PO_4)_3$@CP hybrid electrode delivered a reversible areal capacity of 49, 45, 41, 35, and 24 μAh cm^{-2} when cycled at 0.1, 0.25, 0.5, 1.0, and 2.5 mA cm^{-2}, respectively. When the current density is returned from 2.5 to 0.1 mA cm^{-2} the

cell recovered to 50 μAh cm^{-2}. One of our experimental cells was then cycled at 2.5 mA cm^{-2} for several tens of thousands of cycles, which highlights the exceptional cycling stability of the hybrid material. The best test cell had successfully reached 30 530 full cycles when we discontinued the testing. The capacity retention (inset in Figure 6-7b) of this material was calculated every 10 000 cycles and revealed a capacity loss of around 10% per 10 000 successive deep charge–discharge cycles at a current density of 2.5 mA cm^{-2}. To the best of our knowledge, this is the highest capacity retention reported among all publications since 2002, and furthermore, only the second report on a free-standing paper-like electrode using intercalation type $Na_3V_2(PO_4)_3$. For the sake of completeness, the cycling performance of $Na_3V_2(PO_4)_3$@CP prepared using a 30% more concentrated precursor solution is shown in Figure 6-8. Figure 6-7c displays the cyclic voltammetric (CV) behaviour of $Na_3V_2(PO_4)_3$@CP at various scanning rates from 0.1 to 2.0 mV s^{-1} in the voltage range between 2.0 and 4.0 V versus Na^+/Na when the electrode was cycled for 500 cycles. In this voltage range a single pair of defined redox peaks can be observed at all scan rates, which corresponds to the V^{4+}/V^{3+} redox couple and is in good agreement with the charge and discharge voltage plateau positions displayed in Figure 6-7a.

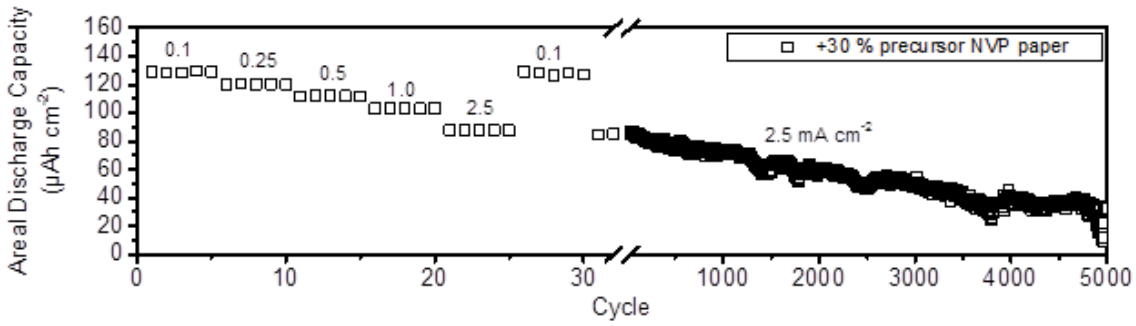

Figure 6-8. Cycling performance of the sample prepared with a 30% higher concentration precursor solution (~32 wt% carbon).

Furthermore, the height and area of the redox peaks increase with increasing scanning rate. The anodic and cathodic peaks move to lower and higher potentials, respectively. Even at a high scanning rate of 2.0 mV s^{-1}, the defined redox reaction peaks are still maintained, indicating good kinetics for sodium intercalation and de-intercalation. The electrode polarization slightly increases with increased scan rate (0.1 to 2.0 mV s^{-1}) from 0.13 to 0.40 V, respectively, which is one of the lowest values reported in recent publications.[354, 468, 476] According to the measured peak currents, a sodium ion diffusion coefficient D (cm^2 s^{-1}) can be calculated using the Randles–Sevcik equation:[462, 483, 484]

$$I_p = 2.69 \cdot 10^5 \, n^{3/2} \, A \, C \, \sqrt{D} \, \sqrt{v} \qquad (6\text{-}2)$$

wherein I_P is the peak current (A), A is the footprint area of the electrode, C is the concentration of sodium ions in a solid (0.0069 mol cm^{-3}), n is the number of electrons involved in the half-reaction for the redox couple (n = 2), and v is the potential scan rate (V s^{-1}). As shown in Figure 6-7d, I_P is proportional to $v^{0.5}$, which is indicative of a diffusion-controlled behaviour. From the slope of the lines calculated based on Equation (6-2) the diffusion coefficient D_{anodic} (positive) = 1.30 × 10^{-11} cm^2 s^{-1}, and the diffusion coefficient $D_{cathodic}$ (negative) = 1.09 × 10^{-11} cm^2 s^{-1} are determined.

The major advantage besides the ultralong cycle life of our $Na_3V_2(PO_4)_3$@CP hybrid electrode is that the carbon scaffold dispenses the need for polymeric binder and additional high-conductivity (metallic) current collectors. This material enables a great reduction in battery costs by simplifying battery packing processes and eliminating weight of electrochemically inactive materials, such as binder, conducting additives, and metallic current collector. In recent years, this concept has been partially implemented in both lithium-ion and sodium-ion battery systems at both anode[485-488] and cathode[488-490] side of the cells. However, most

laboratories use coin cells to conduct half-cell experiments, so the question remains whether the carbon substrate really acts as the current collector. The reason for this is the metallic casing of standard coin cells, which one might argue is in fact the current collector when in contact with electrodes inside. If our free-standing electrode example was applied in commercial 18 650 cylindrical batteries or even pouch cells, there might not be sufficient contact surface area for charge transport as the electrodes are not fully in contact with a conducting cell casing. To confirm or deny that our carbon paper, and not the battery casing, is functioning as the main current collector in CR2032 coin cells used for half-cell testing, we conducted a proof-of-concept experiment. As displayed Figure 6-9, we simulated the more realistic situation of the electrode not being in contact with a conductive cell casing by physically disconnecting the electrode from the cell using a slightly bigger piece of purified paper towel positioned between the two components. A folded small piece of aluminium foil serves as the only electrical connection between electrode and cell casing with the result that the electronically connected surface area of the $Na_3V_2(PO_4)_3$@CP electrode was reduced to around 0.2 cm^2 (10% of electrode footprint area).

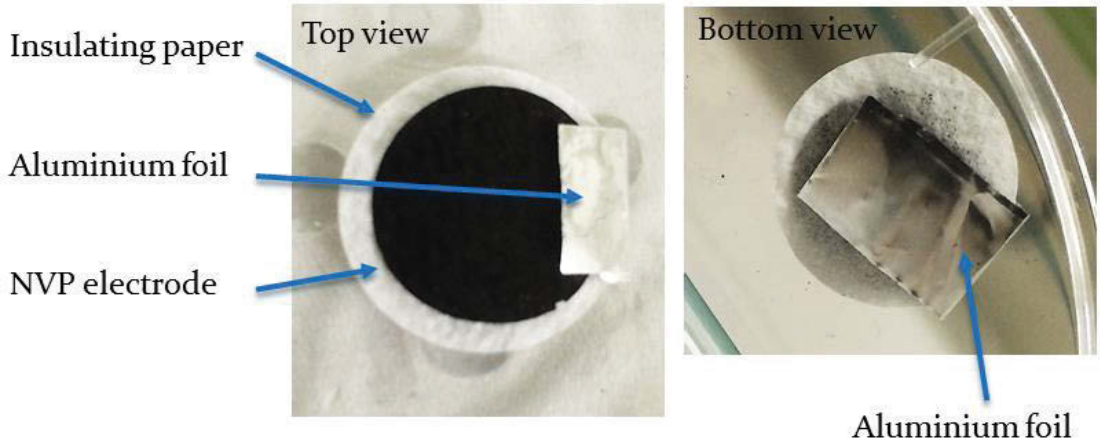

Figure 6-9. Digital image of the proof-of-concept set-up.

The proof-of-concept cell was otherwise identical to the normal cell as described in the Experimental Section 6.2 and both set-ups were electrochemically evaluated under the same cycling conditions (shown in Figure 6-10a). From this image, there is very little difference between the sole $Na_3V_2(PO_4)_3$@CP (□) and the insulated proof-of-concept (Δ) set-up. Initially, we see a capacity value at 0.1 mA cm^{-2} of 49.4 μAh cm^{-2} and 56.5 μAh cm^{-2} for the normal (□) and the proof-of-concept (Δ) set-up, respectively, which translates into a difference of around 14%.

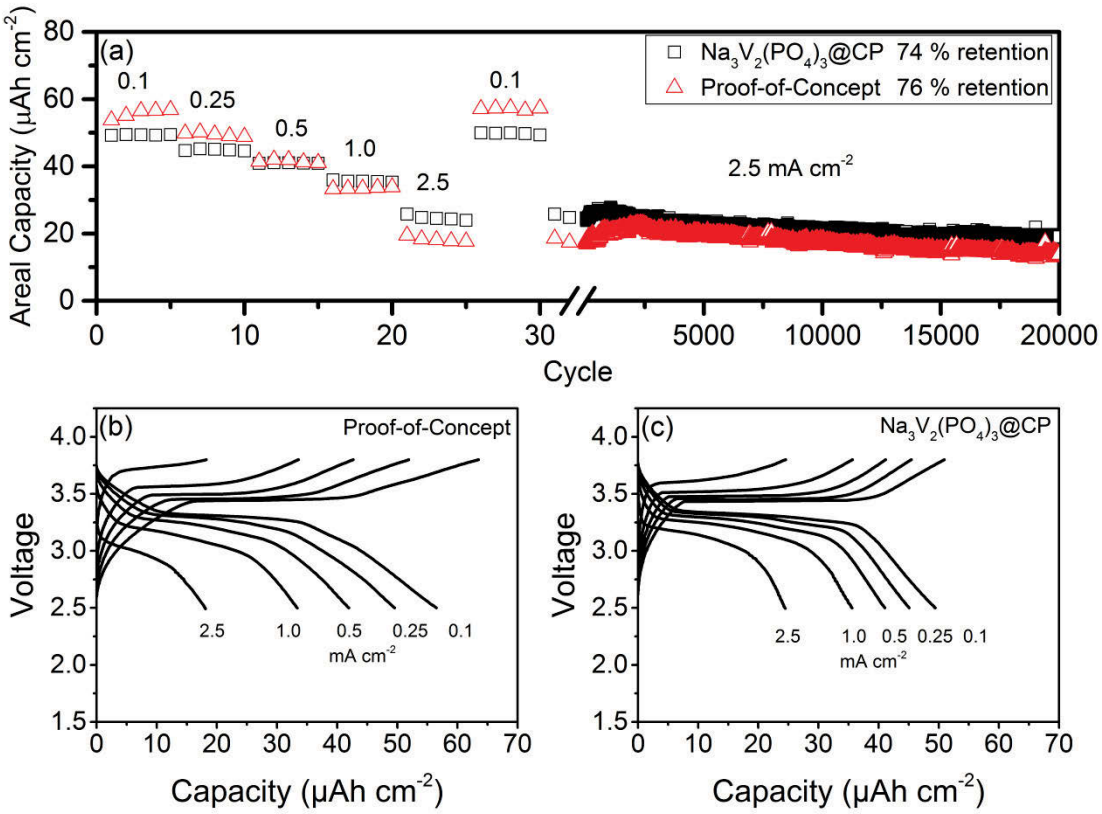

Figure 6-10. (a) Rate performance and cycling stability of $Na_3V_2(PO_4)_3$@CP and the modified proof-of-concept cell assembly with $Na_3V_2(PO_4)_3$@CP at various current densities; Galvanostatic charge–discharge profiles of $Na_3V_2(PO_4)_3$@CP at various current densities in the voltage range between 2.5 and 3.8 V. (b) The modified proof-of-concept cell assembly and (c) $Na_3V_2(PO_4)_3$@CP.

This difference in capacity decreased until a current density of 0.5 mA cm^{-2} was reached whereupon the capacity values difference increased again to a maximum of 26% at a current density of 2.5 mA cm^{-2}. Interestingly, the average difference in capacity between the two set-ups from 0.1 to 2.5 mA cm^{-2} only reaches a total of 1.5%. This means that the drastic surface area restriction of the electronically connected area of the $Na_3V_2(PO_4)_3$@CP electrode has almost no effect on its rate performance. An area reduction of 90% only results in a capacity reduction of around 26% at a current density of 2.5 cm^{-2}, which requires the highest electronic conductivity from the current collector. If the carbon paper substrate was not the main current collector in the proof-of-concept set-up, the observed capacity should be reduced directly proportional to the reduced footprint area electronically connected to the battery casing. Our experiment demonstrates that the capacity reduction was only around 26%, not 90%, which undoubtedly proves the concept that the carbon paper acts fully as a current collector. This also highlights the structural integrity of the $Na_3V_2(PO_4)_3$@CP electrode (shown in Figure 6-10a). The cycling stability test results reveal an almost identical capacity retention for the $Na_3V_2(PO_4)_3$@CP and the proof-of-concept set-up after 20 000 deep charge–discharge cycles at 2.5 mA cm^{-2}, respectively. If the electrode experienced severe cracking upon prolonged high current cycling, the reversible capacity should decline at a much higher rate, as only a small area of the electrode is directly connected to the battery casing. Our experiment proves that the $Na_3V_2(PO_4)_3$@CP electrodes maintain the conducting carbon fibre network as well as good particle contact upon long-term cycling with no rapid capacity degradation observed in the proof-of-concept battery set-up. To visualize the differences and similarities of both battery set-ups, galvanostatic charge–discharge profiles were plotted for every third full cycle at each tested current density. These profiles are displayed in Figure 6-10b-c, wherein Figure 6-10b shows the proof-of-concept cell and Figure 6-10c represents the normal $Na_3V_2(PO_4)_3$@CP cell without any modification. For both

experimental cells, the obvious charging and discharging plateaus are observed at 3.40 and 3.30 V, respectively, shifting with increased current densities. The most noticeable difference between the two battery set-ups is the electrode polarization, or in other words, the potential gap between charge and discharge voltage plateaus at each tested current density, which is likely caused by the small bridging piece of aluminium foil in the proof-of-concept set-up. By definition, electrode polarization is the result of an isolating barrier between electrode and electrolyte, which hinders electrochemical reactions.[491] In case of the proof-of-concept battery set-up, the aluminium foil is responsible for a slight blockage of 10% of the electrode's footprint area and simply replacing this foil with a porous mesh would likely result in indistinguishable profiles as it would improve the electrolyte accessibility to the electrode. Besides this polarization voltage gap, there is very little difference between both battery set-ups in terms of unusual plateaus or unstable charge curves indicating side reactions. This again proves that the $Na_3V_2(PO_4)_3$@CP electrode fulfils multiple functions as one single component in a coin cell battery set-up and potentially also in other commercial battery designs like pouch or cylindrical cells. It serves as the electrochemically active material responsible for capacity, as the structural support ensuring mechanical integrity, and as the sole electronic conductor enabling fast charge transport, which ultimately could make rechargeable sodium-ion batteries lighter, cheaper, and more reliable.

The Nyquist plots in Figure 6-11a,b compare the electrochemical impedance of $Na_3V_2(PO_4)_3$@CP in the normal and the proof-of-concept set-up both freshly constructed and cycled for 20 000 cycles, respectively. It can be seen that both cells show a depressed semicircle in the high frequency region and have a slope in the low frequency region exactly as reported in several previous publications.[347, 472, 473, 475]

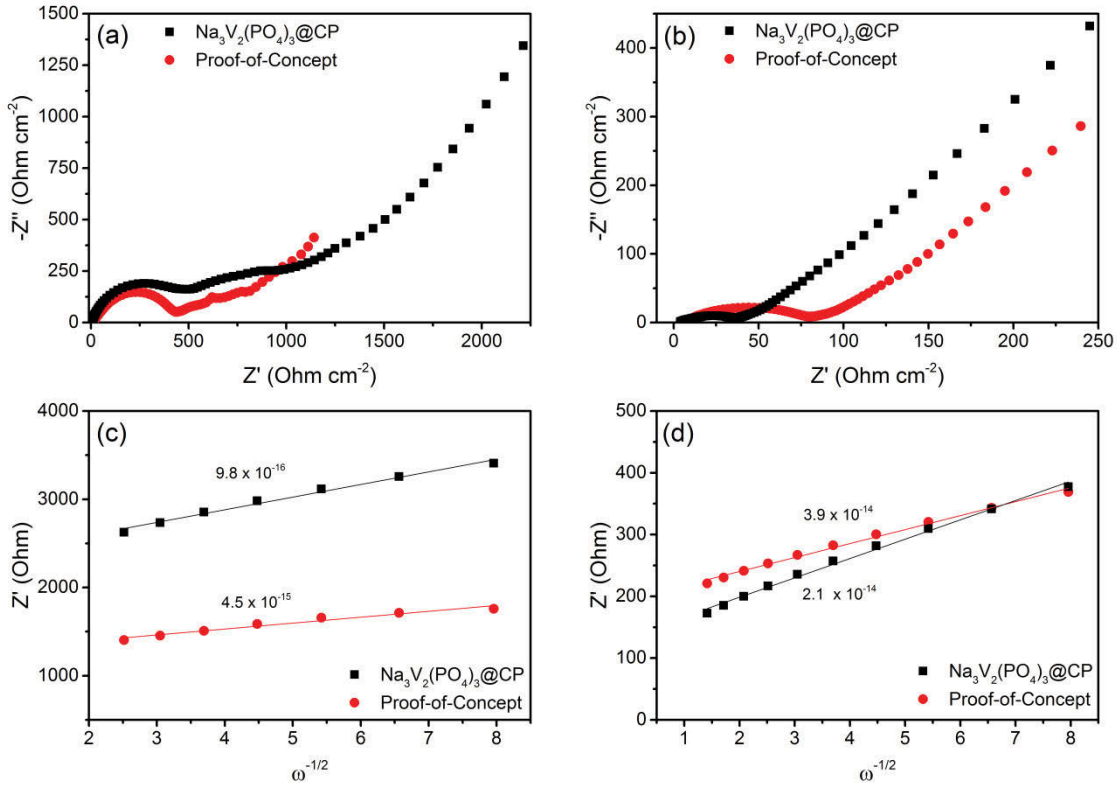

Figure 6-11. Electrochemical impedance spectra of $Na_3V_2(PO_4)_3$@CP and the modified proof-of-concept cell assembly of $Na_3V_2(PO_4)_3$@CP (a) uncycled coin cells; (b) cycled coin cells (cycled for 500 cycles). Corresponding linear fits of the Warburg impedance and the calculated solid-state diffusion coefficient D_{Na} (c) uncycled coin cells; (d) cycled coin cells (cycled for 500 cycles).

First, the high frequency intercept of the semicircle with the real axis (Z') refers to the so called uncompensated resistance (R_u), which is a combination of particle–particle contact resistance, electrolyte resistance, and electrode-current collector resistance. Second, the semicircle diameter represents the charge transfer resistance (R_{CT}), which is associated with the electrochemical reactions at the electrode–electrolyte interface and the particle–particle contact. Lastly, the low frequency slope relates to the sodium-ion diffusion in the bulk active material and can be mathematically transformed to the Warburg coefficient (σ_w).

Accordingly, the solid-state diffusion of sodium ions D_{Na} through the $Na_3V_2(PO_4)_3$ particles can be estimated using the following equations:[466, 492-497]

$$D_{Na} = \frac{1}{2}\left(\frac{RT}{AF^2n^2C\sigma_w}\right)^2 \quad (6\text{-}3)$$

$$Z' = R_u + R_{CT} + \sigma_w\sqrt{\omega} \quad (6\text{-}4)$$

wherein R is the gas constant, T is the absolute temperature, F is the Faraday constant, A is the footprint area of the $Na_3V_2(PO_4)_3$@CP electrode, n is the number of electrons involved in the half-reaction for the redox couple (n = 2), C is the molar concentration of sodium ions in a solid and σ_w is the Warburg coefficient. Electrochemical impedance spectroscopy (EIS) is thus an excellent tool to evaluate transport kinetics inside the $Na_3V_2(PO_4)_3$ nanoparticles independently from the charge transfer kinetics of the current collector. From the experimental data plots in Figure 6-11a, we found that the charge transfer resistances (R_{CT}) of the fresh cells are almost identical, around 490 and 440 Ω for the normal and the proof-of-concept set-up, respectively. Most reports observe an increase in R_{CT} upon long term cycling, which appears to be normal for a traditional active material pasted onto a metallic current collector.[462, 466, 470] Both our tested cells experience an R_{CT} reduction during cycling as displayed in Figure 6-11b, likely caused by an electrode activation process previously observed in carbon paper electrodes tested under similar conditions.[477] The values decreased to 38 and 80 Ω for the normal and the proof-of-concept set-up, respectively. The difference between the two set-ups is likely due to the aforementioned insulation of parts of the proof-of-concept electrode by the aluminium foil piece and can thus be classified as insignificant. Overall, the measured charge transfer resistances indicate excellent ionic and electronic transport along the electrode–electrolyte interface even after 500 high-rate deep charge/discharge cycles. Additionally, the solid-state diffusion D_{Na} calculated using Equations (6-3) and (6-4) from the Warburg impedance reflects

the kinetic properties of the active material as displayed in Figure 6-11c,d. The diffusion coefficients for the fresh cells are 9.8×10^{-16} and 4.5×10^{-15} cm^2 s^{-1}, which increase an order of magnitude to 2.1×10^{-14} and 3.9×10^{-14} cm^2 s^{-1} after cycling for the normal and the proof-of-concept set-up, respectively. Here again, a kinetic improvement upon cycling is likely due to the electrode and material activation process. The very small difference in sodium ion diffusion coefficient between the two cell set-ups after cycling suggests that performance differences only originate from the insulated area covered by the aluminium foil and not from the electrode itself.

6.4 Conclusions

In conclusion, we have successfully demonstrated excellent cycling performance of a novel, free-standing $Na_3V_2(PO_4)_3$@CP hybrid electrode in a sodium-ion battery system. It was shown that $Na_3V_2(PO_4)_3$ nanoparticles decorated on 3D interconnected conducting carbon fibres can achieve outstanding long-term cycling stability (more than 30 000 cycles) without the need of any conducting additives, polymeric binders, or additional current collectors. By using a simple proof-of-concept battery assembly, we have demonstrated the ease and efficiency of the stand-alone carbon paper electrode design, which leads the way toward imminent consideration of alternative free-standing electrode designs in various battery architectures.

Chapter 7: Conclusions and Future Perspective

7.1 Conclusions

7.1.1 Carbon-coated LiFePO4 cathode materials for lithium-ion batteries

Highly graphitic carbon-coated $LiFePO_4$ cathode materials are successfully prepared through industrial ball milling and solid-state reaction by using soluble starch as a carbon source and only environmentally friendly iron, lithium, and phosphate precursors. This method can generate uniform, sp^2-coordinated carbon-coated, grape-like nanoparticles, which are favourable for Li^+ transport and tap density. It has been shown that, even though Fe_2P phases in combination with a high-quality carbon network are beneficial to improve high-rate performance and stability, the capacity reduction at low rates induced by the high carbon content and the Fe_2P phase is disproportionate to justify adding more than 10 wt% carbon to the pre-sintered precursor. Furthermore, adding less than 10 wt% soluble starch as the carbon source results in high capacities at very low current rates, but fails to deliver considerable capacities at high rates, owing to a lack of a highly sp^2-coordinated carbon network to support ion diffusion through the particle collective. Ultimately, adding 10 wt% soluble starch as the carbon source combined with environmentally friendly iron, lithium, and phosphate precursor materials is a suitable and efficient approach to generate large amounts of high-performance and high-power $LiFePO_4$/C cathode materials.

The spray-drying method has been successfully applied to prepare high performance carbon-coated $LiFePO_4$ materials. The optimisation trial has identified the most suitable process conditions for the precursor materials and spray-dryer model used to prepare pure and practical $LiFePO_4$ cathode materials in a large scale. It was found that an inlet temperature of 170 °C, a feed rate of 15 ml min^{-1}, and a suspension concentration of 20 wt% are both practical and efficient

parameter settings for the preparation of $LiFePO_4$ cathode materials. In the subsequent morphology optimisation trial the impact of different additives on particle morphology of the final product was also investigated. In this trial, it was found that the addition of polyvinyl alcohol (PVA) generates micron-sized donut shaped particle clusters that provide a high tap density product without sacrificing electrochemical performance. The $LiFePO_4$ cathode material prepared with the addition of PVA achieved remarkable rate performance results and could maintain a capacity of 113.95 mA h g^{-1} at 10C. Further experimental work has to be conducted in regards to further reducing the nominal carbon content of the final product, the quality of the carbon coating, and cycling stability of the composite to fully evaluate to advantages of a spray-drying process integration into the large scale production of $LiFePO_4$.

7.1.2 Free-standing phosphate-based cathode materials for lithium-ion and sodium-ion batteries

A novel free-standing $LiFePO_4$@CP hybrid electrode has been developed, in which a shell of $LiFePO_4$ crystallites on interwoven carbon fibres is embedded in a conductive carbon network. In this novel architecture, the carbon fibre fabric serves as the current collector, whilst the carbon coating provides conducting pathways and structural support for the $LiFePO_4$ particle collective. This novel electrode design not only ensures close interparticle contact, but also high electronic conductivity for both mass and charge transfer. The $LiFePO_4$@CP hybrid electrode delivered high areal capacity and excellent cycling stability for 1000 cycles at a high current density. It has been shown that metallic current collectors, polymeric binders, and conducting additives can easily be substituted using commercial cellulose fibres and sugar, to generate a high performance $LiFePO_4$@CP hybrid electrode, which could be used as the cathode in flexible lithium-ion batteries.

Excellent cycling performance of a novel, free-standing $Na_3V_2(PO_4)_3$@CP hybrid electrode in a sodium-ion battery system has been successfully demonstrated. It was shown that $Na_3V_2(PO_4)_3$ nanoparticles decorated on 3D interconnected conducting carbon fibres can achieve outstanding long-term cycling stability (more than 30 000 cycles) without the need of any conducting additives, polymeric binders, or additional current collectors. By using a simple proof-of-concept battery assembly, we have demonstrated the ease and efficiency of the stand-alone carbon paper electrode design, which leads the way toward imminent consideration of alternative free-standing electrode designs in various battery architectures.

7.2 Future Perspective

This research project has shown the importance of the quality of carbon coatings applied to $LiFePO_4$ cathode materials. Using Raman spectroscopy, a correlation between hybridization of the carbon coating, carbon content, and electrochemical performance of carbon-coated $LiFePO_4$ was established. This could be a useful tool to evaluate the potential electrochemical performance of any other type of carbon-coated active material to better identify optimal material compositions without the need of a full electrochemical characterization. Importantly, only industry-ready and scalable preparation methods have been applied to prepare the cathode material. However, the mechanism behind the formation of highly graphitic carbon coatings depending on the amount of added carbon precursor remains unclear and requires further experimental and theoretical investigations.

By integrating the spray-drying method into the solid-state preparation process of carbon-coated $LiFePO_4$, high tap-density (micron-sized) particle clusters of different morphologies can be created, which is particularly interesting for the commercial fabrication of this cathode material. This method is not widely

implemented in the battery industry, although large-scale production facilities exist in food manufacturing and pharmaceutical production. A full integration of the spray-drying method could lead to performance improvements in commercial $LiFePO_4$ cathode materials as it enables control over secondary particles size and shape without sacrificing the benefits of the primary particle size reduction induced by the incorporation of a carbon source in the solid-state reaction.

A free-standing electrode design using widely available microcrystalline cellulose and an aqueous solution based approach to combined active material precursors with the cellulose substrate has been shown to be effective in both $LiFePO_4$ and $Na_3V_2(PO_4)_3$ cathode materials. While the process requires further optimization in terms of materials loading, resulting particle morphology, and substrate flexibility, the general concept of the *in situ* formation of the active material and its current collector has been proven. The high solubility of the phosphate and transition metal precursors allows for a homogenous distribution across the highly absorptive surface of the cellulose substrate, which is crucial for the success of the subsequent solid-state reaction. The implementation of this electrode preparation technique could assist in simplifying the industrial production process of battery electrodes as well as significantly reduce the manufacturing cost of both lithium-ion and sodium-ion batteries.

APPENDIX: NOMENCLATURE

Abbreviations/Symbols	Full name
a.u.	Arbitrary unit
Ar	Argon
BET	Brunauer-Emmett-Teller
BJH	Barrett-Joyner-Halenda
CB	Carbon Black
CNT	Carbon Nanotube
CV	Cyclic Voltammetry
C-rate	Current Rate

DI	De-ionized
EC	Ethylene Carbonate
EIS	Electrochemical Impedance Spectroscopy
EVs	Electric Vehicles
FESEM	Field-Emission Scanning Electron Microscopy
g	Gram
h	Hour
Hz	Hertz
I	Intensity
HEVs	Hybrid Electric Vehicles

HRTEM	High-Resolution Transmission Electronic Microscopy
JCPDS	Joint Committee on Powder Diffraction Standards
Li	Lithium
LIBs	Lithium-Ion Batteries
M	Molar Concentration
mA h g^{-1}	Milliampere Hour per Gram
min	Minute
mm	Millimetre
nm	Nanometre
NMP	1-methyl-2-pyrrolidinone

PC	Propylene Carbonate
PVDF	Poly(Vinylidene Difluoride)
R_{ct}	Charge Transfer Resistance
R_{Ω}	Ohmic Resistance
SAED	Selected Area Electron Diffraction
SEI	Solid Electrolyte Interface
SEM	Scanning Electron Microscopy
SIBs	Sodium-Ion Batteries
TEM	Transmission Electron Microscopy
TGA	Thermogravimetric Analysis
XRD	X-ray Diffraction

°	Degree
Ω	Ohm
°C	Degree Celsius
Z_w (σ_w)	Warburg Impedance

REFERENCES

[1] ABC News, *SA heatwave forces blackouts to cope with electricity demand, angering Government*, http://www.abc.net.au/news/2017-02-08/sa-heatwave-forces-rolling-blackouts-angering-government/8252512, 09.02.2017.

[2] B. Dunn, H. Kamath, J.-M. Tarascon, *Science* **2011**, *334*, 928-935.

[3] Woodbank Communications Ltd, Chester (UK), *Grid Scale Energy Storage Systems*, http://www.mpoweruk.com/grid_storage.htm, 18.07.2017.

[4] *World Energy Resources E-Storage*, **2016** World Energy Council, London, UK.

[5] M. Aneke, M. Wang, *Applied Energy* **2016**, *179*, 350-377.

[6] C. Masquelier, L. Croguennec, *Chem Rev* **2013**, *113*, 6552-6591.

[7] A. K. Padhi, K. S. Nanjundaswamy, J. B. Goodenough, *J Electrochem Soc* **1997**, 1180-1194.

[8] A. K. Padhi, K. S. Nanjunclaswamy, C. Masquelier, S. Okada, J. B. Goodenough, *J Electrochem Soc* **1997**, *5*, 1609-1613.

[9] C. Masquelier, A. Padhi, K. Nanjundaswamy, J. Goodenough, *J Solid State Chem* **1998**, *135*, 228-234.

[10] W. Xu, J. Wang, F. Ding, X. Chen, E. Nasybulin, Y. Zhang, J.-G. Zhang, *Energy Environ Sci* **2014**, *7*, 513-537.

[11] H. Kim, G. Jeong, Y.-U. Kim, J.-H. Kim, C.-M. Park, H.-J. Sohn, *Chem Soc Rev* **2013**, *42*, 9011-9034.

[12] Y. Liu, D. Lin, Z. Liang, J. Zhao, K. Yan, Y. Cui, *Nat Commun* **2016**, *7*.

[13] T. Nagaura, K. Tozawa, *Prog Batteries Solar Cells* **1990**, *9*, 209-217.

[14] Andrew Stock, Petra Stock, V. Sahajwalla, *Powerful Potential: Battery Storage for Renewable Energy and Electric Cars*, **2015** Climate Council of Australia Ltd.

[15] P. Roy, S. K. Srivastava, *J Mater Chem A* **2015**, *3*, 2454-2484.

[16] D. Liu, G. Cao, *Energy Environ Sci* **2010**, *3*, 1218-1237.

[17] N. Nitta, F. Wu, J. T. Lee, G. Yushin, *Mater Today* **2015**, *18*, 252-264.

[18] P. Poizot, S. Laruelle, S. Grugeon, L. Dupont, J. Tarascon, *Nature* **2000**, *407*, 496-499.

[19] J. Cabana, L. Monconduit, D. Larcher, M. R. Palacin, *Adv Mater* **2010**, *22*.

[20] N. Godshall, I. Raistrick, R. Huggins, *Mater Res Bull* **1980**, *15*, 561-570.

[21] M. Reddy, G. Subba Rao, B. Chowdari, *Chem Rev* **2013**, *113*, 5364-5457.

[22] D. Larcher, G. Sudant, J. Leriche, Y. Chabre, J. Tarascon, *J Electrochem Soc* **2002**, *149*, A234-A241.

[23] X. W. Lou, D. Deng, J. Y. Lee, J. Feng, L. A. Archer, *Adv Mater* **2008**, *20*, 258-262.

[24] B. Guo, C. Li, Z.-Y. Yuan, *J Phys Chem C* **2010**, *114*, 12805-12817.

[25] H. Guan, X. Wang, H. Li, C. Zhi, T. Zhai, Y. Bando, D. Golberg, *Chem Commun* **2012**, *48*, 4878-4880.

[26] J. C. Park, J. Kim, H. Kwon, H. Song, *Adv Mater* **2009**, *21*, 803-807.

[27] S. Bijani, M. Gabas, G. Subias, J. Garcia, L. Sanchez, J. Morales, L. Martinez, J. Ramos-Barrado, *J Mater Chem* **2011**, *21*, 5368-5377.

[28] F. Lin, D. Nordlund, T. C. Weng, Y. Zhu, C. Ban, R. M. Richards, H. L. Xin, *Nat Commun* **2014**, *5*, 3358.

[29] M. F. Hassan, Z. Guo, Z. Chen, H. Liu, *J Power Sources* **2010**, *195*, 2372-2376.

[30] P. Meduri, E. Clark, J. H. Kim, E. Dayalan, G. U. Sumanasekera, M. K. Sunkara, *Nano Lett* **2012**, *12*, 1784-1788.

[31] A. Kushima, X. H. Liu, G. Zhu, Z. L. Wang, J. Y. Huang, J. Li, *Nano Lett* **2011**, *11*, 4535-4541.

[32] P. Balaya, H. Li, L. Kienle, J. Maier, *Adv Funct Mater* **2003**, *13*, 621-625.

[33] K. E. Gregorczyk, Y. Liu, J. P. Sullivan, G. W. Rubloff, *ACS Nano* **2013**, *7*, 6354-6360.

[34] Y. Y. Hu, Z. Liu, K. W. Nam, O. J. Borkiewicz, J. Cheng, X. Hua, M. T. Dunstan, X. Yu, K. M. Wiaderek, L. S. Du, K. W. Chapman, P. J. Chupas, X. Q. Yang, C. P. Grey, *Nat Mater* **2013**, *12*, 1130-1136.

[35] J. Hu, H. Li, X. Huang, *Electrochem Solid-State Lett* **2005**, *8*, A66-A69.

[36] J. Hu, H. Li, X. Huang, L. Chen, *Solid State Ion* **2006**, *177*, 2791-2799.

[37] S. Yoon, C. Jo, S. Y. Noh, C. W. Lee, J. H. Song, J. Lee, *Phys Chem Chem Phys* **2011**, *13*, 11060-11066.

[38] M. Sasidharan, N. Gunawardhana, M. Yoshio, K. Nakashima, *Nano Energy* **2012**, *1*, 503-508.

[39] D.-M. Kim, S.-J. Kim, Y.-W. Lee, D.-H. Kwak, H.-C. Park, M.-C. Kim, B.-M. Hwang, S. Lee, J.-H. Choi, S. Hong, *Electrochim Acta* **2015**, *163*, 132-139.

[40] S. H. Yu, S. H. Lee, D. J. Lee, Y. E. Sung, T. Hyeon, *Small* **2016**, *12*, 2146-2172.

[41] N. Nitta, G. Yushin, *Part Part Syst Char* **2014**, *31*, 317-336.

[42] A. S. Arico, P. Bruce, B. Scrosati, J. M. Tarascon, W. van Schalkwijk, *Nat Mater* **2005**, *4*, 366-377.

[43] P. G. Bruce, B. Scrosati, J. M. Tarascon, *Angew Chem Int Ed Engl* **2008**, *47*, 2930-2946.

[44] R. Mukherjee, R. Krishnan, T.-M. Lu, N. Koratkar, *Nano Energy* **2012**, *1*, 518-533.

[45] X. Jia, C. Yan, Z. Chen, R. Wang, Q. Zhang, L. Guo, F. Wei, Y. Lu, *Chem Commun* **2011**, *47*, 9669-9671.

[46] N. Pereira, L. Dupont, J. Tarascon, L. Klein, G. Amatucci, *J Electrochem Soc* **2003**, *150*, A1273-A1280.

[47] Z.-W. Fu, Y. Wang, X.-L. Yue, S.-L. Zhao, Q.-Z. Qin, *J Phys Chem B* **2004**, *108*, 2236-2244.

[48] B. Das, M. Reddy, P. Malar, T. Osipowicz, G. S. Rao, B. Chowdari, *Solid State Ion* **2009**, *180*, 1061-1068.

[49] S. W. Kim, D. H. Seo, H. Gwon, J. Kim, K. Kang, *Adv Mater* **2010**, *22*, 5260-5264.

[50] F. Wang, R. Robert, N. A. Chernova, N. Pereira, F. Omenya, F. Badway, X. Hua, M. Ruotolo, R. Zhang, L. Wu, V. Volkov, D. Su, B. Key, M. S. Whittingham, C. P. Grey, G. G. Amatucci, Y. Zhu, J. Graetz, *J Am Chem Soc* **2011**, *133*, 18828-18836.

[51] T.-J. Kim, C. Kim, D. Son, M. Choi, B. Park, *J Power Sources* **2007**, *167*, 529-535.

[52] K. Chang, W. Chen, *ACS Nano* **2011**, *5*, 4720-4728.

[53] Q. Wang, L. Jiao, Y. Han, H. Du, W. Peng, Q. Huan, D. Song, Y. Si, Y. Wang, H. Yuan, *J Phys Chem C* **2011**, *115*, 8300-8304.

[54] N. Mahmood, C. Zhang, Y. Hou, *Small* **2013**, *9*, 1321-1328.

[55] F. Gillot, S. Boyanov, L. Dupont, M. L. Doublet, M. Morcrette, L. Monconduit, J. M. Tarascon, *Chem Mater* **2005**, *17*, 6327-6337.

[56] Y. Kim, H. Hwang, C. S. Yoon, M. G. Kim, J. Cho, *Adv Mater* **2007**, *19*, 92-96.

[57] S. Boyanov, K. Annou, C. Villevieille, M. Pelosi, D. Zitoun, L. Monconduit, *Ionics* **2008**, *14*, 183-190.

[58] J. Wang, Y. c. K. Chen‐Wiegart, J. Wang, *Angew Chem Int Ed Engl* **2014**, *53*, 4460-4464.

[59] C. K. Chan, H. Peng, G. Liu, K. McIlwrath, X. F. Zhang, R. A. Huggins, Y. Cui, *Nat Nanotech* **2008**, *3*, 31-35.

[60] W.-J. Zhang, *J Power Sources* **2011**, *196*, 13-24.

[61] H.-Y. Lee, S.-M. Lee, *Electrochem Commun* **2004**, *6*, 465-469.

[62] H.-Y. Lee, Y.-L. Kim, M.-K. Hong, S.-M. Lee, *J Power Sources* **2005**, *141*, 159-162.

[63] M. Wachtler, J. O. Besenhard, M. Winter, *J Power Sources* **2001**, *94*, 189-193.

[64] H. Kim, J. Choi, H. J. Sohn, T. Kang, *J Electrochem Soc* **1999**, *146*, 4401-4405.

[65] J. Yan, H. Huang, J. Zhang, Y. Yang, *J Power Sources* **2008**, *175*, 547-552.

[66] J. Yang, M. Winter, J. Besenhard, *Solid State Ion* **1996**, *90*, 281-287.

[67] J. Yang, M. Wachtler, M. Winter, J. O. Besenhard, *Electrochem Solid-State Lett* **1999**, *2*, 161-163.

[68] M. Obrovac, L. Christensen, D. B. Le, J. Dahn, *J Electrochem Soc* **2007**, *154*, A849-A855.

[69] J. T. Vaughey, L. Fransson, H. A. Swinger, K. Edström, M. M. Thackeray, *J Power Sources* **2003**, *119-121*, 64-68.

[70] S. S. Zhang, *J Power Sources* **2006**, *162*, 1379-1394.

[71] S. M. Whittingham, A. J. Jacobson, *Intercalation chemistry*, Academic Press, New York, **1982**.

[72] A. R. Kamali, D. J. Fray, *J New Mater Electrochem Syst* **2010**, *13*, 147-160.

[73] V. Etacheri, R. Marom, R. Elazari, G. Salitra, D. Aurbach, *Energy Environ Sci* **2011**, *4*, 3243-3262.

[74] M. Armand, J. M. Tarascon, *Nature* **2008**, *451*, 652-657.

[75] Y. Yamada, K. Usui, C. H. Chiang, K. Kikuchi, K. Furukawa, A. Yamada, *ACS Appl Mater Interfaces* **2014**, *6*, 10892-10899.

[76] K. Teshima, H. Inagaki, S. Tanaka, K. Yubuta, M. Hozumi, K. Kohama, T. Shishido, S. Oishi, *Cryst Growth Des* **2011**, *11*, 4401-4405.

[77] F. Leroux, K. Metenier, S. Gautier, E. Frackowiak, S. Bonnamy, F. Beguin, *J Power Sources* **1999**, *81*, 317-322.

[78] A. S. Claye, J. E. Fischer, C. B. Huffman, A. G. Rinzler, R. E. Smalley, *J Electrochem Soc* **2000**, *147*, 2845-2852.

[79] S.-H. Yoon, C.-W. Park, H. Yang, Y. Korai, I. Mochida, R. Baker, N. M. Rodriguez, *Carbon* **2004**, *42*, 21-32.

[80] G. Wang, J. Yang, J. Park, X. Gou, B. Wang, H. Liu, J. Yao, *J Phys Chem C* **2008**, *112*, 8192-8195.

[81] G. Wang, X. Shen, J. Yao, J. Park, *Carbon* **2009**, *47*, 2049-2053.

[82] S. Goriparti, E. Miele, F. De Angelis, E. Di Fabrizio, R. P. Zaccaria, C. Capiglia, *J Power Sources* **2014**, *257*, 421-443.

[83] C. J. Orendorff, D. H. Doughty, *Interface* **2012**, *21*, 35-35.

[84] N. Takami, K. Hoshina, H. Inagaki, *J Electrochem Soc* **2011**, *158*, A725-A730.

[85] Z. Chen, I. Belharouak, Y. K. Sun, K. Amine, *Adv Funct Mater* **2013**, *23*, 959-969.

[86] Y.-B. He, B. Li, M. Liu, C. Zhang, W. Lv, C. Yang, J. Li, H. Du, B. Zhang, Q.-H. Yang, *Sci Rep* **2012**, *2*.

[87] M.-S. Song, R.-H. Kim, S.-W. Baek, K.-S. Lee, K. Park, A. Benayad, *J Mater Chem A* **2014**, *2*, 631-636.

[88] H.-G. Jung, S.-T. Myung, C. S. Yoon, S.-B. Son, K. H. Oh, K. Amine, B. Scrosati, Y.-K. Sun, *Energy Environ Sci* **2011**, *4*, 1345-1351.

[89] C. Delmas, A. Nadiri, J. Soubeyroux, *Solid State Ion* **1988**, *28*, 419-423.

[90] S. Yu, A. Mertens, R. Schierholz, X. Gao, Ö. Aslanbas, J. Mertens, H. Kungl, H. Tempel, R.-A. Eichel, *J Electrochem Soc* **2017**, *164*, A370-A379.

[91] Z. Jian, Y. S. Hu, X. Ji, W. Chen, *Adv Mater* **2017**.

[92] A. Aatiq, M. Ménétrier, L. Croguennec, E. Suard, C. Delmas, *J Mater Chem* **2002**, *12*, 2971-2978.

[93] H. El-Shinawi, J. Janek, *RSC Adv* **2015**, *5*, 14887-14891.

[94] W. Sun, J. Liu, X. Liu, X. Fan, K. Zhou, X. Wei, *Chem Commun* **2017**.

[95] J. Sun, Y. Sun, L. Gai, H. Jiang, Y. Tian, *Electrochim Acta* **2016**, *200*, 66-74.

[96] J. Y. Luo, Y. Y. Xia, *Adv Funct Mater* **2007**, *17*, 3877-3884.

[97] J.-Y. Luo, W.-J. Cui, P. He, Y.-Y. Xia, *Nat Chem* **2010**, *2*, 760-765.

[98] Z. Jian, W. Han, Y. Liang, Y. Lan, Z. Fang, Y.-S. Hu, Y. Yao, *J Mater Chem A* **2014**, *2*, 20231-20236.

[99] J. Gaubicher, C. Wurm, G. Goward, C. Masquelier, L. Nazar, *Chem Mater* **2000**, *12*, 3240-3242.

[100] A. S. Hameed, M. Reddy, B. Chowdari, J. J. Vittal, *Electrochim Acta* **2014**, *128*, 184-191.

[101] X. Rui, N. Yesibolati, C. Chen, *J Power Sources* **2011**, *196*, 2279-2282.

[102] W.-f. Mao, H.-q. Tang, Z.-y. Tang, J. Yan, Q. Xu, *ECS Electrochem Lett* **2013**, *2*, A69-A71.

[103] X. Zhang, R.-S. Kühnel, M. Schroeder, A. Balducci, *J Mater Chem A* **2014**, *2*, 17906-17913.

[104] K. Mizushima, P. Jones, P. Wiseman, J. B. Goodenough, *Mater Res Bull* **1980**, *15*, 783-789.

[105] M. S. Whittingham, *Chem Rev* **2004**, *104*, 4271-4301.

[106] B. Xu, D. Qian, Z. Wang, Y. S. Meng, *Mater Sci Eng R Rep* **2012**, *73*, 51-65.

[107] J. N. Reimers, J. Dahn, *J Electrochem Soc* **1992**, *139*, 2091-2097.

[108] J. W. Fergus, *J Power Sources* **2010**, *195*, 939-954.

[109] G. Amatucci, *Solid State Ion* **1996**, *83*, 167-173.

[110] G. Amatucci, J. Tarascon, L. Klein, *J Electrochem Soc* **1996**, *143*, 1114-1123.

[111] T. Ohzuku, A. Ueda, *J Electrochem Soc* **1994**, *141*, 2972-2977.

[112] J. Zhou, P. Notten, *J Power Sources* **2008**, *177*, 553-560.

[113] T. Ohzuku, Y. Makimura, *Chem Lett* **2001**, *30*, 744-745.

[114] A. Abdel-Ghany, K. Zaghib, F. Gendron, A. Mauger, C. Julien, *Electrochim Acta* **2007**, *52*, 4092-4100.

[115] J. Bréger, N. Dupré, P. J. Chupas, P. L. Lee, T. Proffen, J. B. Parise, C. P. Grey, *J Am Chem Soc* **2005**, *127*, 7529-7537.

[116] Y. Meng, G. Ceder, C. Grey, W.-S. Yoon, Y. Shao-Horn, *Electrochem Solid-State Lett* **2004**, *7*, A155-A158.

[117] A. Van der Ven, G. Ceder, *Electrochem Commun* **2004**, *6*, 1045-1050.

[118] Z. Lu, D. MacNeil, J. Dahn, *Electrochem Solid-State Lett* **2001**, *4*, A191-A194.

[119] W.-S. Yoon, Y. Paik, X.-Q. Yang, M. Balasubramanian, J. McBreen, C. P. Grey, *Electrochem Solid-State Lett* **2002**, *5*, A263-A266.

[120] M. S. Whittingham, *Science* **1976**, *192*, 1126-1127.

[121] O. Tsutomu, M. Yoshinari, *Chem Lett* **2001**, *30*, 642-643.

[122] Y. Koyama, N. Yabuuchi, I. Tanaka, H. Adachi, T. Ohzuku, *J Electrochem Soc* **2004**, *151*, A1545-A1551.

[123] Y. Koyama, I. Tanaka, H. Adachi, Y. Makimura, T. Ohzuku, *J Power Sources* **2003**, *119*, 644-648.

[124] N. Yabuuchi, Y. Koyama, N. Nakayama, T. Ohzuku, *J Electrochem Soc* **2005**, *152*, A1434-A1440.

[125] K. M. Shaju, P. G. Bruce, *Adv Mater* **2006**, *18*, 2330-2334.

[126] G.-H. Kim, S.-T. Myung, H. Bang, J. Prakash, Y.-K. Sun, *Electrochem Solid-State Lett* **2004**, *7*, A477-A480.

[127] W.-S. Yoon, M. Balasubramanian, X.-Q. Yang, Z. Fu, D. A. Fischer, J. McBreen, *J Electrochem Soc* **2004**, *151*, A246-A251.

[128] W.-S. Yoon, C. P. Grey, M. Balasubramanian, X.-Q. Yang, D. A. Fischer, J. McBreen, *Electrochem Solid-State Lett* **2004**, *7*, A53-A55.

[129] W.-S. Yoon, C. P. Grey, M. Balasubramanian, X.-Q. Yang, J. McBreen, *Chem Mater* **2003**, *15*, 3161-3169.

[130] K. Shaju, G. S. Rao, B. Chowdari, *Electrochim Acta* **2002**, *48*, 145-151.

[131] M. Thackeray, W. David, P. Bruce, J. Goodenough, *Mater Res Bull* **1983**, *18*, 461-472.

[132] F. Jiao, J. Bao, A. H. Hill, P. G. Bruce, *Angew Chem Int Ed Engl* **2008**, *47*, 9711-9716.

[133] F. Cheng, H. Wang, Z. Zhu, Y. Wang, T. Zhang, Z. Tao, J. Chen, *Energy Environ Sci* **2011**, *4*, 3668.

[134] Y. Xia, *J Electrochem Soc* **1996**, *143*, 825.

[135] D. Aurbach, M. Levi, K. Gamulski, B. Markovsky, G. Salitra, E. Levi, U. Heider, L. Heider, R. Oesten, *J Power Sources* **1999**, *81*, 472-479.

[136] Y. Xia, *J Electrochem Soc* **1997**, *144*, 2593.

[137] Y. Shin, A. Manthiram, *J Electrochem Soc* **2004**, *151*, A204-A208.

[138] R. J. Gummow, A. de Kock, M. M. Thackeray, *Solid State Ion* **1994**, *69*, 59-67.

[139] K.-S. Lee, S.-T. Myung, H. J. Bang, S. Chung, Y.-K. Sun, *Electrochim Acta* **2007**, *52*, 5201-5206.

[140] Y. J. Lee, S.-H. Park, C. Eng, J. B. Parise, C. P. Grey, *Chem Mater* **2002**, *14*, 194-205.

[141] L. Hernan, J. Morales, L. Sanchez, J. Santos, *Solid State Ion* **1999**, *118*, 179-185.

[142] J.-H. Kim, S.-T. Myung, C. Yoon, S. Kang, Y.-K. Sun, *Chem Mater* **2004**, *16*, 906-914.

[143] L. Guohua, H. Ikuta, T. Uchida, M. Wakihara, *J Electrochem Soc* **1996**, *143*, 178-182.

[144] J. Molenda, J. Marzec, K. Świerczek, W. Ojczyk, M. Ziemnicki, M. Molenda, M. Drozdek, R. Dziembaj, *Solid State Ion* **2004**, *171*, 215-227.

[145] T. Ohzuku, S. Takeda, M. Iwanaga, *J Power Sources* **1999**, *81*, 90-94.

[146] R. Singhal, S. R. Das, M. S. Tomar, O. Ovideo, S. Nieto, R. E. Melgarejo, R. S. Katiyar, *J Power Sources* **2007**, *164*, 857-861.

[147] J. Tu, X. Zhao, D. Zhuang, G. Cao, T. Zhu, J. Tu, *Physica B Condens Matter* **2006**, *382*, 129-134.

[148] S. Yang, J. Jia, L. Ding, M. Zhang, *Electrochim Acta* **2003**, *48*, 569-573.

[149] M. Kunduraci, G. Amatucci, *Electrochim Acta* **2008**, *53*, 4193-4199.

[150] H. Xia, Y. Meng, L. Lu, G. Ceder, *J Electrochem Soc* **2007**, *154*, A737-A743.

[151] J. Yang, J. J. Xu, *J Electrochem Soc* **2006**, *153*, A716-A723.

[152] R. Dominko, in *SPIE Defense, Security, and Sensing*, International Society for Optics and Photonics, **2010**, pp. 76830J-76830J-76838.

[153] X.-Y. Fan, Y. Li, J.-J. Wang, L. Gou, P. Zhao, D.-L. Li, L. Huang, S.-G. Sun, *J Alloys Compd* **2010**, *493*, 77-80.

[154] Z. Yan, S. Cai, L. Miao, X. Zhou, Y. Zhao, *J Alloys Compd* **2012**, *511*, 101-106.

[155] K. Zaghib, A. A. Salah, N. Ravet, A. Mauger, F. Gendron, C. Julien, *J Power Sources* **2006**, *160*, 1381-1386.

[156] Z. Zhang, T. Zeng, C. Qu, H. Lu, M. Jia, Y. Lai, J. Li, *Electrochim Acta* **2012**, *80*, 440-444.

[157] A. West, P. Bruce, *Acta Crystallogr B* **1982**, *38*, 1891-1896.

[158] A. Nytén, A. Abouimrane, M. Armand, T. Gustafsson, J. O. Thomas, *Electrochem Commun* **2005**, *7*, 156-160.

[159] M. S. Islam, R. Dominko, C. Masquelier, C. Sirisopanaporn, A. R. Armstrong, P. G. Bruce, *J Mater Chem* **2011**, *21*, 9811-9818.

[160] T. Muraliganth, K. Stroukoff, A. Manthiram, *Chem Mater* **2010**, *22*, 5754-5761.

[161] R. Dominko, C. Sirisopanaporn, C. Masquelier, D. Hanzel, I. Arcon, M. Gaberscek, *J Electrochem Soc* **2010**, *157*, A1309-A1316.

[162] R. Dominko, M. Bele, M. Gaberšček, A. Meden, M. Remškar, J. Jamnik, *Electrochem Commun* **2006**, *8*, 217-222.

[163] Q. Cheng, W. He, X. Zhang, M. Li, L. Wang, *J Mater Chem A* **2017**.

[164] R. Dominko, M. Bele, A. Kokalj, M. Gaberscek, J. Jamnik, *J Power Sources* **2007**, *174*, 457-461.

[165] R. J. Gummow, Y. He, *RSC Adv* **2014**, *4*, 11580-11584.

[166] P. Ghosh, S. Mahanty, R. N. Basu, *J Electrochem Soc* **2009**, *156*, A677-A681.

[167] A. Bhaskar, M. Deepa, T. Rao, U. Varadaraju, *J Electrochem Soc* **2012**, *159*, A1954-A1960.

[168] S. Liu, J. Xu, D. Li, Y. Hu, X. Liu, K. Xie, *J Power Sources* **2013**, *232*, 258-263.

[169] L. Li, L. Zhu, L.-H. Xu, T.-M. Cheng, W. Wang, X. Li, Q.-T. Sui, *J Mater Chem A* **2014**, *2*, 4251-4255.

[170] H. Wang, T. Hou, D. Sun, X. Huang, H. He, Y. Tang, Y. Liu, *J Power Sources* **2014**, *247*, 497-502.

[171] S.-S. Liu, L.-J. Song, B.-J. Yu, C.-Y. Wang, M.-W. Li, *Electrochim Acta* **2016**, *188*, 145-152.

[172] E.-Q. Liang, L.-J. Song, S.-S. Liu, Y. Guo, B.-J. Yu, C.-Y. Wang, M.-W. Li, *Int J Electrochem Sci* **2017**, *12*, 5320-5330.

[173] P. Barpanda, D. Dwibedi, S. Ghosh, Y. Kee, S. Okada, *Ionics* **2015**, *21*, 1801-1812.

[174] V. Legagneur, Y. An, A. Mosbah, R. Portal, A. L. G. La Salle, A. Verbaere, D. Guyomard, Y. Piffard, *Solid State Ion* **2001**, *139*, 37-46.

[175] Y. Dong, Y. Zhao, Z. Shi, X. An, P. Fu, L. Chen, *Electrochim Acta* **2008**, *53*, 2339-2345.

[176] Y. Dong, Y. Zhao, P. Fu, H. Zhou, X. Hou, *J Alloys Compd* **2008**, *461*, 585-590.

[177] M. Isono, S. Okada, J.-i. Yamaki, *J Power Sources* **2010**, *195*, 593-598.

[178] A. Yamada, N. Iwane, Y. Harada, S. i. Nishimura, Y. Koyama, I. Tanaka, *Adv Mater* **2010**, *22*, 3583-3587.

[179] A. Yamada, N. Iwane, S.-i. Nishimura, Y. Koyama, I. Tanaka, *J Mater Chem* **2011**, *21*, 10690-10696.

[180] J. C. Kim, C. J. Moore, B. Kang, G. Hautier, A. Jain, G. Ceder, *J Electrochem Soc* **2011**, *158*, A309-A315.

[181] N. Zhang, Y. Zhang, Y. J. Xu, *Nanoscale* **2012**, *4*, 5792-5813.

[182] L. Chen, Y. Zhao, X. An, J. Liu, Y. Dong, Y. Chen, Q. Kuang, *J Alloys Compd* **2010**, *494*, 415-419.

[183] R. Ma, L. Shao, K. Wu, M. Lao, M. Shui, C. Chen, D. Wang, N. Long, Y. Ren, J. Shu, *Ceram Int* **2013**, *39*, 9309-9317.

[184] S. Afyon, D. Kundu, F. Krumeich, R. Nesper, *J Power Sources* **2013**, *224*, 145-151.

[185] S. Afyon, D. Kundu, A. J. Darbandi, H. Hahn, F. Krumeich, R. Nesper, *J Mater Chem A* **2014**, *2*, 18946-18951.

[186] J. C. Kim, X. Li, C. J. Moore, S.-H. Bo, P. G. Khalifah, C. P. Grey, G. Ceder, *Chem Mater* **2014**, *26*, 4200-4206.

[187] Y.-S. Lee, H. Lee, *Electron Mater Lett* **2014**, *10*, 253-258.

[188] Y.-S. Lee, H. Lee, *Materials Letters* **2014**, *132*, 401-404.

[189] T. Ma, A. Muslim, Z. Su, *J Power Sources* **2015**, *282*, 95-99.

[190] A. Tang, D. He, Z. He, G. Xu, H. Song, R. Peng, *J Power Sources* **2015**, *275*, 888-892.

[191] Y. Yamashita, P. Barpanda, Y. Yamada, A. Yamada, *ECS Electrochem Lett* **2013**, *2*, A75-A77.

[192] S.-Y. Chung, Y.-M. Chiang, *Electrochem Solid-State Lett* **2003**, *6*, A278-A281.

[193] P. P. Prosini, M. Lisi, D. Zane, M. Pasquali, *Solid State Ion* **2002**, *148*, 45-51.

[194] C. Ouyang, S. Shi, Z. Wang, X. Huang, L. Chen, *Phys Rev B* **2004**, *69*, 104303.

[195] G. K. P. Dathar, D. Sheppard, K. J. Stevenson, G. Henkelman, *Chem Mater* **2011**, *23*, 4032-4037.

[196] S.-i. Nishimura, G. Kobayashi, K. Ohoyama, R. Kanno, M. Yashima, A. Yamada, *Nat Mater* **2008**, *7*, 707-711.

[197] S. Yang, P. Y. Zavalij, M. S. Whittingham, *Electrochem Commun* **2001**, *3*, 505-508.

[198] J. Wang, X. Sun, *Energy Environ Sci* **2012**, *5*, 5163-5185.

[199] B. Ding, W. C. Tang, G. Ji, Y. Ma, P. Xiao, L. Lu, J. Y. Lee, *J Power Sources* **2014**, *265*, 239-245.

[200] X. Yang, J. Tu, M. Lei, Z. Zuo, B. Wu, H. Zhou, *Electrochim Acta* **2016**, *193*, 206-215.

[201] K. Kretschmer, B. Sun, D. Su, Y. Zhao, G. Wang, *ChemElectroChem* **2015**.

[202] G. X. Wang, H. Liu, J. Liu, S. Qiao, G. M. Lu, P. Munroe, H. Ahn, *Adv Energy Mater* **2010**, *22*, 4944-4948.

[203] S. Deng, H. Wang, H. Liu, J. Lui, H. Yan, *Nano-Micro Lett* **2014**, *6*, 209-226.

[204] Z. Ma, G. Shao, Y. Fan, G. Wang, J. Song, T. Liu, *ACS Appl Mater Interfaces* **2014**, 9236-9244.

[205] K. Bazzi, M. Nazri, V. Naik, V. Garg, A. Oliveira, P. Vaishnava, G. Nazri, R. Naik, *J Power Sources* **2016**, *306*, 17-23.

[206] S. Novikova, S. Yaroslavtsev, V. Rusakov, T. Kulova, A. Skundin, A. Yaroslavtsev, *Electrochim Acta* **2014**, *122*, 180-186.

[207] B. Wang, W. Al Abdulla, D. Wang, X. Zhao, *Energy Environ Sci* **2015**, *8*, 869-875.

[208] B. Wang, B. Xu, T. Liu, P. Liu, C. Guo, S. Wang, Q. Wang, Z. Xiong, D. Wang, X. Zhao, *Nanoscale* **2014**, *6*, 986-995.

[209] I. D. Johnson, M. Lübke, O. Y. Wu, N. M. Makwana, G. J. Smales, H. U. Islam, R. Y. Dedigama, R. I. Gruar, C. J. Tighe, D. O. Scanlon, *J Power Sources* **2016**, *302*, 410-418.

[210] A. Yamada, S.-C. Chung, *J Electrochem Soc* **2001**, *148*, A960-A967.

[211] J. Wolfenstine, J. Allen, *J Power Sources* **2004**, *136*, 150-153.

[212] F. Zhou, M. Cococcioni, K. Kang, G. Ceder, *Electrochem Commun* **2004**, *6*, 1144-1148.

[213] T. Satyavani, A. S. Kumar, P. S. Rao, *Engineering Science and Technology, an International Journal* **2016**, *19*, 178-188.

[214] Z. Yang, Y. Dai, S. Wang, J. Yu, *J Mater Chem A* **2016**, *4*, 18210-18222.

[215] A. Yamada, H. Koizumi, S.-i. Nishimura, N. Sonoyama, R. Kanno, M. Yonemura, T. Nakamura, Y. Kobayashi, *Nat Mater* **2006**, *5*, 357.

[216] G. Chen, X. Song, T. J. Richardson, *Electrochem Solid-State Lett* **2006**, *9*, A295-A298.

[217] L. Laffont, C. Delacourt, P. Gibot, M. Y. Wu, P. Kooyman, C. Masquelier, J. M. Tarascon, *Chem Mater* **2006**, *18*, 5520-5529.

[218] C. Delmas, M. Maccario, L. Croguennec, F. Le Cras, F. Weill, *Nat Mater* **2008**, *7*, 665-671.

[219] G. Brunetti, D. Robert, P. Bayle-Guillemaud, J. Rouviere, E. Rauch, J. Martin, J. Colin, F. Bertin, C. Cayron, *Chem Mater* **2011**, *23*, 4515-4524.

[220] Y. Orikasa, T. Maeda, Y. Koyama, H. Murayama, K. Fukuda, H. Tanida, H. Arai, E. Matsubara, Y. Uchimoto, Z. Ogumi, *J Am Chem Soc* **2013**, *135*, 5497-5500.

[221] H. Liu, F. C. Strobridge, O. J. Borkiewicz, K. M. Wiaderek, K. W. Chapman, P. J. Chupas, C. P. Grey, *Science* **2014**, *344*, 1252817.

[222] T. Mueller, G. Hautier, A. Jain, G. Ceder, *Chem Mater* **2011**, *23*, 3854-3862.

[223] J. Barker, M. Saidi, J. Swoyer, *J Electrochem Soc* **2003**, *150*, A1394-A1398.

[224] R. Gover, P. Burns, A. Bryan, M. Saidi, J. Swoyer, J. Barker, *Solid State Ion* **2006**, *177*, 2635-2638.

[225] M. Kim, S. Lee, B. Kang, *Adv Sci* **2016**, *3*.

[226] J. Barker, R. Gover, P. Burns, A. Bryan, *Electrochem Solid-State Lett* **2005**, *8*, A285-A287.

[227] K. Zaghib, M. Dontigny, A. Guerfi, J. Trottier, J. Hamel-Paquet, V. Gariepy, K. Galoutov, P. Hovington, A. Mauger, H. Groult, *J Power Sources* **2012**, *216*, 192-200.

[228] W. Li, B. Song, A. Manthiram, *Chem Soc Rev* **2017**.

[229] T. Ramesh, K. T. Lee, B. Ellis, L. Nazar, *Electrochem Solid-State Lett* **2010**, *13*, A43-A47.

[230] D. Chen, G.-Q. Shao, B. Li, G.-G. Zhao, J. Li, J.-H. Liu, Z.-S. Gao, H.-F. Zhang, *Electrochim Acta* **2014**, *147*, 663-668.

[231] J. Barker, M. Y. Saidi, J. Swoyer*, Vol. US 7261977 B2*, Valence Technology, Inc., USA, **2007**.

[232] A. Padhi, K. Nanjundaswamy, C. Masquelier, J. Goodenough, *J Electrochem Soc* **1997**, *144*, 2581-2586.

[233] G. Hautier, A. Jain, S. P. Ong, B. Kang, C. Moore, R. Doe, G. Ceder, *Chem Mater* **2011**, *23*, 3495-3508.

[234] D. L. Smiley, L. J. Davis, G. R. Goward, *J Phys Chem C* **2013**, *117*, 24181-24188.

[235] M. Morcrette, C. Wurm, C. Masquelier, *Solid State Sci* **2002**, *4*, 239-246.

[236] J. Cabana, J. Shirakawa, M. Nakayama, M. Wakihara, C. P. Grey, *J Mater Chem* **2011**, *21*, 10012-10020.

[237] C. Masquelier, C. Wurm, J. Rodriguez-Carvajal, J. Gaubicher, L. Nazar, *Chem Mater* **2000**, *12*, 525-532.

[238] A. Andersson, B. Kalska, P. Eyob, D. Aernout, L. Häggström, J. Thomas, *Solid State Ion* **2001**, *140*, 63-70.

[239] X. Rui, Q. Yan, M. Skyllas-Kazacos, T. M. Lim, *J Power Sources* **2014**, *258*, 19-38.

[240] S.-C. Yin, H. Grondey, P. Strobel, M. Anne, L. F. Nazar, *J Am Chem Soc* **2003**, *125*, 10402-10411.

[241] M. Morcrette, J. Leriche, S. Patoux, C. Wurm, C. Masquelier, *Electrochem Solid-State Lett* **2003**, *6*, A80-A84.

[242] J. Yoon, S. Muhammad, D. Jang, N. Sivakumar, J. Kim, W.-H. Jang, Y.-S. Lee, Y.-U. Park, K. Kang, W.-S. Yoon, *J Alloys Compd* **2013**, *569*, 76-81.

[243] M. Saıdi, J. Barker, H. Huang, J. Swoyer, G. Adamson, *J Power Sources* **2003**, *119*, 266-272.

[244] X. Rui, C. Li, C. Chen, *Electrochim Acta* **2009**, *54*, 3374-3380.

[245] S. Chen, C. Wu, L. Shen, C. Zhu, Y. Huang, K. Xi, J. Maier, Y. Yu, *Adv Mater* **2017**.

[246] Z. Dai, U. Mani, H. T. Tan, Q. Yan, *Small Methods* **2017**.

[247] M. D. Slater, D. Kim, E. Lee, C. S. Johnson, *Adv Funct Mater* **2013**, *23*, 947-958.

[248] H. Pan, Y.-S. Hu, L. Chen, *Energy Environ Sci* **2013**, *6*, 2338-2360.

[249] S. Hariharan, K. Saravanan, V. Ramar, P. Balaya, *Phys Chem Chem Phys* **2013**, *15*, 2945-2953.

[250] B. Huang, K. Tai, M. Zhang, Y. Xiao, S. J. Dillon, *Electrochim Acta* **2014**, *118*, 143-149.

[251] P. R. Kumar, Y. H. Jung, K. K. Bharathi, C. H. Lim, D. K. Kim, *Electrochim Acta* **2014**, *146*, 503-510.

[252] D. Y. Park, S. T. Myung, *ACS Appl Mater Interfaces* **2014**, *6*, 11749-11757.

[253] B. Philippe, M. Valvo, F. Lindgren, H. k. Rensmo, K. Edström, *Chem Mater* **2014**, *26*, 5028-5041.

[254] M. Valvo, F. Lindgren, U. Lafont, F. Björefors, K. Edström, *J Power Sources* **2014**, *245*, 967-978.

[255] X. Liu, T. Chen, H. Chu, L. Niu, Z. Sun, L. Pan, C. Q. Sun, *Electrochim Acta* **2015**, *166*, 12-16.

[256] S. Liu, Y. Wang, Y. Dong, Z. Zhao, Z. Wang, J. Qiu, *ChemElectroChem* **2016**, *3*, 38-44.

[257] J. W. Choi, D. Aurbach, *Nat Rev Mater* **2016**, *1*, 16013.

[258] Y. Jiang, M. Hu, D. Zhang, T. Yuan, W. Sun, B. Xu, M. Yan, *Nano Energy* **2014**, *5*, 60-66.

[259] F. Klein, B. Jache, A. Bhide, P. Adelhelm, *Phys Chem Chem Phys* **2013**, *15*, 15876-15887.

[260] H. Liu, F. Cao, H. Zheng, H. Sheng, L. Li, S. Wu, C. Liu, J. Wang, *Chem Commun* **2015**, *51*, 10443-10446.

[261] X. Wang, X. Shen, Z. Wang, R. Yu, L. Chen, *ACS Nano* **2014**, *8*, 11394-11400.

[262] Y. X. Wang, S. L. Chou, D. Wexler, H. K. Liu, S. X. Dou, *Chem Eur J* **2014**, *20*, 9607-9612.

[263] S. Zhang, X. Yu, H. Yu, Y. Chen, P. Gao, C. Li, C. Zhu, *ACS Appl Mater Interfaces* **2014**, *6*, 21880-21885.

[264] F. Zhou, S. Xin, H. W. Liang, L. T. Song, S. H. Yu, *Angew Chem Int Ed Engl* **2014**, *53*, 11552-11556.

[265] C. Zhu, X. Mu, P. A. van Aken, Y. Yu, J. Maier, *Angew Chem Int Ed Engl* **2014**, *53*, 2152-2156.

[266] S. H. Choi, Y. N. Ko, J.-K. Lee, Y. C. Kang, *Adv Funct Mater* **2015**, *25*, 1780-1788.

[267] J. Wang, C. Luo, T. Gao, A. Langrock, A. C. Mignerey, C. Wang, *Small* **2015**, *11*, 473-481.

[268] X. Xiong, W. Luo, X. Hu, C. Chen, L. Qie, D. Hou, Y. Huang, *Sci Rep* **2015**, *5*, 9254.

[269] B. Qu, C. Ma, G. Ji, C. Xu, J. Xu, Y. S. Meng, T. Wang, J. Y. Lee, *Adv Mater* **2014**, *26*, 3854-3859.

[270] C. Ma, J. Xu, J. Alvarado, B. Qu, J. Somerville, J. Y. Lee, Y. S. Meng, *Chem Mater* **2015**, *27*, 5633-5640.

[271] W. Xu, K. Zhao, L. Zhang, Z. Xie, Z. Cai, Y. Wang, *J Alloys Compd* **2016**, *654*, 357-362.

[272] Y. Liu, Y. Yang, X. Wang, Y. Dong, Y. Tang, Z. Yu, Z. Zhao, J. Qiu, *ACS Appl Mater Interfaces* **2017**, *9*, 15484-15491.

[273] Z. Li, J. Ding, D. Mitlin, *Acc Chem Res* **2015**, *48*, 1657-1665.

[274] Y. Kim, K.-H. Ha, S. M. Oh, K. T. Lee, *Chem Eur J* **2014**, *20*, 11980-11992.

[275] N. Yabuuchi, K. Kubota, M. Dahbi, S. Komaba, *Chem Rev* **2014**, *114*, 11636-11682.

[276] Y.-X. Wang, Y.-G. Lim, M.-S. Park, S.-L. Chou, J. H. Kim, H.-K. Liu, S.-X. Dou, Y.-J. Kim, *J Mater Chem A* **2014**, *2*, 529-534.

[277] L. Pei, Q. Jin, Z. Zhu, Q. Zhao, J. Liang, J. Chen, *Nano Res* **2014**, *8*, 184-192.

[278] P. Ge, *Solid State Ion* **1988**, *28-30*, 1172-1175.

[279] D. A. Stevens, J. R. Dahn, *J Electrochem Soc* **2001**, *148*, A803.

[280] B. Jache, P. Adelhelm, *Angew Chem Int Ed Engl* **2014**, *53*, 10169-10173.

[281] H. Kim, J. Hong, Y.-U. Park, J. Kim, I. Hwang, K. Kang, *Adv Funct Mater* **2015**, *25*, 534-541.

[282] H. Kim, J. Hong, G. Yoon, H. Kim, K.-Y. Park, M.-S. Park, W.-S. Yoon, K. Kang, *Energy Environ Sci* **2015**, *8*, 2963-2969.

[283] M. M. Doeff, *J Electrochem Soc* **1993**, *140*, L169.

[284] D. Stevens, J. Dahn, *J Electrochem Soc* **2000**, *147*, 1271-1273.

[285] C. Bommier, T. W. Surta, M. Dolgos, X. Ji, *Nano Lett* **2015**, *15*, 5888-5892.

[286] P.-c. Tsai, S.-C. Chung, S.-k. Lin, A. Yamada, *J Mater Chem A* **2015**, *3*, 9763-9768.

[287] K. Gotoh, T. Ishikawa, S. Shimadzu, N. Yabuuchi, S. Komaba, K. Takeda, A. Goto, K. Deguchi, S. Ohki, K. Hashi, *J Power Sources* **2013**, *225*, 137-140.

[288] H.-G. Wang, S. Yuan, D.-L. Ma, X.-B. Zhang, J.-M. Yan, *Energy Environ Sci* **2015**, *8*, 1660-1681.

[289] H. Xiong, M. D. Slater, M. Balasubramanian, C. S. Johnson, T. Rajh, *J Phys Chem Lett* **2011**, *2*, 2560-2565.

[290] K. T. Kim, G. Ali, K. Y. Chung, C. S. Yoon, H. Yashiro, Y. K. Sun, J. Lu, K. Amine, S. T. Myung, *Nano Lett* **2014**, *14*, 416-422.

[291] L. Wu, D. Bresser, D. Buchholz, G. A. Giffin, C. R. Castro, A. Ochel, S. Passerini, *Adv Energy Mater* **2015**, *5*.

[292] Y. Sun, L. Zhao, H. Pan, X. Lu, L. Gu, Y. S. Hu, H. Li, M. Armand, Y. Ikuhara, L. Chen, X. Huang, *Nat Commun* **2013**, *4*, 1870.

[293] J. Liu, K. Tang, K. Song, P. A. van Aken, Y. Yu, J. Maier, *Phys Chem Chem Phys* **2013**, *15*, 20813-20818.

[294] P. Senguttuvan, G. Rousse, V. Seznec, J.-M. Tarascon, M. R. Palacín, *Chem Mater* **2011**, *23*, 4109-4111.

[295] J.-Y. Liao, A. Manthiram, *Nano Energy* **2015**, *18*, 20-27.

[296] D. Wu, X. Li, B. Xu, N. Twu, L. Liu, G. Ceder, *Energy Environ Sci* **2015**, *8*, 195-202.

[297] A. Rudola, K. Saravanan, S. Devaraj, H. Gong, P. Balaya, *Chem Commun* **2013**, *49*, 7451-7453.

[298] H. Li, H. Fei, X. Liu, J. Yang, M. Wei, *Chem Commun* **2015**, *51*, 9298-9300.

[299] M. Naguib, M. Kurtoglu, V. Presser, J. Lu, J. Niu, M. Heon, L. Hultman, Y. Gogotsi, M. W. Barsoum, *Adv Mater* **2011**, *23*, 4248-4253.

[300] B. Anasori, Y. Xie, M. Beidaghi, J. Lu, B. C. Hosler, L. Hultman, P. R. Kent, Y. Gogotsi, M. W. Barsoum, *ACS Nano* **2015**, *9*, 9507-9516.

[301] M. Naguib, O. Mashtalir, J. Carle, V. Presser, J. Lu, L. Hultman, Y. Gogotsi, M. W. Barsoum, *ACS Nano* **2012**, *6*, 1322-1331.

[302] P. Urbankowski, B. Anasori, T. Makaryan, D. Er, S. Kota, P. L. Walsh, M. Zhao, V. B. Shenoy, M. W. Barsoum, Y. Gogotsi, *Nanoscale* **2016**, *8*, 11385-11391.

[303] M. Naguib, J. Halim, J. Lu, K. M. Cook, L. Hultman, Y. Gogotsi, M. W. Barsoum, *J Am Chem Soc* **2013**, *135*, 15966-15969.

[304] Y. Xie, Y. Dall'Agnese, M. Naguib, Y. Gogotsi, M. W. Barsoum, H. L. Zhuang, P. R. Kent, *ACS Nano* **2014**, *8*, 9606-9615.

[305] X. Wang, X. Shen, Y. Gao, Z. Wang, R. Yu, L. Chen, *J Am Chem Soc* **2015**, *137*, 2715-2721.

[306] E. Yang, H. Ji, J. Kim, H. Kim, Y. Jung, *Phys Chem Chem Phys* **2015**, *17*, 5000-5005.

[307] C. Eames, M. S. Islam, *J Am Chem Soc* **2014**, *136*, 16270-16276.

[308] Y. Dall'Agnese, P. L. Taberna, Y. Gogotsi, P. Simon, *J Phys Chem Lett* **2015**, *6*, 2305-2309.

[309] P. Eklund, M. Beckers, U. Jansson, H. Högberg, L. Hultman, *Thin Solid Films* **2010**, *518*, 1851-1878.

[310] C. Delmas, F. Cherkaoui, A. Nadiri, P. Hagenmuller, *Mater Res Bull* **1987**, *22*, 631-639.

[311] Q. Ni, Y. Bai, F. Wu, C. Wu, *Adv Sci* **2017**.

[312] D. Wang, Q. Liu, C. Chen, M. Li, X. Meng, X. Bie, Y. Wei, Y. Huang, F. Du, C. Wang, *ACS Appl Mater Interfaces* **2016**, *8*, 2238-2246.

[313] C. Wu, P. Kopold, Y.-L. Ding, P. A. van Aken, J. Maier, Y. Yu, *ACS Nano* **2015**, *9*, 6610-6618.

[314] Y. Jiang, J. Shi, M. Wang, L. Zeng, L. Gu, Y. Yu, *ACS Appl Mater Interfaces* **2015**, *8*, 689-695.

[315] Y. Zuo, L. Chen, Z. Zuo, Y. Huang, X. Liu, *Ceram Int* **2017**.

[316] J. Yang, H. Wang, P. Hu, J. Qi, L. Guo, L. Wang, *Small* **2015**, *11*, 3744-3749.

[317] B. Zhao, B. Lin, S. Zhang, C. Deng, *Nanoscale* **2015**, *7*, 18552-18560.

[318] Z. Jian, W. Han, X. Lu, H. Yang, Y. S. Hu, J. Zhou, Z. Zhou, J. Li, W. Chen, D. Chen, *Adv Energy Mater* **2013**, *3*, 156-160.

[319] Z. Jian, L. Zhao, H. Pan, Y.-S. Hu, H. Li, W. Chen, L. Chen, *Electrochem Commun* **2012**, *14*, 86-89.

[320] Z. Jian, Y. Sun, X. Ji, *Chem Commun* **2015**, *51*, 6381-6383.

[321] Y. Zhang, H. Zhao, Y. Du, *J Mater Chem A* **2016**, *4*, 7155-7159.

[322] Q. Zhu, B. Nan, Y. Shi, Y. Zhu, S. Wu, L. He, Y. Deng, L. Wang, Q. Chen, Z. Lu, *J Solid State Electrochem* **2017**, 1-11.

[323] C. Delmas, C. Fouassier, P. Hagenmuller, *Physica B+C* **1980**, *99*, 81-85.

[324] R. Kanno, Y. Takeda, T. Ichikawa, K. Nakanishi, O. Yamamoto, *J Power Sources* **1989**, *26*, 535-543.

[325] X. Ma, H. Chen, G. Ceder, *J Electrochem Soc* **2011**, *158*, A1307-A1312.

[326] N. Yabuuchi, M. Kajiyama, J. Iwatate, H. Nishikawa, S. Hitomi, R. Okuyama, R. Usui, Y. Yamada, S. Komaba, *Nat Mater* **2012**, *11*, 512-517.

[327] J. Xu, D. H. Lee, R. J. Clément, X. Yu, M. Leskes, A. J. Pell, G. Pintacuda, X.-Q. Yang, C. P. Grey, Y. S. Meng, *Chem Mater* **2014**, *26*, 1260-1269.

[328] J. Billaud, G. Singh, A. R. Armstrong, E. Gonzalo, V. Roddatis, M. Armand, T. Rojo, P. G. Bruce, *Energy Environ Sci* **2014**, *7*, 1387-1391.

[329] X. Wang, G. Liu, T. Iwao, M. Okubo, A. Yamada, *J Phys Chem C* **2014**, *118*, 2970-2976.

[330] Y. Lu, L. Wang, J. Cheng, J. B. Goodenough, *Chem Commun* **2012**, *48*, 6544-6546.

[331] D. Kundu, E. Talaie, V. Duffort, L. F. Nazar, *Angew Chem Int Ed Engl* **2015**, *54*, 3431-3448.

[332] Y. Fang, J. Zhang, L. Xiao, X. Ai, Y. Cao, H. Yang, *Adv Sci* **2017**.

[333] K. Zaghib, J. Trottier, P. Hovington, F. Brochu, A. Guerfi, A. Mauger, C. Julien, *J Power Sources* **2011**, *196*, 9612-9617.

[334] P. Moreau, D. Guyomard, J. Gaubicher, F. Boucher, *Chem Mater* **2010**, *22*, 4126-4128.

[335] N. Le Poul, E. Baudrin, M. Morcrette, S. Gwizdala, C. Masquelier, J.-M. Tarascon, *Solid State Ion* **2003**, *159*, 149-158.

[336] S.-M. Oh, S.-T. Myung, J. Hassoun, B. Scrosati, Y.-K. Sun, *Electrochem Commun* **2012**, *22*, 149-152.

[337] Y. Zhu, Y. Xu, Y. Liu, C. Luo, C. Wang, *Nanoscale* **2013**, *5*, 780-787.

[338] A. Whiteside, C. A. Fisher, S. C. Parker, M. S. Islam, *Phys Chem Chem Phys* **2014**, *16*, 21788-21794.

[339] M. Nakayama, S. Yamada, R. Jalem, T. Kasuga, *Solid State Ion* **2016**, *286*, 40-44.

[340] M. Dixit, H. Engel, R. Eitan, D. Aurbach, M. D. Levi, M. Kosa, D. T. Major, *J Phys Chem C* **2015**, *119*, 15801-15809.

[341] J. Kim, D.-H. Seo, H. Kim, I. Park, J.-K. Yoo, S.-K. Jung, Y.-U. Park, W. A. Goddard III, K. Kang, *Energy Environ Sci* **2015**, *8*, 540-545.

[342] K. Saravanan, C. W. Mason, A. Rudola, K. H. Wong, P. Balaya, *Adv Energy Mater* **2013**, *3*, 444-450.

[343] C. Zhu, K. Song, P. A. van Aken, J. Maier, Y. Yu, *Nano Lett* **2014**, *14*, 2175-2180.

[344] S.-J. Lim, D.-W. Han, D.-H. Nam, K.-S. Hong, J.-Y. Eom, W.-H. Ryu, H.-S. Kwon, *J Mater Chem A* **2014**, *2*, 19623-19632.

[345] H. Li, X. Yu, Y. Bai, F. Wu, C. Wu, L.-Y. Liu, X.-Q. Yang, *J Mater Chem A* **2015**, *3*, 9578-9586.

[346] G. Xu, G. Sun, *Ceram Int* **2016**, *42*, 14774-14781.

[347] M. Aragón, P. Lavela, G. Ortiz, J. Tirado, *J Electrochem Soc* **2015**, *162*, A3077-A3083.

[348] B. M. de Boisse, J. Ming, S.-i. Nishimura, A. Yamada, *J Electrochem Soc* **2016**, *163*, A1469-A1473.

[349] M. J. Aragón, P. Lavela, G. F. Ortiz, J. L. Tirado, *ChemElectroChem* **2015**, *2*, 995-1002.

[350] R. Klee, P. Lavela, M. Aragón, R. Alcántara, J. Tirado, *J Power Sources* **2016**, *313*, 73-80.

[351] C. W. Mason, I. Gocheva, H. E. Hoster, Y. Dennis, *ECS Trans* **2014**, *58*, 41-46.

[352] K. Kretschmer, B. Sun, J. Zhang, X. Xie, H. Liu, G. Wang, *Small* **2017**, *13*.

[353] S. Li, Y. Dong, L. Xu, X. Xu, L. He, L. Mai, *Adv Mater* **2014**, *26*, 3545-3553.

[354] Q. Zhang, W. Wang, Y. Wang, P. Feng, K. Wang, S. Cheng, K. Jiang, *Nano Energy* **2016**, *20*, 11-19.

[355] S. Tao, P. Cui, W. Huang, Z. Yu, X. Wang, S. Wei, D. Liu, L. Song, W. Chu, *Carbon* **2016**, *96*, 1028-1033.

[356] W. Duan, Z. Zhu, H. Li, Z. Hu, K. Zhang, F. Cheng, J. Chen, *J Mater Chem A* **2014**, *2*, 8668-8675.

[357] R. Shakoor, D.-H. Seo, H. Kim, Y.-U. Park, J. Kim, S.-W. Kim, H. Gwon, S. Lee, K. Kang, *J Mater Chem* **2012**, *22*, 20535-20541.

[358] B. L. Ellis, W. R. Makahnouk, Y. Makimura, K. Toghill, L. F. Nazar, *Nat Mater* **2007**, *6*, 749-753.

[359] Y. U. Park, D. H. Seo, H. S. Kwon, B. Kim, J. Kim, H. Kim, I. Kim, H. I. Yoo, K. Kang, *J Am Chem Soc* **2013**, *135*, 13870-13878.

[360] P. Barpanda, J. N. Chotard, N. Recham, C. Delacourt, M. Ati, L. Dupont, M. Armand, J. M. Tarascon, *Inorg Chem* **2010**, *49*, 7401-7413.

[361] P. Barpanda, G. Oyama, C. D. Ling, A. Yamada, *Chem Mater* **2014**, *26*, 1297-1299.

[362] P. Barpanda, G. Oyama, S. Nishimura, S. C. Chung, A. Yamada, *Nat Commun* **2014**, *5*, 4358.

[363] D. Andre, M. Meiler, K. Steiner, C. Wimmer, T. Soczka-Guth, D. U. Sauer, *J Power Sources* **2011**, *196*, 5334-5341.

[364] M. K. Devaraju, I. Honma, *Adv Energy Mater* **2012**, *2*, 284-297.

[365] B. Zhao, Y. Jiang, H. Zhang, H. Tao, M. Zhong, Z. Jiao, *J Power Sources* **2009**, *189*, 462-466.

[366] Y. Wang, Y. Wang, E. Hosono, K. Wang, H. Zhou, *Angew Chem Int Ed Engl* **2008**, *47*, 7461-7465.

[367] Z. Chen, J. R. Dahn, *J Electrochem Soc* **2002**, *149*, A1184-A1189.

[368] D. Zhang, X. Yu, Y. Wang, R. Cai, Z. Shao, X.-Z. Liao, Z.-F. Ma, *J Electrochem Soc* **2009**, *156*, A802-A808.

[369] A. V. Murugan, T. Muraliganth, A. Manthiram, *J Phys Chem C* **2008**, *112*, 14665-14671.

[370] C. Ban, W.-J. Yin, H. Tang, S.-H. Wei, Y. Yan, A. C. Dillon, *Adv Energy Mater* **2012**, *2*, 1028–1032.

[371] G. X. Wang, S. Bewlay, S. A. Needham, H. K. Liu, R. S. Liu, V. A. Drozd, J.-F. Lee, J. M. Chen, *J Electrochem Soc* **2006**, *153*, A25-A31.

[372] D. P. Singh, F. M. Mulder, A. M. Abdelkader, M. Wagemaker, *Adv Energy Mater* **2013**, *3*, 572-578.

[373] C. Nan, J. Lu, L. Li, L. Li, Q. Peng, Y. Li, *Nano Res* **2013**, *6*, 469-477.

[374] Y. Wang, P. He, H. Zhou, *Energy Environ Sci* **2011**, *4*, 805-817.

[375] L. Wang, G. C. Liang, X. Q. Ou, X. K. Zhi, J. P. Zhang, J. Y. Cui, *J Power Sources* **2009**, *189*, 423-428.

[376] S. H. Ju, Y. C. Kang, *Mater Chem Phys* **2008**, *107*, 328-333.

[377] J. D. Wilcox, M. M. Doeff, M. Marcinek, R. Kostecki, *J Electrochem Soc* **2007**, *154*, A389-A395.

[378] S. H. Luoa, Z. L. Tang, J. B. Lu, Z. T. Zhang, *Chin Chem Lett* **2007**, *18*, 237-240.

[379] Y. Huang, H. Ren, S. Yin, Y. Wang, Z. Peng, Y. Zhou, *J Power Sources* **2010**, *195*, 610-613.

[380] S.-X. Zhao, H. Ding, Y.-C. Wang, B.-H. Li, C.-W. Nan, *J Alloys Compd* **2013**, *566*, 206-211.

[381] M. Pan, Z. Zhou, *Materials Letters* **2011**, *65*, 1131-1133.

[382] T. Nakamura, Y. Miwa, M. Tabuchi, Y. Yamada, *J Electrochem Soc* **2006**, *153*, A1108-A1114.

[383] S. Yu, S. Dan, G. Luo, W. Liu, Y. Luo, X. Yu, Y. Fang, *J Solid State Electrochem* **2012**, *16*, 1675-1681.

[384] Z. Zhu, F. Cheng, J. Chen, *J Mater Chem A* **2013**, *1*, 9484-9490.

[385] Z. Zheng, Y. Wang, A. Zhang, T. Zhang, F. Cheng, Z. Tao, J. Chen, *J Power Sources* **2012**, *198*, 229-235.

[386] Y. Wang, Z. Liu, S. Zhou, *Electrochim Acta* **2011**, *58*, 359-363.

[387] X. Yang, F. Mou, L. Zhang, G. Peng, Z. Dai, Z. Wen, *J Power Sources* **2012**, *204*, 182-186.

[388] K. Bazzi, B. P. Mandal, M. Nazri, V. M. Naik, V. K. Garg, A. C. Oliviera, P. P. Vaishnava, G. A. Nazri, R. Naik, *J Power Sources* **2014**, 67-74.

[389] J. Li, L. Zhang, L. Zhang, W. Hao, H. Wang, Q. Qu, H. Zheng, *J Power Sources* **2014**, *249*, 311-319.

[390] W. L. Liu, J. P. Tu, Y. Q. Qiao, J. P. Zhou, S. J. Shi, X. L. Wang, C. D. Gu, *J Power Sources* **2011**, *196*, 7728-7735.

[391] M. E. Zhong, Z. T. Zhou, *Mater Chem Phys* **2010**, *119*, 428-431.

[392] Y. Yin, M. Gao, H. Pan, L. Shen, X. Ye, Y. Liu, P. S. Fedkiw, *J Power Sources* **2012**, *199*, 256-262.

[393] R. Chen, Y. Wu, X. Y. Kong, *J Power Sources* **2014**, 246-252.

[394] Y.-F. Wu, Y.-N. Liu, S.-W. Guo, S.-N. Zhang, T.-N. Lu, Z.-M. Yu, C.-S. Li, Z.-P. Xi, *J Power Sources* **2014**, 336-344.

[395] B. Yao, Z. Ding, J. Zhang, X. Feng, L. Yin, *J Solid State Chem* **2014**, 9-12.

[396] J. Guo, L. Chen, X. Zhang, H. Chen, L. Tang, *Materials Letters* **2013**, *106*, 290-293.

[397] Y. Xing, Y.-B. He, B. Li, X. Chu, H. Chen, J. Ma, H. Du, F. Kang, *Electrochim Acta* **2013**, *109*, 512-518.

[398] Z. Chen, M. Xu, B. Du, H. Zhu, T. Xie, W. Wang, *J Power Sources* **2014**, *272*, 837-844.

[399] A. B. D. Nandiyanto, K. Okuyama, *Adv Powder Technol* **2011**, *22*, 1-19.

[400] S. Wang, T. Langrish, *Food Res Int* **2009**, *42*, 13-25.

[401] F. Iskandar, *Adv Powder Technol* **2009**, *20*, 283-292.

[402] K. Okuyama, I. W. Lenggoro, *Chem Eng Sci* **2003**, *58*, 537-547.

[403] Z. Bi, X. Zhang, W. He, D. Min, W. Zhang, *RSC Adv* **2013**, *3*, 19744-19751.

[404] B. Zou, Y. Wang, S. Zhou, *Materials Letters* **2013**, *92*, 300-303.

[405] A. Abdel-Kader, A. Ammar, S. Saleh, *Thermochim Acta* **1991**, *176*, 293-304.

[406] R. Dominko, J. Goupil, M. Bele, M. Gaberscek, M. Remskar, D. Hanzel, J. Jamnik, *J Electrochem Soc* **2005**, *152*, A858-A863.

[407] J. Liu, T. E. Conry, X. Song, M. M. Doeff, T. J. Richardson, *Energy Environ Sci* **2011**, *4*, 885-888.

[408] C. Sun, S. Rajasekhara, J. B. Goodenough, F. Zhou, *J Am Chem Soc* **2011**, *133*, 2132-2135.

[409] A. Vu, A. Stein, *Chem Mater* **2011**, *23*, 3237-3245.

[410] X. Zeng, J. Li, N. Singh, *Crit Rev Env Sci Technol* **2014**, *44*, 1129–1165.

[411] B. Scrosati, J. Hassoun, Y.-K. Sun, *Energy Environ Sci* **2011**, *4*, 3287-3295.

[412] M. Yoshio, R. J. Brodd, A. Kozawa, *Lithium-Ion Batteries*, Springer Science+Business Media, **2009**.

[413] T. Nagaura, K. Tozawa, *Progress in Batteries & Solar Cells* **1990**, *9*, 209-217.

[414] L.-X. Yuan, Z.-H. Wang, W.-X. Zhang, X.-L. Hu, J.-T. Chen, Y.-H. Huang, J. B. Goodenough, *Energy Environ Sci* **2011**, *4*, 269-284.

[415] S.-Y. Chung, J. T. Bloking, Y.-M. Chiang, *Nat Mater* **2002**, *1*, 123-128.

[416] J. Zhang, L. Zhuo, L. Zhang, C. Wu, X. Zhang, L. Wang, *J Mater Chem* **2011**, *21*, 6975-6980.

[417] N. Li, Z. Chen, W. Ren, F. Li, H. M. Cheng, *Proc Natl Acad Sci U S A* **2012**, *109*, 17360-17365.

[418] Z. Cao, B. Wei, *ACS Nano* **2014**, *8*, 3049-3059.

[419] S. Leijonmarck, A. Cornell, G. Lindbergh, L. Wågberg, *Nano Energy* **2013**, *2*, 794-800.

[420] L. Hu, Y. Cui, *Energy Environ Sci* **2012**, *5*, 6423-6435.

[421] The World Bank Group, *Global Economic Monitor (GEM) Commodities*, http://data.worldbank.org/data-catalog/commodity-price-data, 20.07.2017.

[422] T. Song, B. Sun, *ChemSusChem* **2013**, *6*, 408-410.

[423] B. Dyatkin, V. Presser, M. Heon, M. R. Lukatskaya, M. Beidaghi, Y. Gogotsi, *ChemSusChem* **2013**, *6*, 2269-2280.

[424] H. Koga, H. Tonomura, M. Nogi, K. Suganuma, Y. Nishina, *Green Chem* **2016**, *18*, 1117-1124.

[425] L. Hu, N. Liu, M. Eskilsson, G. Zheng, J. McDonough, L. Wågberg, Y. Cui, *Nano Energy* **2013**, *2*, 138-145.

[426] J.-Q. Huang, H.-J. Peng, X.-Y. Liu, J.-Q. Nie, X.-B. Cheng, Q. Zhang, F. Wei, *J Mater Chem A* **2014**.

[427] R. Berenguer, F. García-Mateos, R. Ruiz-Rosas, D. Cazorla-Amorós, E. Morallón, J. Rodríguez-Mirasol, T. Cordero, *Green Chem* **2016**.

[428] N. Jayaprakash, N. Kalaiselvi, Gangulibabu, D. Bhuvaneswari, *J Solid State Electrochem* **2010**, *15*, 1243-1251.

[429] L. C. Zhang, Z. Hu, L. Wang, F. Teng, Y. Yu, C. H. Chen, *Electrochim Acta* **2013**, *89*, 310-316.

[430] L. Jabbour, C. Gerbaldi, D. Chaussy, E. Zeno, S. Bodoardo, D. Beneventi, *J Mater Chem* **2010**, *20*, 7344-7347.

[431] L. Jabbour, M. Destro, C. Gerbaldi, D. Chaussy, N. Penazzi, D. Beneventi, *J Mater Chem* **2012**, *22*, 3227-3233.

[432] L. Jabbour, M. Destro, D. Chaussy, C. Gerbaldi, N. Penazzi, S. Bodoardo, D. Beneventi, *Cellulose* **2013**, *20*, 571-582.

[433] B. S. Lalia, T. Shah, R. Hashaikeh, *J Power Sources* **2015**, *278*, 314-319.

[434] X. l. Huang, R. z. Wang, D. Xu, Z. l. Wang, H. g. Wang, J. j. Xu, Z. Wu, Q. c. Liu, Y. Zhang, X. b. Zhang, *Adv Funct Mater* **2013**, *23*, 4345-4353.

[435] Q. Pang, L. Wang, H. Yang, L. Jia, X. Pan, C. Qiu, *RSC Adv* **2014**, *4*, 41212-41218.

[436] X. Ju, M. Bowden, E. E. Brown, X. Zhang, *Carbohydr Polym* **2015**, *123*, 476-481.

[437] A. P. Voronov, G. N. Babenko, V. M. Puzikov, A. N. Iurchenko, *J Cryst Growth* **2013**, *374*, 49-52.

[438] G. X. Wang, H. Liu, J. Liu, S. Qiao, G. M. Lu, P. Munroe, H. Ahn, *Advanced Materials* **2010**, *22*, 4944-4948.

[439] B. Kang, G. Ceder, *Nature* **2009**, *458*, 190-193.

[440] L. Yang, G. Liang, L. Wang, X. Zhi, X. Ou, *J Alloys Compd* **2010**, *496*, 376-379.

[441] X. Xie, K. Kretschmer, J. Zhang, B. Sun, D. Su, G. Wang, *Nano Energy* **2015**, *13*, 208-217.

[442] S.-L. Chou, Y. Pan, J.-Z. Wang, H.-K. Liu, S.-X. Dou, *Phys Chem Chem Phys* **2014**, *16*, 20347-20359.

[443] K. Kirshenbaum, D. C. Bock, C.-Y. Lee, Z. Zhong, K. J. Takeuchi, A. C. Marschilok, E. S. Takeuchi, *Science* **2015**, *347*, 149-154.

[444] N. J. Dudney, J. Li, *Science* **2015**, *347*, 131-132.

[445] S. Yang, Y. Song, P. Y. Zavalij, M. S. Whittingham, *Electrochem Commun* **2002**, *4*, 239-244.

[446] J.-Z. Wang, S.-L. Chou, J. Chen, S.-Y. Chew, G.-X. Wang, K. Konstantinov, J. Wu, S.-X. Dou, H. K. Liu, *Electrochem Commun* **2008**, *10*, 1781-1784.

[447] M. Thackeray, *Nat Mater* **2002**, *1*, 81-82.

[448] N. Zhou, E. Uchaker, H.-Y. Wang, M. Zhang, S.-Q. Liu, Y.-N. Liu, X. Wu, G. Cao, H. Li, *RSC Adv* **2013**, *3*, 19366–19374.

[449] V. Palomares, P. Serras, I. Villaluenga, K. B. Hueso, J. Carretero-González, T. Rojo, *Energy Environ Sci* **2012**, *5*, 5884-5901.

[450] J. B. Goodenough, K. S. Park, *J Am Chem Soc* **2013**, *135*, 1167-1176.

[451] X. Xiang, K. Zhang, J. Chen, *Adv Mater* **2015**, *27*, 5343-5364.

[452] Y. Uebou, T. Kiyabu, S. Okada, J.-i. YAMAKI, *九州大学機能物質科学研究所報告* **2002**, *16*, 1-5.

[453] S. Y. Lim, H. Kim, R. Shakoor, Y. Jung, J. W. Choi, *J Electrochem Soc* **2012**, *159*, A1393-A1397.

[454] J. Goodenough, H.-P. Hong, J. Kafalas, *Mater Res Bull* **1976**, *11*, 203-220.

[455] J. Maier, *Faraday discussions* **2014**, *176*, 17-29.

[456] C. Zhu, P. Kopold, P. A. van Aken, J. Maier, Y. Yu, *Adv Mater* **2016**, *28*, 2409-2416.

[457] J. Kang, S. Baek, V. Mathew, J. Gim, J. Song, H. Park, E. Chae, A. K. Rai, J. Kim, *J Mater Chem* **2012**, *22*, 20857-20860.

[458] K. Saravanan, C. W. Mason, A. Rudola, K. H. Wong, P. Balaya, *Adv. Energy Mater.* **2013**, *3*, 444-450.

[459] W. Shen, C. Wang, H. Liu, W. Yang, *Chem Eur J* **2013**, *19*, 14712-14718.

[460] S. Kajiyama, J. Kikkawa, J. Hoshino, M. Okubo, E. Hosono, *Chem Eur J* **2014**, *20*, 12636-12640.

[461] C. Zhu, K. Song, P. A. van Aken, J. Maier, Y. Yu, *Nano Lett.* **2014**, *14*, 2175-2180.

[462] G. Li, D. Jiang, H. Wang, X. Lan, H. Zhong, Y. Jiang, *J Power Sources* **2014**, *265*, 325-334.

[463] D. Wang, N. Chen, M. Li, C. Wang, H. Ehrenberg, X. Bie, Y. Wei, G. Chen, F. Du, *J Mater Chem A* **2015**, *3*, 8636-8642.

[464] Y. Jiang, Z. Yang, W. Li, L. Zeng, F. Pan, M. Wang, X. Wei, G. Hu, L. Gu, Y. Yu, *Adv Energy Mater* **2015**, *5*, 1402104.

[465] J. Mao, C. Luo, T. Gao, X. Fan, C. Wang, *J Mater Chem A* **2015**, *3*, 10378-10385.

[466] H. Li, X. Bi, Y. Bai, Y. Yuan, R. Shahbazian-Yassar, C. Wu, F. Wu, J. Lu, K. Amine, *Adv Mater Interfaces* **2016**, *3*, 1500740.

[467] Y. Jiang, Y. Yao, J. Shi, L. Zeng, L. Gu, Y. Yu, *ChemNanoMat* **2016**, *2*, 726-731.

[468] Y. Fang, L. Xiao, X. Ai, Y. Cao, H. Yang, *Adv Mater* **2015**, *27*, 5895-5900.

[469] J. Yang, D.-W. Han, M. R. Jo, K. Song, Y.-I. Kim, S.-L. Chou, H.-K. Liu, Y.-M. Kang, *J Mater Chem A* **2015**, *3*, 1005-1009.

[470] H. Li, Y. Bai, F. Wu, Q. Ni, C. Wu, *Solid State Ion* **2015**, *278*, 281-286.

[471] Y. H. Jung, C. H. Lim, D. K. Kim, *J Mater Chem A* **2013**, *1*, 11350-11354.

[472] J. Z. Guo, X. L. Wu, F. Wan, J. Wang, X. H. Zhang, R. S. Wang, *Chem Eur J* **2015**, *21*, 17371-17378.

[473] X. Rui, W. Sun, C. Wu, Y. Yu, Q. Yan, *Adv Mater* **2015**, *27*, 6670-6676.

[474] Y. Zhou, X. Rui, W. Sun, Z. Xu, Y. Zhou, W. J. Ng, Q. Yan, E. Fong, *ACS Nano* **2015**, *9*, 4628-4635.

[475] Q. Wang, B. Zhao, S. Zhang, X. Gao, C. Deng, *J Mater Chem A* **2015**, *3*, 7732-7740.

[476] W. Zhang, Y. Liu, C. Chen, Z. Li, Y. Huang, X. Hu, *Small* **2015**, *11*, 3822-3829.

[477] K. Kretschmer, B. Sun, X. Xie, S. Chen, G. Wang, *Green Chem* **2016**, *18*, 2691-2698.

[478] X. Xie, T. Makaryan, M. Zhao, K. L. Van Aken, Y. Gogotsi, G. Wang, *Adv Energy Mater* **2015**, *6*, 1502161.

[479] K. Lee, I. Oh, J. Kweon, C. Lee, S. Ahn, *Mater Chem Phys* **2012**, *136*, 802-808.

[480] A. P. Voronov, G. N. Babenko, V. M. Puzikov, A. N. Iurchenko, *J. Cryst. Growth* **2013**, *374*, 49-52.

[481] S. Li, K. Huang, S. Liu, D. Fang, X. Wu, D. Lu, T. Wu, *Electrochim Acta* **2011**, *56*, 5483-5487.

[482] C. Wang, H. Liu, W. Yang, *J Mater Chem* **2012**, *22*, 5281-5285.

[483] W. Song, X. Ji, Y. Zhu, H. Zhu, F. Li, J. Chen, F. Lu, Y. Yao, C. Banks, *ChemElectroChem* **2014**, *1*, 871-876.

[484] W. Song, X. Ji, Z. Wu, Y. Zhu, Y. Yang, J. Chen, M. Jing, F. Li, C. E. Banks, *J Mater Chem A* **2014**, *2*, 5358-5362.

[485] Y. Zhu, X. Han, Y. Xu, Y. Liu, S. Zheng, K. Xu, L. Hu, C. Wang, *ACS Nano* **2013**, *7*, 6378-6386.

[486] J. Jin, Z.-Q. Shi, C.-Y. Wang, *Electrochim Acta* **2014**, *141*, 302-310.

[487] H. Li, F. Shen, W. Luo, J. Dai, X. Han, Y. Chen, Y. Yao, H. Zhu, K. Fu, E. Hitz, L. Hu, *ACS Appl Mater Interfaces* **2016**, *8*, 2204-2210.

[488] J. Zhu, D. Yang, Z. Yin, Q. Yan, H. Zhang, *Small* **2014**, *10*, 3480-3498.

[489] M. Lee, J. Hong, H. Kim, H. D. Lim, S. B. Cho, K. Kang, C. B. Park, *Adv Mater* **2014**, *26*, 2558-2565.

[490] Y. Zhu, X. Fan, L. Suo, C. Luo, T. Gao, C. Wang, *ACS Nano* **2015**, *10*, 1529-1538.

[491] M. Stern, A. L. Geary, *J Electrochem Soc* **1957**, *104*, 56-63.

[492] W. L. Liu, J. P. Tu, Y. Q. Qiao, J. P. Zhou, S. J. Shi, X. L. Wang, C. D. Gu, *J. Power Sources* **2011**, *196*, 7728-7735.

[493] J. Li, L. Zhang, L. Zhang, W. Hao, H. Wang, Q. Qu, H. Zheng, *J. Power Sources* **2014**, *249*, 311-319.

[494] R. Chen, Y. Wu, X. Y. Kong, *J. Power Sources* **2014**, *258*, 246-252.

[495] Z. Ma, G. Shao, Y. Fan, G. Wang, J. Song, T. Liu, *ACS Appl. Mater. Interfaces* **2014**, *6*, 9236-9244.

[496] Z. Chen, M. Xu, B. Du, H. Zhu, T. Xie, W. Wang, *J. Power Sources* **2014**, *272*, 837-844.

[497] H. Liu, P. Zhang, G. Li, Q. Wu, Y. Wu, *J Solid State Electrochem* **2008**, *12*, 1011-1015.